Modelling Lung Physiology and Biology Using Novel Techniques



Haopeng Xu

St Edmund Hall

University of Oxford

A thesis submitted for the degree of

Doctor of Philosophy

Trinity term 2025

Abstract

Asthma remains a significant global health burden, associated with high morbidity, mortality and widespread societal impact. Nitric oxide (NO), commonly measured as the fractional exhaled nitric oxide (FeNO), is a byproduct of type-2 inflammation in conducting airways. Although FeNO has been recognised as a valuable biomarker in the diagnosis and management of asthma, there is no established methodology for estimating NO production depth along the airways, which may provide valuable insights into asthma pathophysiology and its management.

This thesis presents the development of such methodology with the following approach adopted: (i) Measurement of NO (and CO_2) expirograms using a novel Rapid FeNO Device (RFD) and estimation of the personalised parameters of lung physiology using Computed Cardiopulmonography(CCP); (ii) Development of a Dead Space Pipes (DSP) model that incorporates measurements from the RFD and CCP to reconstruct simulated NO expirograms ('wallpaper'); (iii) Derivation of NO depth parameters by comparing the 'wallpaper' with measured NO profiles, reflecting depth and spread of NO production; (iv) Development of a quality control criteria to assess breath-by-breath data quality. Finally, a study with human volunteers demonstrated the repeatability and reliability of these NO depth parameters.

The thesis subsequently presents preliminary clinical studies to demonstrate the application and potential of this methodology in clinical settings. Applying this methodology, I found that treatment-naïve individuals with asthma (TN group) had a more proximal NO depth production site, which was also more widely spread along the airways, compared with patients with more severe difficult-to-treat asthma receiving high-dose inhaled corticosteroid (ICS), referred to as the HD group. Further follow-up studies showed that the TN group

initiating low-dose ICS had no change in NO depth parameters, while a subgroup of the HD group demonstrated a reduction in NO depth following anti-IL5/5R therapy. Furthermore, bronchodilator administration had no effect on the NO depth parameters.

In addition, CCP is introduced as a tool for measuring lung inhomogeneity and providing personalised lung physiological parameters. Its application in two clinical studies in healthy volunteers with high type-2 biomarkers and patients with asthma is presented to demonstrate its sensitivity as an emerging lung function measurement.

Additionally, the thesis includes a separate section providing an overview of published work on $\dot{V}/\dot{Q}$ distributions in severe COVID-19 patients, completed during the pandemic period when I was not able to conduct experimental work.

Acknowledgement

I would first like to express my sincere gratitude to my supervisors, Prof Nayia Petousi, Prof Peter Robbins, and Prof Ian Pavord. I am especially grateful for the weekly discussions with Nayia, which not only fostered a shared vision for the projects but, more importantly, provided unwavering support through each personal and academic challenge. I will always remember the sessions with Peter, whose extraordinary expertise guided me through challenges within or beyond the field of physiology. Conversations with Ian are always inspiring, integrating basic scientific understanding with clinical perspectives and helping to shape the direction of the project.

The completion of this project would not have been possible without the invaluable guidance and support of Dr Lorenzo Petralia. His guidance ranged from understanding the mechanics of the Rapid FeNO Device to grasping the underlying principles of physics. I am also deeply grateful to the members of both groups — Prof Grant Ritchie, Dr Graham Richmond, Dr Asma Alamoudi, Dr Nicholas Smith, Dr Nick Talbot, Dr Dominic Sadhu, Dr Jessica Luiz and Dr Tishan Wellalagodage —for their consistent support and assistance whenever I sought it.

I am profoundly thankful to all the volunteers and patients involved in the clinical studies, whose generous contributions of time and dedication were essential to this research. I am equally grateful to the clinical team, including Ms Catherine Borg, Ms Laura Bermejo

Sánchez, Mr Jack Seymour, Ms Liz Gamlen, Dr James Melhorn and all the clinicians and nurses at the clinic, for their invaluable support in coordinating study visits, recruiting participants, and offering valuable insights into the disease process. Their collective efforts were indispensable to the smooth and successful execution of the clinical research.

Furthermore, I am grateful to the COI and St Edmund Hall for their ongoing support within and beyond my academic development.

I would like to sincerely thank all my friends and family, whose companionship and support over the years have helped me navigate the difficulties encountered during the completion of this thesis.

Above all, I owe my heartfelt thanks to my parents for their unconditional support and encouragement throughout every stage of my life.

Contents

Abstract **I**

Acknowledgement **III**

Contents **i**

1 Introduction **1**

1.1 Motivation for the research 1

1.2 Asthma 3

1.2.1 Asthma diagnosis 3

1.2.2 Phenotypes and endotypes of asthma 4

1.2.3 Pathophysiology of T2H asthma 7

1.2.4 T2H asthma biomarkers 11

1.2.4.1 Fractional exhaled nitric oxide (FeNO) 11

1.2.4.2 Blood eosinophil count (BEC) 12

1.2.5 Management of T2H asthma 13

1.3 Respiratory system 17

1.3.1 Anatomy of the lung 17

1.3.2 Ventilation and deadspace 18

1.3.3 Measurement of dead space volume 20

1.3.4 Pulmonary circulation and gas exchange 22

1.3.5 Ventilation-perfusion ratio($\dot{V}/\dot{Q}$) 23

1.4 Pulmonary function test(PFT) techniques 24

1.4.1 Spirometry 24

1.4.2 Body plethysmography 27

1.4.3 Impulse oscillometry 27

1.4.4 Lung inhomogeneity 28

1.4.4.1 MBW 28

1.4.4.2 CCP 29

1.5 NO production mechanism and measurement 29

1.5.1 Mechanisms of NO production 29

1.5.2 NO measurement techniques 30

1.5.2.1 Chemiluminescence sensor 31

1.5.2.2 Electrochemical sensor 31

1.5.2.3 Laser-based sensor 31

1.5.3 NO production and transport model 32

1.5.3.1 Theoretical development 32

1.5.3.2 Clinical applications 35

1.5.3.3 Limitations of the current model 36

1.6 Thesis outline 37

2 Measuring lung inhomogeneity using Computed Cardiopulmonography (CCP) 39

2.1 Introduction to CCP 40

2.1.1 Molecular flow sensor (MFS) 40

2.1.2 The cardiopulmonary mathematical model 43

2.1.2.1 LNL model 44

2.1.2.2 Physicochemical model of gas dissolution 46

2.1.2.3 Circulation and body gas stores (CBGS) 46

2.1.3 Standardised protocol for CCP 46

2.1.3.1 Measurement protocol 46

2.1.3.2 Data fitting protocol 47

2.1.3.3 Key parameters used in this thesis 49

2.1.4 Summary of results from previous clinical studies on lung inhomogeneity 49

2.2 Lung inhomogeneity assessment using CCP in healthy individuals with elevated Type-2 high (T2H) biomarkers 52

2.2.1 Aims and hypothesis 52

2.2.2 Epidemiology screening study 53

2.2.2.1 Participants and protocol 53

2.2.2.2 Results 53

2.2.3 Lung inhomogeneity in volunteers with T2H inflammation 55

2.2.3.1 Methods 55

2.2.3.2 Results 56

2.2.3.3 Discussion 60

2.3 Lung inhomogeneity in patients with asthma receiving inhaled or systemic corticosteroids 61
2.3.1 Aims and hypothesis 61
2.3.2 Methods 61
2.3.2.1 Participants and protocol 62
2.3.2.2 Statistical analysis: 63
2.3.3 Results 63
2.3.3.1 Baseline data 64
2.3.3.2 Effects of corticosteroid treatment 66
2.3.4 Discussion 69
2.4 Summary 70
2.5 Supplementary material 71
3 Novel measurement for locating the production of nitric oxide (NO) in the conducting airways – the Rapid FeNO Device (RFD) 77
3.1 RFD design 78
3.2 Reconstruction of the NO expirogram from the CEAS to the DAS 82
3.3 Experimental protocol for measuring NO production depth in the conducting airways 87
3.3.1 Experimental protocol 87
3.3.2 Key factors related to data collection 90
3.4 Summary 92
4 Novel measurement for locating the production of nitric oxide (NO) in the conducting airways – the Dead Space Pipes (DSP) Model and the derivation of NO depth parameters 93

4.1 The DSP model 95

4.1.1 Structure of the DSP model 97

4.1.2 General principles and assumptions of the DSP model 98

4.1.3 Construction of the simulated CO_2 expirogram and fitting to measured CO_2 data 99

4.1.3.1 Concept of the single-pipe model 99

4.1.3.2 Concept of the three-pipe model 100

4.1.3.3 Extension of the multiple-pipe model based on CCP outputs 102

4.1.3.4 Fitting of simulated CO_2 expirogram to measured CO_2 data 103

4.1.4 Construction of the simulated NO expirogram 104

4.1.4.1 Speed-independent (SpIn) mode of simulating NO expirogram 105

4.1.4.2 Issues associated with SpIn mode 106

4.1.4.3 Speed-dependent (SpD) mode 108

4.1.5 Fitting process of the DSP model 112

4.1.5.1 Retrieving the alveolar CO_2 concentration (C_{alv,CO_2}) 113

4.1.5.2 Fitting the dead space volume correction(dV) 115

4.1.5.3 Retrieving NO production rate (r_0) 115

4.1.6 Summary 115

4.2 Derivation of NO depth parameters 116

4.2.1 Methods for determination of NO depth parameters 117

4.2.2 Approach to acquiring NO depth parameters 118

4.3 Summary 120

5 Novel measurement for locating the production location of nitric oxide (NO) in conducting airways - Quality control and repeatability/reliability assessment 123

5.1 Quality assessment of NO depth measurement 123

5.1.1 Overview 123

5.1.2 Four determinant factors and their detectable signals 125

5.1.2.1 Setup of the special breath duration (Reason I) 125

5.1.2.2 Contamination from the nasal cavity (Reason II) 126

5.1.2.3 Speed control in special breath (Reason III) 129

5.1.2.4 Model fitting failure (Reason IV) 134

5.1.3 Quality assessment guidelines 137

5.1.4 Retrieving NO depth parameters for each visit 138

5.1.5 Summary 138

5.2 Repeatability and reliability of NO depth parameters 140

5.2.1 Methods 140

5.2.1.1 Participants and protocol 140

5.2.1.2 Comparison of NIOX FeNO measurement and RFD FeNO plateau measurements 142

5.2.1.3 Repeatability and reliability of NO depth parameters 142

5.2.1.4 Statistical analysis 144

5.2.2 Results 144

5.2.2.1 Participants demographic data 144

5.2.2.2 Correlation of FeNO value measurements between NIOX and RFD 145

5.2.2.3 Lung physiology of participants during the test period 146

5.2.2.4 Repeatability and reliability of NO depth parameters 147

5.2.3 Discussion 149

5.3 Determination of the DSP mode for future studies 152

5.4 Conclusion 153

6 Novel measurement for locating the production location of nitric oxide (NO) in conducting airways - Clinical studies 155

6.1 Methods 156

6.1.1 Study protocol 156

6.1.2 Statistical analysis 157

6.2 NO depth parameters in the Healthy (control) group 157

6.2.1 Participants 157

6.2.2 Results 158

6.2.2.1 Basic characteristics of healthy volunteers 158

6.2.2.2 Physiological parameters 158

6.2.2.3 NO Depth parameters in healthy volunteers 159

6.2.2.4 Correlations between depth parameters and other parameters 159

6.2.3 Discussion 160

6.3 Cross-sectional study of NO depth parameters in patients with asthma 162

6.3.1 Introduction 162

6.3.2 Participants....162
6.3.3 Results....163
6.3.3.1 Baseline characteristics....163
6.3.3.2 Lung physiology parameters....163
6.3.3.3 NO depth parameters....164
6.3.3.4 Correlation between NO depth parameters and other variables....165
6.3.4 Discussion....167
6.4 Effects of ICS treatment on NO depth parameters in the TN group....170
6.4.1 Introduction....171
6.4.2 Methods....171
6.4.3 Results....171
6.4.3.1 Changes in biomarkers and physiological parameters....171
6.4.3.2 Depth parameters change....173
6.4.4 Discussion....174
6.5 Effects of biologics (anti-IL5/5R) therapy on NO depth parameters in the HD group 175
6.5.1 Introduction....175
6.5.2 Methods....176
6.5.3 Results....176
6.5.3.1 Basic characteristics of anti-IL5/5R group....176
6.5.3.2 Changes in physiological parameters during biologics therapy....176
6.5.3.3 Depth parameters change....178
6.5.4 Discussion....179

6.6 Summary 182

6.7 BD effects on NO depth parameters 183

6.7.1 Participants 184

6.7.2 Results 184

6.7.2.1 Basic characteristics 184

6.7.2.2 Physiological parameters and CCP parameters 184

6.7.2.3 Depth parameters 185

6.7.2.4 Correlation analysis 186

6.7.3 Discussion 186

6.8 Summary 187

7 Assessment of Ventilation-perfusion ($\dot{V}/\dot{Q}$) in patients with severe COVID-19 189

8 Conclusions and Future Work 191

8.1 Location of NO production within conducting airways 191

8.2 Lung inhomogeneity measured by the CCP 195

8.3 Concluding remarks 196

A Standard Operating Procedure (SOP) for the Rapid FeNO Device (RFD) 197

B Dead Space Pipes (DSP) Model 203

C Identifying putative ventilation-perfusion distributions in COVID-19 pneumonia (published) 229

Bibliography 259

Chapter 1

Introduction

This Chapter begins by outlining the motivation behind the research questions and hypotheses. It then presents a review of the relevant background literature. First, the Chapter introduces the topic of asthma, with a particular focus on type 2-high (T2H) asthma, to provide context for the target disease. This is followed by a review of lung physiology, pulmonary function tests (PFTs) and the process of nitric oxide (NO) production in the airways, all of which are essential background for understanding the methodology adopted in this thesis. Finally, the Chapter concludes by outlining the overall structure of this thesis.

1.1 Motivation for the research

Asthma is a chronic inflammatory airway disease characterised by reversible airway obstruction caused by various factors. It is one of the most prevalent chronic airway diseases. According to the *Lancet* Global Disease Burden summary, asthma has a global prevalence of 3.3% and an incidence of 0.5%. Despite advancements in diagnosis and management, it remains a significant global health concern, accounting for 21.4 million disability-adjusted life years (DALYs) and approximately 436,000 deaths annually[1].

In the UK, approximately 7.2 million people have been diagnosed with asthma, with 12,000 deaths recorded over the past decade[2, 3]. A study estimated that the net present value

of the impact of asthma on the environment, healthcare and society will reach £47 billion between 2022 and 2031[4].

Asthma is diagnosed by recognising patterns of variable symptoms (e.g., wheeze, cough, breathlessness, chest tightness and others) alongside objective evidence while excluding other differential diagnoses[5, 6]. Traditionally, objective evidence has included spirometry, peak expiratory flow (PEF) and bronchial challenge testing. However, the updated BTS/NICE/SIGN guideline also includes two biomarkers of asthma, fractional exhaled nitric oxide (FeNO) and blood eosinophil count (BEC), as part of the initial objective evidence for diagnosis[6]. Once asthma is diagnosed, patients are prescribed reliever and/or maintainer therapy based on their conditions. Although multiple combinations of potential therapies are available, inflammation suppression remains central to asthma management and is achieved through corticosteroids or biologics, delivered either via the inhaled route or the systemic route. Following the initiation of treatment, several objective tests are recommended at regular intervals to monitor asthma conditions and assess the treatment response, including symptom questionnaires, PFTs and FeNO[5, 6].

According to the guidelines, FeNO has been shown to be widely applicable for diagnosis, monitoring, management and adherence assessment[5, 6]. Its level is well established as an indicator of inflammation intensity, as NO is a byproduct of airway wall inflammation and reflects the degree of inflammatory activity in the airway wall[7]. Additional advantages of FeNO measurement include its rapid measurements, typically completed in less than five minutes, and its non-invasive nature.

It is noteworthy that inflammation in asthma involves the entire airway, including both proximal and distal airways. Current FeNO measurements reflect the average inflammation in the airways. However, even when FeNO levels indicate a similar degree of inflammation, variations in the location of airway inflammation, i.e. axial heterogenicity, may lead to

different disease severity, symptoms, objective test results or response to treatment. Different locations of inflammation may be associated with the severity of asthma development, as they can have varying impacts on gas-conducting efficiency. Furthermore, the delivery methods and types of therapy may influence the location of inflammation, which is associated with treatment responses. Inhalation therapy itself has axial heterogeneity in suppressing inflammation, whereas systemic therapy shows more uniform anti-inflammatory effects. Both of them may be linked to differences in treatment responses. Similarly, both corticosteroids and biologics can suppress inflammation through different pathways, which may further influence the location of inflammation in the airways, resulting in distinct treatment responses. In summary, reflecting the location of inflammation by NO production sites may provide unique insights into inflammation in the airways and, clinically, serve as a biomarker for assessing asthma severity and predicting treatment response.

However, no currently established methodology enables us to estimate the locational distribution of NO production in the conducting airways. This thesis focuses on establishing a comprehensive framework for estimating NO production depth in the conducting airways and presenting clinical studies that demonstrate its application and potential in clinical settings. Apart from the framework itself, this thesis also presents estimation methods and clinical findings on lung inhomogeneity, which are not only valuable assessments in lung physiology but also provide key information for the construction of the NO depth estimation system.

1.2 Asthma

1.2.1 Asthma diagnosis

Asthma diagnosis is based on a combination of suggestive symptoms and objective tests, with alternative diagnoses being excluded[5, 6]. The GINA guideline focuses on spirometry or peak expiratory flow (PEF) as objective tests, whereas the BTS/NICE/SIGN guideline

prioritises the biomarkers (BEC and/or FeNO) as objective tests to support asthma diagnosis(illustrated in **Figure 1.1)**. If these show normal results, spirometry with a bronchodilator reversibility test, PEF variability or a bronchial challenge test can be used as alternative objective tests to support the diagnosis of asthma[6].

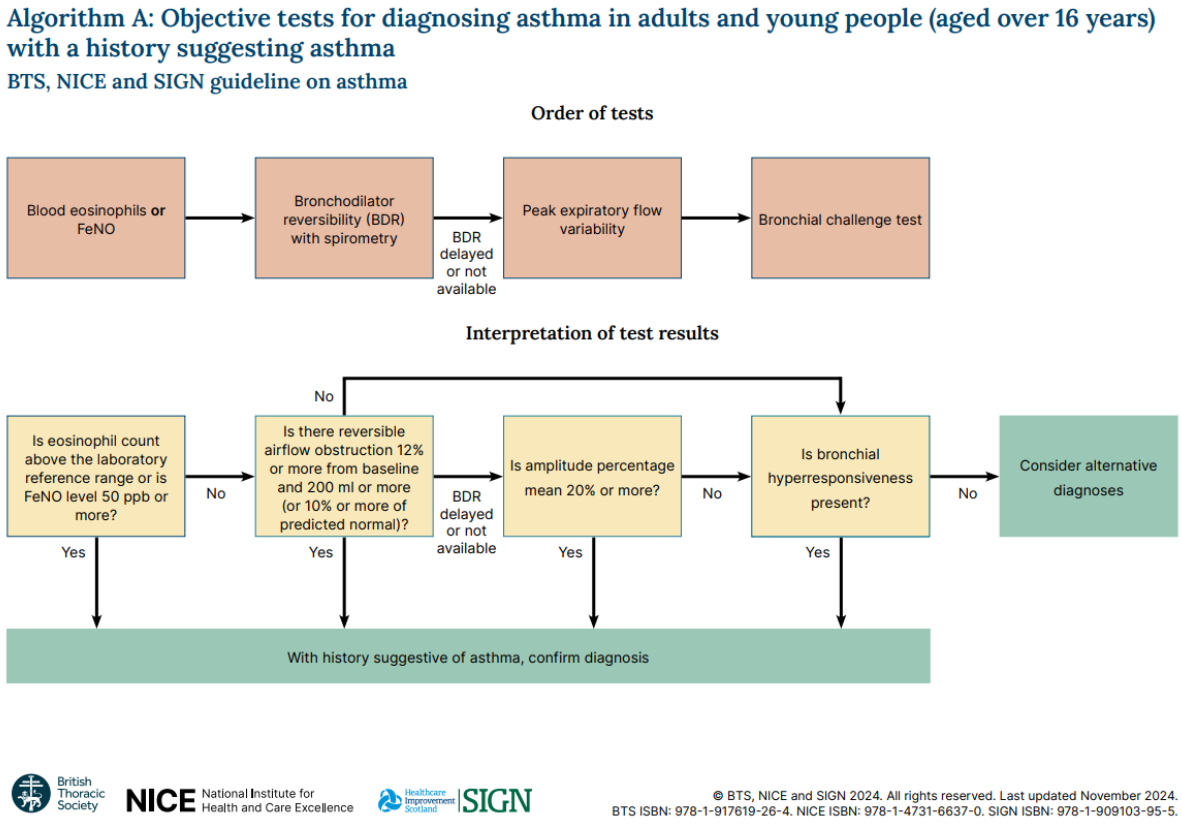


Figure 1.1 Algorithm for objective tests in the diagnosis of asthma in adults. FeNO and blood eosinophils are prioritised in the objective testing, followed by a more traditional bronchodilator test with spirometry. The figure is from the BTS/NICE/SIGN guideline[6].

1.2.2 Phenotypes and endotypes of asthma

The heterogeneous pathogenesis underlying individual patients with asthma leads to variations in clinical presentation and treatment response, underscoring the necessity of defining subtypes of asthma to facilitate precise management. Phenotyping is defined as classification based on clinical presentations, whereas classification based on pathogenic pathways is referred to as endotyping.

The earliest phenotyping efforts classified asthma into 'intrinsic' and 'extrinsic' types[8]. Although this distinction was later found to be inaccurate, it highlighted the heterogeneity of asthma. Later research identified that T helper 2(Th2) cells are more abundant in bronchoalveolar lavage (BAL) fluid in patients with atopic asthma, establishing the foundation for subsequent research [9], which confirmed that Th2-related cytokines, such as interleukin (IL)-4, IL-5 and IL-13, as well as eosinophilic inflammation, are associated asthma[10, 11]. Further discoveries revealed that Th2 cytokines were not only produced by Th2 cells but also by other immune cells, including type 2 innate lymphoid cells(ILC2), mast cells and eosinophils[12].

Accordingly, a distinct and well-characterised asthma phenotype, known as type 2-high (T2H) asthma, was recognised. It is estimated that the proportion of patients with T2H asthma is around 50 - 70%[13-15]. T2H asthma is primarily driven by T2H inflammation involving specific cytokines, IL-4, IL-5, IL-13, and inflammatory cells such as eosinophils, mast cells, ILC2s, Th2 cells and B cells[16] (demonstrated in **Figure 1.2**). As a consequence of increasing cytokines and accumulation of inflammatory cells, two important and easy-to-use biomarkers are recognised in the pathogenic pathway: FeNO and BEC, which serve as indicators of the T2H phenotype.

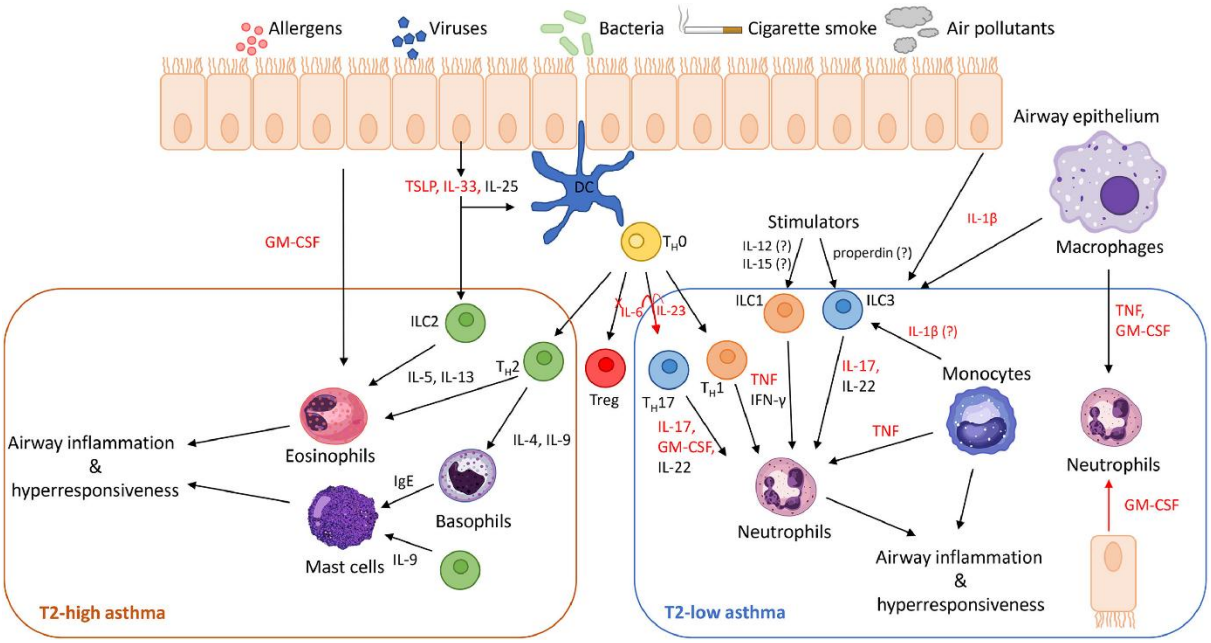


Figure 1.2 Type 2-high (T2H) and type 2-low (T2L) inflammation pathways in asthma. T2H asthma involves eosinophils, mast cells, and dendritic cells. The typical cytokines are IL-4, IL-5 and IL-13. T2L asthma involves neutrophils, IL-1β and IL-17. The figure is from Niessen *et al.*[17].

In contrast, type-2 low (T2L), also shown in **Figure 1.2**, asthma lacks elevated T2H cytokine and is associated with less well-defined cytokines, such as IL-1β and IL-17, as well as lacks established non-invasive biomarkers. It primarily involves neutrophils and is often resistant to corticosteroid therapy[18, 19].

Although asthma is often classified clinically as T2H and T2L, cluster analyses indicate that further heterogeneity exists. This approach has been widely used in large cohorts or cross-sectional studies. The initial study conducted by Hardar *et al.*[20], was followed by several large cohort studies, such as Severe Asthma Research Program (SARP)[21], Unbiased Biomarkers for the Prediction of Respiratory Disease Outcome (U-BIOPRED)[22] and Airways Disease Endotyping for Personalized Therapeutics (ADEPT)[23]. Despite variations in classification methods across studies, a review by Kaur et al.[24] summarised four typical clusters: (1) early-onset mild allergic asthma, (2) early-onset allergic moderate-to-severe

asthma, (3) late-onset nonallergic eosinophilic asthma and (4) late-onset non-eosinophilic nonallergic asthma.

The ultimate goal is to define the 'true endotype', which comprehensively describes the molecular pathways of asthma[25]. As reviewed by Ray et al.[26], a 'true endotype' should clearly define a subgroup of patients with a well-characterised pathophysiological pathway, where targeting this pathway can modulate disease activity. However, current insights remain limited in achieving this goal. In particular, as emerging biologics therapies enable the selective blocking of specific cytokine pathways, inconsistent treatment responses reveal heterogeneity in current asthma endotypes[27].

As this thesis focuses on T2H asthma, the following sections will specifically address it.

1.2.3 Pathophysiology of T2H asthma

The pathophysiology of T2H asthma is driven by T2H inflammation. **Figure 1.3** illustrates the interactions among the various factors contributing to this inflammation. In response to antigen exposure and other stimuli, the airway epithelium undergoes dysfunction and produces thymic stromal lymphopoietin (TSLP), IL-33 and IL-25, which activate several types of immune cells[28]. The activated cells include dendritic cells(DCs), mast cells(MCs), Th2 cells and ILC2s[29]. DCs, located at the basolateral side, interact locally with primed T cells to induce T2H inflammation and also migrate to lymph nodes to interact with naïve T cells[30]. Meanwhile, MCs release bronchoconstrictive mediators, such as leukotrienes and histamine, further contributing to airway constriction[31]. They also infiltrate airway smooth muscles (ASMs), inducing hyperresponsiveness to stimuli. Under normal conditions, ASM maintains a homeostatic state, but triggers induce T2H inflammation and disrupt this balance, leading to excessive constriction[32]. Th2 cells and ILC2s produce the key cytokines in T2H asthma, IL-4, IL-5 and IL-13[33]. The eosinophils recruited to the subepithelial layer undergo degranulation to release key proteins such as major basic proteins (MBP), eosinophil

peroxidase (EPO), eosinophil-derived neurotoxin (EDN) and eosinophils cationic protein(ECP)[34], and secrete cytokines including IL-4 and IL-13[35].

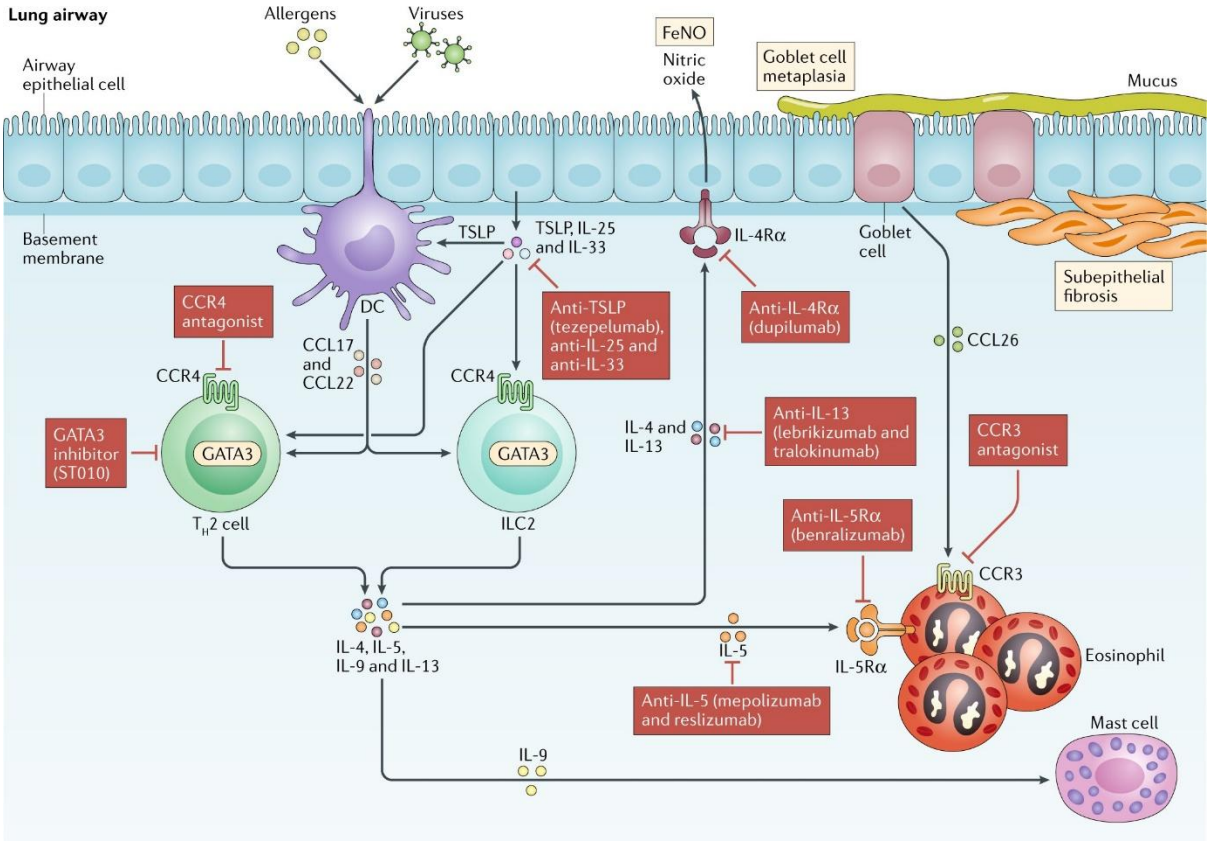


Figure 1.3 Type-2 inflammation in asthma and its targeted therapy. T-helper 2 (TH2) cells and group 2 innate lymphoid cells (ILC2) are triggered by dendritic cells (DCs). The production of IL-5 regulates the development and recruitment of eosinophils, while IL-4 and IL-13 promote nitric oxide (NO) production and mucus overproduction. The activation of mast cells promotes the release of bronchoconstrictive mediators and their infiltration into airway smooth muscle(ASM). The figure is from Barnes *et al.*[36]

The cytokines mentioned above all contributed to the pathogenesis of asthma in various ways. IL-4 plays a crucial role in Th2 cell differentiation and immunoglobulin E (IgE) production by B cells and eosinophil recruitment[14, 37]. IL-5 regulates the growth, differentiation and recruitment of eosinophils into the airways[38]. IL-13 shares function with IL-4 due to their common signal pathway via IL-4Rα and contribute to mucus production and airway remodelling[14, 39](illustrated in **Figure 1.3**). Additionally, elevated IL-4 and/or IL-13 levels can promote inducible nitric oxide synthase (iNOS) expression, resulting in increased

NO production in epithelial cells[40-42]. Furthermore, **Figure 1.3** also shows cytokine targets for suppressing inflammation through monoclonal antibodies, which will be discussed in the following sections on asthma management.

As illustrated in **Figure 1.4**, the pathways described above lead to a series of physiological alterations, including epithelial dysfunction, goblet cell hyperplasia, airway smooth muscle (ASM) pathology and airway remodelling, which underlie the clinical symptoms and objective test abnormalities observed in T2H asthma[43].

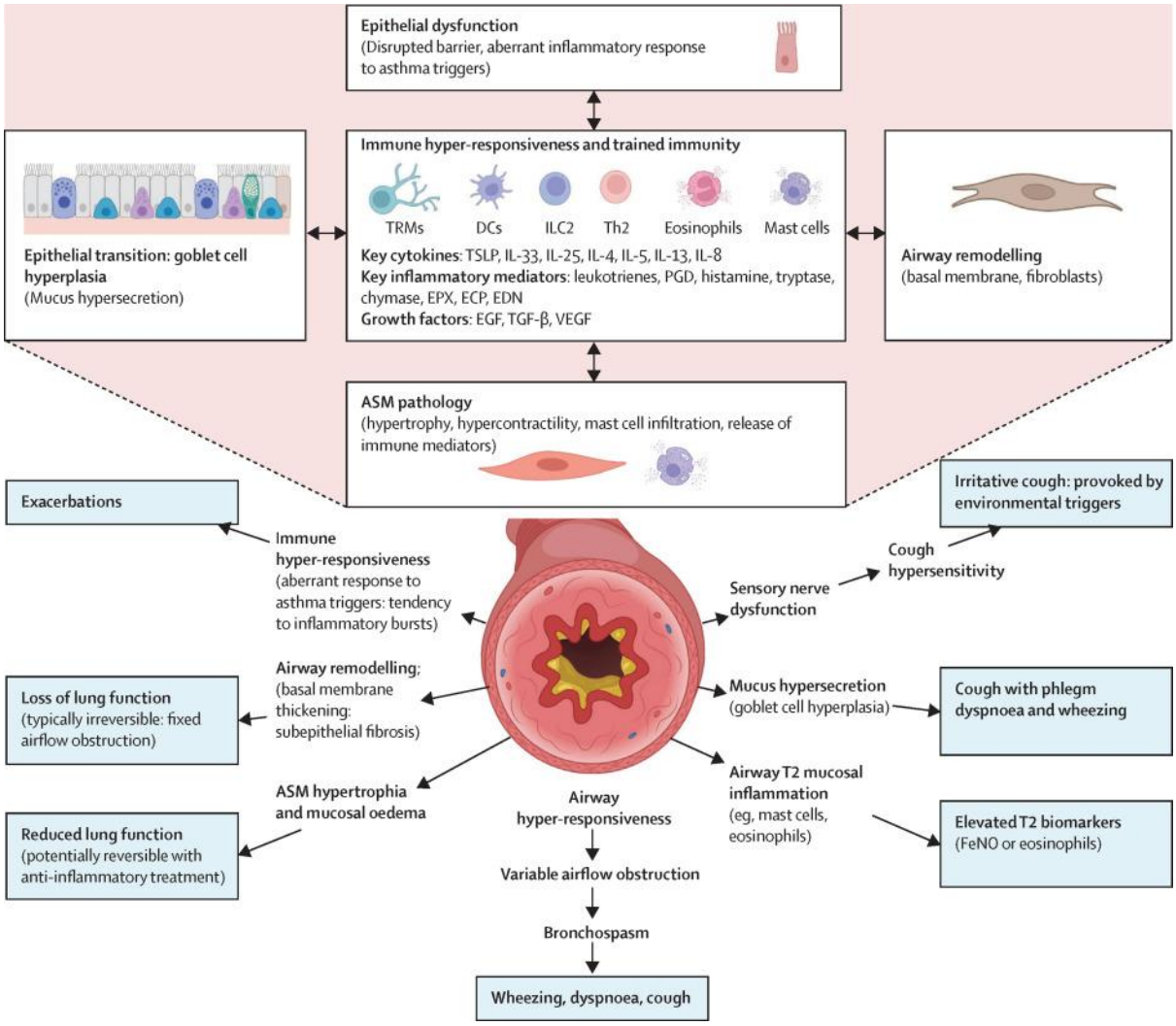


Figure 1.4 Pathophysiology of T2H asthma. The figure illustrates four key physiological changes: epithelial dysfunction, epithelial transition, airway smooth muscle (ASM) pathology and airway remodelling. These physiological changes lead to subsequent symptoms and test abnormalities, including symptoms, elevated biomarkers, exacerbations and lung function decline. Figure is from Porsbjerg *et al.*[43].

Notably, the tree-like morphological features of the airways highlight another key aspect to consider in the pathophysiology of asthma: the distinct contributions of the proximal and distal airways to disease pathophysiology. In the 1960s, attempts were made to measure distal airway (small airway) resistance, which led to the definition of distal airways as those with an internal diameter of less than 2mm[44]. As discussed in Lipworth *et al*.'s commentary, **Figure 1.5** summarises the pathophysiological differences between the proximal and distal airways[45].

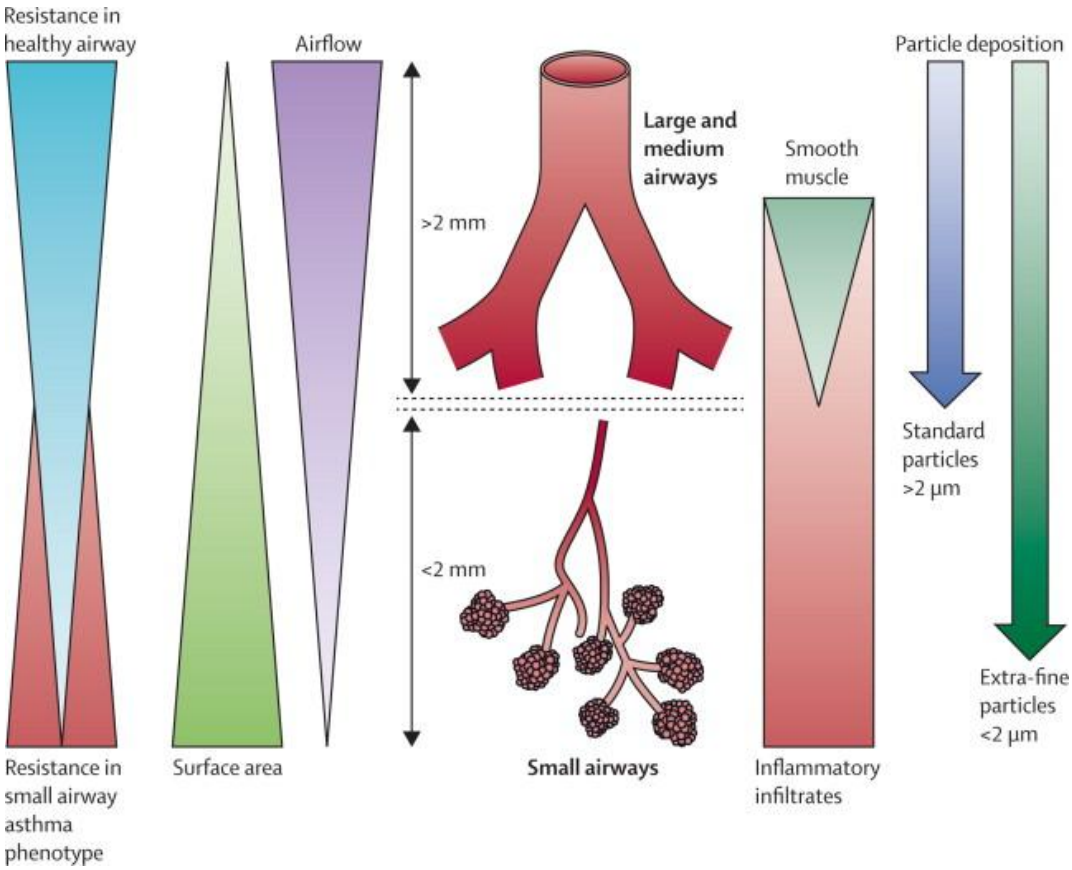


Figure 1.5 Small airway pathophysiological characteristics and their clinical relevance. The figure shows the differences in resistance distributions along the airway tree. While small airway resistance is minimal in healthy individuals, it increases in asthma patients. The large surface area reduces the density of inhaled medicines, and inflammation may be more prevalent in the distal airways. The figure is from Lipworth *et al.*[45].

Although distal airways have traditionally been termed the 'quiet zone' due to their relatively small contribution to airway resistance in healthy individuals[46], their resistance may increase due to the pathophysiological processes described above[47]. The inflammation in

asthma occurs both in the proximal and the distal airways[48]. An increased presence of eosinophils[49], as well as higher levels of IL-5- and IL-4 mRNA-positive cells, has been reported in distal airways[50]. In the same group, the expression of IL-5 mRNA was found in the distal airways[50]. Additionally, mast cells were found to accumulate in distal airways[51]. These findings suggest that spatial differences between proximal and distal airways should be accounted for when assessing inflammatory effects on lung pathophysiology.

1.2.4 T2H asthma biomarkers

From the latest BTS/NICE/SIGN guideline on asthma management, the measurement of two biomarkers, FeNO and BEC, has been prioritised to the early stage of diagnosis[6], representing their value in T2H asthma diagnosis, phenotyping, disease monitoring, treatment responses assessment and adherence check.

1.2.4.1 Fractional exhaled nitric oxide (FeNO)

FeNO is measured according to a standard published by the American Thoracic Society (ATS) and European Respiratory Society (ERS), which recommends that the flow rate for measurement should be 50mL/s[52]. It is a non-invasive test, usually completed in 5 minutes. The normal range of FeNO is less than 25 ppb.

The process of NO production in the airway wall and its connection with T2H inflammation will be introduced in **Section 1.5**, while its clinical significance is introduced as follows. FeNO levels are a biomarker that guides diagnosis, phenotyping, disease monitoring, and adherence assessment.

The BTS/NICE/SIGN guideline recommends FeNO as an objective test for diagnosing asthma, with diagnosis confirmed when the FeNO level exceeds 50 ppb, supported by clinical history and the exclusion of alternative diagnoses[53]. In contrast, the GINA guideline still only recommends the application of FeNO in severe asthma management without recognising its

role in the initial diagnosis of asthma[5]. The FeNO cut-off value and its interpretation in diagnosis should be determined across different populations and economic situations.

In monitoring disease, the BTS/NICE/SIGN guideline also emphasizes the importance of measuring FeNO, if possible, before each change in therapy[6]. As for the FeNO-guided strategy, a meta-analysis showed that following the FeNO level to tailor therapy can decrease the risk of exacerbation but fails to improve clinical symptoms and reduce ICS doses[54].

If the asthma remains uncontrolled despite using medium- or high-dose ICS in combination with a long-acting $beta_2$ agonist(LABA), it is called difficult-to-treat asthma. Many factors may lead to difficult-to-treat situations, including incorrect inhalation technique, poor adherence, wrong diagnosis, non-response to ICS, etc. In difficult-to-treat asthma, GINA has recognised the level of FeNO in phenotyping, considering the phenotype as T2H when the FeNO level is ≥ 20ppb[55]. Furthermore, a FeNO level ≥ 25ppb is one of the criteria for initiating therapy with IL-4Rα monoclonal antibody, supporting the phenotyping of T2H asthma[56].

Furthermore, the FeNO suppression test is used to assess adherence in patients with difficult-to-treat asthma. After one week of supervised high-dose ICS administration, patients, regardless of their prior adherence, receive adequate ICS treatment, and those who were originally poorly adherent to ICS show a greater reduction in FeNO at follow-up visits. Currently, the threshold for the FeNO suppression test is set at $\log(\Delta FeNO) = 0.24$, and a reduction of FeNO greater than this value reflects non-adherent[57, 58]. This test helps to identify the true non-responders from the group with difficult-to-treat asthma.

1.2.4.2 Blood eosinophil count (BEC)

BEC is a minimally invasive biomarker and one of the most commonly tested parameters. However, it is important to note that its normal range may vary between various institutes.

Eosinophils develop and mature in the bone marrow, and their release into the blood requires the expression of IL-5R[59]. Increased IL-5 production enhances eosinophil maturation, release and survival, leading to an increased BEC level. Circulating eosinophils adhere to the vessel endothelium mediated by P-selectin and vascular cell adhesion molecule (VCAM-1), both of which are upregulated in response to IL-4 and IL-13[60]. With adherence to the endothelium, eosinophils enter the subepithelial layer and release both cytokines and cytotoxic eosinophil granule proteins, including ECP, MBP, EPO and EDN, as previously mentioned[61]. Additionally, eosinophilic extracellular traps (EETs), composed of mitochondrial DNA and eosinophil granule proteins, trigger epithelial barrier damage and mucus formation[62]. All of the above processes cause inflammation and tissue damage to the airway walls.

It is widely recognised for the role of BEC in asthma diagnosis, phenotyping, and treatment response assessment, and it may also serve as a potential indicator of small airway involvement. According to the BTS/NICE/SIGN guideline, BEC is recommended as an objective test to support asthma diagnosis[6] while the GINA guideline does not include BEC as a diagnostic tool[5]. BEC is a marker of asthma disease activity and severity[63, 64], and its utility reflects the risk of exacerbation and levels of asthma control[65-67]. In phenotyping, BEC is one of the essential biomarkers, as eosinophil maturation, differentiation and survival are regulated by IL-5[68]. In treatment response assessment, BEC is reliable in predicting the response to anti-IL5/5R therapy[69, 70]. Furthermore, as researchers increasingly highlight the role of small airway contribution in asthma, emerging evidence supports the association of BEC and small airway dysfunction[71-73].

1.2.5 Management of T2H asthma

The aim of asthma management is to optimise outcomes for each patient on an individual basis. While the specific objectives may vary depending on individual situations, the

approach generally consists of symptom control, exacerbation risk control, management of persistent airflow restrictions and minimising side effects. This approach emphasises a cycle of review, assessment and adjustment. Generally, the medications for asthma consist of controllers, relievers and add-on therapies. Controllers, typically containing ICS, are used daily to control symptoms and prevent exacerbations. Relievers, which may include ICS or not, are used on an as-needed basis to quickly relieve sudden symptoms. The add-on therapies, including biologics, are additional options for patients who are poorly controlled despite the optimised application of controllers and relievers(demonstrated in **Figure 1.6**) [5].

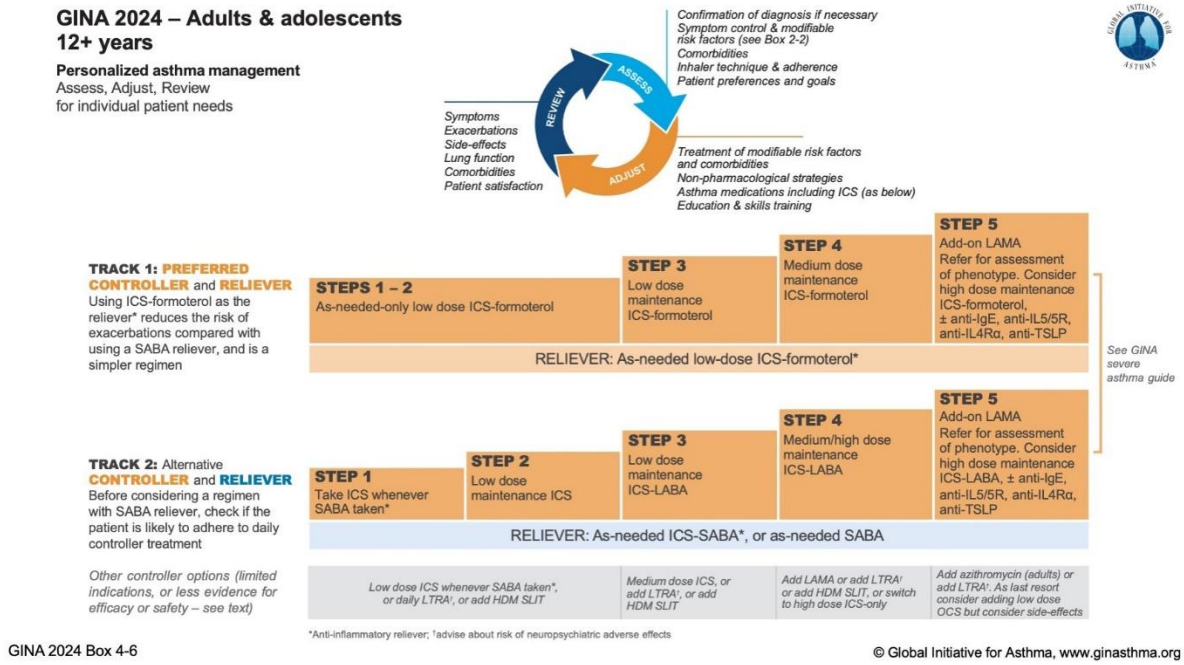


Figure 1.6 Asthma management diagram. There are five steps, with higher step numbers indicating more severe disease. Track 1 recommends using the same ICS/formoterol as controlled and reliever, while track 2 uses ICS/SABA or as-needed SABA as the reliever. Difficult-to-treat asthma and severe asthma patients are usually classified under step 5. ICS: inhaled corticosteroid, SABA: short-acting beta-agonists. The figure is obtained from the GINA 2024 report[5]

An exacerbation is defined as an acute or subacute worsening of symptoms and lung function that differs from the patient's usual status[5]. There are several triggers for the exacerbations, including viral infections, allergen exposures, environmental pollution or seasonal variance. Early or mild exacerbations can be controlled by increased usage of

relievers, whereas severe exacerbations often require oral corticosteroids (OCS). The systemic delivery of OCS offers more effective suppression of airway inflammation compared to the inhaled delivery of ICS. However, the use of OCS requires careful evaluation due to potential adverse effects, including adrenal suppression and osteoporosis[5].

According to BTS/NICE/SIGN recommendations, the initial therapy for newly diagnosed asthma involves the use of low-dose ICS/formoterol on an as-needed basis for symptom relief. If symptoms persist or exacerbations occur, the physicians may consider initiating maintenance and reliever therapy (MART), where ICS/formoterol is used for both daily maintenance and as-needed symptom relief. For patients with poorly controlled asthma, despite this approach, stepping up to moderate-dose ICS/formoterol should be considered.

Patients who continue to exhibit uncontrolled asthma, characterised by persistent symptoms or frequent exacerbations, despite moderate-dose therapy, may be classified as having difficult-to-treat asthma[5]. Both GINA and BTS/NICE/SIGN guidelines generally recommend the assessment of adherence and the performance of phenotyping. Adherence can be evaluated by pharmacists or via the FeNO suppression test, and good adherence suggests a diagnosis of severe asthma. Phenotyping parameters include FeNO, BEC, sputum eosinophil percentage, allergen testing, IgE and others, while the most widely used and accessible parameters are FeNO and BEC.

In patients with severe asthma, biologics therapy has emerged as a targeted approach to asthma management, particularly in T2H asthma. They are monoclonal antibodies designed to neutralise the interactions between cytokines and their receptors. Currently available biologics include anti-IgE, anti-IL5/5R, anti-IL4Rα and anti-TSLP treatments (illustrated in **Figure 1.3**). This thesis presents a focused review of anti-IL5/5R as subsequent studies examine their effects on NO production depth in conducting airways.

Anti-IL5/IL5R therapies inhibit IL-5 receptor signalling, thereby inhibiting the subsequent inflammatory cascade associated with eosinophilic asthma. Mepolizumab is a monoclonal antibody that binds directly to IL-5, blocking its interaction with IL-5 receptors[74]. Reslizumab and benralizumab are monoclonal antibodies that target the IL-5 receptor directly, blocking IL-5 binding and subsequent activation[75, 76].

Table 1.1 summarises the eligibility and efficiency for mepolizumab and benralizumab[77-79]. All biologic pathways require reassessment after one year of treatment, and the outcome of this review determines whether therapy should be continued or adjusted. Anti-IL5/5R therapy decreases blood eosinophil count significantly due to IL-5 being a cytokine directly related to blood eosinophil count, while it has minimal effects on FeNO level[79, 80].

Table 1.1 Summary of eligibility criteria, efficiency and safety of anti-IL5/5R biologics.

Biologics	Eligibility	Efficiency and Safety[79]
Mepolizumab (Anti-IL5 antibody)	Either condition: Option 1: - BEC ≥ 300μL AND exacerbations in the previous year ≥ 4 OR OCS 5mg in the previous 6 months Option 2: -BEC ≥ 400μL AND -Exacerbations in the previous year ≥ 3 [77]	-Reduction in asthma exacerbations -Increase in FEV_1, which may fall within inter-test variability -Improved symptoms (ACQ-6), though they may not meet the minimum clinically important difference (MCID) -Similar clinically significant adverse events leading to discontinuation
Benralizumab (Anit-IL5R antibody)	Either condition: Option 1: - BEC ≥ 300μL AND - Exacerbations in the previous year ≥ 4 OR - OCS 5mg in the previous 6 months Option 2: -BEC ≥ 400μL AND -Exacerbations in the previous year ≥ 3[78]	-Reduction in asthma exacerbations -Increase in FEV_1, which may fall within inter-test variability -Improved symptoms (ACQ-6), though they may not meet the minimum clinically important difference (MCID) -Similar clinically significant adverse events leading to discontinuation

Exacerbation rate: rate of exacerbations requiring emergency department treatment or admission, ACQ: Asthma Control Questionnaire, SAE: serious adverse events, as defined in original study.

1.3 Respiratory system

The respiratory system consists of the lungs, the upper airways, the chest wall, the respiratory circulation, and the nervous system, which regulates respiration. Its core function is gas exchange, delivering oxygen (O_2) and removing carbon dioxide (CO_2) generated by metabolism. Additional functions include maintaining acid-base balance, immune defence, and metabolic activities. This section will focus on the lung and its key components that ensure efficient gas exchange.

1.3.1 Anatomy of the lung

The gas entering the human body passes through the upper airway including the oral/nasal cavity, sinus, pharynx and larynx. It then enters the lower airway (bronchial tree), as demonstrated in **Figure 1.7**, comprising the trachea, bronchi, bronchioles, and respiratory bronchioles. The bronchial tree can be divided into conducting airways (trachea, bronchi, and bronchioles) and respiratory airways (respiratory bronchioles). The conducting airways transport gas into the alveoli without participating in gas exchange, whereas the respiratory airways include both bronchioles and alveoli, enabling gas exchange. At the end of the lower airways, the respiratory bronchioles are connected to air sacs composed of alveoli, which function as the primary site of O_2 and CO_2 exchange between the air and the blood.

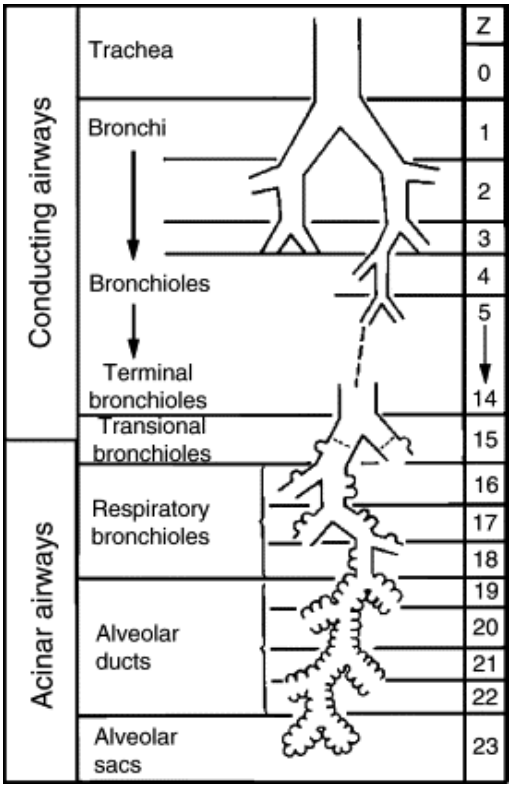


Figure 1.7 Model of the human airway system. Generation 0 is the trachea, generation 0 to generation 16 are the conducting airways, generation 17 to generation 22 are the respiratory airways, and generation 23 is the alveoli. The figure is from Weibel *et al*.[81]

The morphology of airways is first described by Weibel[82], who identified 24 generations of airways in the lung, as also illustrated in **Figure 1.7**. Generation 0 is the trachea, and generation 23 corresponds to the alveolar sacs. Generations 0 to 15 are conducting airways, and the rest are respiratory airways. The volume and surface area of each generation both increase exponentially, consequently influencing gas transfer.

1.3.2 Ventilation and deadspace

Ventilation is the process of moving gas into and out of the lungs to facilitate pulmonary gas exchange. An adult typically breathes 12-20 times per minute with an inhalation volume of ~0.5L. Different breath behaviours result in variances in lung volumes, as illustrated in **Figure 1.8**. In normal breathing behaviour, the lung volume is expanded and contracted within the tidal volume (Vt). The residual volume at the end of tidal expiration is the functional residual volume (FRC). If an exhalation is performed to its extreme, the remaining

gas volume in the lung is the residual volume (RV), which cannot be exhaled. In contrast, if an inhalation is performed to its extreme, the lung volume reaches the total lung capacity(TLC).

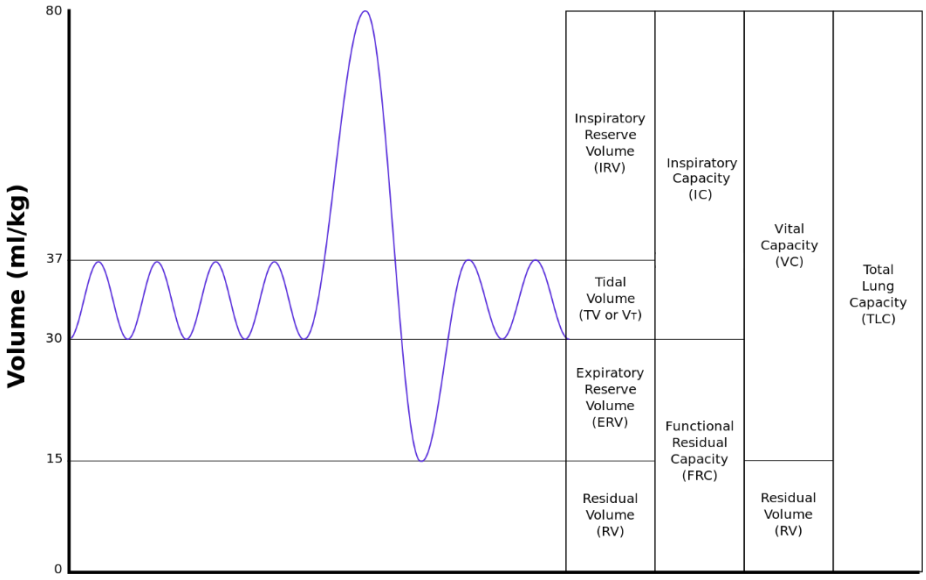


Figure 1.8 Lung capacity demonstration. A normal breath corresponds to the tidal volume (Vt). At the end of exhalation, the lung volume is referred to as the functional residual capacity (FRC). During maximal exhalation, the lung volume decreases to the residual volume (RV), while during maximal inhalation, the lung volume expands to the total lung capacity(TLC). The maximum volume during a single breath is called the vital capacity (VC), ranging from RV to TLC. The figure is from Wikipedia[83].

Alveolar volume is defined as the volume of the lung available for gas exchange at FRC. The remaining portion of gas that does not participate in gas exchange is referred to as dead space. The dead space is divided into anatomical dead space and alveolar dead space. Anatomical dead space refers to the portion of gas that remains in the conducting airways and never reaches the alveoli. If a portion of gas enters the alveoli but remains unexchanged because ventilation exceeds the alveolar exchange capability, it is referred to as alveolar dead space. The sum of alveolar dead space and anatomical dead space is referred to as physiological dead space. In healthy volunteers, the physiological deadspace is generally considered approximately equal to the anatomical deadspace, suggesting that the alveolar

dead space is approximately zero. In certain respiratory diseases, however, the physiological dead space is significantly larger than the anatomical dead space.

1.3.3 Measurement of dead space volume

The previous section introduced the concept of ventilation and dead space. This section focuses on reviewing methods for the measurement of dead space volume, as it is closely linked to the estimation of NO production sites. The primary idea behind measuring dead space volume is the use of expirograms, which can clearly distinguish phases of exhalation to differentiate gas from dead space and alveolar region.

Nitrogen (N_2) single-breath washout was first introduced as a method for anatomical dead space estimation[84], and it also suggests that the gas expirogram contains information on dead space. When the participant switches from breathing ambient air to pure O_2, the N_2 in exhaled gas comes entirely from the lung, which avoids inhalation gas influence. Due to ventilation factors such as inhomogeneity, the emergence time of N_2 in different airway branches varies, turning a clear step function (blue line in **Figure 1.9**) into a curve. When the areas labelled A and B are equal, the volume corresponds to anatomical dead space volume, as it simplifies the lung structure to a single pipe, marking the N_2 emergence volume, the volume that does not contain any N_2 molecules (i.e., the anatomical dead space).

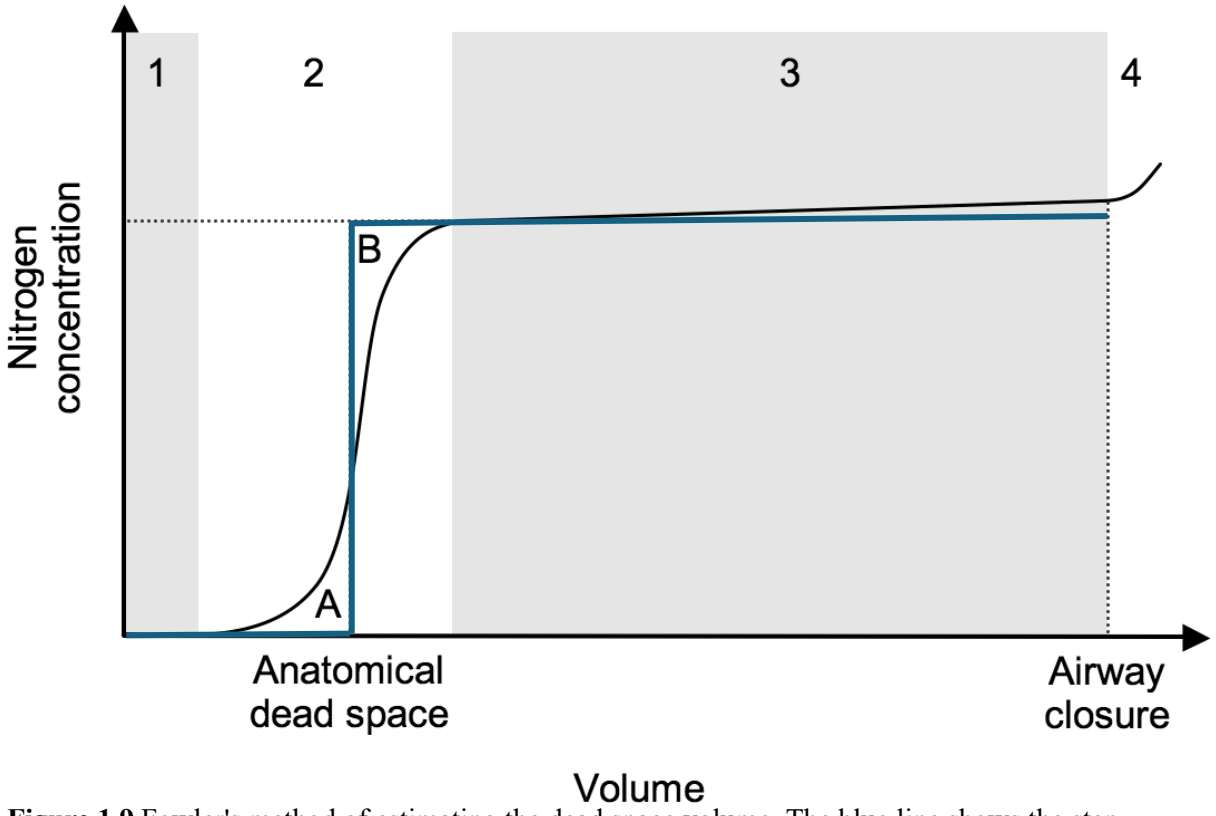


Figure 1.9 Fowler's method of estimating the dead space volume. The blue line shows the step function, assuming the N_2 flow is a single plug flow. When area A is equal to area B, the volume is the deadspace volume. The figure is adapted from Mattew *et al*.[85].

Apart from the estimation of anatomical dead space, **Figure 1.9** also demonstrates the phases in one exhalation (labelled as 1, 2, 3 and 4). Phase I is the anatomical dead space phase when the participant exhales the conducting airway gas. Phase II is the transition period of exhalation, in which the exhaled gas contains both conducting airway and alveolar gas. Phase III is the alveolar plateau phase, where the gas comes entirely from the alveoli. Phase IV is the closing volume period, where a sudden increase may occur caused by the sequential closing of small airways.

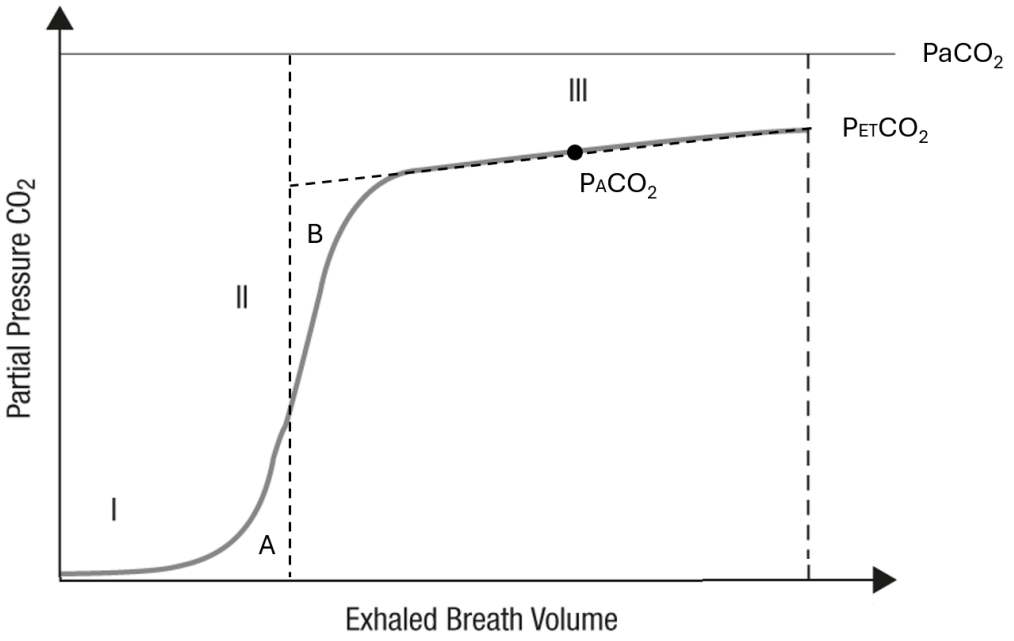


Figure 1.10 CO_2 expirogram in estimating anatomical dead space. When area A equals area B, the exhaled volume corresponds to the anatomical dead space. Phase III of the CO_2 expirogram slopes upwards as CO_2 is continuously produced by metabolism. P_ACO_2 : alveolar CO_2 partial pressure, $P_{ET}CO_2$: CO_2 partial pressure at end-tidal, P_aCO_2: arterial CO_2 partial pressure. The figure adapted from Anderson *et al.*[86].

Similarly, the CO_2 expirogram can also be used to retrieve the anatomical dead space, as shown in **Figure 1.10**. However, because CO_2 is stored in the blood and produced by metabolism, it produces an increasing slope during phase III. But the principle is the same: when the vertical line divides areas A and B to be equal, the corresponding volume is anatomical dead space volume. Using CO_2 for estimation has an advantage in that it is easier than N_2 washout, which requires pure O_2 inhalation[87, 88]. The CO_2 expirograms also provide information on physiological conditions in intensive care and anaesthesia situations[89-91].

1.3.4 Pulmonary circulation and gas exchange

Pulmonary circulation receives all the output from the right cardiac ventricle. The pulmonary artery branches into pulmonary capillaries, perfusing each of the alveoli, carrying mixed venous blood with high CO_2 and low O_2 contents. In pulmonary capillaries, the CO_2 in

the blood diffuses into the alveoli and O_2 in the alveoli diffuses into the blood to complete the gas exchange.

In blood, the majority of O_2 is stored in haemoglobin (Hb) due to the limited solubility of O_2 in water. The partial pressure of O_2 is ~40mmHg in mixed-venous blood, leading the Hb to exhibit high affinity for O_2 (binding cooperativity), while in alveoli, the O_2 partial pressure is approximately 100 mmHg. When mixed-venous blood enters the pulmonary capillaries, the partial pressure gradient of O_2 from the alveoli to the blood drives O_2 into the blood, where the Hb rapidly captures O_2 from the alveoli[92]. In healthy individuals, the diffusion of O_2 from alveoli to the capillaries (~0.25s) occurs rapidly enough to reach full equilibrium before the blood exits the capillaries (~0.75s) [93].

CO_2 is stored in blood due to its high solubility in water and its conversion to hydrogen carbonate($HCO3^-$), which can bind with Hb (and other proteins) or be directly dissolved in plasma[92]. In pulmonary capillaries, the gradient between blood and alveolar space drives CO_2 to diffuse into the alveoli for exhalation. Similar to O_2, CO_2 in a healthy individual reaches equilibrium before the blood leaves the capillary (~0.75s)[93].

When a portion of blood bypasses the ventilated area, gas exchange does not occur, which is referred to as a shunt. An anatomical shunt is caused by structural abnormalities that provide no ventilation to perfused areas, while a physiological shunt occurs when ventilation is relatively insufficient compared to perfusion, preventing the blood from becoming fully saturated with gases before exiting the capillaries.

1.3.5 Ventilation-perfusion ratio($\dot{V}/\dot{Q}$)

The ventilation-perfusion ratio($\dot{V}/\dot{Q}$) is defined as the ratio of alveolar ventilation to pulmonary blood perfusion in a given period. In a healthy person, the $\dot{V}/\dot{Q}$ distributions are narrowly unimodal with a similar peak position, which provides the most efficient gas exchange process. Typically, alveolar ventilation is ~4L/min, and blood perfusion is ~5L/min,

resulting in a $\dot{V}/\dot{Q}$ of around 0.8[94]. The two extremes of this ratio correspond to shunt and dead space: a $\dot{V}/\dot{Q}$ value of 0 indicates no ventilation to an alveolus, representing a shunt; whereas a $\dot{V}/\dot{Q}$ value approaching infinity indicates no blood flow to that region, indicating dead space.

1.4 Pulmonary function test(PFT) techniques

1.4.1 Spirometry

Spirometry is one of the most widely used PFT techniques due to its capabilities and cost-effectiveness. The most common application of spirometry is forced spirometry, where participants use maximal forced effort to exhale gas from full lung capacity. It is recognised as an essential PFT in screening, diagnosis, and monitoring of airway diseases such as asthma and chronic obstructive pulmonary disease (COPD).

In 2019, American Thoracic Society(ATS)/European Respiratory Society (ERS) published a comprehensive statement on standard measurements and quality of results[95]. **Figure 1.11** presents an example of a flow-volume curve and key parameters of spirometry. In the subsequent Chapters, the spirometry results are presented in raw value, percentage predicted, and z-score, based on the ERS/ATS updated interpretation guidelines for spirometry[96]. The predicted value and z-score are provided by the Global Lung Function Initiative (GLI) reference values[97]. According to the interpretation guide, an abnormal z-score is defined as less than -1.65[96], while the abnormal percentage predicted depends on the parameters.

This thesis generally presents the following parameters in the spirometry assessment of participants:

(1) Forced expiratory volume in 1s (FEV_1). The volume of gas exhaled from full-capacity lungs during the first second of exhalation. The normal limit for the percentage

predicted is 80%. A lower FEV_1 value reflects that airway obstructions occur due to various reasons.

(2) Forced vital capacity (FVC). The maximum volume of gas that can be expired from a full-capacity lung under conditions requiring maximum effort. It represents the lung capacity. The lower normal boundary for the percentage predicted is 80%. A lower-than-normal FVC indicates the potential presence of restrictive airway diseases.

(3) FEV_1/FVC ratio. The normal lower limit is 70%. A reduced FEV_1/FVC ratio indicates obstructive airway patterns.

(4) Forced expiratory flow at 25% to 75% of FVC (FEF_{25-75}). It measures the average flow rate during the middle 25% to 75% of the FVC. This parameter is one of the markers of small airway function[98].

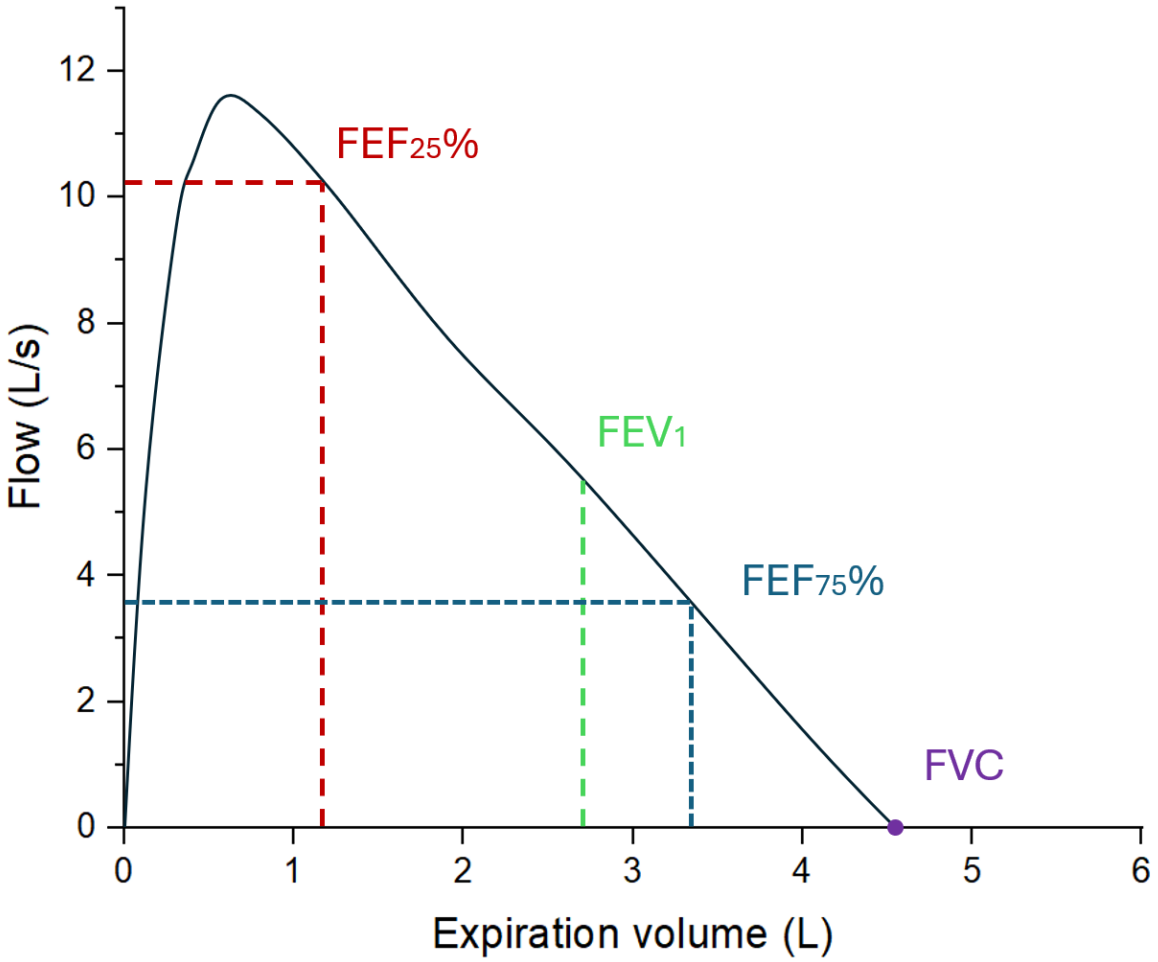


Figure 1.11 A figure of the flow-volume graph during a forced exhalation test conducted on spirometry. FEV_1: Forced exhalatory volume in 1s, green corresponding x value. FVC: forced vital capacity, purple corresponding x value. FEF25%: forced expiratory flow at 25% of FVC, red dashed line corresponding to the y value. FEF75%: forced expiratory flow 75% of FVC: forced expiratory flow at 75% of FVC, blue dashed line corresponding y value. FEF_{25-75}%: forced expiratory flow between 25% to 75% of FVC, the average flow between red and blue lines.

In many cases, the participants are administered a bronchodilator (BD) for a bronchodilator responsiveness test (BDR) to reveal the degree of improvement in FEV_1 after using the BD. This thesis follows the protocol outlined in the 2019 guideline[95]. Spirometry is repeated after 15 minutes of bronchodilator administration to evaluate the FEV_1 and FVC improvements. The BDR response is calculated by dividing the change of FEV_1 between Post-BD and Pre-BD values by the Pre-BD value. A positive BDR response is defined as an increase of $\geq$ 12% or an absolute increase of $\geq$ 200ml.

1.4.2 Body plethysmography

Body plethysmography is another well-established technique for measuring lung volumes. Unlike spirometry, it only requires the participant to perform unforced breathing during the measurement, making it more suitable for participants who cannot perform spirometry. The plethysmography is conducted in a sealed air chamber, where participants are required to perform different breathing manoeuvres. This sealed environment allows the device to measure the volume parameters comprehensively, including those that remain unexhaled in the lungs. As such, it can measure functional residual capacity (FRC), lung residual volume (RV) and total lung capacity (TLC)[99]. However, limitations in portability and cost restrict its application.

1.4.3 Impulse oscillometry

Compared with spirometry and body plethysmography, impulse oscillometry is a recently developed technique for the assessment of airway resistance (Rs) and reactance (Xs). It is a non-invasive technology that generates forced oscillation by employing extra small pressure signals to the participants' normal breathing. By receiving and analysing the signal, the system can extract specific information regarding airway resistance and reactance[100]. The common parameters used in impulse oscillometry include[101]:

(1) R5 (resistance at 5Hz): resistance of the total airway. Elevated value indicates an increase in airway resistance.

(2) R20 (resistance at 20Hz): resistance of the large airway. Elevated value indicates an increase in large airway resistance.

(3) R5-20 (the difference between 5Hz and 20Hz resistance): resistance of the small airway. Elevated value indicates an increase in small airway resistance.

(4) Freq: resonant frequency, the dividing point between elasticity and inertance.

(5) X5(reactance at 5Hz): combined effect of tissue elasticity and inertance.

(6) Area of reactance (AX): total reactance between 5Hz and Freq.

A z-score can be calculated based on the study by Oostveen *et al*.[102].

Impulse oscillometry has the potential to be widely used due to its portability and the absence of forced exhalation requirements, making it particularly suitable for paediatric participants and adults who cannot complete a spirometry test. Apart from its wider coverage in participants, impulse oscillometry demonstrates its capability to assess resistance and reactance in the small airway, which is a potential early sign of airway disease[103, 104].

1.4.4 Lung inhomogeneity

Lung inhomogeneity, in the current context, refers to ventilation inhomogeneity. The most common method for measuring ventilation inhomogeneity is the multiple-breath inert gas washout (MBW), which originated in Fowler *et al.*'s study that observes the multiple washout of N_2[105]. The CCP, which combines laser-based spectroscopy with physiological modelling, is an emerging technique for assessing ventilation inhomogeneity.

1.4.4.1 MBW

Ventilation inhomogeneity originates from three sources: convection-dependent inhomogeneity(CDI), diffusion-dependent related inhomogeneity and convection- and diffusion-dependent inhomogeneity(DCDI). The diffusion-dependent related inhomogeneity results from enlarged acinar structures, which are rare, while the CDI and DCDI occur in normal airways[106]. The MBW technique involves inhaling an inert gas (for example, N_2 or helium) and washing out the inert gas. In lungs with higher inhomogeneity, a larger portion of the conducting airways exhibits a slower washout speed, prolonging the washout time. Since the test is performed under tidal breathing, it is suitable for children and people with limited respiratory capacity. The inert gas must be safe for inhalation at the administered concentration and have a minimum solubility in blood. The possible gas options include N_2, sulfur hexafluoride(SF_6), helium or methane.

The most common parameters include Scond, Sacin and lung clearance index (LCI), [107]. Sacin, representing DCDI, is derived from the standardised slope of the first washout breath and Scond, representing CDI, is calculated from the rate of increase in the subsequent breath[108]. The LCI functions as an index of ventilation efficiency, defined as the number of breaths required to reduce the inert gas concentration to less than 1/40.

The MBW can detect early changes in lung structures. Scond, Sacin and LCI have shown sensitivity in identifying smokers with normal spirometry results[109], in monitoring asthma control with changes in ICS[110] and in detecting the severity of asthma[111].

1.4.4.2 CCP

As Chapter 2 provides a detailed description of CCP and its model, the related content is not repeated here. CCP ensures high-temporal-resolution and accurate gas measurement, enabling precise calculations through an advanced mathematical model[112, 113]. Furthermore, the model generates key structure parameters for locating the NO production sites in conducting airways.

1.5 NO production mechanism and measurement

NO is a colourless gas at room temperature and atmospheric pressure, and it is distributed across various body tissues, including the respiratory, circulatory, intestinal and nervous systems[114], where it plays diverse physiological roles. This section focuses on the NO production in the airway walls. We begin with an introduction to the mechanisms of NO production and their association with T2H inflammation, followed by an overview of methods for measuring NO concentrations and of models that describe NO production and transport in exhaled breath. The section then concludes by discussing the limitations of current models and highlighting the need for NO depth measurements.

1.5.1 Mechanisms of NO production

NO is produced from L-arginine and O_2 in a reaction catalysed by nitric oxide synthase (NOS) enzymes[115]. Three major NOS isoforms have been identified: neuronal NOS (nNOS or NOS I), endothelial NOS (eNOS or NOS III) and inducible NOS (iNOS or NOS II) [116]. Each of these enzymes exhibits distinct tissue distribution and regulatory mechanisms, while all are present in the airways[116].

nNOS and eNOS are Ca^{2+}- and calmodulin-dependent, functioning constitutively and generating low concentrations of NO, typically in the nanomolar range[117]. nNOS is localised in the epithelium, alveolar lining and neural structures[118-120]. Although eNOS is primarily found in blood vessels, as indicated by its name[121], it can also be detected in the epithelium of the trachea, bronchi and alveoli[122, 123].

iNOS is traditionally thought to be induced by proinflammatory cytokines, including tumour necrosis factor-α (TNF-α), interferon-γ (IFN-γ), and interleukin (IL)-1β[124]. However, some evidence suggests that certain cell types constitutively express iNOS, producing nanomolar levels of NO[125]. Different triggers may regulate iNOS expression through different pathways. Lipopolysaccharide (LPS)-simulated epithelial cells activate nuclear factor-kappa B (NF-κB), whereas IFN-γ activates the JAK/STAT-1 pathway[117]. Both pathways promote transcription of the iNOS gene.

T2H inflammation is characterised by elevated levels of IL-4, IL-5 and IL-13. IL-4 promotes iNOS transcription via the JAK/STAT1 pathway induced by IFN-γ, whereas higher concentrations of IL-4 alternatively activate the STAT-6 pathway, leading to increased iNOS gene transcription[40, 41]. IL-13 induces the iNOS expression in STAT-6 pathway[42]. IL-5, in contrast, does not induce iNOS expression as it typically activates the STAT3 pathway, which is independent of iNOS expression[126].

1.5.2 NO measurement techniques

A reliable technique for measuring gas-phase NO is required to quantify the epithelial NO production in the exhalation air. The three most common techniques for measuring NO are introduced here, and they differ in their features, making them suitable for different applications.

1.5.2.1 Chemiluminescence sensor

NO is measured indirectly by chemiluminescence, which relies on a chemical reaction,

$$NO + O_3 \longrightarrow NO_2 + O_2 + \text{photon},$$

where NO reacts with ozone (O_3) to form excited-state nitrogen dioxide (NO_2*), which emits a photon as it returns to a stable state. A sensor detects the emitted light(at >600 nm wavelength), producing a signal directly proportional to NO concentration. This method is widely regarded as the gold standard for NO concentration measurement, offering a detection limit of ~0.1ppb and a response time of ~0.5s. However, because of the device's large size, lack of portability and frequent calibration requirements, this sensor is predominantly restricted to use in research laboratories[127].

1.5.2.2 Electrochemical sensor

The electrochemical sensor operates by utilising chemical reactions to generate electrical signals. It provides a practical alternative for NO measurement in clinical settings, thanks to its portability and lack of calibration requirements[128]. Although it exhibits lower sensitivity (~5ppb) and longer response time (<10s), it has proven sufficient for daily clinical usage[129, 130] and has demonstrated good repeatability in practice[131]. However, its prolonged response time makes it impossible to capture the NO expirogram, which is essential for estimating the location of NO production.

1.5.2.3 Laser-based sensor

An alternative method for measuring NO concentrations is a laser-based sensor. It typically consists of three components: the laser source, a cell that contains the gas sample

and a laser detector that records signal absorption after the laser passes through the gas sample. For the detection of NO, the sensor operates in the mid-infrared (IR) region at 5.3μm (5.1μm to 5.7μm). Various studies have supported these measurements, using different laser types, including direct absorption spectroscopy[132], Faraday rotation spectroscopy (FRS)[133] and quantum cascade laser (QCL)[134, 135]. Laser-based technology has the advantage of providing real-time measurements, benefiting from its short response time and maintaining sensitivity to NO concentration. However, its cost is significantly higher than that of previously discussed technologies[127].

The technology presented in this thesis is based on laser technology, adapted for precise measurement in NO expirogram while simultaneously capturing CO_2 expirogram and other essential parameters[135], with a full introduction provided in Chapter 3.

1.5.3 NO production and transport model

To assist NO measurements, it is essential to understand the mechanism of NO production and transport and to recognise its uniqueness compared to other gases in the breath, such as CO_2 and N_2, which are produced in the alveoli[7]. This section introduces the model in theory development and clinical applications, followed by the limitations of current models.

1.5.3.1 Theoretical development

The two-compartment model establishes a framework describing NO production and transport within the airways[136].

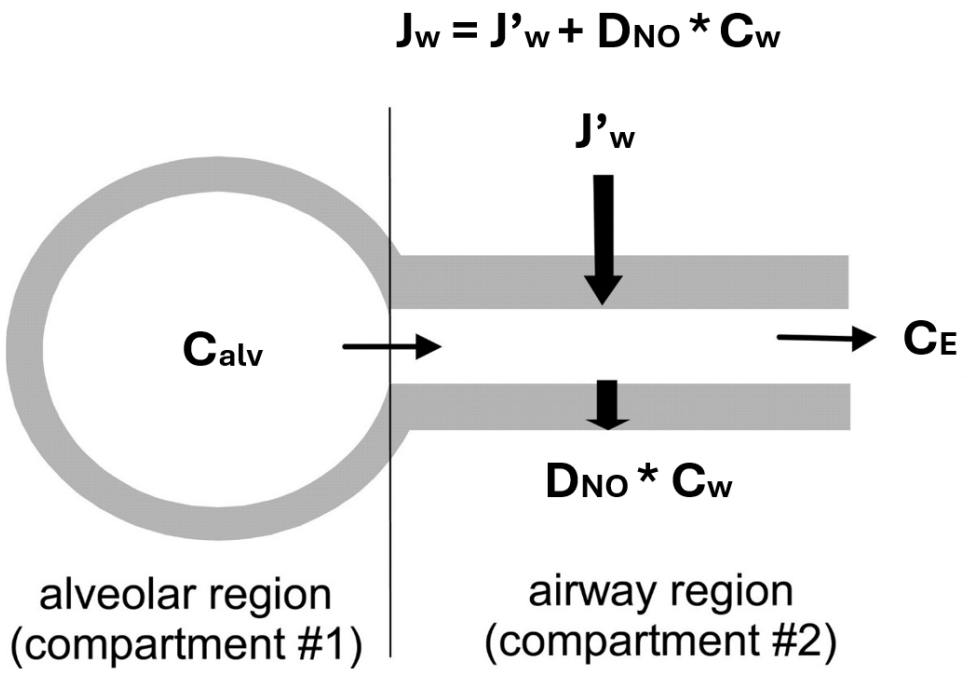


Figure 1.12 Schematic of the 2-compartment model. The model is composed of two compartments: the alveolar region and the airway region. The exhaled NO concentration (C_E) is composed of the sum of the total volumetric flux of NO from the airway wall and alveolar concentrations (C_{alv}). The diffusing capacity of NO (D_{NO}) determines the diffusion between the airway wall and lumen. *Jw*: the net flux rate from the airway, *J'w*: the flux rate leaving the airway wall. C_w: NO concentration in the gas phase within the airway compartment. The figure is adapted from George *et al.*[137].

Figure 1.12 illustrates the schematic figure of a two-compartment model. The alveolus compartment is connected to the airway compartment, represented as a single pipe. NO molecules are released into the airway lumen via diffusion from the airway wall, while the alveolus compartment has achieved a balance between ventilation and perfusion. Due to the high diffusion capacity of NO, its alveolar concentration is typically low, and, in many cases, it can be approximated as zero[138].

The basic formula for NO concentration measured at the plateau phase can be expressed as follows, assuming a constant exhalation speed,

$$C_E = C_w \cdot (1 - \exp(-D_{NO} / v)) + C_{alv} \cdot \exp(-D_{NO} / v)), \quad (1.1)$$

where C_E represents the plateau NO concentration in exhaled air, C_w is the average NO concentration produced at the airway wall, D_{NO} is the NO diffusion capacity, C_{alv} is the alveolar NO concentration, and v is the constant exhalation speed.

In ***Eq.* 1.1**, two extreme conditions are particularly worth considering. First, when v is 0 L/s, such as a breath-hold, NO concentration in the airway lumen rises to equilibrium with the epithelial cell. Conversely, at infinite exhalation speed, the C_w tends to be zero ppb, and the C_E tends to the C_{alv}.

Although the two-compartment model established the foundations of NO production and transport in airways, overlooked factors in this model can influence the measured NO concentration at the mouth, including axial diffusion and ventilation inhomogeneity.

Due to increased cross-sectional area in the lung, the single pipe model in a two-compartment model does not account for axial diffusion of gas, which can be addressed using the 'trumpet' shaped conducting airway model[139]. The concept of 'backdiffusion' is established as at the end of conducting airways, the axial diffusion tends to make NO diffusing into alveoli rather to proximal airways[139]. Under the condition that the inhaled gas is helium and oxygen (heliox), 'backdiffusion' can be amplified, as the NO diffusion coefficient in heliox is ~2.2 times larger than in air[140, 141]. To account for 'backdiffusion' when measuring C_{alv}, an adjusted method for correcting C_{alv} is proposed[142]. Further investigation has revealed the potential linear relationship between C_w and C_{alv}, which may be caused by 'backdiffusion'[140].

Furthermore, the ventilation inhomogeneity may impact the NO measurement value at the mouth level. In a multicompartment model, Suresh *et al.* assigned different ventilation to two parallel peripheral compartments, showing that when the partition of the two compartments is different, a distinct exhaled NO expirogram can be observed[143].

With the development of computing technology, NO production and transport models are built based on morphological lung structure, while the complexity of the bronchial tree leads

these models to be constructed using idealised representative lung morphology rather than individualised physiological lung data[144, 145].

1.5.3.2 Clinical applications

The previous section introduced the two-compartment model. To make it practical in clinical measurement, one common approximation approach involves the first-order linear approximation,

$$exp(- D_{NO} / v) = 1 - D_{NO} / v, \quad (1.2)$$

which holds true when v is greater than five times D_{NO} (or roughly >50ml/s).

If the flux of NO from the airway wall is substituted for Cw, another commonly used equation can be generated,

$$V_{NO} = J_w + C_{alv} \cdot v, \quad (1.3)$$

V_{NO} is the NO exhalation amount, J_w represents the net flux rate from the airway.

Several methods have been proposed to estimate the J_w, C_w and C_{alv} using various exhalation speeds[136, 146-149].

Alternatively, single-breath methods can be employed, including breath-hold manoeuvre[150] and tidal-breath with simulations[151, 152]. Additionally, the area under the curve has been suggested as a new parameter to estimate the airway NO production[153].

Karvonen *et al.* conducted a meta-analysis on NO parameters derived from a two-compartment model, comparing the NO parameters among treatment-naïve, steroid-treated patients with healthy controls. Its findings strongly support that both asthma groups exhibited elevated J_w and C_{alv} compared to the healthy group, while data on other parameters, such as C_w and D_w, remain limited to draw a definitive conclusion[154]. However, this study prioritises the use of data uncorrected for 'backdiffusion' over $Calv$ measurements due to the lack of corrected data. In another multicentre clinical study, the findings failed to show any correlations between asthma severity and asthma control with J_w and corrected C_{alv}[155].

In one study, ICS intervention has been shown to reduce corrected C_{alv} in mild-to-moderate groups of 50 patients, as well as reduce J_w [156]. In contrast, another retrospective study shows that ICS failed to reduce corrected C_{alv} in 107 mild asthmatic patients group[157]. A study involving mild-to-moderate (N=25) and refractory asthmatic (N=27) patients found that only OCS can reduce the C_{alv} (uncorrected), while ICS failed in reducing alveolar NO[158]. Another study involving 24 participants applying corrected C_{alv} shows consistent results [159]. In exacerbation, one study observing 15 patients found that increased FeNO was mainly due to J_w, with C_{alv} (corrected) similar to a stable condition[160].

Although these studies fail to present consistent results, they support the idea that 'backdiffusion' has a significant impact on C_{alv}. Furthermore, the difference in C_{alv} may result from ‘backdiffusion’ of C_w rather than from C_{alv} itself. It also indicates that the determinate parameter may be C_w for conducting airways rather than C_{alv}. These findings reveal the need to observe the variation of NO production locations in conducting airways.

1.5.3.3 Limitations of the current model

Despite plenty of NO production and transport models, this thesis still needs to develop a new model. Firstly, the objective of this thesis differs from that of other research. Most other studies divide the lung into alveoli and conducting airways, representing NO production in conducting airways by an average production rate. In contrast, this thesis focuses on the investigation of NO production in the conducting airways only, aiming to reveal NO distributions in the conducting airways. Secondly, the estimation approach in this thesis is different, focusing on phase I and phase II of the NO expirogram. However, most existing methods apply phase III of the NO expirogram and differentiate the average alveolar and conducting airways by varying exhalation speed. Lastly, as a consequence of examining phase I and phase II of NO expirograms, this approach requires higher temporal resolution in

the measurement of NO expirograms and a much more precise description of lung physiology to control variables, which is not required in other NO measurements.

1.6 Thesis outline

Chapter 1 explains the motivation for this thesis and presents a concise literature review of relevant knowledge. Chapter 2 focuses on lung inhomogeneity assessment, covering its techniques and presenting two clinical studies that demonstrate its sensitivity. This Chapter also introduced the measurement and model fitting from CCP, laying the groundwork for its role in controlling variables in NO depth measurements in the following Chapters. Chapter 3, Chapter 4 and Chapter 5 cover the development of NO depth estimation in conducting airways in three parts: Chapter 3 introduces the hardware, the Rapid FeNO Device (RFD) and the reconstruction of NO expirogram at the mouth level; Chapter 4 gives the underlying model and idea of how to generated NO depth parameters; Chapter 5 presents the quality assessment system and a repeatability/reliability test. Chapter 6 presents a series of clinical studies illustrating the potential applications of NO depth parameters. Chapter 7 is an additional Chapter that offers a summary of work conducted during the COVID-19 pandemic period. Chapter 8 concludes the thesis with a summary of the findings, their significance and future research directions.

Chapter 2

Measuring lung inhomogeneity using Computed Cardiopulmonography (CCP)

Lung inhomogeneity has attracted growing interest as a potential early indicator of airway diseases. It enables the detection of regional changes before global impairments become evident through conventional lung function tests such as spirometry. However, there is still a lack of widely recognised parameters for assessing lung inhomogeneity.

This Chapter introduces a novel methodology known as Computed Cardiopulmonography (CCP) to measure lung inhomogeneity. It also presents two clinical studies demonstrating the sensitivity of parameters measured by CCP in clinical applications. The first study focuses on healthy volunteers with type 2-high (T2H) inflammation biomarkers and assesses the presence of subclinical physiological alterations in the airways. The second study assesses lung function changes (lung inhomogeneity in particular) in patients with asthma who initiated either the inhaled corticosteroid (ICS) or systemic corticosteroid (SCS) to investigate how lung inhomogeneity changes following these interventions in patients with asthma.

Additionally, the CCP parameters introduced in this Chapter provide a description of individual lung physiology, which will be used in Chapter 4 to construct the simulated NO expirograms.

2.1 Introduction to CCP

CCP incorporates two advances: a novel measurement technology — the molecular flow sensor (MFS) — and a cardiopulmonary mathematical model. MFS uses laser absorption spectroscopy to directly measure the total flow and the concentrations of CO_2, O_2 and H_2O with unprecedented accuracy. The concentration of the remaining gas (N_2) is indirectly calculated by subtraction. The cardiopulmonary mathematical model accounts for ventilation, gas diffusion at the blood-air interface, and the storage and circulation of gases to simulate the gas exchange process in the human body[112, 113, 161].

A standardised protocol for CCP measurement includes 7 minutes of air-breathing followed by 5 minutes of pure O_2 breathing. The latter period aims to achieve a full washout of N_2 from the lung. CCP recovers a set of parameters reflecting lung inhomogeneity by fitting the simulated data from the model to the measured data from MFS during the measurement period.

The following sections introduce the MFS and the cardiopulmonary model, followed by a standardised protocol for CCP measurement. Furthermore, this section reviews findings from several published clinical studies on the CCP.

2.1.1 Molecular flow sensor (MFS)

MFS uses laser absorption spectroscopy to measure the gas concentrations and a pneumotachograph to measure the flow rate at the mouth, achieving a temporal resolution of 10ms. In addition to the data mentioned above, it also measures the physical parameters such

as temperature and barometric pressure at the same frequency[162]. A schematic design graph is shown in **Figure 2.1**.

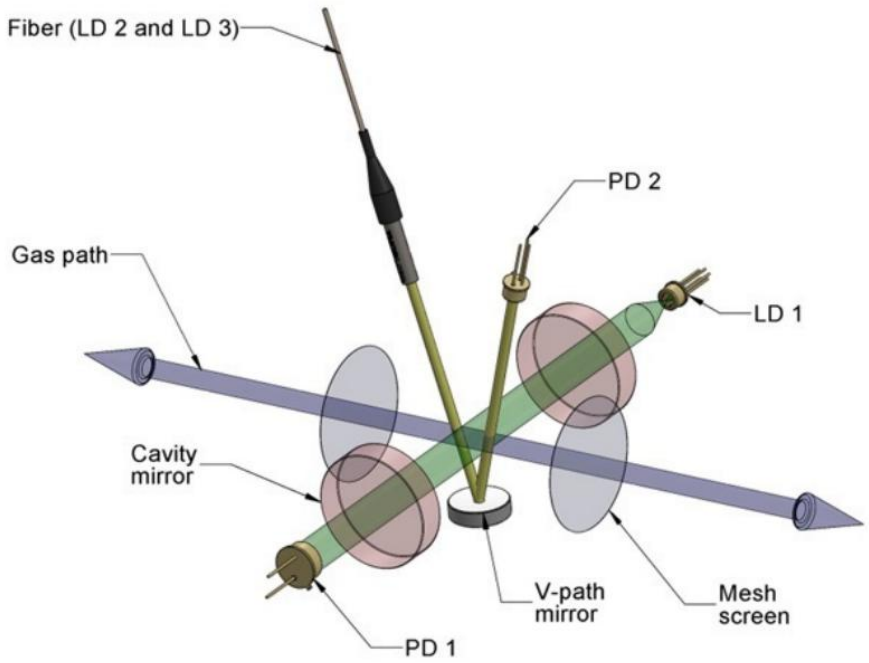


Figure 2.1 A schematic design graph of the MFS. The gas path indicates the mainstream gas flow. LD1 and PD1 represent the laser for O_2 measurements, accompanied by a pair of highly reflective mirrors in the cavity. LD2/LD3 and PD2 represent CO_2 and H_2O measurements via a V-path. The mesh screens show the position of the pneumotachograph for flow measurement. LD: laser diode, PD: photodiode.

A photo of the MFS and a healthy volunteer breathing through it is displayed in **Figure 2.2**. The black cell contains the MFS system, with a mouthpiece and a heat-moisture exchanger with an antibacterial filter connecting to the participant.



Figure 2.2 A healthy volunteer is breathing through the MFS in a CCP measurement. A mouthpiece and a heat-moisture exchanger with an antibacterial filter are used to connect the mouth to the sensor. A nose clip is used.

All atoms and molecules absorb electromagnetic radiation with a specific frequency-dependent absorption profile. This profile offers the potential for the identification of gas species and the measurement of their concentrations. Absorption spectroscopy relies on the attenuation of electromagnetic radiation to quantify the gas concentration. The absorption process follows the Beer-Lambert law,

$$log(I_0/I) = \varepsilon lc, \tag{2.1}$$

where I represents the intensity of transmitted light, I_0 is the initial intensity before being absorbed by molecules, ε is the molar attenuation coefficient, l is the optical path length and c is the concentration of the absorbing molecules. When MFS measures a specific type of gas, the parameters I, l and ε are known and I_0 can be measured. Thus, the concentration c can be determined from ***Eq. 2.1***.

The CO_2 and H_2O can be directly measured by laser absorption technology due to their strong absorption features. A V-shaped optical path approximately 5cm in length is used to measure the concentration of CO_2 and H_2O.

However, O_2 exhibits much weaker absorption of electromagnetic radiation, making direct spectroscopic measurement challenging. A technique named Cavity-Enhanced Absorption Spectroscopy (CAES) is employed to overcome this issue, which uses two highly reflective mirrors and a modified form of Beer-Lambert law,

$$(I_0 - I)/I = \sigma(v)cl/(1-R) \quad (2.2)$$

where R represents the geometric mean of mirror reflectivity, which approaches 1, $\sigma(v)$ is the absorption cross section at frequency v, and the other parameters are the same as ***Eq. 2.1***. Using this equation, the optical path length is extended to $1/(1-R)$ times the original path length, enhancing measurement sensitivity. Calibration with a known concentration of O_2 is required to determine the R value under specific temperature and pressure conditions.

Other physical properties are required to complete the measurement process, such as flow rate, temperature and barometric pressure. The flow is captured by a Lilly-style pneumotachograph, in which two meshes are placed at each end of the flow meter. By measuring the pressure drop (δP) between two meshes, the flow can be calculated[163]. Four thermocouples are installed in the device cell to obtain the average gas temperature. A barometric pressure sensor is installed to measure the ambient pressure.

All data, including gas concentrations and physical properties, are collected simultaneously at high frequency, with a 10 ms sampling interval. Pulmonary gas exchange can be accurately described using these measurements.

2.1.2 The cardiopulmonary mathematical model

The cardiopulmonary mathematical model consists of three components: The lognormal lung (LNL) model, which describes gas exchange in the lung during the breathing cycle[112]; The physicochemical model of gas dissolution describes the CO_2 and O_2 exchange at the interface between air and blood, or more generally, the dissolution of any gas in blood[113]; The

circulation and body gas store (CBGS) model simulates systemic circulation and the storage of gases in various organs[161]. Together, the models describe the process of gas ventilation into the lungs, exchange with blood, circulation, and storage in body tissues, allowing for a comprehensive simulation of the gas exchange cycle within the body.

2.1.2.1 LNL model

In the LNL model, the lung structure is simplified to *N* similar compartments (with N = 125 currently used). Under ideal circumstances, referred to as a homogeneous lung, each compartment behaves identically, receiving equal ventilation and perfusion and performing gas exchange uniformly. In reality, however, each compartment receives a different level of ventilation and perfusion and undergoes varying levels of gas exchange, resulting in variations in gas composition in the alveoli and in the exhaled gas flow[112].

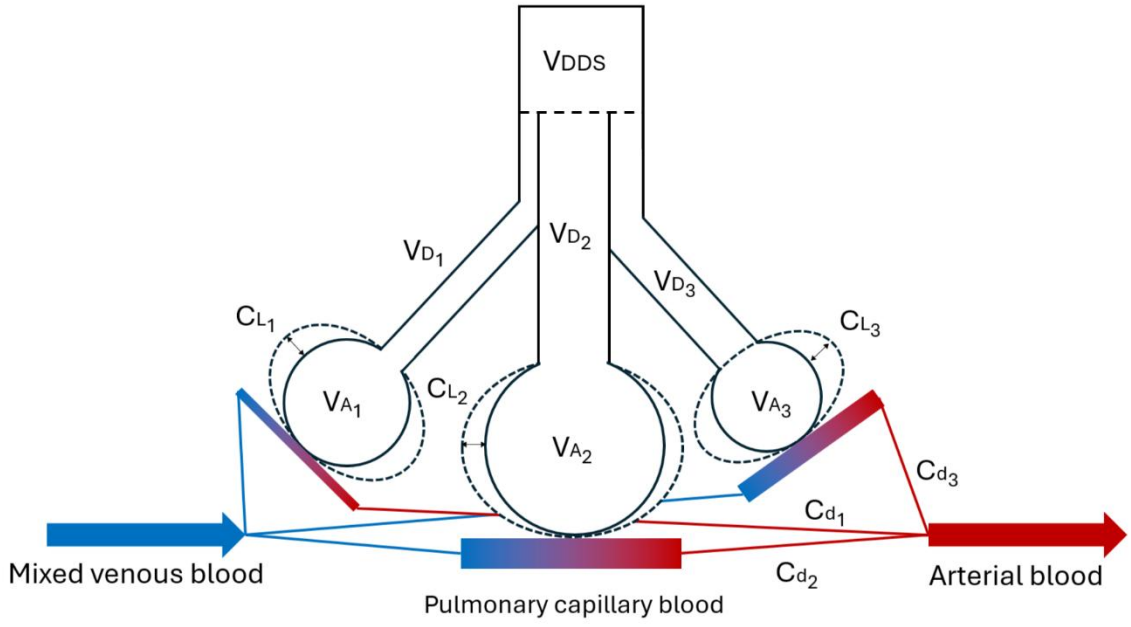


Figure 2.3 Structure of the LNL model. The model is composed of N compartments (N=3 here), each of which has its own alveolar volume (V_{Ai}), its own compliance (C_{Li}) and is supplied by a capillary with its own conductance (C_{di}) and possesses its own deadspace volume (V_{Di}). At the top, the compartments merge into the device deadspace(DDS) with a volume of V_{DDS}. Gas is homogeneous within each alveolus and fully mixed upon entering the DDS.

As illustrated in **Figure 2.3**, the LNL model is a multi-compartment model composed of 125 compartments. Each compartment has its own alveolar volume, ventilation compliance, dead space volume and perfusion conductance. These parameters are expressed as fractions of the total value. For i^{th} compartment: it has its own fraction of compliance (F_{CL}^{i}) relative to the total compliance ($C_{L_{tot}}$), its own fraction of dead space volume ($F_{V_D}^{i}$) relative to the total dead space volume ($V_{DS_{tot}}$), its own fraction of conductance (F_{Cd}^{i}) relative to the total conductance (Cd_{tot}) of the blood vessel. However, different compartments share the same fraction of alveolar volume, $F_{V_A}^{i}$, relative to the total alveolar volume ($V_{A_{tot}}$) at the end of the exhalation stage, i.e., the functional residual capacity (FRC) stage.

It is unrealistic to recover the exact distribution of F_{CL}, F_{Cd} and F_{VD} relative to F_{VA} only through gas profiles measured at the mouth. However, it appears possible to recover the key statistical characteristics of the distribution, particularly with highly accurate and highly temporal resolved data.

As such, the LNL model assumes that $F_{CL} : F_{VA}$ and $F_{Cd} : F_{VA}$ follow a bivariate lognormal distribution with a correlation coefficient ρ, while $F_{VD} : F_{VA}$ follows an independent and normal distribution. The standard deviation of lognormal distributions for $F_{CL} : F_{VA}$ is denoted as $\sigma \ln C_L$, reflecting ventilation inhomogeneity, and the standard deviation of lognormal distributions for $F_{Cd} : F_{VA}$ is referred to as $\sigma \ln C_d$. The standard deviation of normal distribution for $F_{VD} : F_{VA}$ is termed σV_D, revealing the variance in dead space volume distribution.

In addition, the apparatus from the MFS introduces additional dead space into the system. To differentiate the two components, device dead space (DDS) refers to the apparatus dead space and is modelled uniformly using the *BurrXII* distribution with 11 pipes, while biological dead space is referred to as personal dead space (PDS), which corresponds to the

V_D described above. V_D represents the volume of PDS at the end-exhalation stage, i.e., at the FRC stage.

In the LNL model, gas is assumed to be transported by convection modelled by plug flow, neglecting diffusion, and each alveolar unit is assumed to contain a homogeneous gas mixture.

2.1.2.2 Physicochemical model of gas dissolution

O'Neil *et al.* published this model to describe the carriage of CO_2 (and O_2) in pulmonary blood using a physicochemical approach[113]. When gas ventilation and blood perfusion are determined, the model provides the balanced pair of gas content and partial pressure for CO_2 and O_2, considering the Haldane effects. The ventilation and perfusion data are provided by the LNL model, while the gas content in blood is supplied by the next model.

2.1.2.3 Circulation and body gas stores (CBGS)

The CBGS model describes circulatory delay and gas storage in the body, starting from the left cardiac ventricle as blood enters the systemic circulation[161].

This model's calculations are based on a 'standard man' (25 years old, male, height 1.8m and weight 70kg), but it allows rescaling based on individual characteristics, including age, sex, height and weight. The model assumes the human body is composed of 11 compartments, which are mostly independently connected to the pulmonary circulation and arranged in parallel. The only exceptions are the gastrointestinal tract and liver, which are arranged in series to simulate the portal system. Each compartment is assigned a unique weight, density, perfusion rate, and blood-containing capacity, with reference values drawn from published literature[164]. The blood transport outside the organs is modelled using a morphometric model of the arterial tree developed by Avolio[165].

2.1.3 Standardised protocol for CCP

2.1.3.1 Measurement protocol

The protocol of the CCP measurement consists of 7 minutes of room air breathing followed by 5 minutes of pure oxygen breathing. The protocol is applied in all CCP measurements in this thesis, including those used in the NO production depth measurement protocol described in Chapter 3.

Prior to the test, the CCP device must warm up for at least 45 minutes to stabilise the device cell temperature, followed by a calibration process using N_2 and O_2 gases. Calibration should be performed at least once daily, with additional repetitions if required.

The volunteer should avoid large meals for at least 4 hours before the test and rest for a minimum of 30 minutes beforehand. The volunteer undertakes the test wearing a nose clip and breathing through a mouthpiece. Although the standard duration is approximately 12 minutes, it can be adjusted depending on the N_2 washout conditions. The washout is identified as complete when the concentration of N_2 in exhaled air decreases to less than 2.5% of the original N_2 concentration (~78%). The test duration should not exceed 15 minutes. Oxygen saturation and heart rate are continuously monitored throughout the test.

2.1.3.2 Data fitting protocol

In addition to data collected during the experimental procedure, fitting the model requires additional information, including the participant's age, gender, height and weight, to tailor the standard man data to individual profiles. The University of Oxford Advanced Research Computing (ARC) is used to perform the fitting.

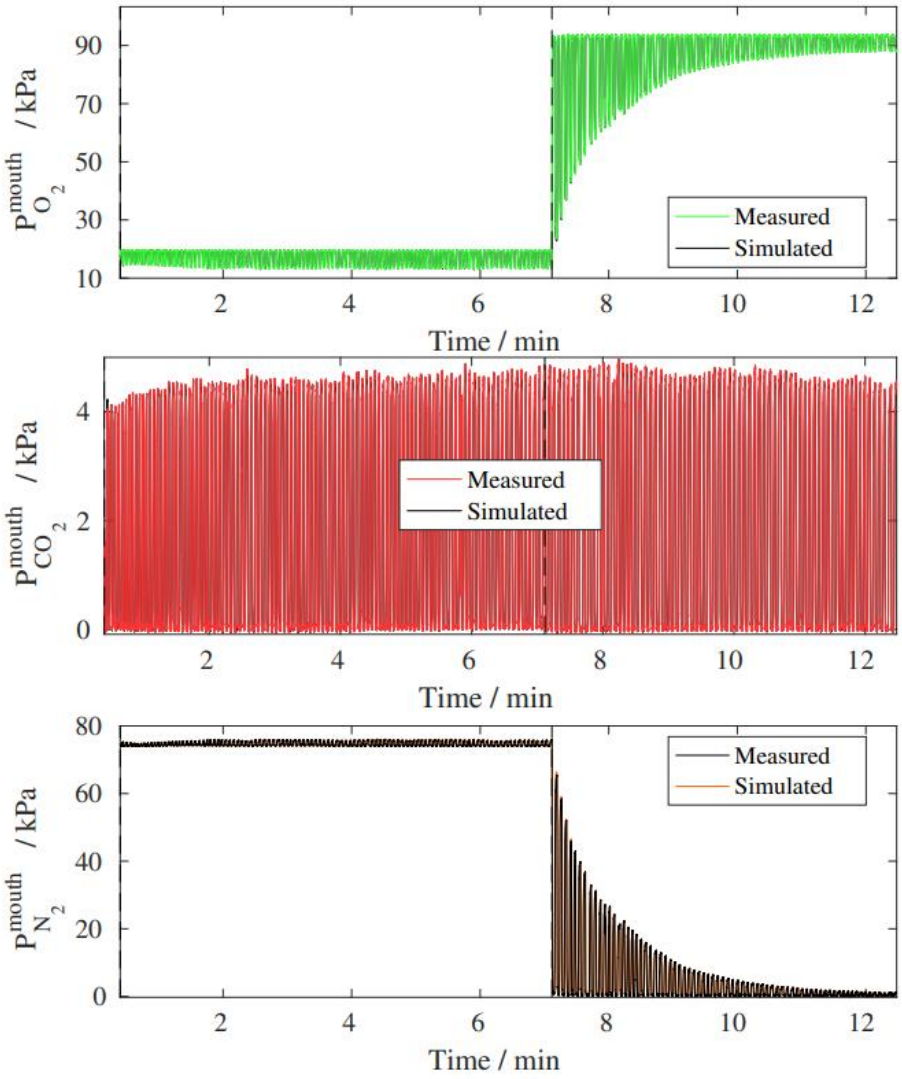


Figure 2.4 Partial pressures of O_2, CO_2 and N_2 during a standard CCP test. Green line: simulated O_2; red line: simulated CO_2; Orange line: simulated N_2; Black lines: measured data from MFS. At ~7 minutes, the gas is transferred from room air to pure oxygen. The tail value of N_2 is less than 2.5% of its original partial pressure.

The cost function is the sum of squared differences between the measured and modelled exhalation flows for each gas species. The optimisation algorithm is non-linear least squares optimisation (NLSQ) from MATLAB. **Figure 2.4** illustrates an example of N_2, O_2 and CO_2 concentration profiles over the breathing test period. The algorithm is repeated four times with independent initial starting points to increase the likelihood of identifying the global optimum.

Table 2.1 lists the parameters fitted in CCP tests.

Table 2.1 Parameters fitted in CCP test

Parameter	Explanation
V_A	Alveolar volume at end-expiration (i.e., FRC stage)
σlnC_L	The standard deviation of lognormal distributions for normalised alveolar compliance.
C_{V_D}	The compliance of dead space volume.
V_D	Personal deadspace volume at end-expiration (i.e., FRC stage).
σV_D	The standard deviation of normal distribution for normalised deadspace across lung volume.
V_{O_2}	O_2 consumption rate.
P_{CO_2}	The initial ideal point of partial pressure of CO_2
RQ	Respiratory quotient

2.1.3.3 Key parameters used in this thesis

The parameters listed below play a crucial role as indicators of lung function or as key variables for obtaining NO depth parameters.

(i) FRC, functional residual capacity. FRC equals $V_A + V_D$ and is a variable that describes the volume of the lung after a tidal expiration.

(ii) V_D, the volume of personal dead space at the end-expiration.

(iii) σV_D: Standard deviation of normal distribution for normalised dead space across lung volume. It reflects the range over which individual personal dead space volumes are distributed.

(iv) σlnC_L: Standard deviation of lognormal distributions for normalised alveolar compliance. It is the primary parameter for assessing lung ventilation inhomogeneity, reflecting the range over which alveolar compliance values are distributed across 125 compartments.

2.1.4 Summary of results from previous clinical studies on lung inhomogeneity

The development of the CCP methodology has led to multiple clinical studies aimed at validating, exploring and utilising its application in clinical settings, particularly σlnC_L as an indicator of small-airway function.

In their study, Mountain *et al.* have not only established the LNL model but also assessed the repeatability and reliability of relevant parameters across three groups of participants: six young healthy volunteers, six older healthy volunteers and six patients with chronic obstructive pulmonary disease (COPD). Their findings have demonstrated that the primary parameters of the CCP test exhibited high repeatability and reliability[112].

Several studies have demonstrated the association between the core inhomogeneity parameter, σlnC_L, and traditional lung function assessment parameters. FEV_1% predicted has been shown to significantly correlate with σlnC_L in patients with asthma and COPD[73, 166, 167]. In addition, σlnC_L has been shown to correlate with small airway function parameters in patients with asthma, including FEF_{25-75}% and R5-20 measured by oscillometry[168].

In a study involving 17 healthy volunteers and 17 patients with asthma, Smith *et al.* reported that σlnC_L was significantly elevated in the asthma group. The study also showed that σlnC_L was a better predictor than FEV_1 for asthma control based on physician evaluations of whether treatment escalation was needed or not [166]. Following these findings in asthma, another study evaluated 91 patients initiating anti-IL5/5R biologic therapy using CCP testing on baseline and at a 3-to-4-month follow-up, with an additional 1-year review. It demonstrated that the blood eosinophil counts were associated with σlnC_L at baseline visits and across visits. Additionally, the early change of σlnC_L at 3 to 4 months was able to predict the 1-year clinical response to biologics[73].

In a study, Smith *et al.* recruited 16 patients with COPD and 10 healthy volunteers, demonstrating that σlnC_L and σV_D were increased in COPD patients compared with healthy volunteers. In addition, the indicators of inhomogeneity, σlnC_L and σV_D, combined with

volume parameters, including V_D and FRC, worsened with the advancing COPD stage[167]. In another study, smoking history, a known risk factor for COPD, of more than 5 pack-year was associated with elevated σlnC_L, a difference not identified by FEV_1% predicted. More importantly, the range of σlnC_L in smokers with > 5 pack-year did not include any data points from non-smokers, highlighting its ability to differentiate a 5 pack-year smoking history from that of non-smokers. These findings suggested that σlnC_L may have greater sensitivity in detecting subclinical abnormalities in the lungs of smokers, potentially due to its ability to reflect distal airway function[169].

CCP test also revealed its ability to assess other respiratory conditions, including cystic fibrosis(CF) and post-COVID-19. In the study about CF, σlnC_L was found elevated in early CF patients (N = 11) compared with healthy volunteers (N=14), while FEV_1 could not separate these two groups. Moreover, the CCP-measured parameters, specifically $\sigma lnC_L * V_D/FRC$, align well with the lung clear index ($LCI_{2.5}$). They also offer the potential to 'untangle' $LCI_{2.5}$, providing deeper insights into disease assessment. The post-COVID-19 study demonstrated a lower V_D in the mild or control group, a reduced FRC in the hospitalised group and an elevated σlnC_L in post-COVID-19 patients[170].

In order to establish a standardised reference value, Alamoudi *et al.* conducted CCP testing in 112 healthy volunteers, calculating the normal reference value for FRC, V_D, σV_D and σlnC_L. By incorporating the individual's age, height, gender and BMI, they developed the z-score calculation of these parameters to support standardised interpretation in future assessment[171]. This thesis also applies the z-score established in that study.

In the following sections, I present two further studies involving healthy volunteers and patients with asthma, highlighting the sensitivity of CCP measurements to assess lung function under different clinical conditions.

2.2 Lung inhomogeneity assessment using CCP in healthy individuals with elevated Type-2 high (T2H) biomarkers

2.2.1 Aims and hypothesis

T2H inflammation biomarkers, FeNO and BEC, are often elevated in patients with asthma and play a crucial role in diagnosis and management. However, elevated T2H inflammation biomarkers can also be found in apparently healthy volunteers. It is estimated that the proportion of healthy volunteers with FeNO ≥ 50ppb can be up to 11%[172], and with BEC ≥ 300μL ranges from 5-19%[173-175].

There are several studies that associate high biomarker levels with lung function decline in healthy participants. In a longitudinal study assessing 4634 individuals over a 15-year range, it was found that the BEC value was associated with a decline in FEV_1[176]. Similarly, Hancox *et al.* conducted a longitudinal study of 971 participants with and without asthma. Among 527 participants without asthma, they demonstrated that BEC was associated with declines in FEV_1 and FEV_1/FVC in individuals, and so was in patients with asthma[177]. The BEC value has also been linked with the development of obstructive airway disease in a 15-year cohort containing over 35,000 participants who did not have a reduced FEV_1 and FEV_1/FVC ratio at baseline[178]. However, none of the above studies included FeNO as a test variable. Çolak *et al.* studied a 10-year cohort from the Danish general population, and they showed that both FeNO and BEC were associated with FEV_1 decline[179].

An unanswered research question is whether elevated biomarkers in healthy individuals, without a diagnosis of any chronic airway disease, are associated with subclinical physiological changes in the lungs of these individuals, even in the absence of FEV_1 abnormalities, and whether such changes can be detected using current techniques. To investigate this, we employed CCP and other lung function tests in healthy volunteers with

elevated biomarker levels to detect early alterations of lung function. To efficiently find suitable participants, we designed an epidemiological study to screen the general population and evaluate the relative prevalence of high type-2 biomarkers in the general population. Accordingly, I first present the screening study findings, followed by an analysis of lung function in healthy individuals.

2.2.2 Epidemiology screening study

2.2.2.1 Participants and protocol

Individuals aged 18 to 50 years old were recruited from public places.

The exclusion criteria included a prior diagnosis of respiratory disease (e.g. asthma and COPD), use of respiratory medications (inhaled corticosteroids or salbutamol), and any other conditions that might affect white cell counts (e.g. immunosuppressive disease, use of systemic corticosteroids).

This study was under the ethics: epidemiology of type 2 biomarkers in healthy individuals (Ref R87777/RE001). All participants provided written informed consent prior to testing.

The participants were studied according to this protocol:

(i) Fractional exhaled nitric oxide (FeNO, *NIOX Vero, Sweden*).

(ii) Finger-prick blood test to measure white blood cell count (*HemoCue, WBC DIFF system, Sweden*): the device provides measurements with a resolution of 100/μL.

(iii) A questionnaire assessing medical history and symptoms (see supplementary material for a copy).

(iv) Smoking and vaping history.

Proportions were analysed using the Chi-square test or Fisher's exact test, depending on the sample size.

2.2.2.2 Results

Table 2.2 presents the demographic characteristics of the participants. The cohort consisted of relatively young adults.

Table 2.2 Demographic characteristics of the participants

Group	Healthy volunteers
Number	122
Age /yr, mean ± SD	30 ± 9
Gender Female (%)	79 (65)
BMI /kg · m^{-2}, median (IQR)	22.5(20.7, 24.6)
Smoking history (%)	22 (18)
Atopy (%)*	52 (43)
FeNO /ppb, median (IQR)	18 (13, 33)
BEC /10^{9}·L^{-1}, median (IQR)	0.1(0.1, 0.2)

* Atopy: patient reporting nasal allergies OR hay fever OR eczema. BMI: body mass index, FeNO: fractional exhaled nitric oxide, BEC: blood eosinophil count.

The epidemiology results are presented in **Table 2.3**. Nine (8%) participants had FeNO ≥ 50ppb and 17(15%) participants had BEC ≥ 300/μL. A total of 21 (18%) participants had either a high FeNO (≥ 50ppb) or a high BEC (≥ 300 /μL). Male participants had significantly higher FeNO, a median (IQR) of 27(17, 39) ppb, compared with the female group, 16(11, 24) ppb $p < 0.001$, while no significant sex difference was observed in BEC levels.

Table 2.3 Distribution of biomarkers within the group

	BEC ≤ 100 /μL, N(%)	**BEC = 200 /μL N(%)**	**BEC ≥ 300 /μL N(%)**	**Total**
FeNO ≤ 25 ppb	54(47%)	11(10%)	7(6%)	72(63%)
25 ppb < FeNO < 50 ppb	17(15%)	11(10%)	5(4%)	33(29%)
FeNO ≥ 50 ppb	3(3%)	1(1%)	5(4%)	9(8%)
Total	74(65%)	23(20%)	17(15%)	114(100%)*

* HemoCue results were not obtained from 8 participants. FeNO: fractional exhaled nitric oxide, BEC: blood eosinophil count. BEC was measured using HemoCue, with a resolution of 100 cells/μL.

2.2.3 Lung inhomogeneity in volunteers with T2H inflammation

As the previous section showed, nearly 20% of the healthy participants had elevated biomarker levels. We conducted a subsequent study to investigate whether these apparently healthy volunteers exhibited subtle lung physiological parameters abnormalities associated with T2H airway inflammation.

2.2.3.1 Methods

Twenty-three young (≤45 years) volunteers with no prior asthma diagnosis, $FEV_1 \geq 80\%$ predicted and $FEV_1/FVC \geq 70\%$ predicted, were recruited for this cross-sectional study. The study was conducted under the ethics: Oxford Airway Study (OAS), 18/CS/0361. All participants gave their written informed consent prior to participation.

The participants were grouped based on their T2H biomarkers. Group H (N = 11) included volunteers with at least one elevated T2H biomarker (FeNO ≥ 50ppb AND/OR BEC ≥ 300/μL); and Group L (N = 12) were volunteers with FeNO < 50 ppb AND BEC < 300/μL.

Participants underwent the following tests:

(i) Fractional exhaled nitric oxide (FeNO, *NIOX Vero, Sweden*)

(ii) Spirometry: the forced expired volume in 1s (FEV_1), the forced vital capacity (FVC), the expiratory flow between 25% and 75% of forced vital capacity (FEF_{25-75}%) and FEV_1/FVC ratio.

(iii) Impulse oscillometry. Parameters obtained include the resistance at 20Hz (R20), the resistance at 5Hz (R5), the R5-20 = R5 – R20, presented in standardized z-score.

(iv) Standard CCP measurement, as described in the previous section.
Parameters obtained included the functional residual capacity (FRC), deadspace volume (V_D), the standard deviation for the standardised volume of deadspace(σV_D), The standard deviation of lognormal distributions for normalised alveolar compliance($\sigma \ln C_L$),

(v) Blood sampling for full blood count.

(vi) Sputum induction is performed according to the description by Pizzichini *et al.*[180].

Differences between groups were compared by Student t-test (unpaired) for normally distributed continuous variables. Mann-Whitney U test was used for variables that were not normally distributed. Proportions were compared using the Chi-square test or Fisher's exact test, depending on the sample size. Receiver operating characteristics (ROC) analysis was performed on lung function parameters to evaluate the ability of different measurements to identify early lung alterations.

2.2.3.2 Results

2.2.3.2.1 Demographic characteristics of participants

As demonstrated in **Table 2.4**, each group had similar demographic characteristics. Differences in FeNO and BEC were expected, as they resulted from the grouping strategy.

Table 2.4 Comparison between Group H and Group L

	Group H	**Group L**	**p***
Number	11	12	-
Age /yr, mean ± SD	30 ± 7	32 ± 7	0.612
Gender, Female (%)	4(36%)	2(17%)	0.371
BMI /kg · m^{-2}, median (IQR)	24.7(21.9, 28.2)	24.1(20.4, 25.8)	0.622
FeNO /ppb, median (IQR)	55(21, 83)	25(19, 42)	**0.036**
BEC /10^{9}·L^{-1}, median(IQR)	0.37(0.29, 0.55)	0.09(0.05, 0.19)	**<0.001**

2.2.3.2.2 Physiological parameters

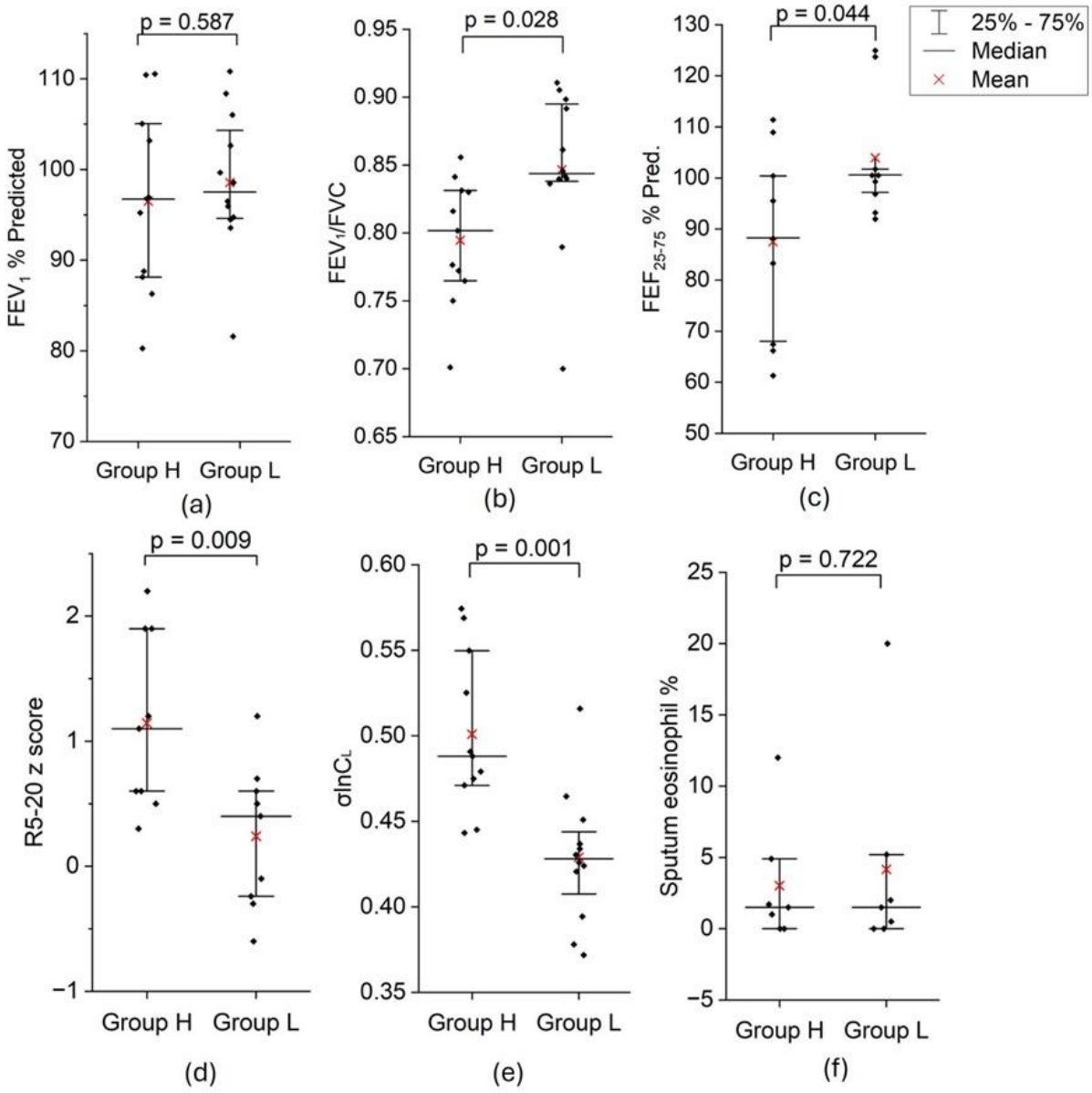


Figure 2.5 Lung physiological parameters in Group H and Group L. (a) FEV_1 % predicted, (b) FEV_1/FVC, (c) FEF_{25-75}% predicted, (d) R5-20 z-score, (e) σlnCL, (f) σlnCL z score. Parameters reflecting large airway function, small airway function and lung inhomogeneity all indicate that Group H had poorer lung function. The sputum eosinophil percentage was similar between the groups.

Figure 2.5 compares the physiological parameters between Group H and Group L.

FEV_1 % predicted did not differ significantly between the groups (Group H 96.5 ± 10.0% vs Group L 98.6 ± 7.8%, p = 0.587), but FEV_1/FVC was significantly lower in Group H (Group H: 0.79 ± 0.46 vs Group L: 0.85 ± 0.58 vs, p = 0.028).

Small airway function was reduced in Group H, as reflected by FEF_{25-75}% predicted (Group H 87.5 ± 18.9% vs Group L 104.0 ± 12.4%, p = 0.044) and R5-20 z score (Group H 1.1 ± 0.7 vs Group L 0.2 ± 0.6, p = 0.009).

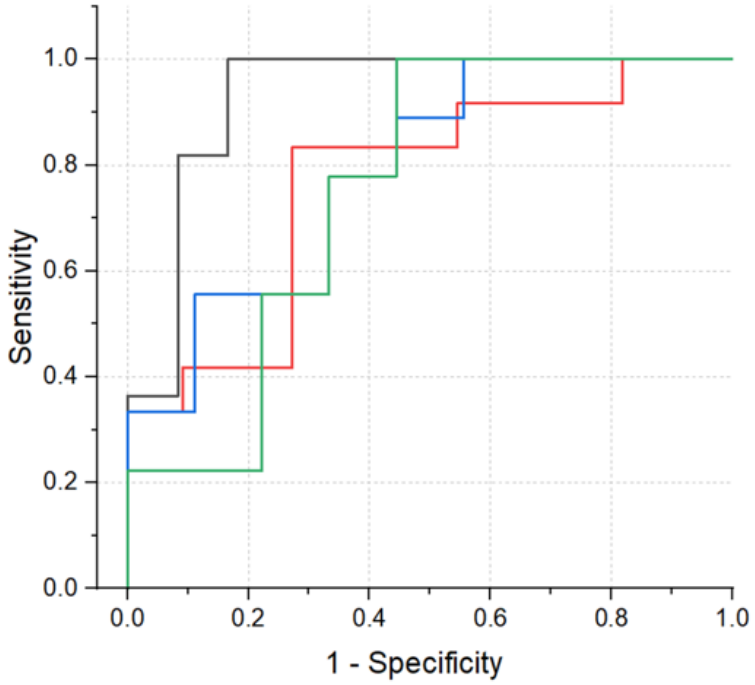
σlnC_L, the indicator of lung inhomogeneity, was significantly elevated in Group H compared to Group L (Group H: 0.50 ± 0.05 vs Group L: 0.43 ± 0.04, p = 0.001), as was its z-score (Group H: 0.40 ± 0.63 vs Group L: -0.60 ± 0.44, p = 0.001).

Sputum eosinophil percentage was not significantly different between the groups (Group H: 3.0 ± 4.3% vs Group L: 4.2 ± 7.2%, p = 0.722).

Table S2.1 provides a full list of lung physiology parameters in Supplements, showing the remaining parameters were similar between the groups.

2.2.3.2.3 ROC analysis for lung function test to represent the groups

Since all lung function changes remain within the normal range, ROC analysis was conducted to evaluate their ability to identify the T2H inflammation group, as indicated by the grouping of this study. **Figure 2.6** demonstrates the findings of ROC. Among all significant lung function parameters, σlnC_L had the highest Area Under the Curve (AUC = 0.93), showing the greatest discriminative ability for Group H and Group L.



Label	Parameter	AUC	95% CI
	σlnCL z score	0.93	0.82, 1.05
	FEV1/FVC z score	0.77	0.56, 0.97
	R5-20 z score	0.81	0.62, 1.01
	FEF25-75 z score	0.75	0.52, 0.99

Figure 2.6 ROC analysis of four significant parameters. All parameters were transformed into z-scores to exclude the effects of age, gender, BMI, etc. AUC: Area under the curve. CI: confidence interval.

2.2.3.3 Discussion

This study identified that healthy individuals with elevated T2 biomarkers exhibit subclinical lung function alterations, as evidenced by differences in conventional spirometry measures (FEV_1/FVC, FEF_{25-75}% predicted), emerging measurements technique (R5-20 in oscillometry), and the lung inhomogeneity parameter(σlnC_L) when compared with those with low biomarkers.

These findings suggested that the observed alterations may primarily involve peripheral airways, as indicated by reductions in both widely recognised and newly developed small

airway function parameters. Furthermore, when comparing the discriminative power of various parameters in identifying individuals defined in this study, σlnC_L demonstrated the highest AUC in ROC analysis, indicating its potential value as a sensitive assessment of lung function abnormalities in these apparent healthy volunteers.

These findings highlight the need for a larger-scale cross-sectional study to validate and compare the effectiveness of different detection parameters in identifying abnormality among healthy volunteers. More importantly, a longitudinal study is needed to follow-up such individuals over the years, monitoring their lung function alterations and linking the subclinical changes to pathological changes in the lung and the prognosis of participants (i.e. whether they develop respiratory morbidity in the future, e.g. asthma).

The major limitation of this study is its cross-sectional design, which lacks longitudinal data to establish the associations between biomarkers and prognostic results. In addition, the sample size is small, limiting its ability to consider other factors related to lung functions. The small sample size also restricts the ability to explore the distinct roles of FeNO and BEC.

2.3 Lung inhomogeneity in patients with asthma receiving inhaled or systemic corticosteroids

2.3.1 Aims and hypothesis

This study focuses on assessing inhomogeneity parameters in asthmatic patients of varying severity and before and after treatment with either inhaled corticosteroids (ICS) or systemic corticosteroids (SCS). The aim is to evaluate whether corticosteroid therapy leads to significant changes in inhomogeneity parameters generated by CCP.

2.3.2 Methods

This was an observational study conducted alongside the patients' clinical pathway, approved under the ethics reference: Oxford Airway Study (OAS), 18/SC/0361. All patients gave informed consent prior to participating.

2.3.2.1 Participants and protocol

There were two groups in this study: the ICS group and the SCS group. The ICS group consisted of 17 patients who never received any regular ICS treatment before (i.e. they were steroid-treatment naïve). In this study, they generally received an equivalence of 400 mcg BDP daily for 8 weeks, as decided by their physicians. The SCS group consisted of 12 patients who were already on inhaled corticosteroid treatment (GINA steps IV-V, BDP equivalence 1000-2000mcg). They went on to receive systemic corticosteroids in the form of either oral corticosteroids (OCS) (prednisolone 40 mg daily dose for 10-14 days, n = 4 patients) or intramuscular injection of triamcinolone (80 mg once, n = 8 patients), as decided by their clinicians.

Participants from both groups were studied twice: at a Baseline visit (immediately before the initiation of their respective treatment, ICS or SCS) and at a follow-up visit. The interval between baseline visits and follow-up visits was determined by group assignment. The ICS group had their follow-up visit 8 weeks after the baseline. The follow-up interval in the SCS group was 10-14 days for patients receiving OCS and 30 days for those given a triamcinolone injection.

At each research visit, participants underwent the following assessments:

(i) ACQ-5 symptom questionnaire

(ii) Fractional exhaled nitric oxide (FeNO, *NIOX, Sweden*)

(iii) Spirometry: FEV_1, FVC, FEF_{25-75}% and FEV_1/FVC ratio.

(iv) Standard CCP measurement, as described in the previous section.

Parameters obtained included: FRC, V_D, $\sigma \ln C_L$ and σV_D.

Spirometry and CCP were performed twice at each visit, before and after bronchodilation (BD), with 400 mcg of salbutamol inhaled via a spacer.

(v) Blood samples were collected to measure the full blood count.

2.3.2.2 Statistical analysis:

For normally distributed continuous variables, differences between groups were compared using the Student's t-test (paired or unpaired, as appropriate). If the variable was not normally distributed, Wilcoxon Signed Rank test (paired) or Mann-Whitney U (unpaired) test was used. Proportions were compared in Chi-square test or Fisher's exact test depending on the sample size.

To assess the effect of corticosteroid treatment on physiological parameters (e.g. spirometry and CCP parameters), a linear mixed-effects model was employed:

$$Y \sim Age + isMale + BMI + Visit + BD + Visit * BD + 1/Participant\ No,$$

Where the fixed effects factors included the binary fixed and the continuous fixed factors, the binary fixed effects factors: *Visit* (0 for baseline visit, 1 for follow-up visit), BD *(*0 for before BD use, 1 for after BD use), isMale (0 for female, 1 for male) and the continuous fixed factors: *Age*, and *BMI* (body mass index).

And the random effects factor was *Participant No*.

Non-significant factors were removed from the model sequentially, starting with interaction terms followed by the least significant fixed effects factors. If the dependent variable already accounted for physiological characteristics of participants such as age, BMI, and gender, these related independent variables were not included in the model (e.g. *FEV_1 % predicted* with *age*, *isMale*). However, the fixed effects factor *Visit* is always retained, as the objective was to evaluate the relationship between parameters and visits.

2.3.3 Results

2.3.3.1 Baseline data

Table 2.5 shows the demographic information and baseline characteristics of both groups. The SCS group appears to have more severe asthma, as indicated by the GINA step. Patients in the SCS group also had higher BEC and higher GINA steps, while FeNO values were similar between the two groups.

Table 2.5 Demographic characteristics in the ICS and SCS group

	ICS group	**SCS group**	**p***
Number	21	12	-
Age /yr, mean ± SD	57 ± 15	56 ± 11	0.815
Gender Female (%)	8(38%)	1(8%)	0.065
BMI /kg · m^{-2}, median (IQR)	27.5 (24.6, 29.2)	24.8 (23.0, 26.2)	0.099
GINA step	0	IV-V	-
ACQ-5 value, mean ± SD	1.4 ± 0.9	2 ± 1.2	0.09
FeNO /ppb, median (IQR)	55 (45, 91)	79 (51, 113)	0.231
BEC /10^{9}·L^{-1}, median (IQR)	0.29(0.19, 0.44)	0.54(0.29, 0.90)	**0.026**
Sputum eosinophil %, median (IQR)$^{\#}$	3.5(0.3, 9)	30.9(4.8, 83)	0.100

***** Statistic methods depended on the distribution of the data, as detailed in the methods section. BMI: the body mass index, GINA: Global Initiative for Asthma, FeNO: fractional exhaled nitric oxide, BEC: blood eosinophil count. $^{\#}$ limited sample size: ICS group (n = 13), SCS group (n = 4).

Table 2.6 presents the physiological parameters from spirometry and CCP at the baseline visit for the two groups. The SCS group showed worse lung function, as evidenced by a lower FEV_1 % predicted, a lower FVC % predicted and a lower FEV_1/FVC ratio both pre-BD and post-BD. While the SCS group had higher FRC values than the ICS group, this difference was only significant at post-BD. The σlnC_L presented consistent results with spirometry, with significantly higher values in the SCS group at both pre-BD and post-BD.

Table 2.6 Physiological parameters at the baseline visit

	Pre BD			Post BD		
Group	**ICS**	**SCS**	**p***	**ICS**	**SCS**	**p***
FEV_1 /L, mean ± SD	2.98 ± 0.93	2.31 ± 0.53	-	3.08 ± 0.87	2.60 ± 0.54	-
FEV_1 % pred., mean ± SD	89.6 ± 15.4	64.5±12.6	**<0.001**	93.3 ± 14.1	72.0 ± 12.9	**<0.001**
FEV_1 z score, mean ± SD	-0.67 ± 1.02	-2.41 ± 0.82	**<0.001**	-0.43 ± 0.96	-1.89 ± 0.86	**<0.001**
FVC /L, mean ± SD	4.25 ± 1.10	4.00 ± 0.98	-	4.19 ± 1.08	4.41 ± 0.93	-
FVC % pred., mean ± SD	100.8 ± 12.3	86.3±12.9	**0.003**	99.2 ± 12.4	93.7 ± 10.6	0.224
FVC z score, mean ± SD	0.06 ± 0.84	-0.95 ± 0.91	**0.003**	-0.05 ± 0.83	-0.42 ± 0.75	0.224
FEV_1/FVC /%, mean ± SD	69.5 ± 8.8	58.4 ± 9.4	**0.002**	73.8 ± 8.2	59.7 ± 9.6	**<0.001**
FEV_1/FVC z score, mean ± SD	-1.19 ± 0.97	-2.55 ± 1.12	**0.001**	-0.64 ± 0.90	-2.24 ± 1.14	**<0.001**
FEF_{25-75}% pred, mean ± SD	77.9 ± 26.4	- **	-	88.5±29.9	-**	-
FEF25-75 z score, mean ± SD	-0.79 ± 0.92	- **	-	-0.44 ± 0.98	- **	-
R5-20 z score, mean ± SD	1.3±1.8	-**	-	1.1±1.3	-**	
FRC /L, mean ± SD	3.01 ± 0.70	3.81 ± 1.02	-	2.88 ± 0.69	3.87 ± 1.04	-
FRC z score, mean ± SD	-0.30 ± 1.22	0.75 ± 1.71	0.055	-0.54 ± 0.93	1.02 ± 1.63	**0.007**
V_D /L, mean ± SD	0.16 ± 0.04	0.21 ± 0.10	-	0.18 ± 0.06	0.19 ± 0.05	-
lnV_D z score, mean ± SD	0.29 ± 0.98	0.97 ± 1.68	0.166	1.10 ± 0.80	0.69±1.1	0.309
σV_D, mean ± SD	0.34 ± 0.10	0.29 ± 0.14	-	0.30 ± 0.06	0.32 ± 0.11	-
σV_D z score, mean ± SD	0.15 ± 1.81	-0.57 ± 2.53	0.361	-0.47 ± 0.97	-0.20 ± 1.92	0.656
σlnC_L, mean ± SD	0.64 ± 0.16	0.84 ± 0.26	**0.011**	0.54 ± 0.13	0.79 ± 0.18	**0.001**
σlnCL z score, mean ± SD	1.21 ± 1.63	4.02 ± 3.38	**0.004**	0.15 ± 1.23	3.51 ± 2.44	**<0.001**

* Statistic methods depended on the distribution of the data, as detailed in the methods section. ** FEF_{25-75}% was not collected in the SCS group. FEV_1: the forced expired volume in 1s, FVC: the forced vital capacity, FEF_{25-75}% pred.: the percentage of the expiratory flow between 25% and 75% of vital capacity to predicted, FRC: the functional residual capacity, V_D: volume of deadspace, σV_D:

standard deviation of the volume of deadspace, σlnCL: standard deviation for the natural logarithm of the standardised lung compliance. p value reflects the comparison between the ICS group and the SCS group.

2.3.3.2 Effects of corticosteroid treatment

Figure 2.7 shows the effects of corticosteroid treatment on biomarkers and symptoms (ACQ5) in each group. FeNO level and BEC decreased in both groups following treatment. There appears to be a greater reduction in FeNO following ICS than SCS (delta median in ICS vs SCS -35 vs -21 ppb, $p > 0.05$), but this difference was not statistically significant. In contrast, the reduction in BEC was significantly greater following SCC treatment (delta median in ICS vs SCS -60 vs -370 /μL, $p < 0.001$).

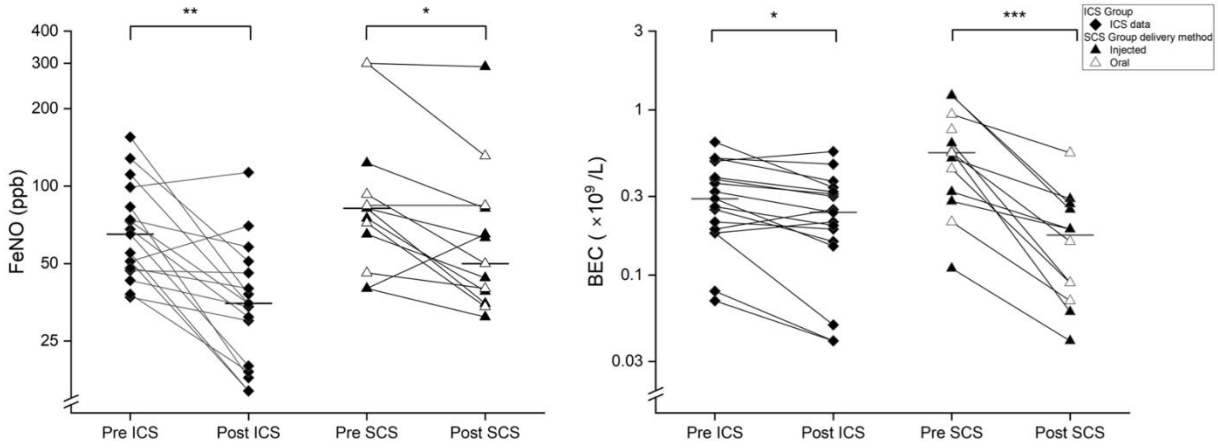


Figure 2.7 (a) FeNO and (b) BEC values before and after intervention. The horizontal line shows the median of each group. *: <0.05, **: <0.01, ***: <0.001. FeNO: fractional exhaled nitric oxide. BEC: blood eosinophil count.

Figure 2.8 demonstrates the effect of ICS and SCS on FEV_1% predicted and σlnCL for both pre-BD and post-BD values. Supplementary **Table S2.2** presents follow-up values for all other parameters.

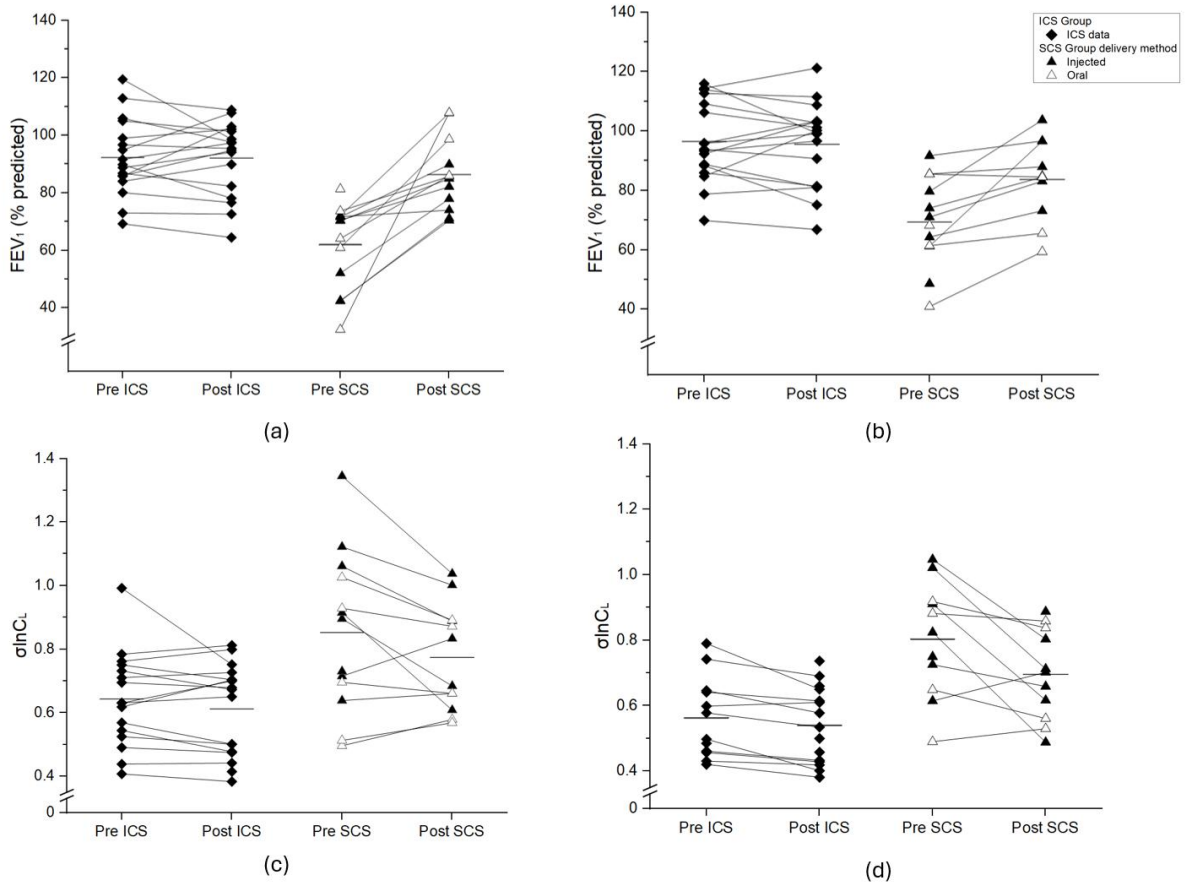


Figure 2.8 Effects of the ICS and SCS on physiological parameters. (a) Pre-BD FEV1 % predicted; (b) Post-BD FEV_1 % predicted; (c) Pre-BD σlnCL; (d) Post-BD σlnCL. Horizontal line shows the mean of each group. The horizontal line shows the median of each group.

To account for repeated measures (e.g. Pre- and Post-BD) when comparing an individual's change before and after treatment, a linear mixed-effects model was employed to analyse the data, as shown in **Table 2.7**.

If the variable *Visit* is found significant, it indicates that the treatment (receiving ICS or SCS) had a measurable significant effect on the parameter. Although ICS did not alter the spirometry results for the ICS group, it significantly improved (reduced) the σlnCL (z-score coefficient = -0.41, $p = 0.029$). For SCS, improvements at post-treatment were more evident, as treatment significantly improved FEV_1 (z-score coefficient = 0.73, $p < 0.001$), FEV_1/FVC (z-score coefficient = 0.57, $p < 0.001$) and σlnCL (z-score coefficient = -1.5, $p < 0.001$).

Table 2.7 Effects of intervention on physiological parameters

ICS group					SCS group				
Predictors	**Coefficient**	**SE**	**df**	**p***	**Predictors**	**Coefficient**	**SE**	**df**	**p***
	FEV_1 % pred.					**FEV_1 % pred.**			
Intercept	93.5	3.4	28	<0.001	**Intercept**	63.6	3.9	16	<0.001
Visit	-0.59	1.3	49	0.661	**Visit**	11.9	2.1	35	<0.001
BD	2.71	1.3	49	0.047	**BD**	8.2	2.0	35	<0.001
	FEV_1 z score					**FEV_1 z score**			
Intercept	-0.48	0.20	20	0.028	**Intercept**	-2.47	0.3	16	<0.001
Visit	-0.05	0.09	49	0.610	**Visit**	0.73	0.13	35	<0.001
BD	0.173	0.09	49	0.055	**BD**	0.56	0.12	35	<0.001
	FEV_1/FVC /%					**FEV_1/FVC /%**			
Intercept	70.3	1.6	21	<0.001	**Intercept**	58.0	3.2	14	<0.001
Visit	1.2	0.86	49	0.167	**Visit**	5.2	1.1	35	<0.001
BD	3.9	0.86	19	<0.001	**BD**	2.8	1.1	35	0.016
	FEV_1/FVC z score					**FEV_1/FVC z score**			
Intercept	-1.02	0.20	22	<0.001	**Intercept**	-2.6	0.4	14	<0.001
Visit	0.14	0.11	49	0.174	**Visit**	0.57	0.13	35	<0.001
BD	0.505	0.106	49	<0.001	**BD**	0.31	0.12	35	0.018
	FEF_{25-75} % pred.					**FEF_{25-75} % pred.**			
Intercept	76.0	7.7	12	<0.001	**-**	-	-	-	-
Visit	-5.7	3.0	27	0.070					
BD	12.8	2.9	27	<0.001					
	FEF_{25-75} z score					**FEF_{25-75} z score**			
Intercept	-0.81	0.26	12	0.008	**-**	-	-	-	-
Visit	-0.17	0.11	27	0.141					
BD	0.410	0.10	27	<0.001					
	FRC z score					**FRC z score**			
Intercept	-0.30	0.33	18	0.371	**Intercept**	0.76	0.4	14	0.083
Visit	-0.030	0.13	41	0.825	**Visit**	-0.07	0.1	33	0.566
BD	-0.175	0.13	41	0.195	**BD**	-0.11	0.1	33	0.371
	ln(V_D) z score					**ln(V_D) z score**			
Intercept	0.19	0.24	20	0.449	**Intercept**	0.97	0.3	24	0.005
Visit	-0.085	0.12	41	0.482	**Visit**	-0.37	0.27	34	0.170
BD	1.10	0.12	41	<0.001	**BD**	-0.03	0.26	34	0.912
	σV_D z score					**σV_D**			
Intercept	0.13	0.35	31	0.714	**Intercept**	-0.28	0.5	20	0.575
Visit	0.11	0.30	41	0.712	**Visit**	0.05	0.4	34	0.892

BD	-0.43	0.30	40	0.167	**BD**	0.14	0.4	34	0.685
	σlnCL z score					**σlnCL z score**			
Intercept	1.15	0.33	21	0.002	**Intercept**	4.2	0.7	16	<0.001
Visit	-0.41	0.18	42	0.029	**Visit**	-1.5	0.4	34	<0.001
BD	-0.93	0.18	41	<0.001	**BD**	-1.0	0.4	33	0.011

*Statistical method: linear mixed regression, as detailed in the method section. SE: standard error, df: degree of freedom, FEV_1: the forced expired volume in 1s, FVC: the forced vital capacity, FEF_{25-75}% pred.: the percentage of the expiratory flow between 25% and 75% of vital capacity to predicted, FRC: the functional residual capacity, V_D: volume of deadspace, σV_D: standard deviation of volume of deadspace, σlnC_L: standard deviation for the natural logarithm of the standardised lung compliance.

2.3.4 Discussion

This study is the first to evaluate lung inhomogeneity measured by CCP following treatment with ICS or SCS in patients with asthma. Its findings demonstrate that CCP is a reliable tool for assessing asthma severity and treatment response.

The SCS group comprises patients with more severe asthma disease (as evidenced by their GINA step) compared to the ICS group, which consists of treatment-naïve patients newly diagnosed with asthma. The results show that the SCS group has greater systemic inflammation (as indicated by BEC), similar FeNO levels, and worse lung function compared with the ICS group. The σlnC_L, the primary CCP parameter for assessing lung inhomogeneity, was consistent with these findings, showing significantly higher values in the SCS group than in the ICS group. These findings further support the validity of CCP as a reliable tool not only for identifying a disease like asthma, as reported by Smith *et al.*'s[166], but also for assessing asthma disease severity.

Moreover, after patients received ICS treatment, σlnC_L showed a small but statistically significant reduction, while spirometry (FEV_1) did not. This difference in response suggests that CCP, through σlnC_L, is more sensitive to treatment-induced changes in lung physiology than spirometry in patients with mild asthma. In contrast, in the SCS group, significant improvements are observed both in spirometry and σlnC_L following treatment. Given that the

change in σlnC_L in the SCS group was larger than that in the ICS group (z score coefficient in ICS vs SCS -0.41 vs -1.5), these findings may reflect a dose-dependent effect, or alternatively, suggest that SCS exerts a greater impact on the small airways, as σlnC_L typically captures abnormalities in small airway function. Indeed, σlnC_L has been shown to correlate with other small airway function parameters, such as FEF_{25-75}% Pred and the oscillometry R5-20 z-score[168].

The primary limitation of this study is the relatively small sample size, which requires combining the OCS group with the intramuscular corticosteroid group. This grouping may have introduced confounding factors, as the two delivery methods differ in terms of dosage, frequency and duration of administration. Secondly, although a low-dose of ICS was administrated, systemic effects could not be completely avoided, as indicated by the decreasing BEC. The mechanism underlying the improvement in σlnC_L in the ICS group could not be determined, whether through suppression of local inflammation or systemic effects. Lastly, the lack of FEF_{25-75}% data in the SCS group has limited the comparison of traditional small airway functions between the two groups and across treatments.

This study highlights the potential of lung inhomogeneity as a key parameter for monitoring lung function during therapeutic intervention. It proposes that this association may be closely related to small airway function. Longitudinal studies incorporating small airway parameters could provide a more comprehensive understanding of changes in lung inhomogeneity throughout asthma progression and further support its application in asthma monitoring.

2.4 Summary

This Chapter introduces the inhomogeneity measurement technique, CCP, and presents two studies based on this method. The core advantage of CCP is its ability to detect gas

compositions with high accuracy and time resolution. This capability facilitates mathematical modelling to compute differences between lung physiology. Previous studies have highlighted its potential as a more sensitive tool for assessing lung function. This Chapter extends its application to healthy volunteers with elevated T2H biomarkers and to patients with varying degrees of asthma. The studies in this Chapter support the higher sensitivity of CCP in assessing lung function compared to conventional tools such as spirometry.

Moreover, the NO depth estimation builds on this advantage of accurately capturing lung physiology. The Chapter 4 will explain how CCP outputs are incorporated into the estimation process to account for inter-individual variations in airway structure, thereby enabling the generation of precise NO depth parameters in the conducting airways.

2.5 Supplementary material

Table S2.1 Comparison of physiological parameters between Group H and Group L.

Group	Group H	Group L	p
FEV_1 /L, mean ± SD	4.06 ± 0.90	4.17 ± 0.79	-
FEV_1 % pred., mean ± SD	96.5 ± 10.0	98.6 ± 7.8	0.587
FEV_1 z score., mean ± SD	-0.28 ± 0.84	-0.18 ± 0.86	0.795
FVC /L, mean ± SD	5.12 ± 1.16	4.17 ± 0.79	-
FVC % pred., mean ± SD	101.0 ± 10.6	96.6 ± 11.5	0.354
FVC z score, mean ± SD	0.11 ± 0.90	-0.43 ± 1.24	0.255
FEV_1/FVC /%, mean ± SD	79.4 ± 4.6	84.7 ± 5.8	0.028
FEV_1/FVC z score, mean ± SD	-0.62 ± 0.84	0.35 ± 0.88	0.013
FEF_{25-75}% pred, mean ± SD	87.5 ± 18.9	104.0 ± 12.4	0.044
FEF_{25-75}% z score, mean ± SD	-0.59 ± 0.86	0.14 ± 0.46	0.040
R5-20 z score, mean ± SD	1.1 ± 0.7	0.2 ± 0.6	0.009
Sputum eosinophil %	3.0 ± 4.3	4.2 ± 7.2	0.722
FRC /L, mean ± SD	3.05 ± 0.92	3.23 ± 0.73	-
FRC z score, mean ± SD	-0.46 ± 1.48	-0.15 ± 0.65	0.515
V_D /L, mean ± SD	0.13 ± 0.04	0.15 ± 0.03	-
lnV_D z score mean ± SD	-0.36 ± 0.91	0.14 ± 0.79	0.178
σV_D, mean ± SD	0.35 ± 0.07	0.31 ± 0.08	-
σV_D z score, mean ± SD	0.00 ± 1.35	-0.74 ± 1.50	0.229
σlnC_L, mean ± SD	0.50 ± 0.05	0.43 ± 0.04	-
σlnC_L z score, mean ± SD	0.40 ± 0.63	-0.60 ± 0.44	<0.001

FEV_1: the forced expired volume in 1s, FVC: the forced vital capacity, FEF_{25-75}% pred.: the percentage of the expiratory flow between 25% and 75% of vital capacity to predicted, FRC: the functional residual capacity, V_D: volume of deadspace, σV_D: standard deviation of the volume of deadspace, $\sigma \ln C_L$: standard deviation for the natural logarithm of the standardised lung compliance.

Table S2.2 Physiological parameters at the follow-up visit

Group	ICS group		SCS group	
BD	**Pre-BD**	**Post-BD**	**Pre-BD**	**Post-BD**
FEV_1 /L, mean ± SD	3.00±0.81	3.07± 0.81	2.54 ±0.53	2.88±0.65
FEV_1 % pred., mean ± SD	92.1±12.8	95.5± 14.2	86.4±12.8	83.7±13.4
FEV_1 z score, mean ± SD	-0.51 ± 0.82	-0.36± 0.78	-1.88±0.89	-1.19±0.97
FVC /L, mean ± SD	4.19±0.92	4.05± 0.99	4.22±0.99	4.43±1.03
FVC % pred., mean ± SD	101.0± 14.0	97.1± 12.2	94.0±11.3	99.6± 8.7
FVC z score, mean ± SD	0.05±0.90	-0.19± 0.81	-0.03±0.60	-0.03± 0.60
FEV_1/FVC /%, mean ± SD	71.2±7.2	75.9± 5.9	51.0±10.7	65.3±9.9
FEV_1/FVC z score, mean ± SD	-0.91±0.83	-2.49±1.21	-2.22±1.30	-1.77±0.21
FEF_{25-75} % pred, mean ± SD	90.9±28.8	86.6±22.5	- **	- **
FEF_{25-75} z score, mean ± SD	-0.92±0.79	-0.43±0.71	- **	- **
FRC /L, mean ± SD	3.05±0.79	3.03±0.71	3.82±1.00	3.79±0.95
FRC z score, mean ± SD	-0.31± 1.67	-0.40± 1.09	1.10±1.08	1.07±1.05
V_D /L, mean ± SD	0.15±0.04	0.19±0.05	0.18±0.05	0.19±0.05
lnV_D z score, mean ± SD	0.02±1.10	0.17±0.82	0.53±1.09	0.53±1.08
σV_D, mean ± SD	0.34±0.11	0.31±0.05	0.32±0.10	0.33±0.06
σV_D z score, mean ± SD	0.25±2.03	-0.25±0.84	-0.17±1.75	0.02±1.05
σlnC_L, mean ± SD	0.61±0.14	0.54±0.12	0.77±0.17	0.70±0.14
σlnC_L z score, mean ± SD	0.77±1.54	-0.24±1.17	3.10±2.20	2.08±1.82

**The SCS group did not collect FEF_{25-75}%. FEV_1: the forced expired volume in 1s, FVC: the forced vital capacity, FEF_{25-75}% pred.: the percentage of the expiratory flow between 25% and 75% of vital

capacity to predicted, FRC: the functional residual capacity, V_D: volume of deadspace, σV_D: standard deviation of the volume of deadspace, $\sigma \ln C_L$: standard deviation for the natural logarithm of the standardised lung compliance.

Chapter 3

Novel measurement for locating the production of nitric oxide (NO) in the conducting airways – the Rapid FeNO Device (RFD)

The next three Chapters, beginning with this one, introduce the methodology for measuring NO production depth in the conducting airways. They sequentially cover the measurement hardware —the Rapid FeNO Device (RFD) (Chapter 3); the underlying software — the Dead Space Pipes (DSP) model and the derivation method of NO depth parameters(Chapter 4); and a quality assessment framework (Chapter 5). The last one also evaluates the repeatability and reliability of NO depth parameters. Following the introduction of methodology, I present the clinical studies in Chapter 6 to demonstrate the clinical applications of this newly developed approach.

Traditional fractional exhaled nitric oxide (FeNO) measurement relies on the plateau phase of the NO expirogram, which approximately corresponds to phase III of the CO_2 expirogram, to determine the concentration of NO produced at a specific flow rate. However, this method obscures information about NO production depth, which is more precisely reflected by the gas stored in the conducting airways at the end of inhalation. The

methodology proposed in this thesis, in contrast, focuses on those gases in the conducting airways, which are expected to be exhaled earlier, typically during phase I and phase II on the CO_2 expirogram. This shift in focus makes the shape of the NO expirogram essential for extracting information about the depth of NO production while simultaneously requiring higher temporal resolution in NO concentration measurement.

In order to meet those requirements for data collection, a recently reported device, the RFD, which employs laser absorption spectroscopy to measure gas concentrations, is used for the NO depth measurements[135]. This Chapter first introduces the design of the RFD, followed by an approach to solve the time delay and dynamic issues associated with the sidestream measurement of NO concentration. The RFD is able to accurately measure the NO and CO_2 expirograms at a high temporal resolution of 100ms. Furthermore, this Chapter outlines the standard NO depth measurement protocol involving measurements from both the RFD and Computed Cardiopulmonography (CCP). This protocol produces NO and CO_2 expirograms measured at the mouth from the RFD, along with CCP-fitted outputs generated according to the process described in Chapter 2.

3.1 RFD design

Three main types of sensors are commonly used for NO detection: chemiluminescence, electrochemical, and laser-based sensors. The choice of the NO sensor depends on the specific application. Chemiluminescence sensors are regarded as the gold standard, detecting NO through NO reaction with ozone and offering a sensitivity of 1 ppb[127]. However, its temporal resolution, typically around 0.5 to 0.7s, is insufficient to provide high-resolution NO expirograms. Electrochemical sensor, though cost-effective and sensitive, still exhibits slow response time, making it unsuitable for detecting the rapid changes in phase I and phase II. In

contrast, a laser-based sensor combines fast response times (< 1s) with adequate sensitivity (< 5ppb)[127], making it the most suitable option for the RFD.

In addition to the laser-based sensing technology, two distinct approaches are used to measure the concentration of gas species: diverting (sidestream) and non-diverting (mainstream) measurements. A sidestream sensor diverts a portion of gas flow to a sampling site, offering more flexibility and higher sensitivity, while a mainstream sensor measures the gas concentration directly in the main flow path, preventing issues associated with sidestream sensors, including signal delay, risk of obstruction and the effects of water vapour[181, 182].

Considering the technology described above and the properties of NO, the RFD employs two laser spectroscopy sensors and features a hybrid design combining mainstream and sidestream sensors for sensitive, high-temporal-resolution in NO measurement, achieving a sensitivity threshold of 4.7ppb and a temporal resolution of 100ms[135].

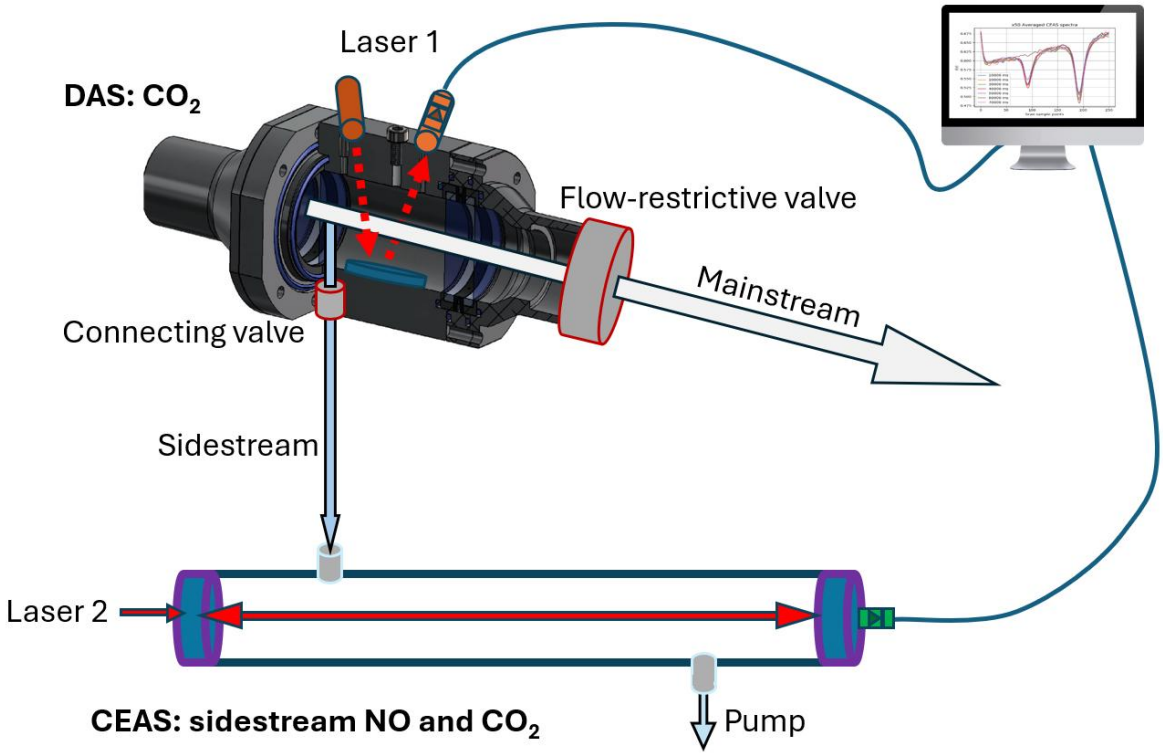


Figure 3.1 Design of the Rapid FeNO Device (RFD). The sidestream connects the mainstream from DAS to the CEAS cavity. There is a connecting valve at the entrance of the sidestream to the CEAS, whose status transition provides crucial information for reconstructing the mainstream NO expirogram. The flow-restrictive valve is installed in the mainstream, assisting participants in maintaining a constant flow rate. A pump connecting to the CEAS creates a reduced pressure in the CEAS. DAS: direct absorption spectroscopy. CEAS: cavity enhanced absorption spectroscopy.

The schematic structure of the device is shown in **Figure 3.1**. The RFD is composed of two spectroscopies: Direct Absorption Spectroscopy (DAS) and Cavity Enhanced Absorption Spectroscopy (CEAS). The DAS in the mainstream is able to measure CO_2 concentration but not NO concentration, and the design of a sidestream to the CEAS enables accurate NO measurement, though it introduces disadvantages associated with sidestream sampling. To overcome the issues of dynamic and temporal delay from sidestream measurement, the CEAS simultaneously measures the CO_2 concentration.

The DAS subunit is a simplified version of the Molecular Flow Sensor (MFS) described in Chapter 2 but is limited to the detection of CO_2 and H_2O. The DAS is also equipped with a temperature sensor and a flow sensor.

The CEAS is a newly developed design aimed at measuring NO concentrations drawn through a sidestream into the cavity. Due to the NO detection range lying between 5.1-5.7μm (in the mid-infrared region), it overlaps with that of CO_2 and H_2O, leading to spectral interference that reduces accuracy. This issue can be mitigated by using a reduced-pressure cavity, which diminishes pressure broadening. Accordingly, the cavity operates at reduced pressure (~50mbar), which is maintained by a continuously running pump and monitored using a pressure gauge.

A distributed feedback quantum cascade laser (DFB-QCL) is used to measure the gas concentration of NO and CO_2 in the CEAS, which is equipped with two highly reflective mirrors having an average reflectivity of 99.975%. By this approach, the cavity, originally measuring 42.5cm in length, extends its effective optical path length to ~1700 m, allowing accurate measurement of NO concentration.

One Connecting Valve is installed in the connecting tube that links the mainstream and sidestream (marked 'Connecting Valve' in **Figure 3.1**). This 3-way valve can be set to 'open to sidestream', 'open to room air', or 'closed'. During measurement, it alternates between 'open to sidestream' and 'open to room air' based on the measurement stage. In particular, as the exhalation nears completion, the Connecting Valve switches from 'open to sidestream' to 'open to room air', thereby closing the connection between the mainstream and sidestream. The transition of the Connecting Valve provides essential data for analysing sidestream dynamics, enabling the reconstruction of the NO expirogram in the mainstream and also allowing sufficient time for the pump to clear the cavity.

Furthermore, the Enfield Proportional Flow Valve (Ref. RCV-075-u05) is installed in the mainstream to restrict the flow (labelled as the flow-restrictive valve in **Figure 3.1**), with the aim of helping participants maintain a constant exhalation flow rate. It is controlled by a computer that sets different voltages: a voltage of 5V corresponds to unrestricted flow, while

a reduced voltage (< 5V) indicates increased restriction to help maintain the target flow rate, which allows a clear distinction between the two statuses during data analysis. Further explanation regarding the choice of the target flow rate is provided in **Section 3.3.** However, for participant safety, the valve will open automatically if any inhalation flow is detected, allowing air intake without any flow restrictions.

Figure 3.2 presents a photo alongside the corresponding design of the RFD.

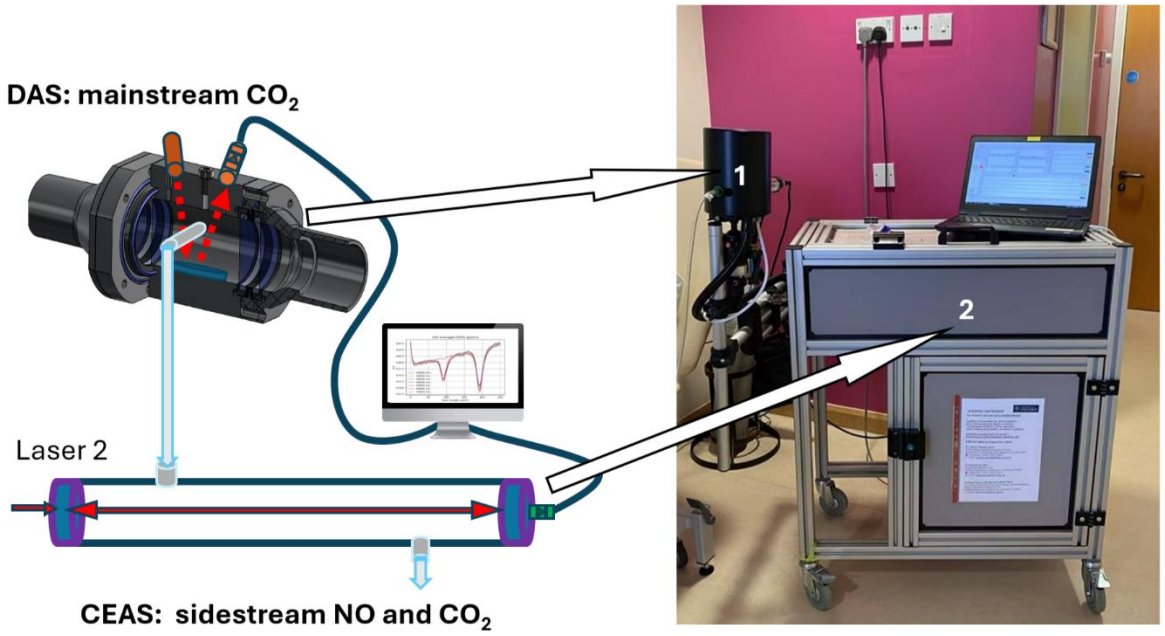


Figure 3.2 Design of the RFD and its corresponding photograph. Mark 1 indicates the DAS unit, and Mark 2 indicates the CEAS unit. DAS: Direct Absorption Spectroscopy, CEAS: Cavity Enhanced Absorption Spectroscopy.

3.2 Reconstruction of the NO expirogram from the CEAS to the DAS

One of the prominent issues in this design is that the NO expirogram in the mainstream (at mouth level) is not directly measured, while the sidestream NO measurement in CEAS represents a convolution of the true mainstream NO expirogram with sidestream dynamics response and time delay. **Figure 3.3** demonstrates CO_2 expirograms from both DAS and

CEAS. It is clear a delay and distortion exist between the two curves. As these effects are independent of gas species, they can be characterised by comparing CO_2 expirograms from both the CEAS and DAS. The extracted characteristics can then be applied to the NO expirogram measured by the CEAS, also shown in **Figure 3.3**, to reconstruct the corresponding NO expirogram at the DAS.

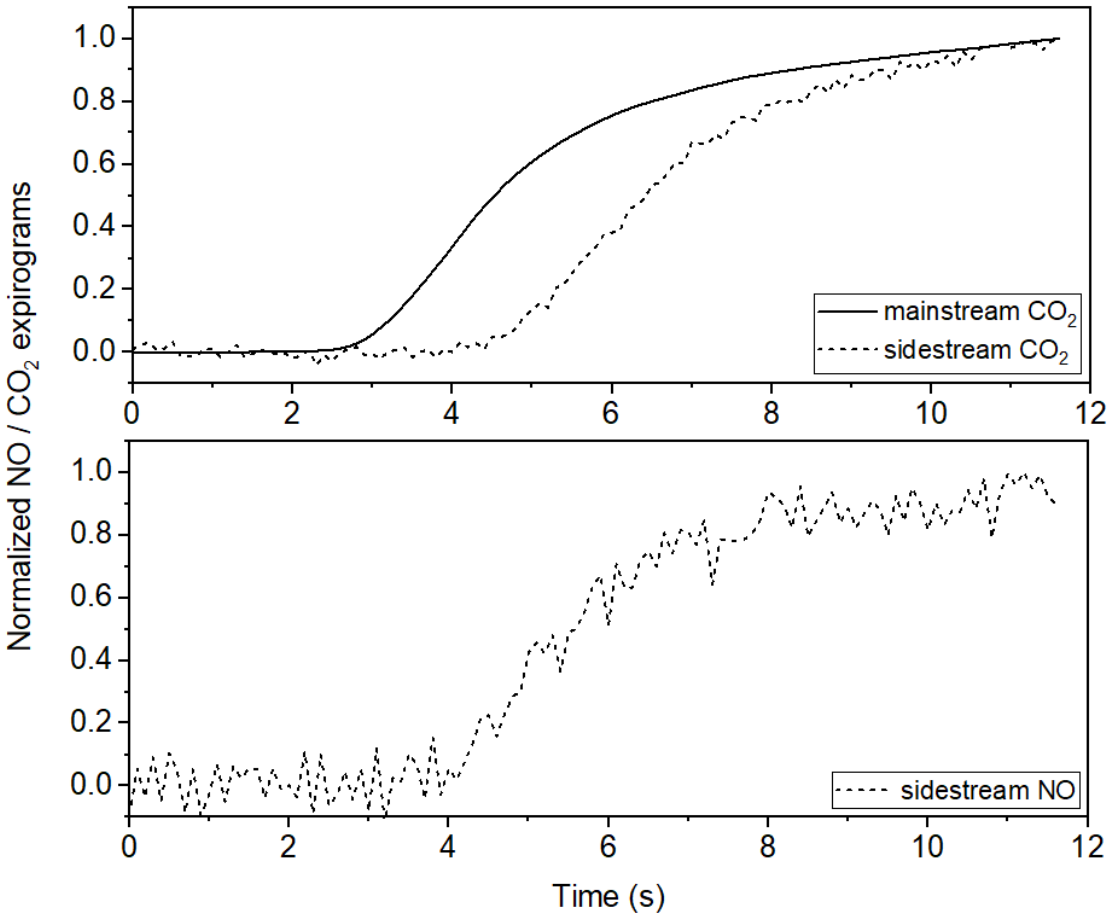


Figure 3.3 CO_2 expirogram and NO expirogram from RFD measurements. Comparing CO_2 expirogram in the mainstream and sidestream, it is evident that there is a time delay and dynamic change between them. The RFD only measures the sidestream NO expirogram, while the NO expirogram in the mainstream is required to proceed to the next step.

The approach to extract the correction is modelled by treating the DAS and CEAS as a first-order system, in which the input signal is the gas expirogram measured by the DAS and the output is the gas expirogram measured by the CEAS. A first-order system is a system that

describes its transfer function only by a first-order derivative. The transfer function defines the relationship between an input signal and its corresponding output signal. If we assume that the system received a unit impulse signal, we can write the transfer function as,

$$\frac{C(s)}{R(s)} = K\frac{1}{\tau s + 1} \tag{3.1}$$

where *C(s)* is the output signal, *R(s)* is the input signal, and both are in the Laplace domain (frequency domain), *K* is the DC Gain (the ratio of steady-state output to the input), and τ is the time constant of the system.

When expressed in the time domain, the function becomes,

$$\frac{dc(t)}{dt} + \frac{c(t)}{\tau} = r(t)\frac{K}{\tau} \tag{3.2}$$

where *r(t)* and *c(t)* are the time-domain input and output signals, respectively.

One additional parameter, a time delay of the system (t_0), is used to adapt to the measurement, as a time delay is expected for sidestream sampling compared with mainstream. With the consideration of time delay t_0, the transfer function in the Laplace domain becomes,

$$\frac{C(s)}{R(s)} = K\frac{e^{-st_0}}{\tau s + 1} \tag{3.3}$$

The expression in the time domain becomes,

$$\frac{dc(t)}{dt} + \frac{c(t)}{\tau} = r(t - t_0)\frac{K}{\tau} \tag{3.4}$$

The time point when the Connecting Valve switches from ‘open to sidestream’ to ‘open to room air’ offers an ideal observation point for assessing whether the RFD’s mainstream and sidestream responses can be represented by a first-order system. This time point represents the input signal undergoing a clear step decrease within the system, directly dropping from a certain value to zero, which enables the extraction of parameters for constructing the first-

order system. Comparing the modelled simulation with the actual measured data allows for the evaluation of whether the system aligns with a first-order system.

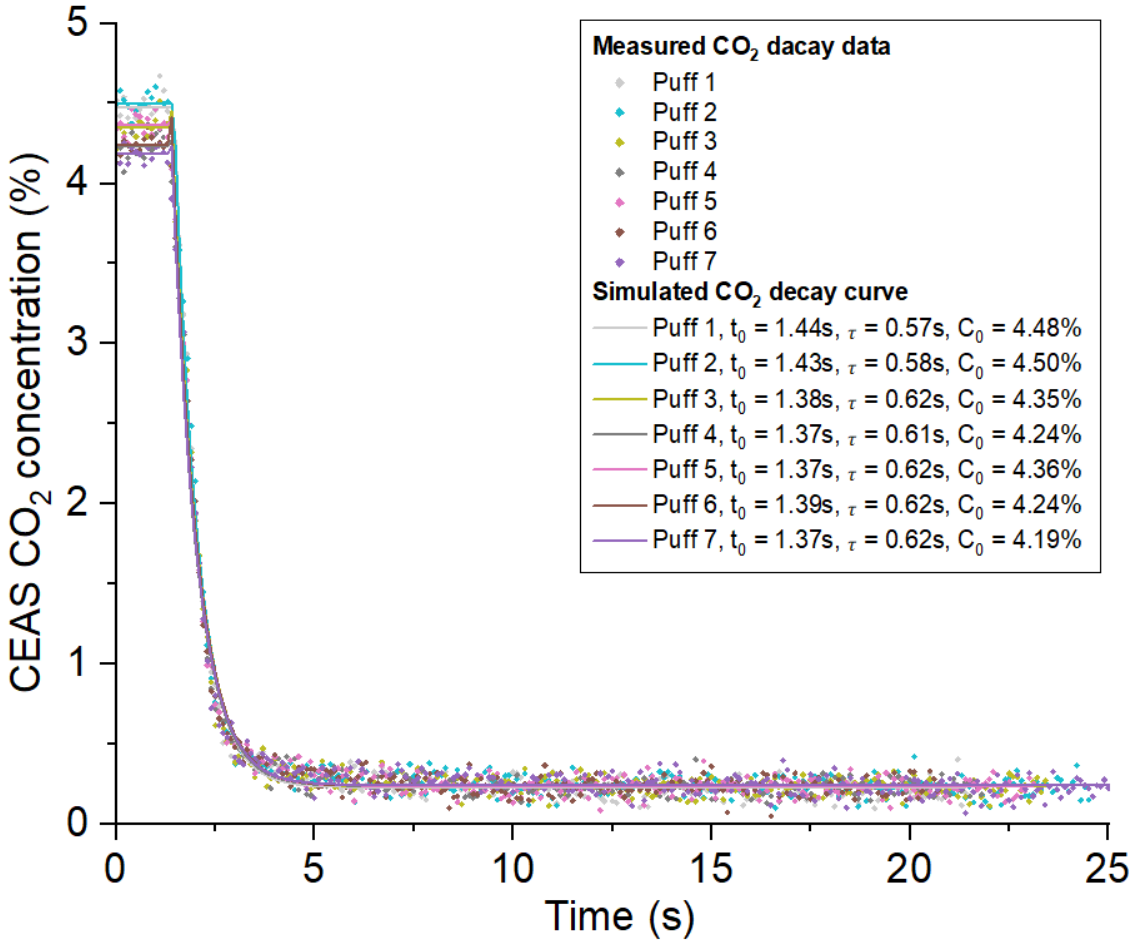


Figure 3.4 CO_2 decay in the cavity when the Connecting Valve is momentarily closed. It includes seven breaths from the same participant. The decay patterns show similar τ and t_0.

Figure 3.4 illustrates seven end-breath CO_2 concentrations in the CEAS cavity from the same participant at the moment the Connecting Valve switches to close the sidestream, presenting both simulated and measured data. The measured CO_2 data (dots) closely aligns the simulated data (curves) based on a first-order system, supporting the assumption that the RFD dynamics follow first-order behaviour. Additionally, it provides the key parameters used in a first-order system, τ and t_0, which remain consistent across different breaths, indicating

that the system dynamics are stable between measurements. Variability in initial CO_2 concentrations (C_0) reflects differences in breath depth between individual breaths.

Given the confirmation that the system follows the first-order system, solving ***Eq. 3.4*** in each time interval ($\Delta t = 0.1s$) generates the following equation,

$$c^{(n+1)} = c^n e^{-\frac{\Delta t}{\tau}} + Kr(t_{n+1} - t_0)(1 - e^{-\frac{\Delta t}{\tau}}) \quad (3.5)$$

where n is the number of measurements, ranging from 0 to n_{end}-1, n_{end} represents the number of points at the end of exhalation. t_{n+1} represents the $(n+1)^{th}$ point corresponding to time.

Mainstream and sidestream CO_2 expirograms provide input signal and output signal in the equations. Fitting the equations allows for the refinement of τ, t_0 and K, whose initial values are obtained by the Connecting Valve shut process. These refined parameters are applied again in ***Eq. 3.5*** with the measured NO expirogram in the sidestream to reconstruct the corresponding NO expirogram in the mainstream, as illustrated in **Figure 3.5**.

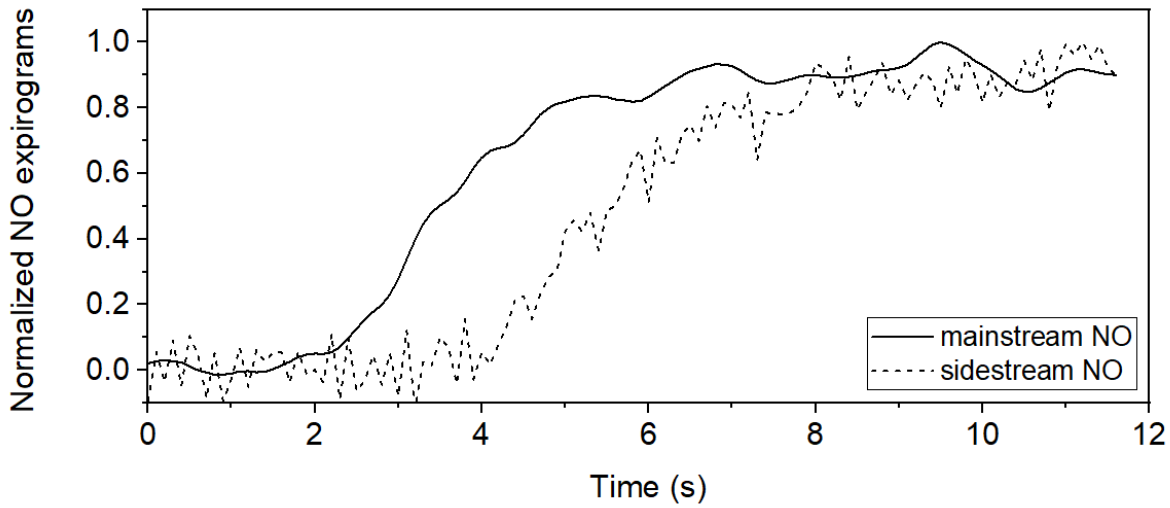


Figure 3.5 Mainstream and sidestream NO expirogram on a time scale. Mainstream NO expirogram is reconstructed from the sidestream NO expirogram based on a first-order system, with parameters recovered from the mainstream and sidestream CO_2 expirogram.

The first-order system successfully reconstructed the NO expirogram in the mainstream in the time domain. Since gas expirogram analysis is performed in the volume domain, the

expirograms of CO_2 and NO are converted to the volume domain using the measured breath volume (as demonstrated in **Figure 3.6**). This completes the data preparation required for the next stage of analysis, which involves fitting the DSP model.

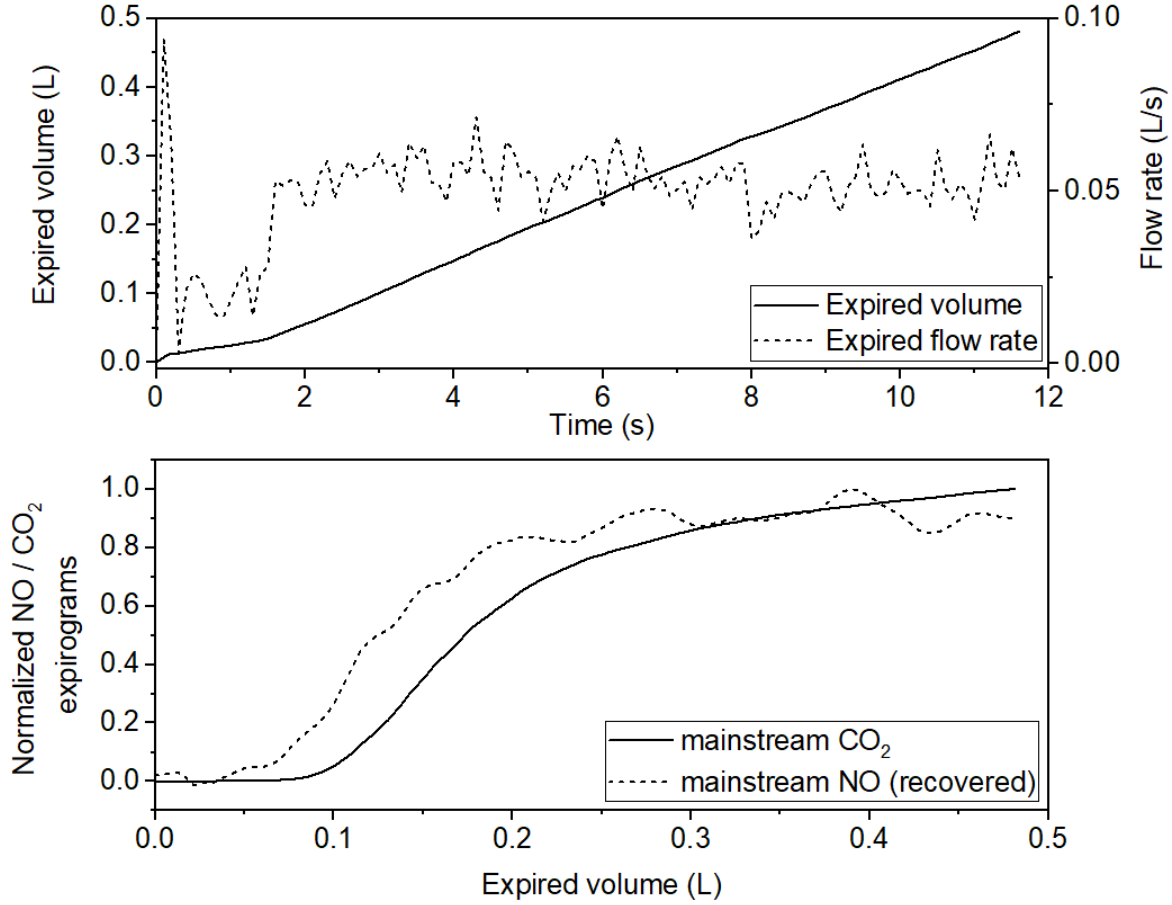


Figure 3.6 Volume and volumetric flow on the time domain and NO/CO_2 expirogram on the volume domain. The first-order system provides a reconstruction approach for NO in the mainstream, which can produce the volume expirogram by combining volume/flow-time information.

3.3 Experimental protocol for measuring NO production depth in the conducting airways

3.3.1 Experimental protocol

In this thesis, the protocol described here is applicable to all sections involving NO production depth measurements unless otherwise specifically stated. A full standard operating

procedure (SOP) is provided in **Appendix A**. That SOP reflects the challenges of applying a newly developed device in clinical settings, where all procedures are listed in alignment with the chronological order of data collection, sacrificing a well-organized structure and focusing on numerous details.

The RFD requires ~45 minutes of pre-warming to reach the target cell temperature of 35 °C before testing can begin. This is followed by a two-step calibration using pure N_2 and 5% CO_2. Both gases are introduced sequentially at a flow rate of 5L/min. The 5% CO_2 calibration provides the reflectivity for the mirrors. Once CO_2 calibration is complete, no further calibration is needed for NO measurements, as the absorption cross-section is a known physical constant. Calibration must be performed at least once daily, with additional calibrations as necessary.

Participants receive introductions on using the mouthpiece and nose clip before starting any tests, and they are also guided on how to inspire and expire through the head of the RFD. Each test involves two breathing manoeuvres: normal breathing and special breathing. Normal breathing does not require any specific instructions, and the participants can breathe with any force, speed, and duration. The special breath requires immediate exhalation after inhalation. Participants must maintain a constant exhalation speed of 50ml/s for approximately 10s.

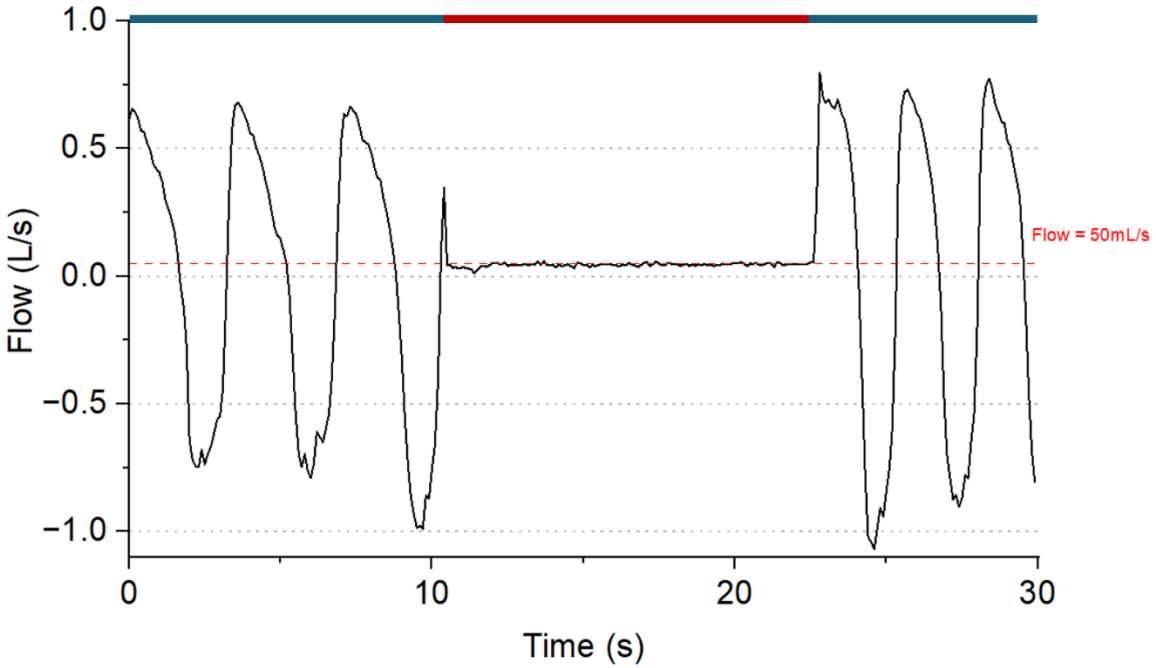


Figure 3.7 An example of normal and special breathing patterns. The blue line indicates normal breathing and the red line indicates special breathing. The red dashed line indicates the target flow rate, 50ml/s.

As demonstrated by **Figure 3.7**, Participants start with normal breaths, and after five normal breaths (as indicated by the blue line), they perform one special breath(as indicated by the red line). This cycle is expected to repeat 7 times in one test, resulting in a total duration of ~7 minutes. The maximum duration of each test is limited to 10 minutes to avoid excessive exertion in participants. All steps in the test are guided by audio and visual instructions. Audio instructions remind participants to start the breathing test and transition between breath manoeuvres. Visual instructions provide real-time feedback on exhalation speed during the special breath, as shown in **Figure 3.8**.



Figure 3.8 Examples of the Visual feedback system of the RFD. The colour of the bar indicates the flow rate variations. Green: within 5% of 50ml/s, amber: between 5% to 10% of 50ml/s, red: over 10% of 50ml/s.

The exhalation speed goal is indicated by a blue arrow in the middle, representing 50ml/s. The coloured bar indicates how far the exhalation speed is from the target. Green, amber and red bars represent errors within 5%, 5 - 10% and beyond 10%, respectively. With this feedback system, participants can adjust their exhalation to maintain a stable breathing speed of approximately 50ml/s.

Following the NO depth breathing test on the RFD, the participant takes a brief rest before undertaking a standard CCP test to provide accurate lung physiology data. The detailed protocol for the CCP test is described in Chapter 2.

3.3.2 Key factors related to data collection

During the whole protocol, certain specific aspects are worth further explanation, as they are closely associated with physiological principles and/or measurement quality.

3.3.2.1 Constant exhalation speed of 50ml/s

The measurement sensor is located at mouth level. A constant exhalation speed is necessary because NO is produced by bronchial epithelial cells, and its concentration in the exhaled gas is inversely related to the exhalation speed. Variations in flow rate led to changes in NO concentration along the axial axis. Larger variations create greater axial gradients of

NO concentration, leading to more pronounced axial diffusion, which makes it necessary to maintain a stable exhalation speed. When selecting the target speed, a balance should be considered. A lower exhalation speed allows more time for the gas to reach the measurement level (the mouth), making axial diffusion more prominent. Conversely, a high exhalation speed diminishes the effects of diffusion but requires higher sensitivity of the RFD due to the inverse relationship between flow rate and NO concentration. Finally, a target speed of 50ml/L is selected, which is consistent with the ERS/ATS consensus on FeNO measurements[183]. However, it is important to recognise that NO production depth measurement differs from FeNO measurements in terms of exhalation stage selection and measurement protocols (FeNO measurements reflect the plateau of NO in expiration), which lead to many steps in this protocol having procedures that differ from the ERS/ATS consensus on FeNO measurements[183].

3.3.2.2 Application of a nose clip

Compared with the consensus on FeNO measurements[183], the use of a nose clip is required by NO depth measurement. The main reason is that the nasal NO contribution during inhalation can affect the NO depth measurement while having negligible effects on FeNO measurements. If the participant is not using a nose clip, it is possible that inhaled gas may leak from the nasal cavity into the airways, introducing a high level of NO, which is then exhaled first from the conducting airways, leading to inaccurate NO depth estimation. If the participant is wearing the nose clip, the possibility of gas leakage from the nose during the inhalation phase is largely reduced, if not diminished, ensuring that the gas in the dead space is not contaminated with NO from the nasal cavity.

3.3.2.3 Breath test round settings

Each breath test round is set to consist of five normal breaths followed by one special breath based on two key considerations. The first consideration is the tolerance and comfort

of participants breathing through the device. A special breath requires a slow flow, which can be physically demanding and may lead to muscle fatigue. Second, the number of normal breaths between special breaths should be sufficient to allow the CEAS cavity to clear itself via the pump. When the connecting valve switches to 'open to room air' status, the pump clears the cavity of NO. As shown in **Figure 3.4**, the cavity requires ~4.5s to clear ~99% NO, which may necessitate a duration of at least two full breaths.

3.4 Summary

This Chapter outlines the hardware design for measuring NO production depth and presents a standardised measurement protocol. By applying a first-order system, NO expirograms in the mainstream can be accurately reconstructed, providing the model with accurate and highly time-resolved data that is vital for estimating NO production depth.

Chapter 4

Novel measurement for locating the production of nitric oxide (NO) in the conducting airways – the Dead Space Pipes (DSP) Model and the derivation of NO depth parameters

According to the nitric oxide (NO) depth measurement protocol described in Chapter 3, participants are not only required to breathe through the Rapid FeNO Device (RFD) using a specialised manoeuvre (known as special breathing) but also to perform a standardised Computed Cardiopulmonography (CCP) test following the protocol outlined in Chapter 2. This Chapter describes further analyses of these collected data, establishing a framework for generating the NO depth parameters.

Since the 1940s, it has been a common approach to estimate gas depth in the airways using expirograms (e.g. N_2 and CO_2)[84, 87], as introduced in Chapter 1. The CO_2 and N_2 gases are exhaled from a fixed location, the alveoli, which makes the gas depth equivalent to the anatomical dead space, i.e., the full length of the conducting airways. NO, however, is

produced throughout the conducting airways, making it unrealistic to estimate its spatial distribution of production along the conducting airways solely from an expirogram, as shown in **Figure 4.1(a)**. This figure illustrates the scenario when the airway structure is simplified to a single-pipe model.

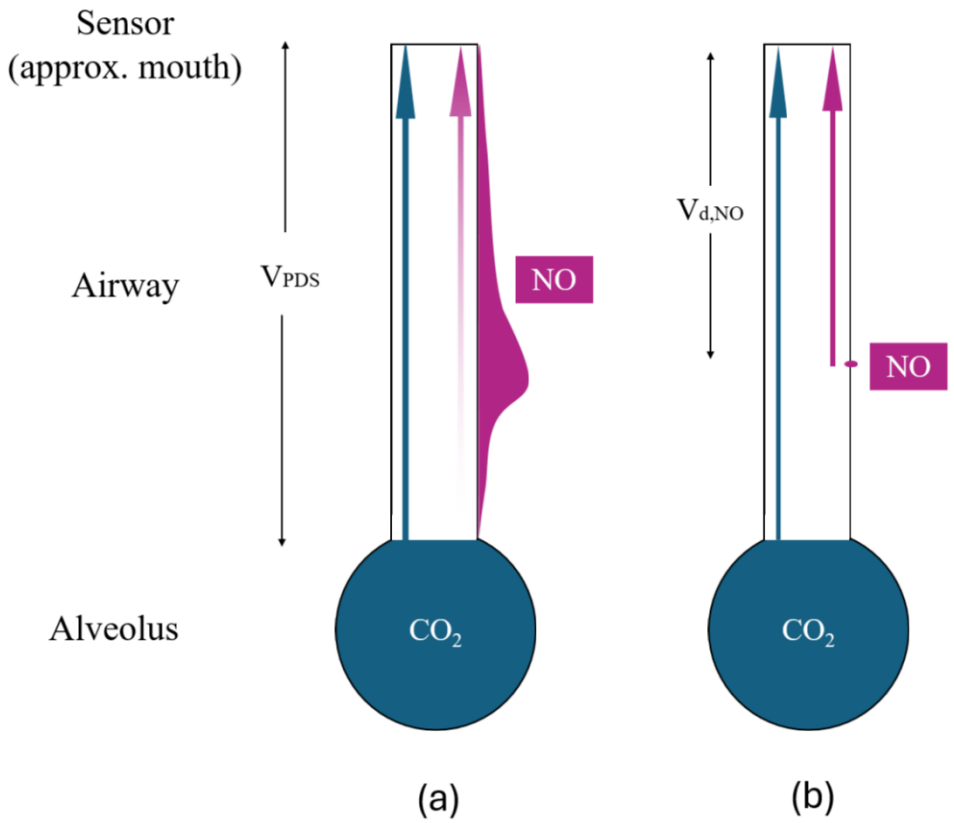


Figure 4.1 Schematic illustration of NO production depth along the single airway. (a) NO is produced as a continuous distribution along the volume of the airway. (b) Simplified representation of NO production as a single-point source. The arrows indicate that CO_2 (blue) and NO (pink) are exhaled from the airways. V_{PDS}, the volume of personal dead space. $V_{d,NO}$, the NO depth, assuming NO production occurs at a single point.

Nevertheless, it is still possible to estimate statistical characteristics of NO production depth, such as the mean depth, which indicates the average production location, and the standard deviation of depth, which reflects the axial spatial spread. The approach I adopted to achieve this is to construct a series of simulated NO expirograms as a reference map, assuming NO is produced only at a single specific point along the conducting airways, as

indicated in **Figure 4.1(b)**. This map, also referred to as the 'wallpaper', is then compared with the measured NO expirogram to derive the NO depth parameters.

Accordingly, the first section in this Chapter presents an introduction to the Dead Space Pipes (DSP) model, which applies the data from the CCP and the RFD to generate personalised and breath-specific simulations of NO expirograms ('wallpaper', as illustrated in **Figure 4.2**). It is a series of expirograms assuming NO is produced at 0%, 10%, 20% … 100% of personal dead space (PDS), where 100% PDS indicates the alveoli and 0% PDS indicates the upper end of the trachea. The following section introduces how the 'wallpaper' is combined with a measured NO expirogram to produce NO depth parameters.

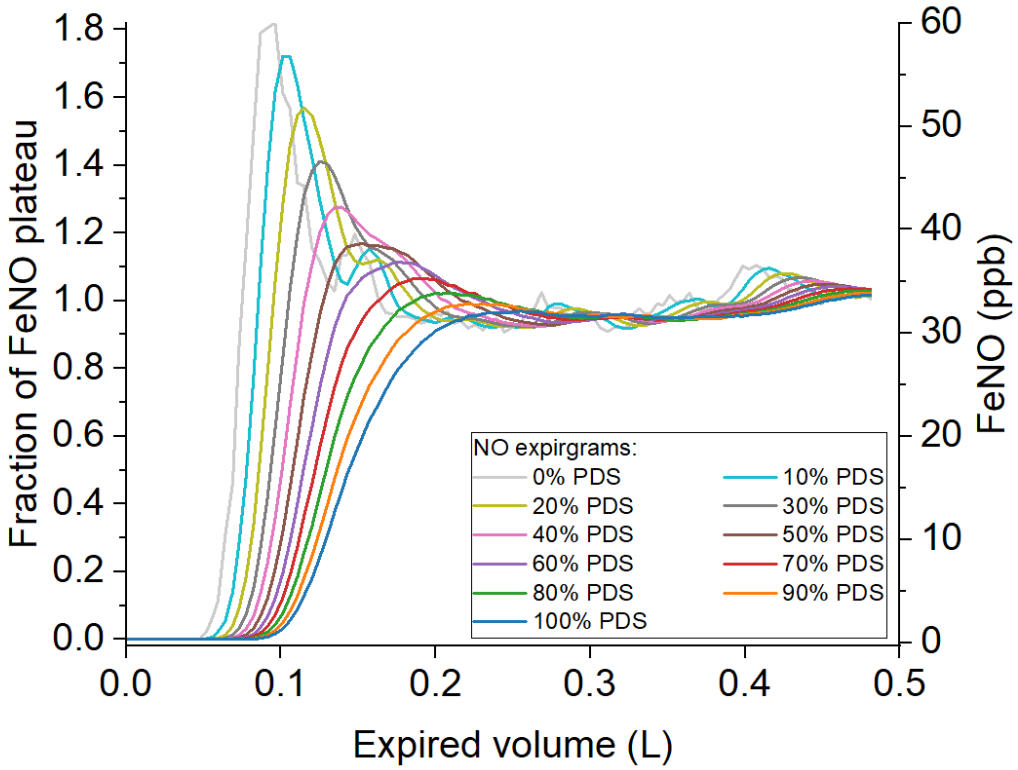


Figure 4.2 An example of 'wallpaper': the simulated NO expirograms assume NO is produced at 0%, 10%, 20% …, and 100% of personal dead space (PDS).

4.1 The DSP model

The DSP model aims to simulate the NO expirograms that closely match a specific real breath. However, the variation in the shape of gas expirograms is caused by various factors, which can be divided into inter-individual variation, including lung volume and lung inhomogeneity, and intra-individual variation, such as differences in breath depth and fluctuations in breathing speed.

To minimise the influence of these factors in deriving NO depth parameters, several aspects are considered in the simulation of NO expirograms within the DSP model. For controlling inter-individual variation, the dead space outputs of the CCP (dead space volume and the fraction of flow rate in each pipe) from the same individual during the same visit are used to provide highly accurate dead space physiological parameters. As for intra-individual variation, variations in breath depth are controlled by fitting the CCP output parameters to the CO_2 expirogram in the same breath as the targeted NO expirogram, and fluctuations in breathing speed are also considered when simulating the NO expirogram.

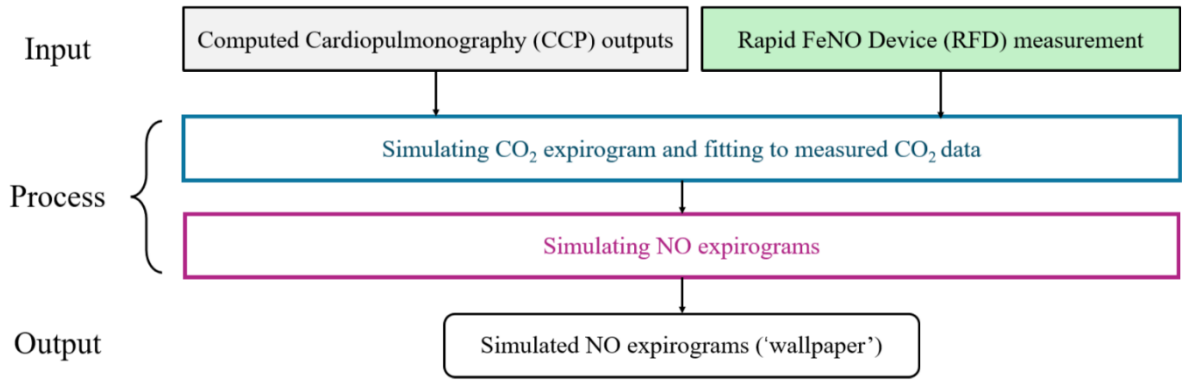


Figure 4.3 Workflow of the DSP model. Inputs include the CCP outputs and the RFD measurements. The process involves simulating the CO_2 expirogram and fitting it to the measured CO_2 data, as well as the simulating of NO expirograms. The output of the DSP is the simulated NO expirograms, referred to as 'wallpaper'.

Figure 4.3 outlines a schematic workflow of the DSP model. The inputs include dead space fitting results from the CCP and measured data from the RFD. The process involves simulating and fitting the CO_2 expirogram to adapt the model to a specific breath (blue box in

Figure 4.3), followed by simulating the NO expirograms for that same breath (pink box in **Figure 4.3**). While CO_2 and NO follow the same transport dynamics within the airways, they are produced in distinct ways: NO is produced in the airway wall, whereas CO_2 originates in the alveoli. As a result, accurately simulating NO expirograms requires modifications to the simulation methods rather than duplicating the CO_2 simulation process.

The following sections start with the general principles and assumptions of the DSP model and then introduce conceptual approaches for simulating and fitting CO_2 expirogram, as well as simulating NO expirograms (blue and red sections in **Figure 4.3**, respectively). In addition to these, the next section provides detailed procedures in the workflow of the DSP, with an emphasis on deriving three essential parameters: alveolar CO_2 concentration(C_{alv,CO_2}), dead space volume correction(dV) and NO production rate(r_0). Moreover, a step-by-step calculation of the DSP is presented in **Appendix B** for reference.

4.1.1 Structure of the DSP model

The DSP model is structured as a multi-pipe model and is consistent with the dead space settings of CCP to adapt to its outputs, which consist of 125 pipes for the personal dead space (PDS) and 11 pipes for the device dead space (DDS), as demonstrated in **Figure 4.4**.

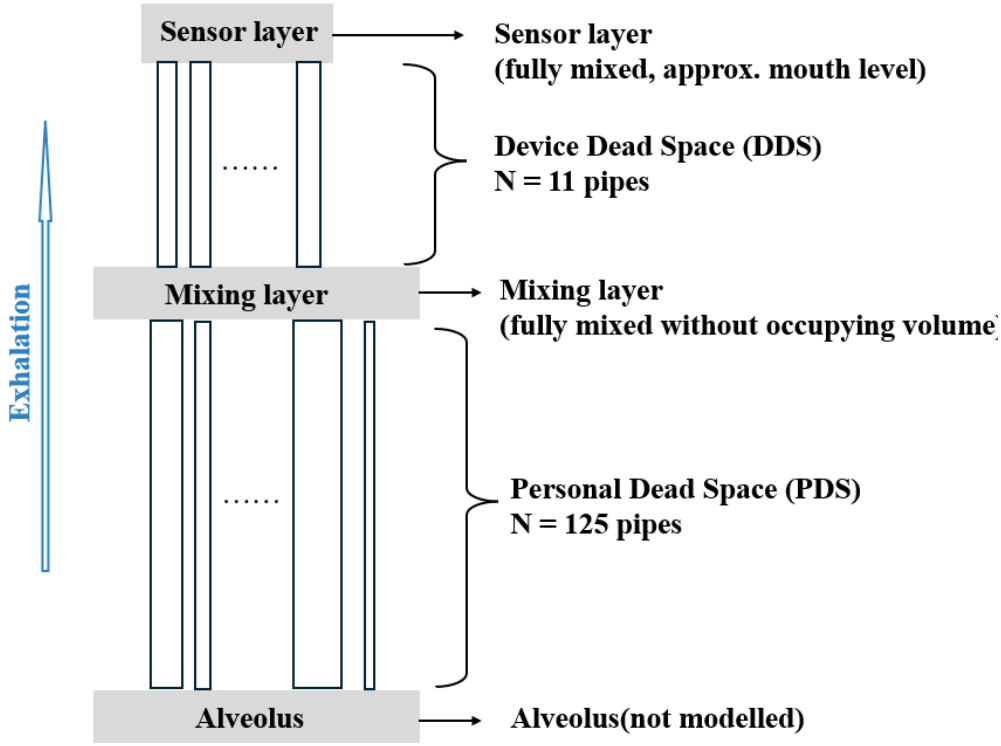


Figure 4.4 Structure of the DSP model. During exhalation, the gas is transported from the alveolus through the PDS, through the mixing layer, then through the DDS, and finally out through the mouth to be detected by the sensor.

The value of volume and flow rate of each pipe in the DSP model is adjusted according to the CCP outputs of each participant. Although the DDS remains unchanged between breath cycles, the PDS volume should be corrected by a variable — the dead space volume correction (dV) — at the end of inhalation to reflect the volume expansion of the PDS during inhalation. dV is obtained by fitting the CCP outputs to the measured CO_2 data from the same breath used for measuring the NO expirogram.

4.1.2 General principles and assumptions of the DSP model

The DSP model is based on several principles and assumptions.

(i) Gas transport is modelled purely by convection, with diffusion effects ignored. Flow within each pipe follows a plug-flow pattern.

(ii) The alveolus is assumed to contain a homogeneous gas mixture, and CO_2 metabolic production is not accounted for in the DSP model, resulting in phase III (alveolar plateau phase) appearing as a flat line rather than a sloped one.

(iii) NO depth at a certain percentage of PDS volume indicates that the NO is produced uniformly at that percentage of volume across all PDS pipes.

(iv) The NO concentration at any time point is given as r_0 / v, which approximates an inverse proportional relationship between flow speed and NO concentration. r_0 is the NO production rate, with units of ppb·L/s, and v is the flow rate at that time point.

(v) The NO concentration in alveolar gas is assumed to be zero, whether originating from alveolar cells or from NO transported to the alveoli.

4.1.3 Construction of the simulated CO_2 expirogram and fitting to measured CO_2 data

I first present a simplified model in which CO_2 transport is simulated in a single pipe for illustration. This is followed by a more complex three-pipe model that represents the simulation within a setup of multiple pipes. Based on this, I introduce the DSP setup that extends the three-pipe model to a 125-pipe model in the PDS part and to an 11-pipe model in the DDS part while preserving the same methods of simulating the CO_2 expirogram as in the three-pipe model. The corresponding simulation of the CO_2 expirogram is then fitted to CO_2 data measured by the RFD for dV, which estimates the variations in breath-by-breath depth.

4.1.3.1 Concept of the single-pipe model

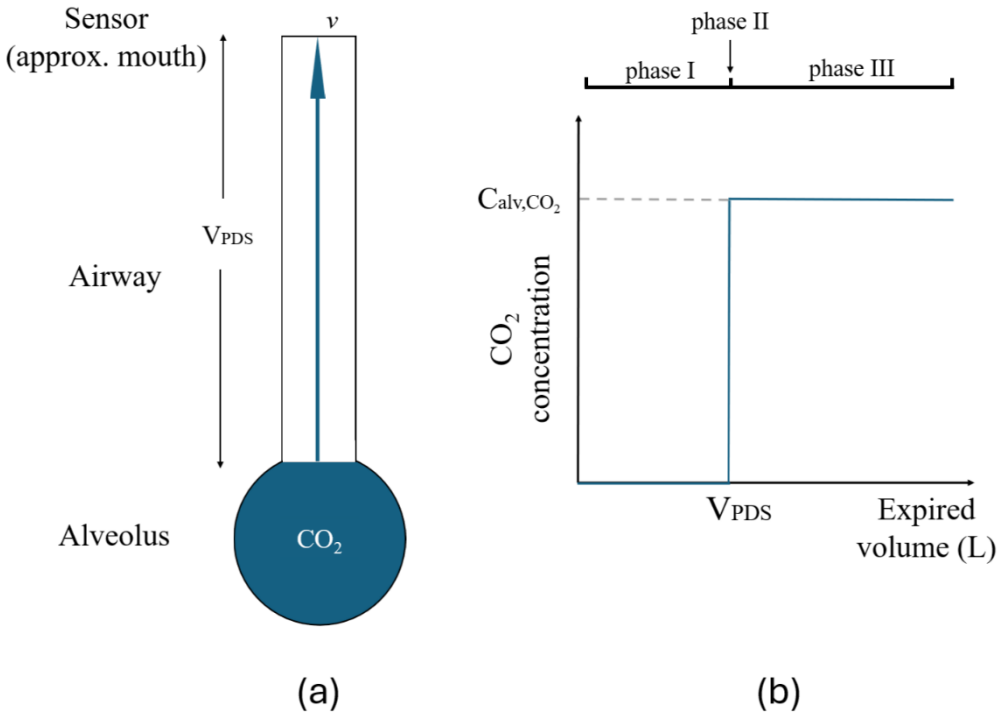


Figure 4.5 A single-pipe model for CO_2 expirogram. (a) Structure of the single-pipe model, with the sensor located at the mouth. V_{PDS} represents the volume of personal dead space(PDS). (b) CO_2 expirogram generated from the single-pipe model. Phase II is collapsed into a single point. C_{alv,CO_2}, alveolar CO_2 concentration. v: exhalation flow rate.

Figure 4.5 (a) demonstrates the structure of a single-pipe model and the corresponding CO_2 expirogram shown in **Figure 4.5(b),** which appears as a step function with a switching point at the volume of PDS (V_{PDS}). The volumetric exhaled speed is v. The CO_2 concentration at the sensor remains zero until the exhaled volume (on the x-axis) reaches the switching point (V_{PDS}), after which the CO_2 concentration suddenly rises to the alveolar CO_2 concentration(C_{alv,CO_2}). The rise to this value reflects that all exhaled gas originates from the alveolus and marks the start of the alveolar phase (i.e. phase III) of the CO_2 expirogram. Correspondingly, phase II, which represents the transition between the anatomical dead space phase (phase I) and the alveolar phase (phase III), has been reduced to a single point in the single-pipe model.

4.1.3.2 Concept of the three-pipe model

Figure 4.6 shows both the model structure and the corresponding simulated CO_2 expirogram. In this example, three pipes are used to represent the dead space, each with a distinct volume and flow rate (as labelled in **Figure 4.6**). Despite differences in the individual pipes, the total dead space volume and overall volumetric exhalation speed remain at V_{PDS} and at v, respectively.

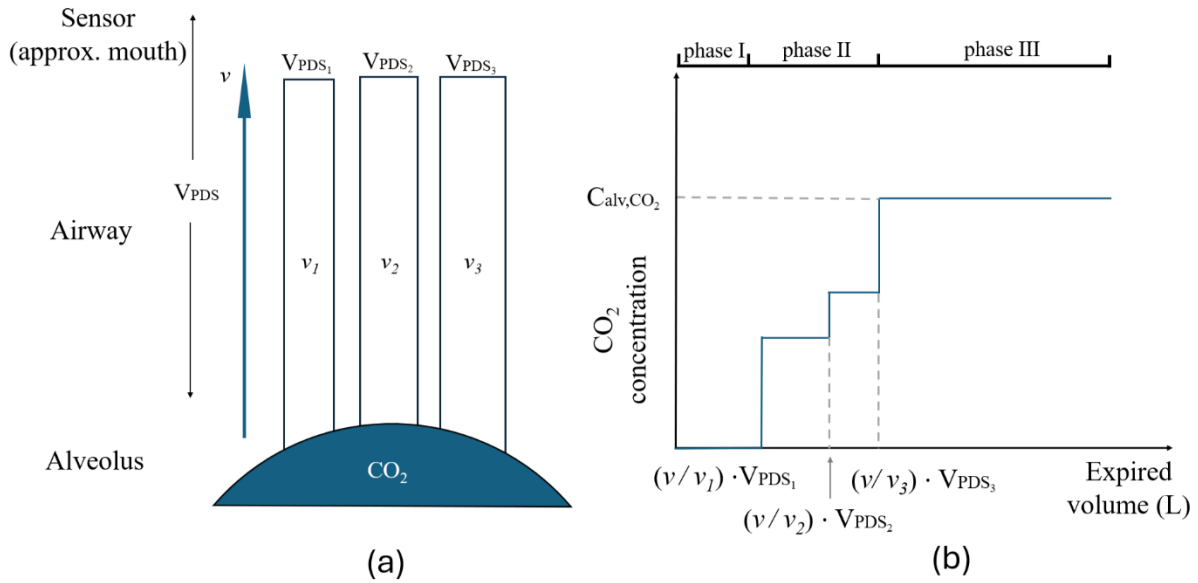


Figure 4.6 A three-pipe model (representation of a multi-pipe model) and its CO_2 expirogram. (a) Structure of the three-pipe model, with the sensor located at the mouth. V_{PDS} represents the volume of personal dead space (PDS). V_{PDS_i} is individual shared dead space volume (i = 1, 2 and 3). v_i is the individual shared exhalation volumetric speed (i = 1, 2 and 3). (b) CO_2 expirogram generated from the three-pipe model. Phase II spans from V_{PDS_1} to V_{PDS_3}. C_{alv,CO_2}, alveolar CO_2 concentration.

The simulated CO_2 expirogram is constructed as the cumulative sum of three individual step functions, representing the contributions of each of the three pipes, as demonstrated in **Figure 4.6(b)**. The value of the switching point on the x-axis for each step function is determined by the exhaled volume at which the alveolar gas begins to emerge at the sensor from the corresponding pipe. The presence of three switching points extends the transition phase (phase II) to a volume range from the smallest switching point to the largest switching point.

Additionally, the three-pipe model requires defining the amplitude of the rise of each step function on the y-axis, which fundamentally reflects the proportion of gas molecules that each pipe contributes to the total exhaled gas. In this example, since all pipes share the same CO_2 concentrations (C_{alv,CO_2}) when exhaling the alveolar gas, the amplitude of each step function is directly proportional to the flow rate in each pipe.

4.1.3.3 Extension of the multiple-pipe model based on CCP outputs

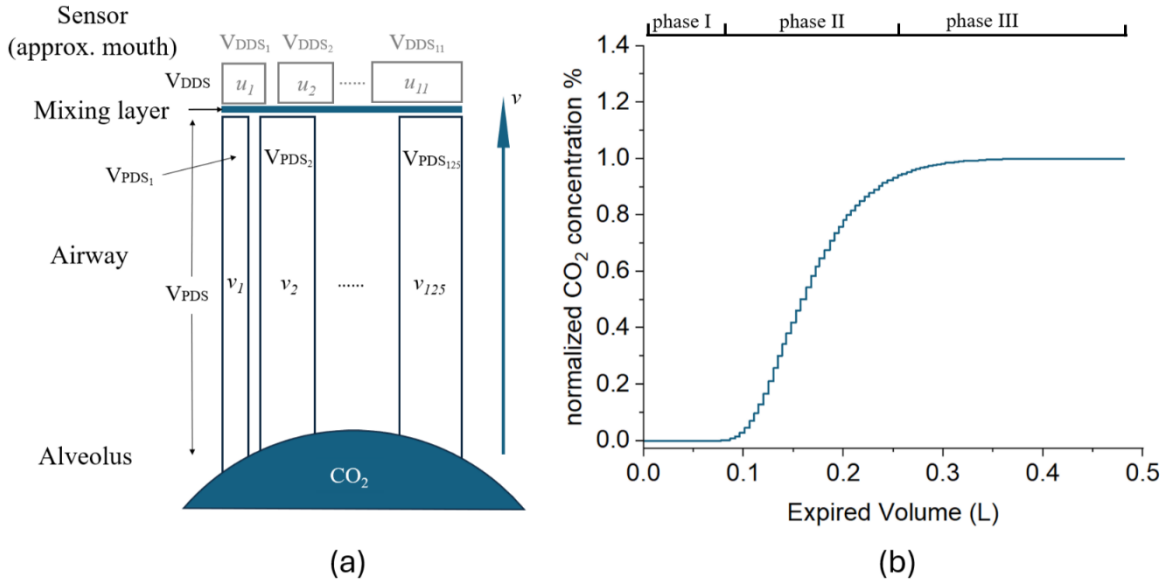


Figure 4.7 A multiple-pipe model based on CCP outputs and its CO_2 expirogram. (a) Structure of the multiple-pipe model, with the sensor located at the mouth. V_{PDS} represents the volume of personal dead space (PDS). $V_{PDS,i}$ is the individual shared dead space volume (i = 1, 2 … 125). v_i is the individual shared exhalation volumetric speed in PDS (j = 1, 2 …125). $V_{DDS,j}$ is the individual shared device dead space volume (DDS, i = 1, 2 … 11). u_j is the individual shared exhalation volumetric speed in DDS(j = 1, 2 …11) (b) CO_2 expirogram generated from the multiple-pipe model. C_{alv,CO_2}, alveolar CO_2 concentration.

The DSP model structure is an extension of the three-pipe model to match the CCP dead space outputs, where the PDS is connected to the DDS by a mixing layer, as illustrated in **Figure 4.7(a)**. The addition of the mixing layer, shown as the blue layer in **Figure 4.7(a)**, makes the DSP model process slightly more complex than that of the three-pipe model. However, the PDS itself functions identically to the three-pipe model, generating a CO_2 expirogram from the 125-pipe model at the mixing layer. The mixing layer also supplies CO_2

to the DDS in the same way that alveolus supplies CO_2 to the PDS. The DDS part, consisting of 11 pipes, also follows the same rules as the three-pipe model in identifying switching points along the x-axis. As for the amplitude on the y-axis, the amplitude of the DDS can be determined by identifying the corresponding CO_2 concentration in the expirogram at the mixing layer, which is generated by the PDS part. The expirogram from DDS represents the overall CO_2 expirogram generated by the DSP model. The step-by-step calculation is given in **Appendix B**, while the simulation result is displayed in **Figure 4.7(b)**. However, the CO_2 metabolic production is not included in the DSP model, resulting in a flat line during phase III.

4.1.3.4 Fitting of simulated CO_2 expirogram to measured CO_2 data

The CCP outputs minimise the impact of inter-individual variance on the expirogram, while a fitting procedure is necessary to standardise breath depth since the dead space volume expands differently in deep and shallow breaths. The DSP model introduces the parameter *dV*, reflecting the extent to which the PDS volume expands compared to the FRC status. The PDS volume at the end of inhalation is the sum of *dV* and PDS volume at the FRC status, which is provided by the CCP outputs. Each pipe is assigned a volume from *dV*, in proportion to its volume and exhalation speed. The exact fitting range of the measured CO_2 expirogram and the algorithm is introduced in **Section 4.1.5.1** and **Section 4.1.5.2**, while an example of the fitting is shown in **Figure 4.8**, demonstrating a good fit to the CO_2 data.

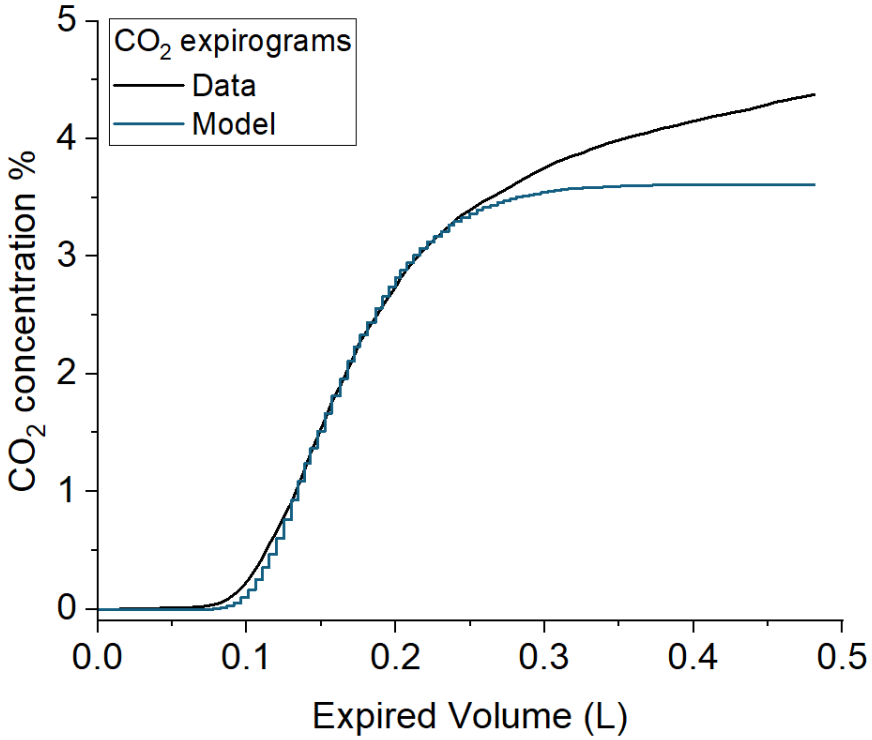


Figure 4.8 Measured and simulated CO_2 expirograms based on the CCP outputs, incorporating the contribution of the DDS. The blue curve represents the simulated CO_2 expirogram, while the black curve shows the measured data. DDS: device dead space. The neglect of CO_2 metabolic production leads to the deviation between the simulated CO_2 expirogram and measured CO_2 data in phase III.

4.1.4 Construction of the simulated NO expirogram

When adapted with CCP outputs and fitted with the *dV* parameter, the DSP model can generate a simulated CO_2 expirogram that closely aligns with the measured CO_2 data.

In contrast, simulating NO expirograms requires further modifications. Alveolar CO_2 concentration is independent of exhalation speed, whereas NO concentration exhibits an inverse relationship with flow rate, often approximated as a negative proportional relationship, as is the case here.

In the following sections, a simpler example is first presented to simulate the NO expirogram while eliminating the influence of exhalation speed variation by assuming a constant exhalation speed, referred to as the speed-independent (SpIn) mode. This is followed by a section summarising the limitations identified in SpIn mode. An upgraded simulation

approach, referred to as the speed-dependent (SpD) mode, is then presented to account for exhalation speed variation. The choice between SpIn and SpD modes for future clinical studies will be presented at the end of Chapter 5, based on a more comprehensive comparison of quality control, repeatability, reliability and potential utility.

4.1.4.1 Speed-independent (SpIn) mode of simulating NO expirogram

A constant exhalation speed of 50ml/s is assumed, making the NO concentration a constant during the exhalation period.

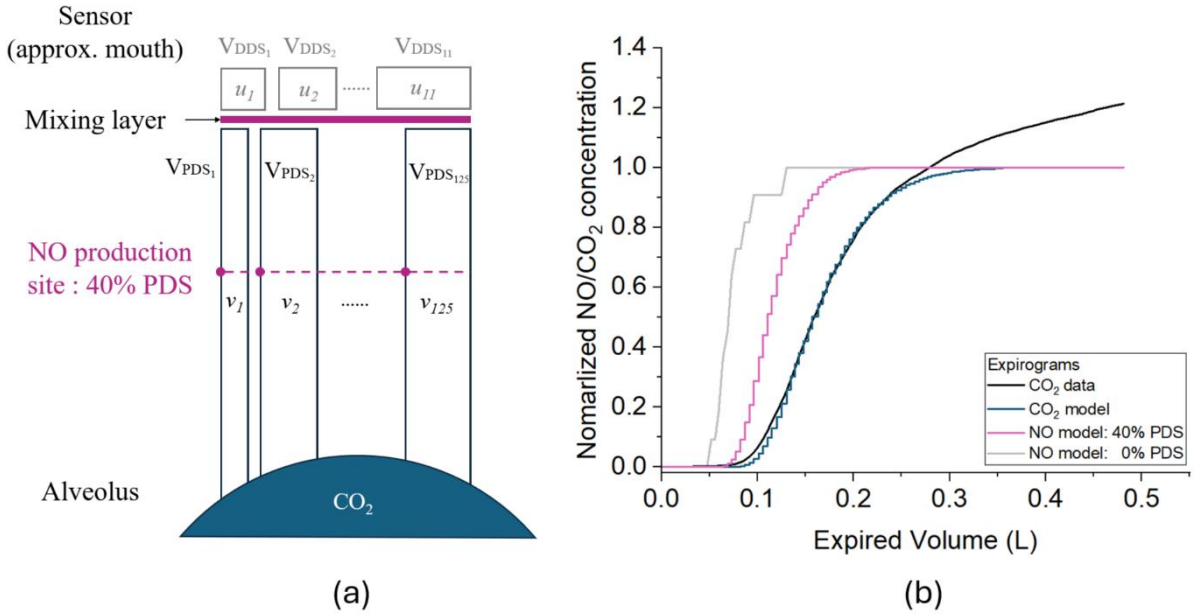


Figure 4.9 Structure of the DSP based on CCP outputs and corresponding simulated NO expirogram under the assumption of constant exhalation speed. (a) CCP outputs the structure of the multi-pipe model, which incorporates device dead space (DDS). Each PDS pipe has a specific shared volume (V_{PDS_i}) and exhalation speed (v_i), where i = 1, 2, … 125. Note that v_i remains constant over time. Each DDS pipe also has a specific volume (V_{DDS_j}) and exhalation speed (u_j), where j = 1, 2, … 11. (b) Simulated NO expirogram at 40% PDS (pink curve), alongside the 0% PDS condition (grey curve), illustrating the direct contribution of DDS. Measured (black) and simulated (blue) CO_2 expirograms are also shown for comparison. PDS: personal dead space.

Figure 4.9(a) demonstrates the structure of the DSP model, assuming NO is produced at 40% of the PDS depth, labelled with pink points, and **Figure 4.9(b)** shows the corresponding simulated NO expirogram as the pink curve. The process of NO simulation under the SpIn mode is identical to that of CO_2 expirogram simulation. The only adjustment needed is shrinking the PDS volume to 40% of its original size, as this simulates NO expirogram at

40% PDS depth. **Figure 4.9(b)** also shows the effects of the DDS (i.e., 0% PDS depth) on the simulated NO expirograms, marked by the grey curve.

Using the same approach, I generated a series of NO expirograms corresponding to NO production depths ranging from 0% to 100% of the PDS in 10% intervals, as shown in **Figure 4.10**.

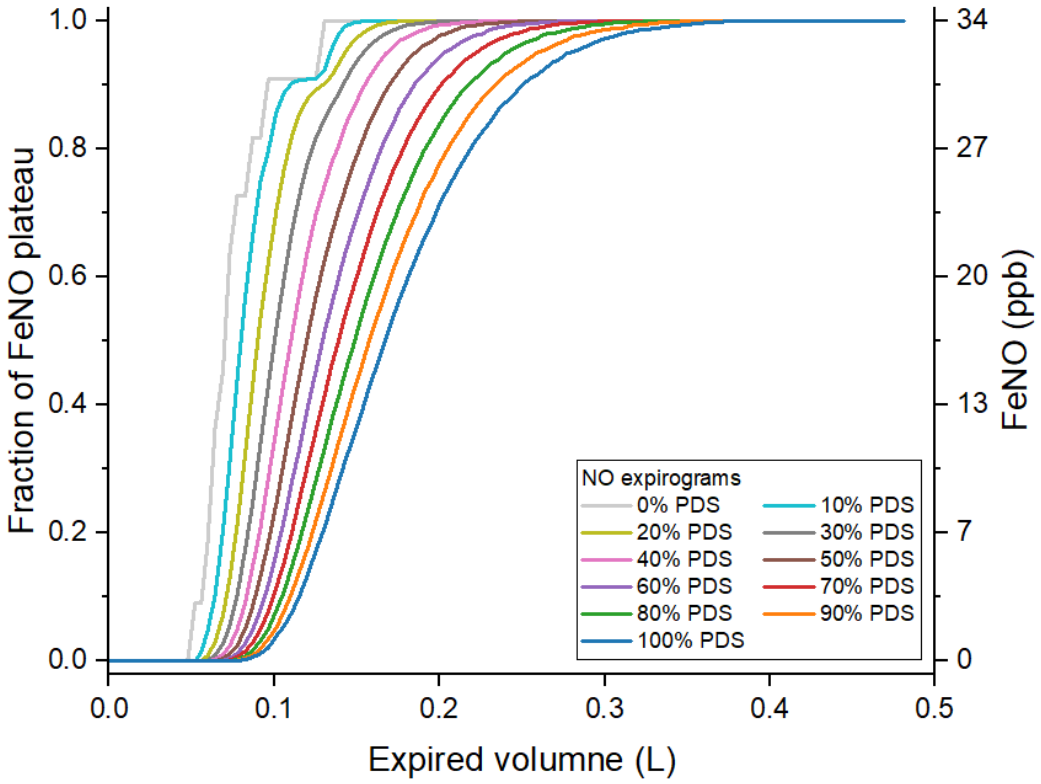


Figure 4.10 NO expirograms 'wallpaper'. Simulated NO expirograms, assuming NO is produced at a single point and exhalation speed variations are ignored(SpIn mode), ranging from 0% of the PDS (grey curve) to 100% of the PDS (dark blue curve).

4.1.4.2 Issues associated with SpIn mode

The primary disadvantage of SpIn mode is that it assumes a constant exhalation speed, which affects the simulated NO expirograms in two ways: by neglecting the inhaled residual gas and by causing inaccurate simulations during the exhalation period.

NO is continuously produced into the airway lumen during both inhalation and exhalation from a production site along the PDS. As a result, at the end of inhalation, a portion of NO

remains in the conducting airways and does not reach the alveolus, thereby avoiding clearance in the alveolar region. During exhalation, this portion of residual NO stored in the conducting airways mixes with newly produced NO, temporarily elevating NO levels during phases I and II. When phase III begins, the elevated NO declines towards the plateau value, which reflects only the level of NO newly produced. In the NO expirogram, this is expected to generate a peak during phase I and II. In the SpIn model, however, the assumption of a 50ml/s exhalation speed cannot be applied to inhalation, as the actual inhalation speed is significantly higher due to unrestricted inhalation flow. As a result, the SpIn mode does not account for the effects of residual NO in the simulation.

In terms of speed variation, a well-performed exhalation is illustrated in the volume/flow-to-time graph, as shown in **Figure 4.11,** revealing that the exhalation speed (dotted curve) still continuously fluctuates throughout the exhalation period.

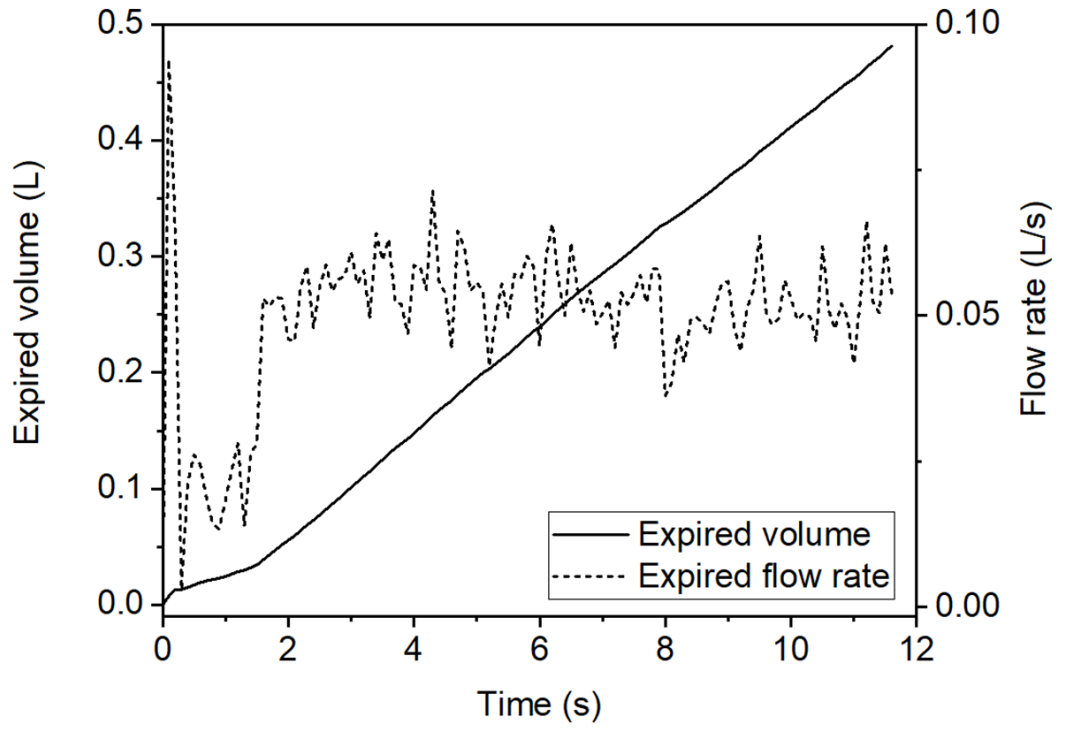


Figure 4.11 Expired volume and flow rate over time. During the initial phase (approximate time < 2s), the exhalation speed is lower than the target value of 50 mL/s, resulting in a slow increase in expired volume. Solid curve: expired volume. Dotted curve: exhalation flow rate.

In this case, illustrated by **Figure 4.11,** the initial 2 seconds of slow exhalation (relative to the target rate) are expected to produce a higher NO concentration than would occur at the target speed and to appear as a peak in the simulated NO expirogram. However, by assuming a constant exhalation speed of 50mL/s, the SpIn mode is unable to reproduce such a peak in the simulated NO expirogram.

Therefore, further developments are required to consider the retained NO from inhalation and the effects of NO concentrations variation due to flow rate, which could potentially simulate the NO expirograms more closely aligned with reality.

4.1.4.3 Speed-dependent (SpD) mode

The previous section presents two issues associated with SpIn mode: the inhalation storage of NO and speed variation during exhalation. Both issues fundamentally originate from a lack of consideration of speed effects (during inhalation and exhalation) on NO concentration. From the perspective of simulated NO expirograms, this fundamental problem is reflected in the calculation of amplitudes on the y-axis, whereas it does not affect the position of switching points on the x-axis.

This section first outlines the modifications to the amplitude calculation on the y-axis in the SpD mode compared to the SpIn mode and then separately presents solutions to the two previously identified issues. It concludes by integrating these solutions to generate the final simulated NO expirograms. This section continues to use the previous example, assuming that NO is produced at a depth of 40% PDS. This section focuses on presenting the results obtained using the SpD mode, while the complete calculation steps are available in **Appendix B**.

Despite the NO concentration becoming speed-dependent, the fundamental method for calculating amplitude on the y-axis remains the same, as described in the CO_2 simulation section using the three-pipe model: the amplitude of each step function is proportional to the

fraction of gas molecules contributed by each pipe to the total exhaled gas. In contrast to the SpIn mode (and the simulation in the CO_2 expirogram), where the amplitude is solely proportional to exhalation speed, the amplitude in SpD mode becomes proportional to the product of the corresponding NO concentration and exhalation speed, both of which fluctuate with time.

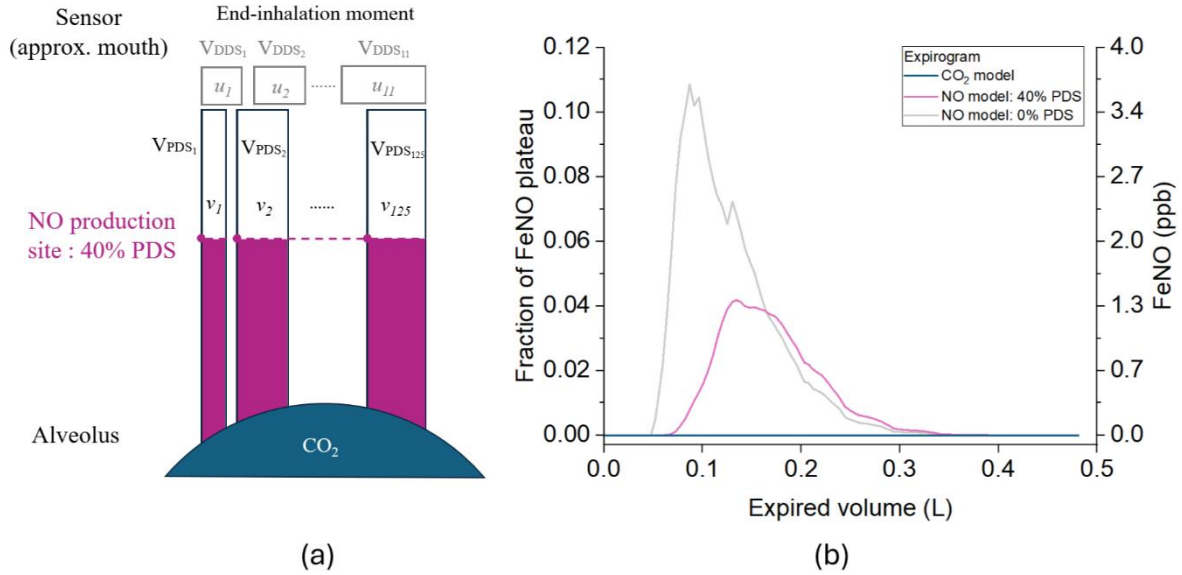


Figure 4.12 CCP output structures at the end of inhalation and corresponding simulated NO expirogram accounting only for NO storage in the airway lumen during the inhalation phase. (a) CCP output structure of the multi-pipe model, incorporating device dead space (DDS). Each pipe has a defined shared volume (V_{PDS_i}) and time-varying exhalation speed (v_i), where i = 1, 2, … 125. The pink area indicates the NO stored in the lumen of conducting airways at the end of inhalation. (b) Simulation of an expirogram produced only by stored NO at 40% PDS (pink curve), alongside the 0% PDS condition (grey curve).

Figure 4.12 demonstrates the contribution of NO storage during the inhalation phase. **Figure 4.12(a)** shows the moment at the end of the inhalation phase when a portion of NO molecules remains stored in the lumen of conducting airways (pink area). If only this stored NO portion is exhaled, ignoring NO production during exhalation, the resulting NO expirogram is shown in **Figure 4.12(b).** Due to the high inhalation speed (usually exceeding 100mL/s), the contribution of the stored NO is approximately 10% (as indicated by the maximum grey curve in **Figure 4.12(b)**), although it may vary significantly between breaths. In addition, when NO is produced deeper in the airways, these effects are reduced due to the

limited storage space between the production site and the alveolar sacs, which clears the NO molecules.

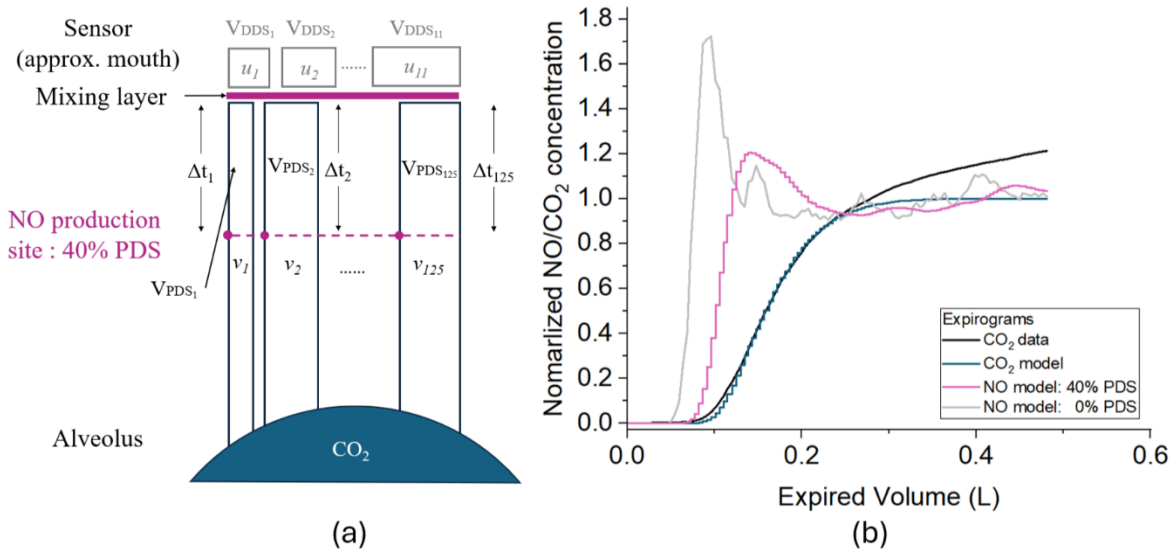


Figure 4.13 CCP output structures and corresponding simulated NO expirogram accounting only for variation in exhalation speed. (a) CCP output structure of the multi-pipe model, incorporating device dead space (DDS). Each pipe has a defined shared volume (V_{PDS_i}) and time-varying exhalation speed (v_i), where i = 1, 2, … 125. The fluctuation of v_i over time leads to corresponding temporal changes in NO concentration within each pipe, requiring back-tracing of Δt_i to determine the NO concentration at the production point. (b) Simulated NO expirogram at 40% PDS (pink curve), alongside the 0% PDS condition (grey curve). Measured (black) and simulated (blue) CO_2 expirograms are shown for comparison. Both simulated NO curves exhibit a peak due to the slow initiation of exhalation. PDS: personal dead space.

Figure 4.13 presents the structure of the DSP and results of the simulated NO expirogram, considering only the speed variation during the exhalation period. In resolving the issue related to speed variance, the primary task is to identify the NO contribution from each pipe. As suggested at the start of this section, this contribution is the product of exhalation speed and the NO concentration.

The first step is to determine the simulated NO expirograms at the mixing layer, where NO is contributed by the PDS pipes. The exhalation speed can be directly determined from the fraction of speed share for each pipe, denoted as v_i (i = 1, 2, …, 125), as shown in **Figure 4.13(a)**. In contrast, the NO concentration at a given time point is determined earlier, specifically at the moment when this gas segment passes through the NO production site

(40% PDS, pink points in **Figure 4.13(a)**). Therefore, a unique Δt_i (i = 1, 2, … 125) is defined for each pipe as the travel time of the gas between the NO production point (at 40% PDS) and the mixing layer in each individual pipe. With a known Δt_i, the exhalation speed at Δt_i earlier can be determined, along with the corresponding NO concentration at the NO production point at that time. This NO concentration is equal to the concentration contributed by that pipe to the mixing layer at the current time point. Consequently, the amplitude is determined by the product of exhalation speed and NO concentration in each individual pipe. Once the NO expirogram at the mixing layer is determined, the NO expirogram at the sensor layer can be calculated using the identical procedure. **Figure 4.13(b)** presents the simulated NO expirogram at 40% PDS (pink line) and at 0% PDS (grey line), considering only the effect of speed variation.

Figure 4.14 presents the final NO expirograms, incorporating NO storage during the inhalation period and speed variation. The 'wallpaper' simulates the NO expirograms, assuming NO is produced across 0% to 100% of the PDS in 10% intervals. The SpD mode successfully simulates the peak that occurs around 0.1L of exhaled volume in the 'wallpaper' compared to the SpIn mode.

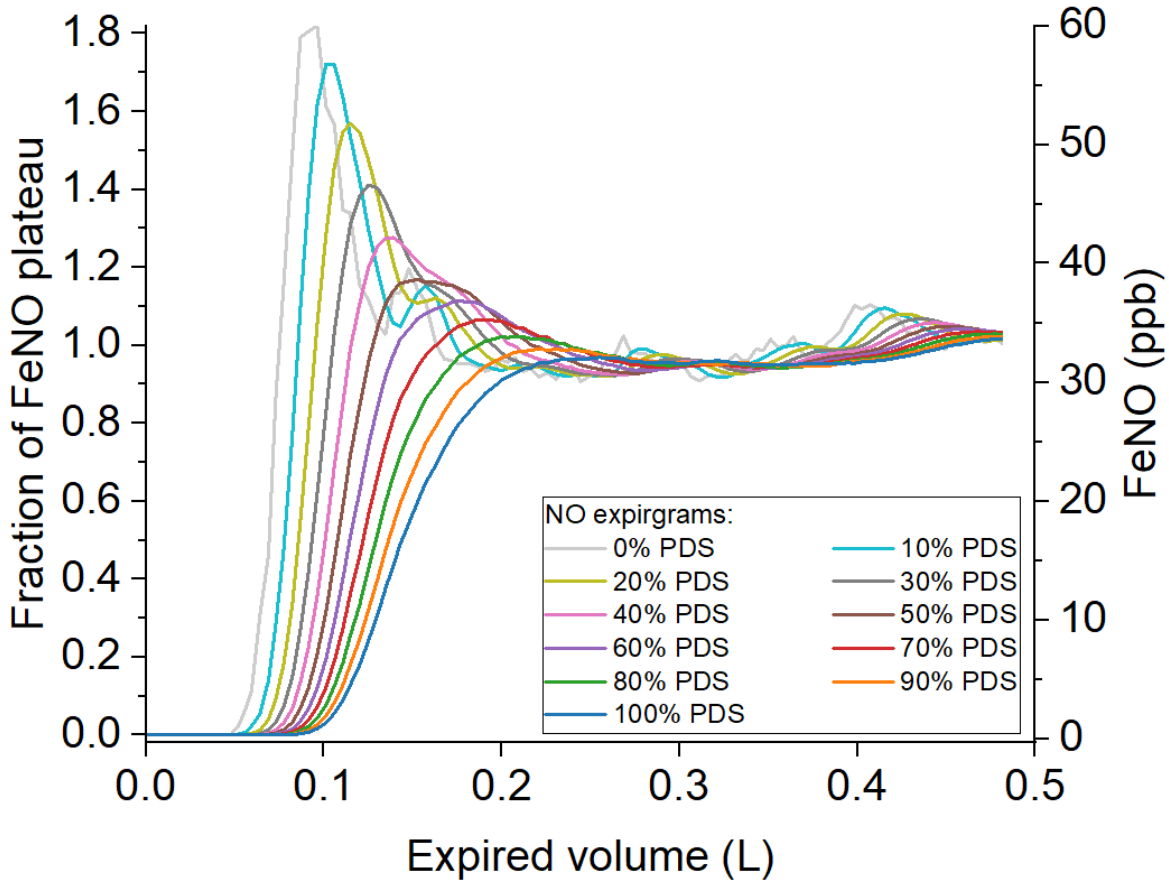


Figure 4.14 NO expirograms 'wallpaper' accounting for flow rate variation(SpD mode) . Simulated NO expirograms assuming NO is produced at a single point, ranging from 0% PDS (grey curve) to 100% PDS (dark blue curve).

4.1.5 Fitting process of the DSP model

Figure 4.15 presents a detailed fitting procedure for the DSP model as an extension of **Figure 4.3**, with particular focus on three key parameters (as indicated by the red sections in **Figure 4.15**): the alveolar CO_2 concentration(C_{alv,CO_2}), NO production rate (r_0) and dead space volume correction(dV). The former two are derived from the RFD measurements, while dV is obtained by fitting the CO_2 expirogram to measured CO_2 data. The following sections present the methods for determining the values of these three parameters.

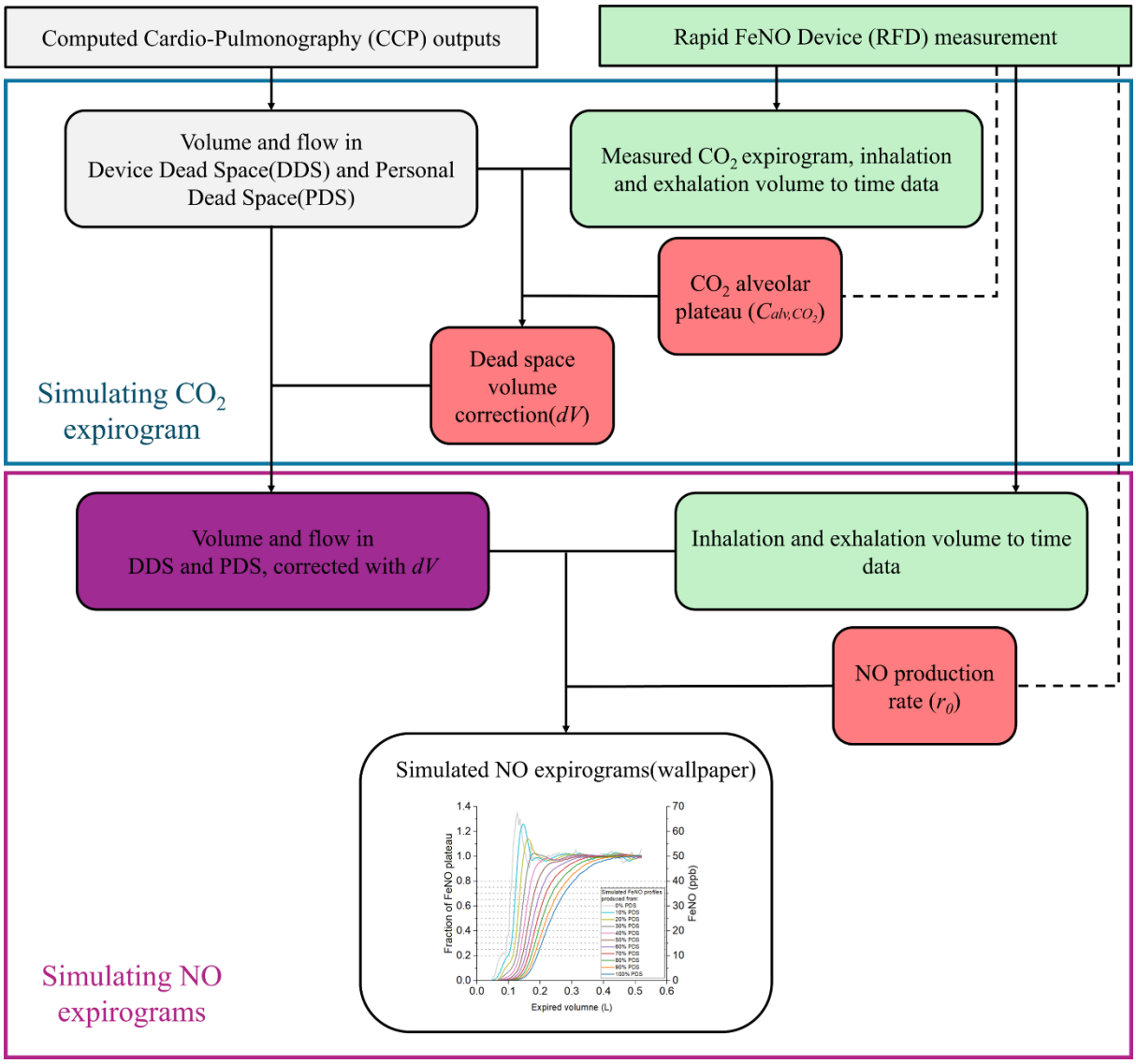


Figure 4.15 Fitting process of the DSP model. Grey sections: CCP outputs. Green sections: RFD measurements. Red sections: parameters requiring fitting or derivation. Purple section: corrected PDS volume and DDS volume. Blue box: simulating CO_2 expirogram. Pink box: simulating NO expirograms. Dashed line: indicates that data are provided by the source.

4.1.5.1 Retrieving the alveolar CO_2 concentration (C_{alv,CO_2})

CO_2 originates from diffusion across the pulmonary capillaries into the alveolar sacs. Its concentration in the alveolus (C_{alv,CO_2}) is equal to the plateau value of the CO_2 expirogram when metabolic production is ignored. However, the measured CO_2 expirogram includes the effect of ongoing metabolic CO_2 production, causing a slope in phase III of the CO_2

expirogram. A boundary point between phase II and phase III is used to estimate the C_{alv,CO_2} [184], as illustrated by the green dot in **Figure 4.16**.

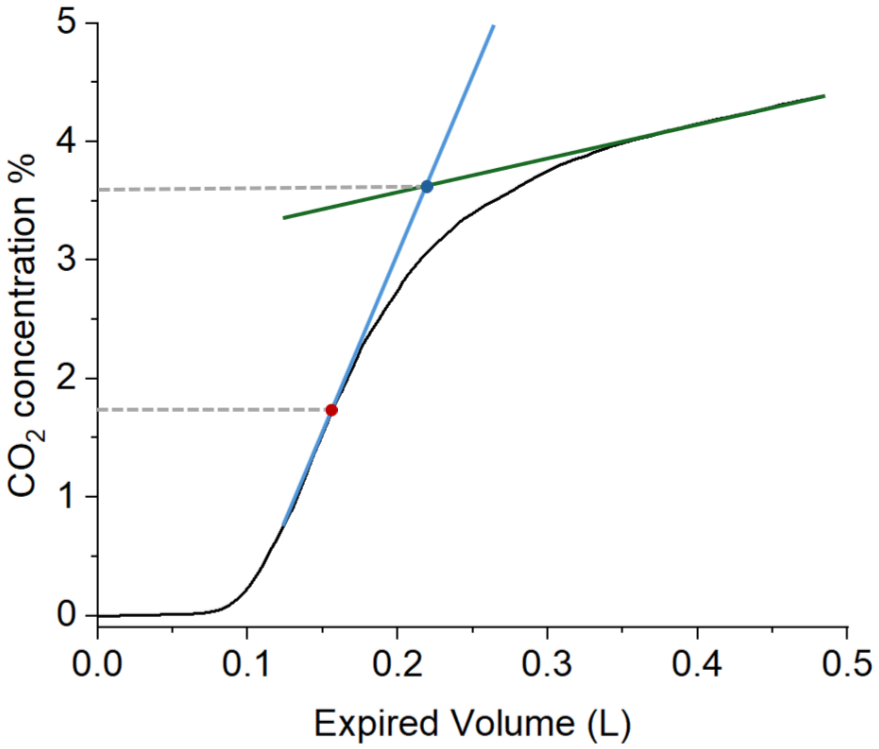


Figure 4.16 Determination of the boundary point and associated components. Blue line: tangent to phase II. Green line: tangent to phase III. Green dot: the intersection of the blue and green lines, with the corresponding y value representing C_{alv,CO_2}. Red line: horizontal line at C_{alv,CO_2} / 2, indicating the fitting range for dV. dV reflects the degree of breath depth.

This boundary point is identified by the intersection of two tangent lines. The criteria for the selection of these tangent lines are provided below,

(1) In phase II, the blue line is from the linear regression of the points where the increase in CO_2 concentration between adjacent points is ≥ 75% of the maximum increase, as shown in **Figure 4.16**.

(2) In phase III, the green line is from the linear regression of the points with CO_2 concentration ≥ 90% of the final CO_2 concentration during that measurement, as shown in **Figure 4.16**.

(3) The y-value of the intersection point between these two lines represents the plateau CO_2 concentration, which also corresponds to the alveolar CO_2 concentration (C_{alv,CO_2}, y-value of the green dot in **Figure 4.16**).

4.1.5.2 Fitting the dead space volume correction(dV)

dV represents the volume difference between the end-exhalation and end-inhalation phases of a breath, reflecting the breath depth. The *dV* is then distributed among PDS pipes in proportion to each pipe's volume and flow rate. It is obtained through least-squares fitting of the simulated CO_2 expirogram to measure CO_2 data. The boundary point obtained in the previous section is used to define the fitting range, which includes y-values from 0 to $C_{alv,CO_2}/2$ (i.e., half of the y-value at the boundary point, as indicated by the red dot in **Figure 4.16**). The reason for setting this range is that the fitting focuses on the exhalation of the conducting airway gas, i.e. phases I and II.

4.1.5.3 Retrieving NO production rate (r_0)

It is necessary to know the NO production rate (r_0), expressed in units of ppb·L/s, to generate the simulated NO expirograms. r_0 is estimated from phase III of the measured NO expirogram under the assumption that all PDS pipes contribute to NO concentration measured at the mouth during this phase. In addition, the flow rate during phase III is relatively constant, ensuring a more reliable estimation.

The NO plateau value is obtained by the volumetric average of NO concentrations over the final 25% of the exhalation volume, which, when divided by the average flow rate over the same period, yields r_0. Furthermore, this NO plateau value is comparable to the conventional fractional exhaled nitric oxide (FeNO) measurement, and a comparison of these two methods will be presented in Chapter 5.

4.1.6 Summary

Based on DDS and PDS data fitted in CCP, the DSP model produces the simulated NO expirograms by fitting the CO_2 expirogram to retrieve the correction of PDS, generating the 'wallpaper' with (SpD mode) or without (SpIn) consideration of speed variance and conducting airway storage NO.

4.2 Derivation of NO depth parameters

The establishment of the individualised 'wallpaper' enables comparison between the simulated NO expirograms and the measured NO expirogram.

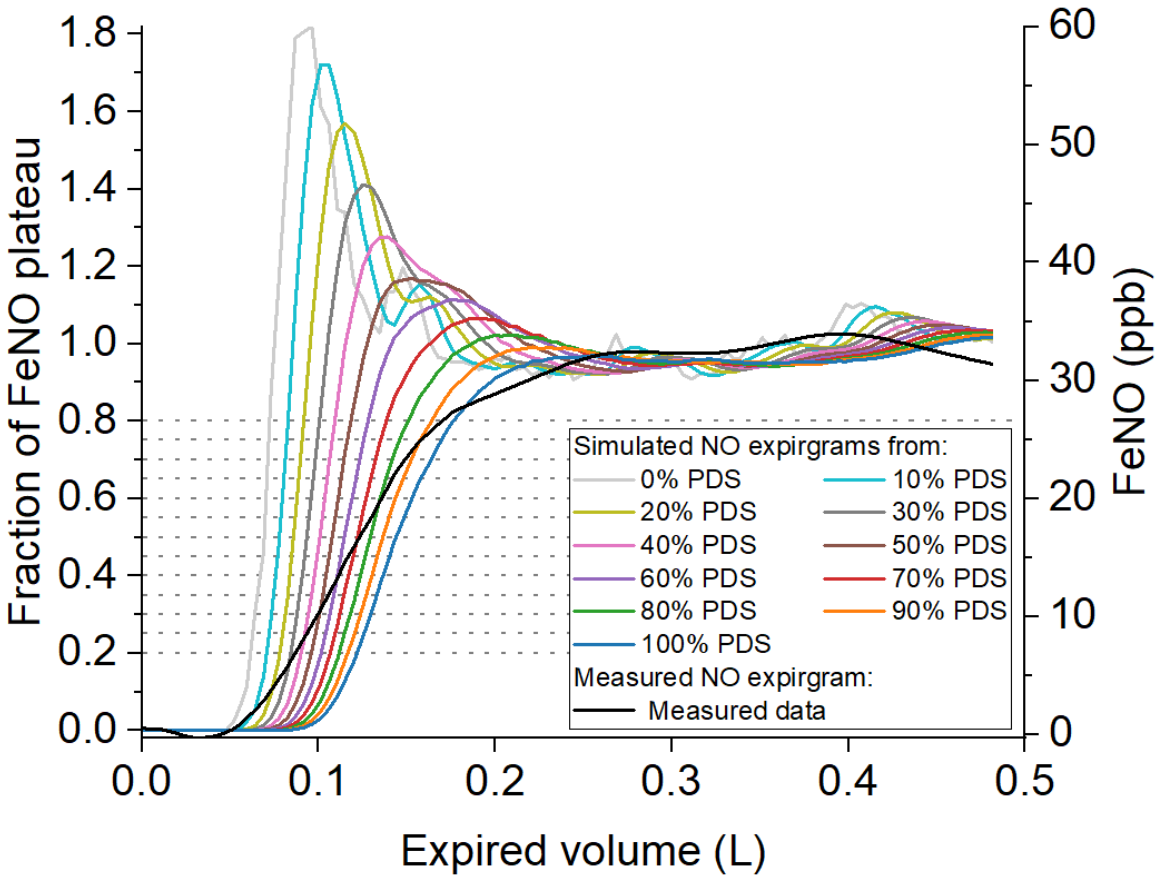


Figure 4.17 'Wallpaper' and the superposed measured NO expirogram. Coloured curve: simulated NO expirograms, black curve: measured NO expirograms.

Figure 4.17 shows a comparison between measured (black curve) and simulated NO expirograms(coloured curve), demonstrating that the measured NO expirogram does not

match any of the simulated curves, which supports the assumption that NO molecules are produced across a region rather than at a single point. It also underscores the need to establish a statistical framework to estimate the NO depth parameters.

4.2.1 Methods for determination of NO depth parameters

After constructing the 'wallpaper', horizontal auxiliary lines are drawn from 20% to 80% of the FeNO plateau in 5% increments (as shown in **Figure 4.17** and **Figure 4.18**, grey dotted lines). The measured NO expirogram (black curve in **Figure 4.17** and **Figure 4.18**) is superimposed onto the 'wallpaper' and auxiliary lines, generating one intersection point for each auxiliary line.

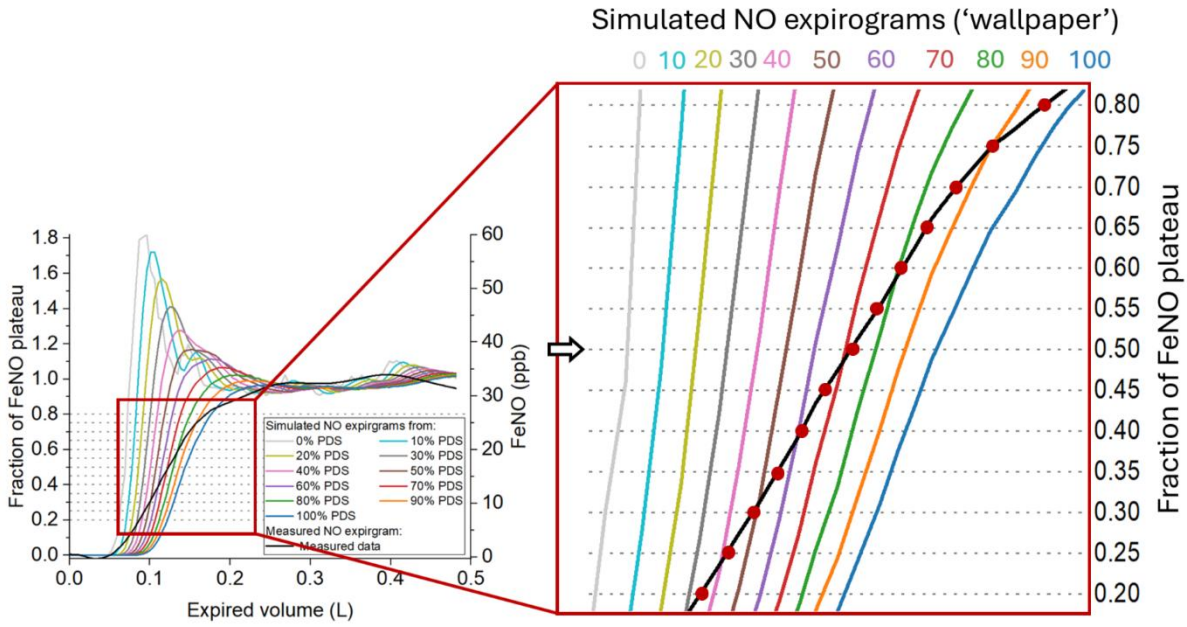


Figure 4.18 Intersections between NO profile and auxiliary lines. Red dots: the intersection points between NO measured profile (black curve) with auxiliary lines (grey dotted horizontal lines). Coloured curves: simulated NO expirogram from different PDS depths, black curve: measured NO expirogram. The hollow black arrow indicates the 0.5 fraction of the FeNO plateau.

The adjacent 'wallpaper' curves are used to determine the location of each intersection point in the airways. As illustrated in **Figure 4.18**, the red dots represent the intersection points used to quantify their depth in the conducting airways based on the horizontal distance to neighbouring coloured curves, i.e., the simulated NO expirograms. For instance, the

intersection point (red dot) for the 0.50 fraction of the FeNO plateau (marked by the black hollow arrow) lies horizontally between the 70% PDS (red curve) and 80% PDS (green curve) curves, and its exact location (71.6% PDS) can be determined by the proportion it divides. This method provides 13 depth measurements for normalised FeNO levels ranging from 20% to 80% to avoid unstable results at the extremes of NO concentration (< 20% or > 80% of the FeNO plateau).

4.2.2 Approach to acquiring NO depth parameters

A common approach to representing the 13 depth values obtained from the previous section is to use either the mean and standard deviation or the median and interquartile range, depending on the underlying distribution. Analysis of the test results indicates that the depth values do not consistently follow a normal distribution across all cases.

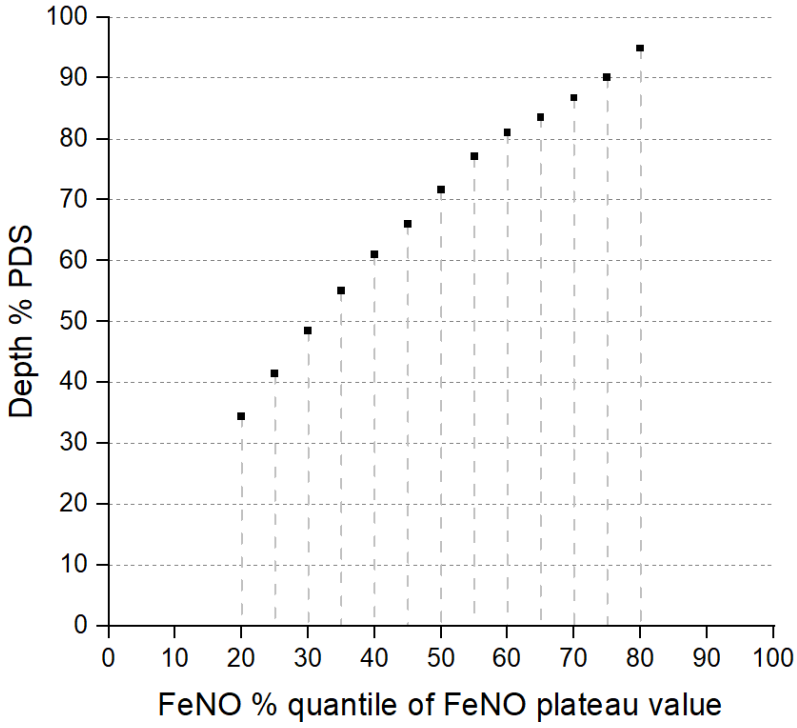


Figure 4.19 Demonstration of depth parameters with FeNO % quantile values. The grey dashed lines indicate the corresponding FeNO quantile values. It is evident that the distribution of 13 points is skewed.

In most cases, the distribution of NO production depth is left-skewed (negatively skewed) among participants. **Figure 4.19** illustrates an example where FeNO quantiles (%) are plotted on the x-axis and depth (% PDS) on the y-axis. The depth between the 25th and 50th percentiles is 31.1% PDS, while the depth between the 50th and 75th percentiles is 18.5% PDS.

To quantify and assess the skewness of the NO depth distribution, I used NO depth data from 12 participants to calculate the Pearson coefficient of skewness (*Sk*), with the median of *Sk* value reported in **Table 4.1**. If $|Sk| \geq 0.5$, the dataset is considered moderately skewed, whereas if $|Sk| < 0.5$, it is considered approximately normally distributed. Most participants show negative skewness ($Sk < 0$), indicating that the NO production is distributed with high density in the distal airways. The skewness values range from -1.03 to 0.12 across participants, suggesting that the assumption of a normal distribution may be inaccurate for the data distribution.

Table 4.1 Skewness coefficient for 12 participants

ID	Condition	Skewness(Sk)
H1	Healthy	-0.90
H2	Healthy	0.12
H3	Healthy	-0.30
H4	Healthy	-0.01
H5	Healthy	-0.81
H6	Healthy	-0.53
A1	Asthmatic	-0.80
A2	Asthmatic	-0.61
A3	Asthmatic	-0.59
A4	Asthmatic	-0.41
A5	Asthmatic	-0.54
A6	Asthmatic	-1.03

As a result, the NO depth parameters are reported using a non-parametric approach, yielding four parameters that describe the depth of NO production. Among the parameters, three describe NO production depth: (i) Q25, the depth at which the FeNO value reaches the 25th percentile of its plateau value, (ii) Q50, the depth at which the FeNO value reaches the

50th percentile of its plateau value, and (iii) Q75, the depth at which the FeNO value reaches the 75th percentile of its plateau value. A fourth parameter, IQR, describes the depth range between the 25th and 75th percentiles of the FeNO plateau (IQR = Q75 - Q25), indicating the spread of NO production within the conducting airways. To summarise this information, **Figure 4.20** illustrates the four NO depth parameters on the graph.

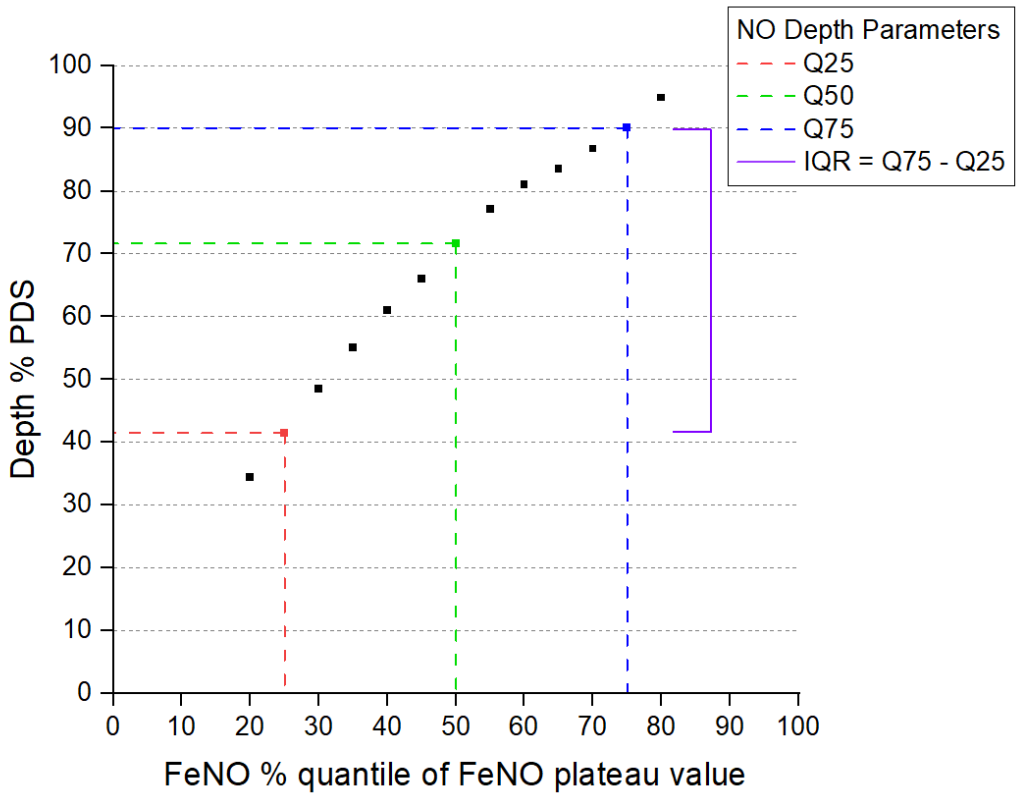


Figure 4.20 Four parameters are used to describe the NO production depth. Q25: the depth at which the FeNO value reaches the 25th percentile of its plateau value (red), Q50: the depth at which the FeNO value reaches the 50th percentile of its plateau value (green). Q75: the depth at which the FeNO value reaches the 75th percentile of its plateau value (blue), IQR: the depth range between the 25th and 75th percentile of the FeNO plateau (IQR = Q75 - Q25, purple).

4.3 Summary

This Chapter introduces the DSP model that underlies the estimation of the NO production site, with two modes, SpIn and SpD, and also defines four key parameters for

describing NO depth: IQR, Q25, Q50 and Q75. Although these complete the software development, the analysis of breath involves complex interactions between participants, devices and the accompanying model. Therefore, a quality assessment process still needs to be developed to ensure that the collected data meets the quality control criteria. Furthermore, tests of repeatability and reliability are needed before processing to clinical applications.

Chapter 5

Novel measurement for locating the production location of nitric oxide (NO) in conducting airways - Quality control and repeatability/reliability assessment

The previous Chapter described the methodology for generating simulated nitric oxide (NO) expirograms and producing the NO depth parameters. This Chapter discusses the quality assessment of individual special breaths, completing the framework for measuring NO depth parameters. This Chapter also presents the repeatability and reliability of NO depth parameters. Furthermore, it discusses the advantages and disadvantages of the Speed-Independent (SpIn) and Speed-Dependent (SpD) modes in the Dead Space Pipes (DSP) model, thereby selecting the SpD mode for future clinical applications.

5.1 Quality assessment of NO depth measurement

5.1.1 Overview

Overall, four main factors contribute to the failure of data from a special breath to produce NO depth parameters (the differences between a special breath and a normal breath are described in Chapter 3, **Section 3.3**):

(i) Setup of the special breath duration: this setup defines how long the participants are required to exhale during special breaths. Incorrectly configured setup may cause failure in measurement. (***Reason I***)

(ii) Contamination from nasal cavity: the nasal cavity epithelial cells produce a large amount of NO. The protocol for breathing through the Rapid FeNO Device (RFD) requires nasal clips to prevent inhaled NO contamination. However, applying nasal clips may increase the possibility of nasal contamination during exhalation. (***Reason II***)

(iii) Speed control in special breaths: special breath ideally requires a constant exhalation speed to ensure the assumption of negligible axial diffusion in the airway holds. The SpD mode is developed to reduce the effects of speed variability. However, significant fluctuations in exhalation speed may violate the assumption of negligible axial diffusion, thereby compromising the accuracy of the estimation. Moreover, the SpIn mode requires more stability in exhalation speed, as it inherently assumes a constant exhalation speed. (***Reason III***)

(iv) Failure in model fitting: the DSP model requires obtaining three parameters: the alveolar CO_2 concentration (C_{alv,CO_2}), the dead space volume correction(dV) and the NO production rate (r_0). Any failure to obtain these parameters results in a failure to fit the model. (***Reason IV***)

However, the factors themselves may be challenging to detect. In the following sections, I introduce how these factors are connected to signals that are easily observable from volume/flow rate-to-time figures, CO_2 expirogram, NO expirogram or other data outputs. As a result, I conclude this section with a practical set of criteria for quality assessment.

5.1.2 Four determinant factors and their detectable signals

5.1.2.1 Setup of the special breath duration (Reason I)

This setup refers to the duration between the initiation of inhalation and the release of the restrictive valve in a special breath (**Figure 5.1**, between the blue and red arrows). The special breath duration is usually set at 13 - 17 seconds, though it should be specified depending on the participant's lung condition and breathing behaviour.

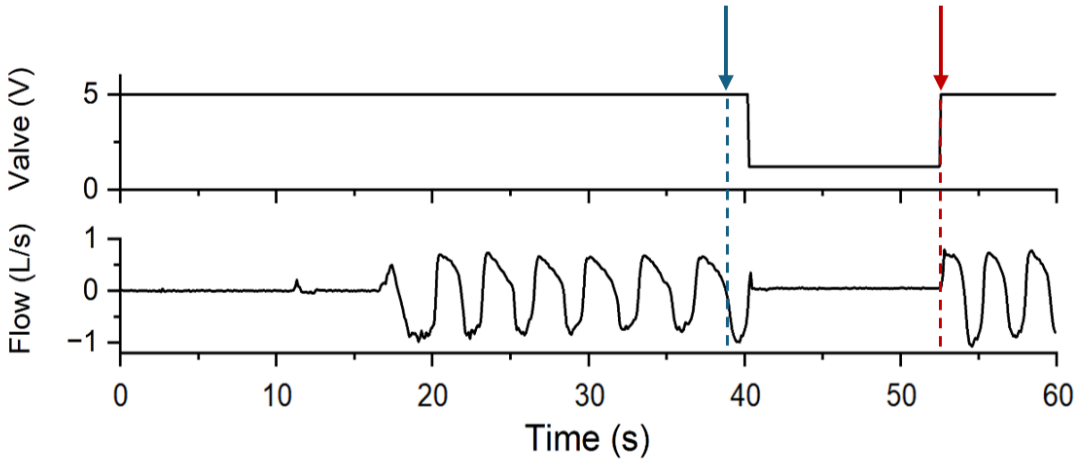


Figure 5.1 Special breath duration configuration. The setting of special breath length is illustrated in the figure. The upper figure shows the voltage change in the restrictive valve. The lower figure shows the change in flow rate. Blue arrow: marks the start of inhalation in a special breath, and the blue dashed line indicates the flow rate = 0L/s. Red arrow: marks the end of special breath, when the restrictive valve is released.

When the special breath duration is set too short, the CO_2 expirogram of participants fails to reach phase III. As I introduced in Chapter 4, phase III of the CO_2 expirogram is required to identify the CO_2 plateau and the fitting range. The absence of phase III in the CO_2 expirogram causes an inaccurate estimation of the dV value, resulting in an unreliable calculation of the NO depth parameters.

On the other hand, a prolonged duration of special breath may introduce issues, such as insufficient gas storage in the lungs to sustain exhalation. Moreover, maintaining a slow exhalation speed for too long may cause discomfort for participants, increasing the risk of

loss of speed control, which usually occurs as a sudden drop in exhalation speed or even a complete interruption of exhalation.

Both conditions are generally evident when monitored through real-time CO_2 expirogram. Apart from real-time monitoring, a secondary check is conducted post-measurement to exclude these conditions.

5.1.2.2 Contamination from the nasal cavity (Reason II)

The nasal epithelial cells produce significantly higher levels of NO than airway epithelial cells[185]. The soft palate functions as a control valve between the nasal and oral cavities (illustrated in **Figure 5.2**). Chapter 3 introduced the use of a nasal clip during measurement to prevent NO produced in the nasal cavity from entering the inhaled gas flow during inhalation. However, during the exhalation period, pressure fluctuations in airways are inevitable and originate from the oral side of the palate. When a decrease of pressure occurs from the oral side, it might induce gas from the nasal side to leak into the oral side, forming a flow of gas containing additional nasal-produced NO molecules into the exhalation airflow.

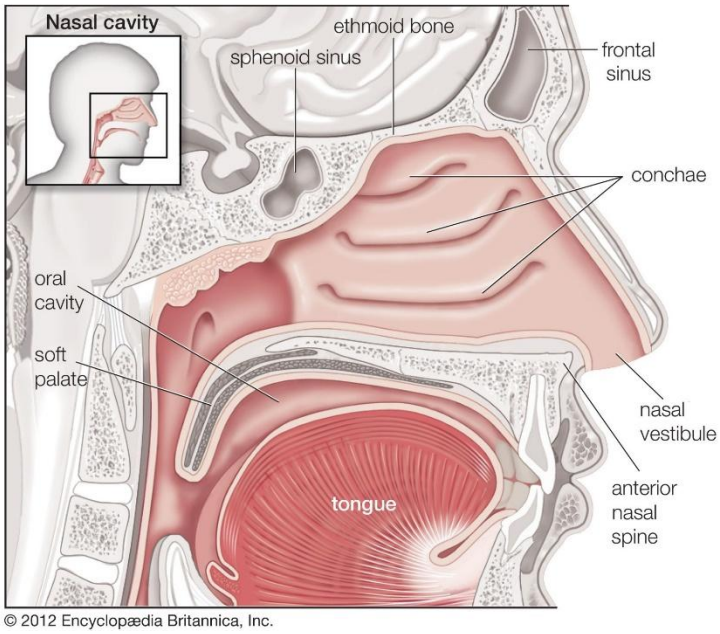


Figure 5.2 An anatomical illustration showing the nasal cavity, oral cavity and soft palate as a barrier. The soft palate should close off the passage between the oral and nasal cavities during exhalation through the mouth[186].

The most evident signal of contamination from the nasal cavity is an early rise or early peak appearance in the measured NO expirogram, using the simulated NO expirograms as a reference.

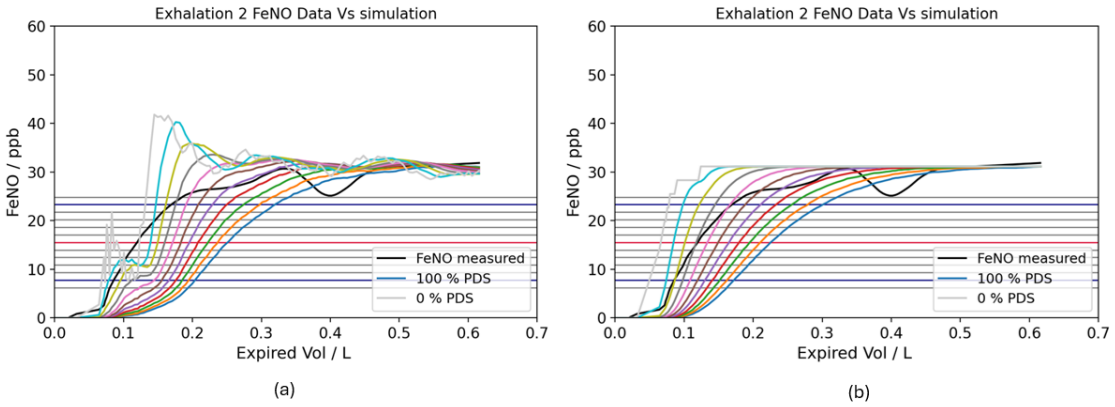


Figure 5.3 Demonstration of early rise. (a): Early rise in expiration simulated using the SpD mode. The early rise of the NO concentration curve extended beyond the left edge of the simulated curve; (b) Early rise using the SpIn mode. No sign of early rise can be observed in the SpD mode.

Figure 5.3 illustrates an example of an early rise in NO expirogram. In the SpD mode of simulation, as shown in **Figure 5.3(a)**, the grey curve represents the expirogram of NO produced at the laryngeal level(the upper end of the tracheal). When the measured NO data appear to the left of the grey curve, it suggests the presence of NO produced at a location higher than the larynx, indicating nasal cavity leakage. In contrast, the SpIn mode in **Figure 5.3(b)** has limited ability to reflect such abnormalities in the NO data, as it assumes a constant flow speed. From this example, we can see that an early rise can be more sensitively detected in the SpD mode than in the SpIn mode.

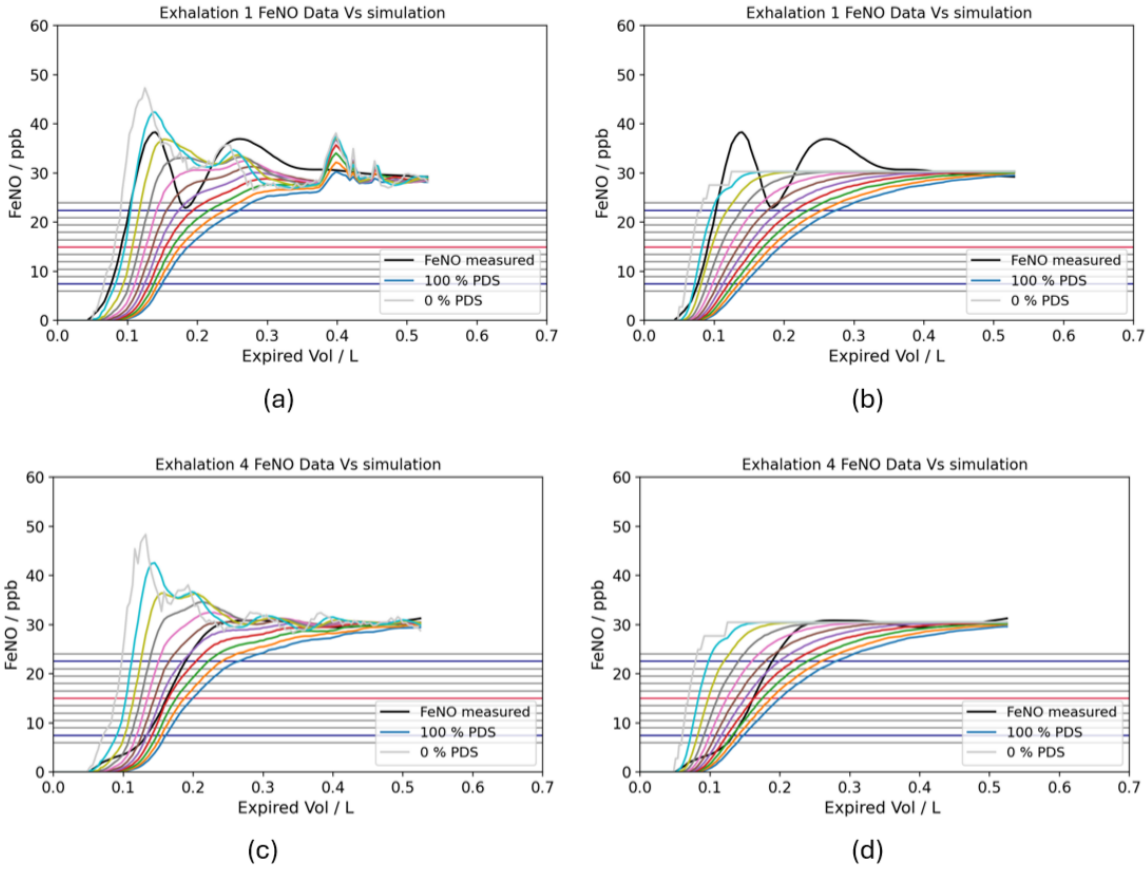


Figure 5.4 Example of early peak and comparison with another exhalation. (a) and (b): Early peak occurrence using SpD mode and SpIn mode, respectively. (c) and (d): Another special exhalation performed by the same participant during the same visit, showing a more distal NO production depth than the previous one, using SpD mode and SpIn mode, respectively. This indicates that the first set of special breaths was contaminated by nasal NO.

When the degree of nasal leakage becomes extreme, it may show an early peak instead of an early rise in the NO expirogram, as illustrated in **Figure 5.4(a)** and **(b)**. The early peak is defined as a peak exceeding the FeNO plateau value by more than 10% and occurring before the exhaled volume surpasses the sum of PDS and DDS volumes. In SpD mode, nasal contamination should be differentiated from slow exhalation initiation, as both can generate early peaks. Nasal contamination can be identified by comparing other NO expirograms from the same visit. If the remainder of the exhalation shows NO production from deeper locations, it suggests that the early peak is caused by nasal cavity leakage rather than by slow exhalation initiation. **Figure 5.4(c)** and **(d)** show that SpD mode and SpIn mode in the same

participants without early peak, respectively. This distal NO production in other breaths from the same visit suggests nasal leakage.

Additionally, nasal contamination may begin and stop at any stage of expiration, although it is more likely to occur during the initiation of exhalation due to variations in breathing force. Early rise and early peak patterns strongly suggest nasal cavity leakage. However, both patterns in the expirogram can be caused by other factors. The early rise may result from NO diffusion, and the early peak may be due to a slow initiation of exhalation. Therefore, each case should be carefully analysed in comparison with the 'wallpaper' before drawing conclusions.

5.1.2.3 Speed control in special breath (Reason III)

Variations in the exhalation speed are inevitable, while different types of variations are associated with varying degrees of calculation inaccuracy, which can determine whether a breath should be excluded.

5.1.2.3.1 Overshoot occurrence

The definition of overshoot is a temporary increase in exhalation speed exceeding 0.1L/s, as shown in **Figure 5.5** by a red arrow. It is common to see overshoot when participants initiate exhalation. **Figure 5.5(a)** demonstrates a single overshoot during a special exhalation. In some cases, participants perform a second or even a third overshoot within the same breath, as shown in **Figure 5.5(b)**, which represents a double overshoot.

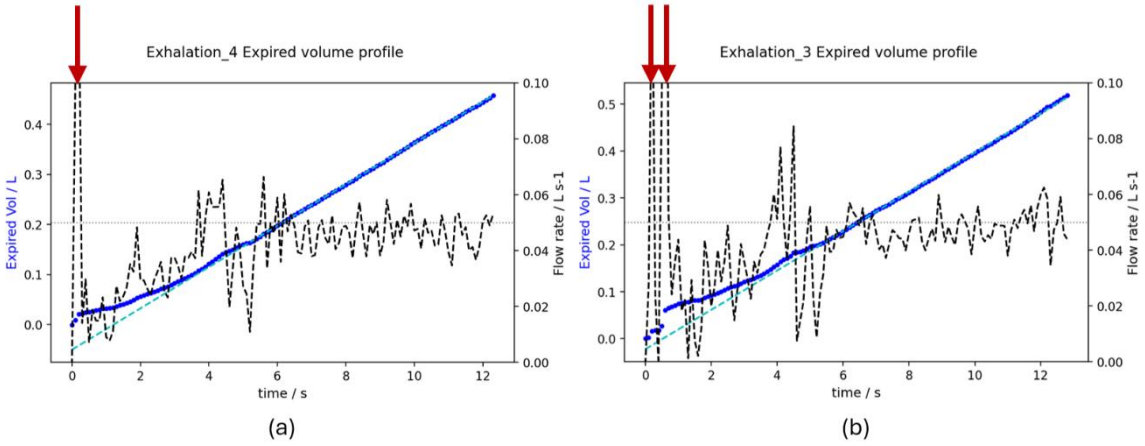


Figure 5.5 Examples of single and double overshoot. A Red arrow indicates an overshoot event. (a) a special exhalation with a single overshoot, (b) a special exhalation with double overshoots.

A single overshoot does not significantly affect the depth parameters, particularly in SpD mode, where speed variations are accounted for. However, when multiple overshoots occur, more significant diffusion is likely to arise. In the case of multiple overshoots, the slow exhalation period between two overshoots generates a gas segment with high NO concentration, causing significant axial diffusion to adjacent segments that contain very few NO molecules due to the overshoots. The model ignores the gas diffusion in its assumptions, leading to an inaccurately simulated NO expirogram.

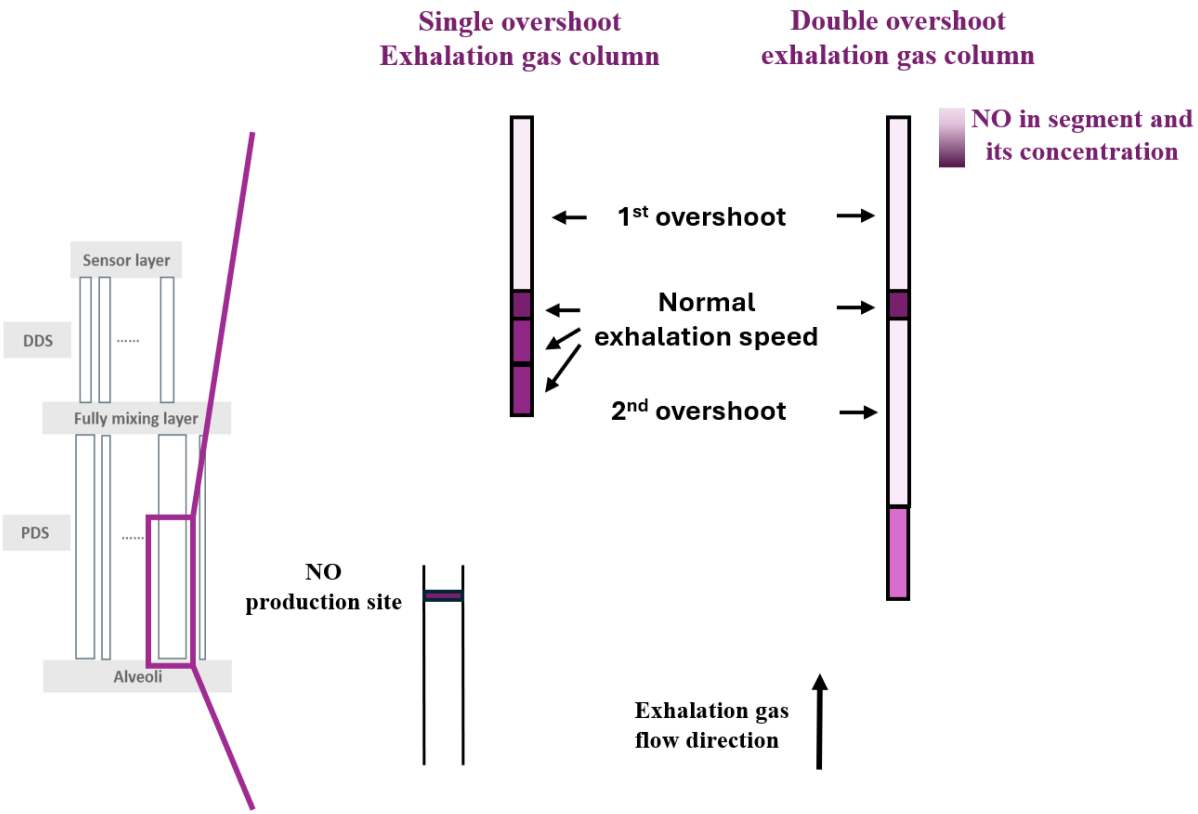


Figure 5.6 Gas columns from a single and double overshoot. The gas column is divided into time intervals of 0.1s. The length of each rectangular indicates the volume of the segment exhaled during that 0.1s. The purple colour represents the NO concentration, with darker shades indicating higher concentrations. In the single overshoot gas column, the segments at normal exhalation speed show similar NO concentrations. In the double overshoots gas column, the segments at normal exhalation speed show a significantly higher NO concentration compared to adjacent overshoot segments.

Figure 5.6 shows how double overshoots generate more severe violations of the convective flow assumption. In a single-overshoot gas column, the normal-speed exhalation segments have limited diffusion effects due to relatively uniform axial concentration gradients. Additionally, the diffusion between the overshoot-gas segment and normal-speed gas segment is diminished, as the diffusion and convection occur in the same direction. However, the double overshoots (right column of gas in **Figure 5.6)** create a 'sandwich' column, where two low-NO-concentration segments (lighter purple segments in **Figure 5.6**) enclose a high-NO-concentration segment (darker purple segment in **Figure 5.6**). The high-NO-concentration segment diffuses into the adjacent segments, particularly the following

segment (the second overshoot segment), violating the assumption that no axial diffusion occurs during gas transport.

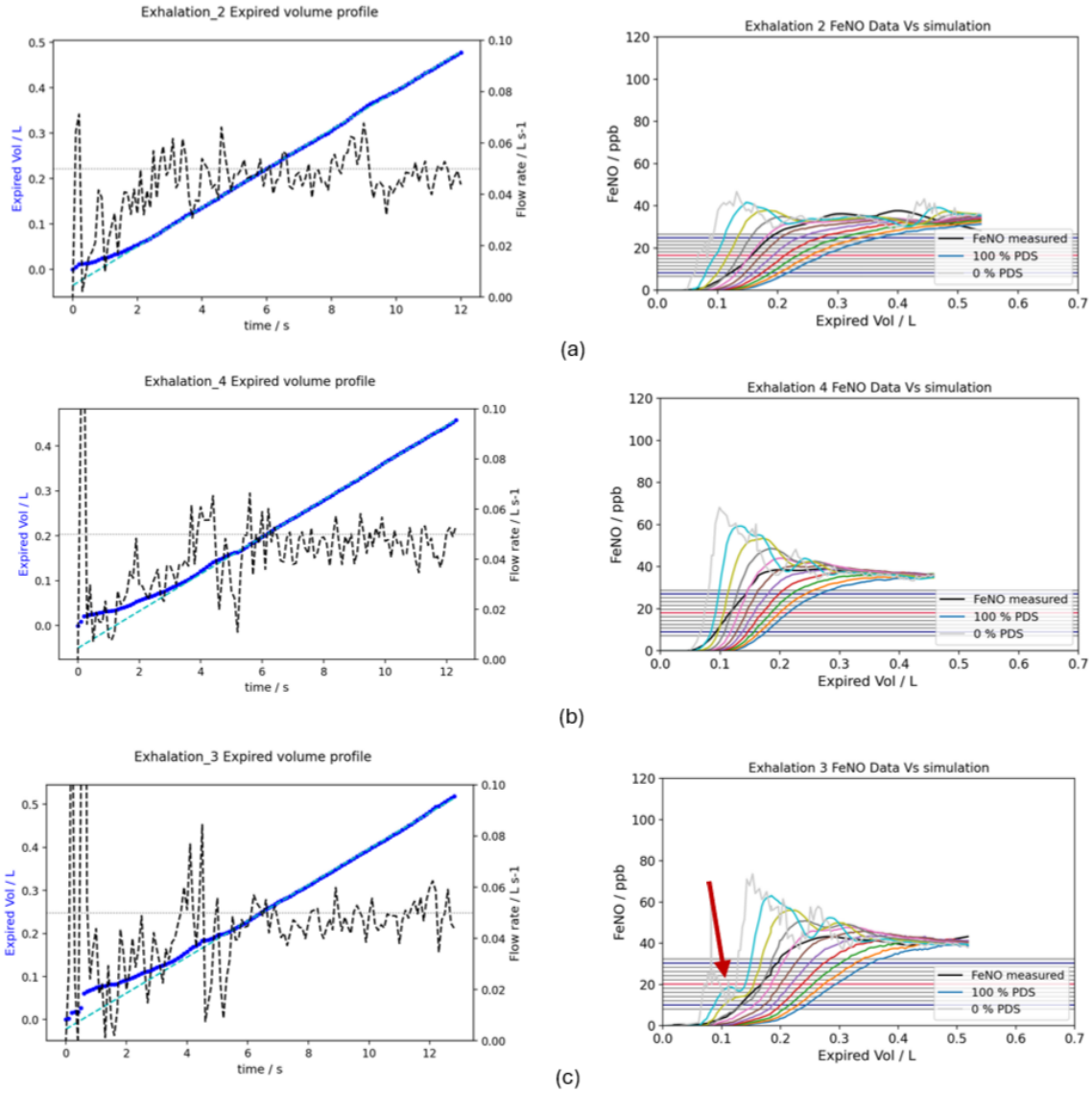


Figure 5.7 Demonstration of (a) exhalation without overshoot. The FeNO wallpaper(right) shows a smooth change in both the simulated and measured data; (b) exhalation with a single overshoot. Though there is one overshoot at the start of exhalation (left, a peak with speed over 0.1L/s), the FeNO wallpaper(right) still shows a smooth change in both simulated and measured data; (c) exhalation with multiple overshoots. With multiple overshoots, the simulated NO curve shows a 'bump' around 0.1-0.15L(red arrow in the right-handed figure, coloured curves), while the measured curve does not show a similar 'bump'(right-hand figure, black curve).

The influence of overshoots can be observed from the 'wallpaper' and measured NO profile. **Figure 5.7** presents three conditions: **(a)** no overshoot, **(b)** single overshoot and **(c)**

double overshoots. In double overshoots, shown in **Figure 5.7(c)**, there is a 'bump' (red arrow) in the simulated NO expirogram, indicating the simulated NO level forms a peak in the early phase. On the contrary, in the actual NO measured profile, the 'bump' disappears due to axial diffusion. In both the no-overshoot or single-overshoot conditions, there is no sign of a 'bump' in the simulated NO profile. Given the inconsistency introduced by multiple overshoots, breaths with multiple overshoots are excluded from the analysis.

5.1.2.3.2 Unstable expiration speed

During a participant's breathing through the RFD, a sudden loss of breath speed control may occur. The instability in exhalation speed may appear as a flow drop (in most cases, potentially triggering the release of the restrictive valve) or an overshoot (less common due to the restrictive valve) after achieving the target speed. **Figure 5.8** shows an example of instability in exhalation. In most cases, the unstable exhalation speed can be identified and excluded during real-time measurements. However, a routine secondary check is performed after measurement to ensure breath stability.

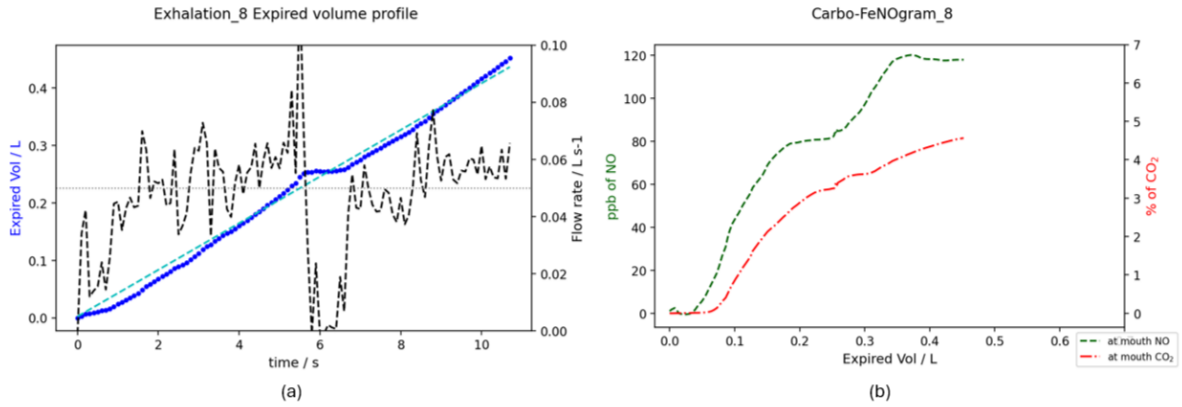


Figure 5.8 Demonstration of unstable exhalation flow. (a) The expired volume-time graph shows an unstable change of around 6s; (b) The same breath is represented as a NO/CO2 versus time graph, where a corresponding change in NO appears at around 0.3L. As the NO plateau is used to determine the NO production rate, unstable flow speed can affect NO concentrations. In this case, a slower exhalation speed led to an increase in NO concentration, resulting in an inaccurate estimation of the NO production rate.

5.1.2.3.3 Transition period between inhalation and exhalation

The NO concentration in airways is inversely proportional to the flow rate. The transition period between inhalation and exhalation determines how many NO molecules are retained in the dead space.

In real-time measurement, the flow-time profile is carefully monitored to detect and exclude any potential breath-hold. A breath-hold aggravates the back-diffusion into the alveolar space. Therefore, an immediate transition between inhalation and exhalation is expected in the special breath.

In post-measurement checks, early peaks are one of the signs of a prolonged transition period.

A prolonged transition period results in an early peak in the measured NO expirogram. In SpIn mode, as this mode cannot differentiate the underlying causes of early peaks, any measured NO expirogram that displays an early peak is excluded during quality control.

Conversely, the SpD mode considers the speed variations during exhalation. The 'wallpaper' can simulate the prolonged transition period, thereby incorporating an early peak in the simulated NO profile. As a result, the transition period does not influence the NO production depth in SpD mode.

5.1.2.4 Model fitting failure (Reason IV)

5.1.2.4.1 Quality of CO_2 fitting

The DSP model uses fitted outputs from the CCP to define a personalised dead space. CCP outputs are used to fit the measured CO_2 expirograms from a special breath, producing dead space volume correction (*dV*) for each breath. CCP fitting quality has been discussed in previous work and is beyond the scope of this thesis[187]. However, the fitting quality of CCP outputs to measured CO_2 expirograms should still be evaluated.

To quantify fitting accuracy, we used the average square of residuals per timepoint (*aveRes*) as a representative parameter. The *aveRes* is given by

$$aveRes = \Sigma(CO_2_data(k) - C_{s,CO_2}(k))^2 / kn, \quad (5.1)$$

where CO_2_data is an array of measured CO_2 concentration data, C_{s,CO_2} is an array of simulated CO_2 concentration data, k is the index ranging from 0 to $kn - 1$, kn is the number of time points used for fitting. The *aveRes* indicates the standardised residual between fitted and measured values.

A threshold value for *aveRes* is established based on a repeatability test involving 12 participants who each completed five visits within three weeks, generating a total of 801 breaths. This threshold is consistently applied in subsequent clinical studies.

Figure 5.9 gives the *aveRes* distribution in the repeatability test group. The threshold value is selected as 0.005, which excludes approximately 5% of the breath. **Figure 5.9(b)** illustrates a breath sample with an *aveRes* of 0.0047, demonstrating a boundary condition.

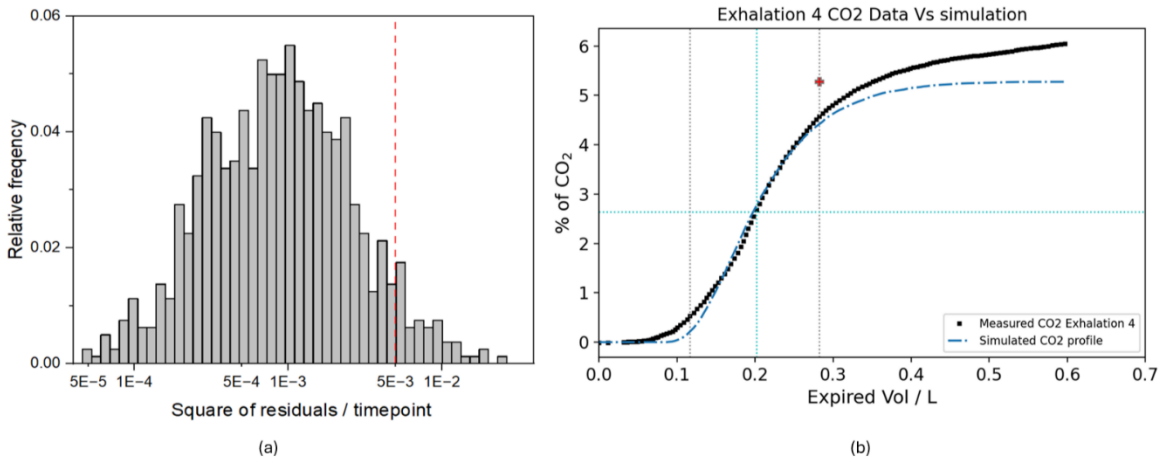


Figure 5.9 Histogram of *aveRes* distribution and an example of threshold fitting. (a) The red line indicates the threshold of 0.005. Approximately 95% of the values fall below this boundary. The x-axis is log-transformed. (b) An example of a CO_2 fitting profile with *aveRes* = 0.0047. The black line shows the measured CO_2 profile, the blue curve shows the fitted profile, and the red dot indicates the CO_2 plateau value. *aveRes*: the average square of residuals per time point.

However, the aveRes calculation favours slow initiation in breathing patterns, as it is an unweighted average across all time points. Phase I of exhalation typically shows lower

residuals since this period is free of CO_2. A prolonged phase I tends to produce a lower *aveRes* value, even when phase II remains unchanged. This indicates that a smaller *aveRes* is not sufficient to guarantee fitting quality. To avoid misjudgement, the following adjusted routine is applied in assessing CO_2 fitting quality:

(i) If *aveRes* ≥ 0.005, the breath is excluded.

(ii) If *aveRes* < 0.005, the assessment result depends on visual inspection of CO_2 fitting quality.

This routine ensures that all accepted breaths are well-fitted to the CO_2 profile.

5.1.2.4.2 Miscalculation on wallpaper

The method for defining the NO plateau value is outlined in Chapter 4. It generally provides a reliable fit for the data. However, an unstable breathing pattern can generate a NO expirogram that lacks a stable plateau, leading to an inaccurate estimation of the NO production rate. Such cases are identified by comparing the simulated 'wallpaper' with the measured NO expirogram. **Figure 5.10** presents an instance of an unstable NO expirogram, even when the CO_2 expirogram follows a stable curve. Similar cases are excluded from future analysis.

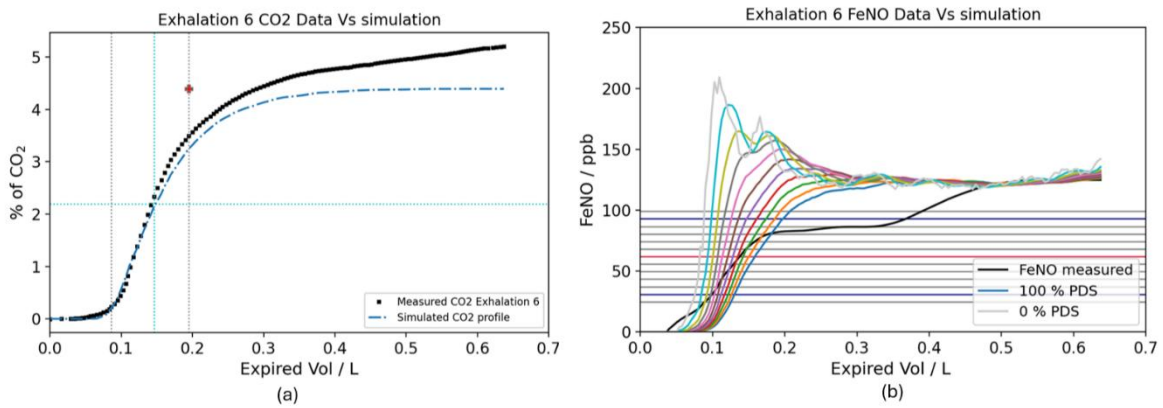


Figure 5.10 Unstable NO plateau value. (a) The CO2 versus expired volume plot indicates that the CO_2 is well-fitted. (b) The FeNO versus expired volume plot shows that the FeNO plateau value is unstable enough to support a constant NO production rate, which is essential for estimating NO production depth.

5.1.3 Quality assessment guidelines

Although the key factors are explained above, a practical framework is necessary for real-world application. To achieve this, I designed the quality assessment criteria comprising three parts: Real-time quality check, Measurement quality check and Model quality check(see **Table 5.1**). Each entry in this table is connected to one or more key factors introduced previously, providing a practical and structured system for quality assessment.

Table 5.1 Quality assessment criteria

Real-time quality check	
Too short an exhalation period to reach phase III ***Reason I***	The exhalation period is too short, preventing the CO_2 expirogram from reaching phase III.
Unstable pattern of flow ***Reason I, III***	Either a drop in flow that triggers restrictive valve intervention or an increase in flow exceeding 0.1L/s after reaching the target exhalation speed is considered an unstable pattern.
Measurement quality check	
Early rise pattern of NO expirogram ***Reason II***	It is determined by whether measured NO data lies to the left of 0% simulated NO expirogram.
Occurrence of early peak ***Reason II, III***	Early peak: A peak (NO concentration > 1.1* NO plateau value) occurs within the range of deadspace volume. It is identified by (1) whether the early peak exceeds the simulated data boundary in SpD mode. (2) whether an early peak occurs in SpIn mode.
Multiple overshoots ***Reason III***	Overshoot: a peak in the flow rate-time graph where the maximum flow rate ≥ 0.1L/s. It is identified by the presence of multiple overshoots during the exhalation period or by the presence of a ‘bump’ in simulated ‘wallpaper’.
Unstable pattern of flow ***Reason I, III***	Either a drop in flow that triggers restrictive valve intervention or an increase in flow exceeding 0.1L/s after reaching the target exhalation speed is considered an unstable pattern.
Model quality check	
CO_2 fitting quality ***Reason IV***	A breath with an *aveRes* less than 0.005 also passes the visual check.
Miscalculation on wallpaper ***Reason IV***	It is identified by the presence of an incorrectly estimated NO plateau value.

The Real-time quality check focuses on issues that can be visually identified during the measurements, with assistance from the real-time figures, including the flow-time profile, NO expirogram from the cavity and CO_2 expirogram. The Measurement quality check addresses problems arising during measurements but are not evident through real-time visual inspection and, therefore, requires additional calculation and model fitting. The Model quality check involves only model fitting and is independent of measurement. These checks are conducted sequentially, in Real-time, Measurement and Model. Any breath that fails an earlier check is excluded from further assessment.

As the table indicates, both visual inspection and quantitative quality checks are implemented. While a fully quantitative approach would facilitate automation, its development requires a significant amount of time and relies on validation using real-world data. As a result, a more feasible and effective strategy is adopted: a hybrid approach combining visual inspection and quantitative checks.

5.1.4 Retrieving NO depth parameters for each visit

After the selection of qualified breaths, there are often multiple qualified breaths during a single measurement by a participant. The median of each NO depth parameter is obtained from each measurement to increase the signal-to-noise ratio further. Finally, a value representing each NO depth parameter is obtained for each measurement.

5.1.5 Summary

The previous section provides a comprehensive introduction to quality control in the estimation of NO production depth parameters. The quality control framework consists of two parts: the key factors that can lead to failure in estimating NO depth parameters and a practical set of criteria for quality assessment. The first part explains why the quality is affected by these factors, while the second part provides an accessible tool to assess breath

quality. All subsequent data adhere to this framework to ensure they all meet the quality control standards for NO depth estimation.

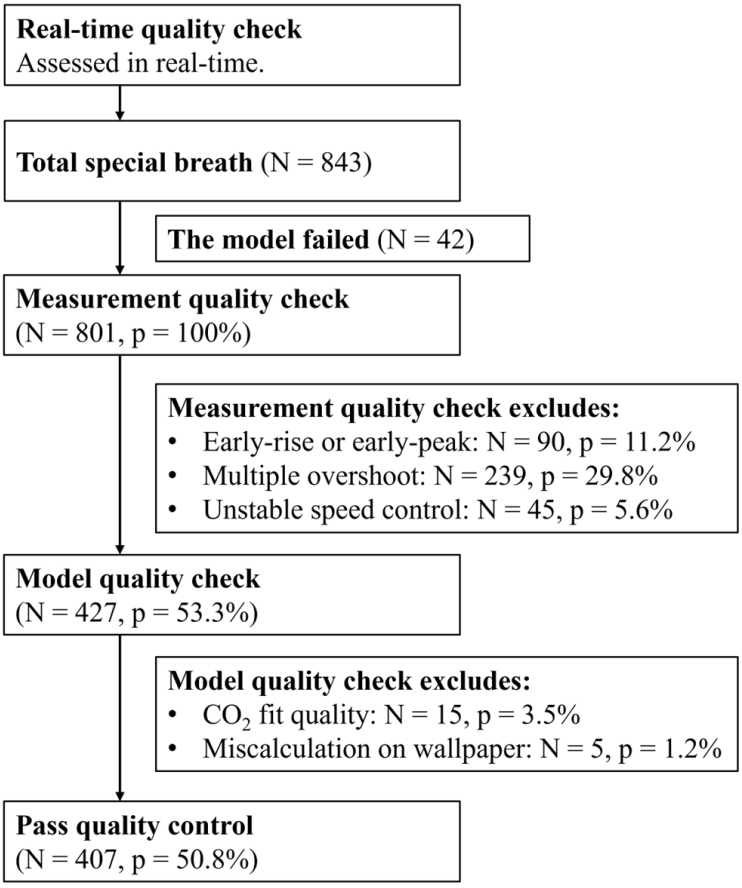


Figure 5.11 Quality check results for the repeatability dataset. N indicates the number of special breaths, and p indicates the percentage of these relative to the total number that entered measurement quality control.

Figure 5.11 illustrates an example of the application of this framework using a cohort of patients and their measurements, which were used to assess repeatability and reliability. N indicates the number of special breaths, and p represents the percentage of breaths relative to the total breath(N = 801). The number of excluded breaths during Real-time quality assessment is not recorded since they are evaluated during the measurement process. 801 out of 843 special breaths completed the model fitting and entered the quality assessment framework. In general, about 50% of breaths pass the quality check. These findings highlight why the RFD measurement protocol in Chapter 3 requires collecting at least seven special

breaths per visit, aiming to obtain at least three breaths that meet the quality assessment criteria.

5.2 Repeatability and reliability of NO depth parameters

The establishment of the quality control criteria marks the completion of constructing a framework for generating NO depth parameters from a single breath. A study of human participants is then conducted to evaluate the repeatability and reliability of these parameters across daily tests. Repeatability of NO depth parameters represents the consistency of these parameters when the same participant performs the tests across several visits, assuming the participant's lung physiology remains stable during this period. Reliability assesses whether the NO depth parameters can generate greater inter-individual variance than within-individual variance. Furthermore, a comparison is made between FeNO values obtained using the NIOX device and those obtained using the RFD to assess the consistency between these two FeNO measurement methods.

5.2.1 Methods

I conducted an observational study in which volunteers were required to visit the study site five times over three weeks. I undertook the research project under the ethics: Oxford Airway Study (OAS), 18/SC/0361. All participants have provided written informed consent.

5.2.1.1 Participants and protocol

I recruited six healthy participants (H group, subject ID: H1 to H6) and six patients with asthma (A group, subject ID: A1 to A6). The visit schedule is demonstrated in **Figure 5.12**.

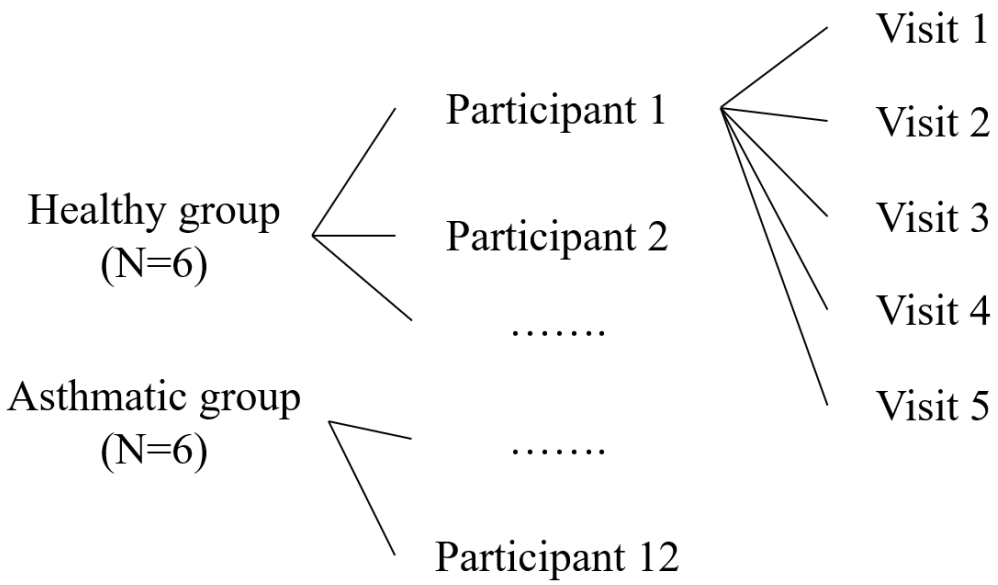


Figure 5.12 Visit schedule for repeatability test. Twelve participants were recruited, and each participant was scheduled to attend five repeated visits within three weeks.

For each visit, the protocol for participants' assessments is as follows:

(i) Fractional exhaled nitric oxide (FeNO, *NIOX, Sweden*).

(ii) Spirometry.

Parameters obtained include: Forced expiratory volume in one second(FEV_1), forced vital capacity (FVC), forced expiratory flow between 25% to 75% of FVC(FEF_{25-75}) and FEV_1/FVC ratio.

(iii)Standard RFD measurement, as described in Chapter 3.

Parameters obtained include:

(a) Speed-dependent (SpD) mode: the depth range between the 25th and 75th percentiles of the FeNO plateau (IQR_{SpD}), the depth at which the FeNO value reaches the 25th percentile of its plateau value ($Q25_{SpD}$), the depth at which the FeNO value reaches the 50th percentile of its plateau value ($Q50_{SpD}$), and the depth at which the FeNO value reaches the 75th percentile of its plateau value ($Q75_{SpD}$).

(b) Speed-independent (SpIn) mode: IQR_{SpIn}, $Q25_{SpIn}$, $Q50_{SpIn}$ and $Q75_{SpIn}$.

(4) Standard CCP measurements, as described in Chapter 2.

Parameters obtained include: the functional residual capacity (FRC), deadspace volume (V_D), the standard deviation for the natural logarithm of the standardised lung compliance($\sigma \ln C_L$), the standard deviation for the standardised volume of deadspace(σV_D).

5.2.1.2 Comparison of NIOX FeNO measurement and RFD FeNO plateau measurements

To evaluate the consistency, I compared the two methods of FeNO measurement: the NIOX and RFD measurement. The procedures used to obtain the FeNO value differ between the two methods. The NIOX device provides a FeNO value based on the last 3-second window during a 10-second exhalation, while the RFD measures the FeNO plateau value from the last 25% of the exhaled volume in each special exhalation. Additionally, the RFD provides a FeNO plateau reading for each breath, while NIOX only provides one FeNO value per visit. To enable a comparison between the two methods, I obtained the RFD FeNO values using the same approach for NO depth parameters by computing the median of all qualifying special breaths in each visit.

5.2.1.3 Repeatability and reliability of NO depth parameters

I evaluated the repeatability by Coefficient of Variation (CV) and quantile Coefficient of Dispersion (CD).

Coefficient of Variation (CV) calculations are,

$$CV = standard\ deviation / mean. \tag{5.2}$$

Quartile Coefficient of Dispersion (CD) calculations is,

$$CV = (Q3 - Q1) / (Q1 + Q3). \tag{5.3}$$

where Q1 and Q3 are 1st quartile and 3rd quartile.

In NO depth parameters, IQR of depth may get a negative value, and I discussed the reason in the discussion section. To make the test method robust for the IQR test, I adjusted

the calculation of CV and CD in IQR test. I retrieved the absolute CV and CD for IQR parameter to make it comparable, where

$$CV_{abs} = standard\ deviation / |mean|. \quad (5.4)$$

and

$$CD_{abs} = (Q3 - Q1) / |Q1 + Q3|. \quad (5.5)$$

Lower *CV* and *CD* values (or CV_{abs} and CD_{abs}) indicate relatively less dispersion of parameters from the same patients across different visits. One disadvantage of CV is that it becomes sensitive to small changes when the mean is close to zero, whereas the CD is less sensitive. So, I present both test results, especially for IQR, which has a high possibility of getting a near-zero value.

I evaluate the reliability of each parameter using Analysis of Variance (ANOVA) and Intraclass Correlation Coefficient (ICC),

ANOVA enables the separation of variance sources at different levels. This approach compares the variance in two levels: between-group (BG, whether the participants have asthma) variance to within-group (WG) variance and between-participants (BP) variance to within-participants (WP) variance. $F_{(BG:WG)}$ represents the variance ratio for BG to WG, and $F_{(BP:WP)}$ represents the variance ratio for BP to WP,

$$F_{(BG:WG)} = BG\ variance / WG\ variance, \quad (5.6)$$

And

$$F_{(BP:WP)} = BP\ variance / WP\ variance. \quad (5.7)$$

Intraclass Correlation Coefficient (ICC) is a statistical parameter used to quantify the similarity among individuals in the same group. It ranges from 0 to 1 and is calculated as

$$ICC = \sigma^2_i / (\sigma^2_i + \sigma^2_\varepsilon), \quad (5.8)$$

where σ^2_i is random effect variance, σ^2_ε is the residual variance.

ICC is interpreted as[188]:

ICC < 0.4, poor reliability,

ICS between 0.4 to 0.49, fair reliability,

ICC between 0.6 to 0.74, good reliability,

ICC between 0.75 to 1.0, excellent reliability.

5.2.1.4 Statistical analysis

The student-t test (unpaired or paired determined by whether the data is related) is applied if the data is normally distributed. Mann-Whitney (unpaired) or Wilcoxon Signed Rank test (paired) is applied for non-normally distributed data. In correlation analysis, Spearman correlation is used. I used OriginPro 2024(v10.1.0.178) and R language (v4.3.2) for statistical analysis.

5.2.2 Results

5.2.2.1 Participants demographic data

Table 5.2 presents the basic characteristics of the participants. In asthmatic patients, the GINA step ranged from I to V, including patients receiving biologics(anti-IL4Rα) treatment. All patients were in a stable condition during visits.

Table 5.2 Demographic characteristics

ID	Sex, female (%)	Age /yr, mean ± SD	BMI /kg m^{-2} , median(IQR)	FeNO NIOX /ppb, mean ± SD	GINA step
H1	M	34	25.2	43 ± 4	-
H2	M	30	24.9	41 ± 5	-
H3	M	25	20.7	39 ± 3	-
H4	M	27	20.2	62 ± 12	-
H5	F	23	19.2	31 ± 5	-
H6	M	25	23.5	55 ± 6	-
A1	M	28	23.6	85 ± 6	I
A2	F	67	26.4	48 ± 4	V*
A3	F	47	33.7	79 ± 10	V
A4	M	62	31.2	61 ± 16	V
A5	M	73	25.0	83 ± 6	V*
A6	M	53	25.6	50 ± 11	III
H group	1(17%)	27 ± 4	22.1 (20.0, 24.9)	45 ± 11	-
A group	2(33%)	55 ± 16	26.0 (24.7, 31.8)	68 ± 17	-
Total	3(25%)	41 ± 18	24.9 (21.4, 26.2)	56 ± 18	-

* anti-IL4Rαreceiver. GINA: global initiative in asthma. ACQ5: asthma control questionnaire. FeNO: fractional exhaled nitric oxide. BMI: body mass index.

5.2.2.2 Correlation of FeNO value measurements between NIOX and RFD

I evaluated the consistency between two measurements of FeNO value by conducting a Spearman correlation. It gave a strong correlation between two FeNO values. The Spearman correlation coefficient was 0.85, as illustrated in **Figure 5.13(a)**.

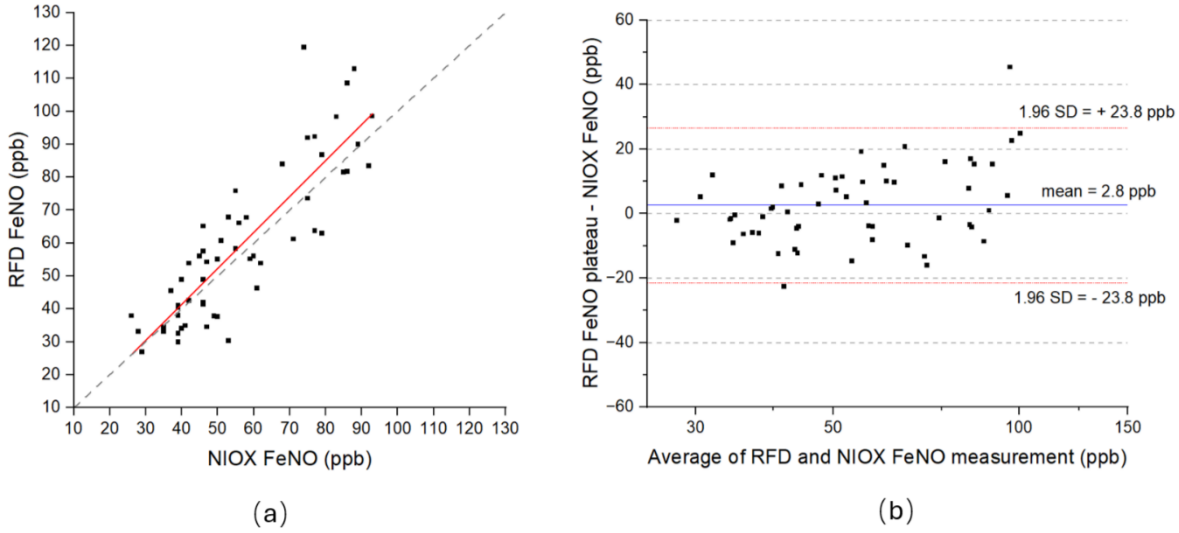


Figure 5.13 (a) Correlation between FeNO values between two measurement methods: NIOX and RFD. Red line: linear regression line. (b) FeNO differences between the two methods in each participant (Bland-Altman plot). Mean difference = 2.8 ppb (blue horizontal line), confidence interval = ± 21.0 ppb (red horizontal line). **RFD**: rapid FeNO device. Grey dashed horizontal line: diagonal reference line.

Figure 5.13(b) presents the FeNO differences between the two methods. The average bias between the two measurements was 2.8 ppb, with a 95% confidence interval of ± 23.8 ppb. These results suggested that the two FeNO measurement methods are consistent. The RFD methods provided a valid FeNO value reading.

5.2.2.3 Lung physiology of participants during the test period

Data on physiology and biomarker for each individual are shown in **Table 5.3**, which demonstrates that each participant's lung physiology remained stable during the test period. FEV_1% and σlnC_L remained stable over time, as demonstrated by CV values below 10%. As expected, FeNO displayed greater CV and CD values across visits compared to FEV_1% and σlnC_L while still showing good repeatability. Furthermore, measurements from NIOX and RFD were consistent. All parameters showed significantly high $F_{(BG:WG)}$ and $F_{(BP:WP)}$ as well as ICC values, indicating good reliability.

Table 5.3 Physiological parameters and FeNO in each individual.

Subject	FEV_1 % pred.	σlnC_L	FeNO NIOX /ppb	FeNO RFD /ppb	ΔFeNO /ppb
H1	110 ± 3	0.37 ± 0.03	43 ± 4	34 ± 3	-9 ± 3
H2	100 ± 5	0.39 ± 0.02	41 ± 5	41 ± 4	0 ± 5
H3	99 ± 2	0.34 ± 0.04	39 ± 3	44 ± 9	5 ± 6
H4	113 ± 3	0.39 ± 0.01	62 ± 12	60 ± 5	-2 ± 10
H5	97 ± 3	0.48 ± 0.05	31 ± 5	33 ± 4	1 ± 7
H6	102 ± 2	0.47 ± 0.05	55 ± 6	63 ± 11	8 ± 11
Mean	104	0.40	45	46	1
CV	3%	8%	14%	15%	-
CD	1%	5%	9%	6%	-
A1	72 ± 7	0.47 ± 0.05	85 ± 6	91 ± 12	6 ± 15
A2	56 ± 6	0.84 ± 0.05	48 ± 4	58 ± 4	10 ± 6
A3	105 ± 5	0.54 ± 0.02	79 ± 10	91 ± 18	12 ± 20
A4#	66 ± 2	0.70 ± 0.05	61 ± 16	44 ± 17	-17 ± 5
A5	71 ± 7	0.65 ± 0.08	83 ± 6	96 ± 10	13 ± 9
A6	96 ± 3	0.44 ± 0.03	50 ± 11	48 ± 10	-2 ± 9
Mean	78	0.61	68	71	4
CV	7%	8%	14%	18%	-
CD	4%	5%	11%	13%	-
ANOVA					
$F_{(BG:WG)}$	9.1*	9.4*	7.0*	6.1*	-
$F_{(BP:WP)}$	48.1***	32.3***	15.8***	17.4***	-
ICC	0.947	0.924	0.833	0.839	-

ΔFeNO represents the difference between RFD and NIOX measurements. CV: coefficient of variation, calculated as the average of individual variance. CD: Coefficient of Dispersion, calculated as the average of individual CD. ICC: intraclass correlation coefficient. Errors are shown as ±1SD. #CV_{abs} (absolute CV) or CD_{abs} (absolute CD) are used. * p<0.05, **p<0.01, ***p<0.001.

5.2.2.4 Repeatability and reliability of NO depth parameters

Figure 5.14 presents the NO depth measurement of each participant. Notably, the two modelling modes, SpD and SpIn, could produce divergent NO depth parameters. For example, in the H1 participant, the IQR differed substantially between SpD and SpIn modes, 40% vs 7% PDS, respectively. The A4 participant exhibited a negative IQR, which might reflect model limitations discussed later.

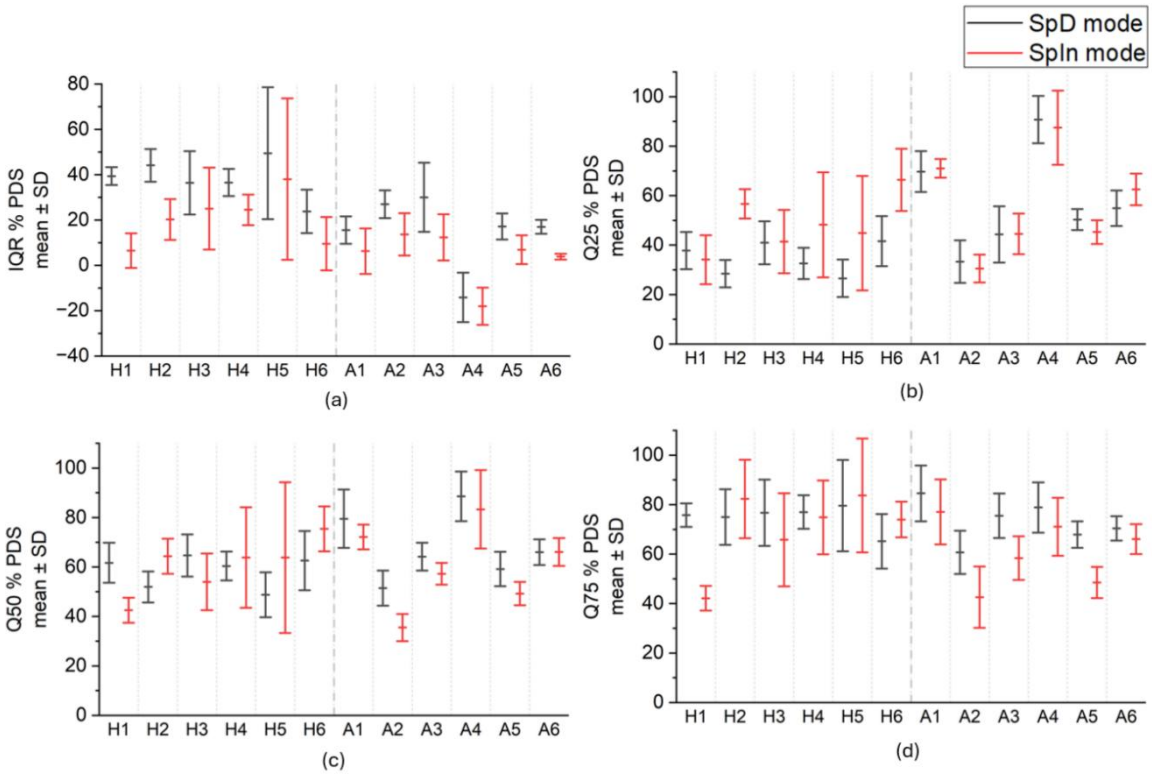


Figure 5.14 Mean (dot) and standard deviation (error bar) of NO depth parameters for each participant.(a) IQR, (b) Q25, (c) Q50 and (d) Q75.

Table 5.4 demonstrates the repeatability and reliability of NO depth parameters.

Based on CV and CD values, the SpD mode generally demonstrates better or comparable repeatability to the SpIn mode, particularly in the healthy group. CV values of Q25, Q50 and Q75 in SpD mode were below 20%, whereas the CV of IQR_{SpD} exceeded 20% but remained lower than that of IQR_{SpIn}.

In evaluating the reliability of NO depth parameters, the SpD mode generally performs better than the SpIn mode. Except for $Q75_{SpD}$, ANOVA tests revealed that all remaining parameters, regardless of generation mode, were capable of differentiating between participants, as demonstrated by $F_{(BP:WP)}$ values. However, $F_{(BG:WG)}$ values indicated that only IQR_{SpD}, IQR_{SpIn} and $Q25_{SpD}$ demonstrated the ability to differentiate disease conditions. In terms of ICC, the SpD mode showed higher values for IQR, Q25 and Q50 parameters, all of which had ICC $\geq$ 0.6.

While the $Q75_{SpD}$ appeared to have low reliability, its repeatability remained strong, supported by CV and CD values (both ≤ 20%), suggesting that its lower reliability potentially results from the parameter being consistently stable across participants and their health status.

Table 5.4 NO depth parameters in each individual and related tests.

Subject	IQR		Q25		Q50		Q75	
	IQR_{SpD}	IQR_{SpIn}	$Q25_{SpD}$	$Q25_{SpIn}$	$Q50_{SpD}$	$Q50_{SpIn}$	$Q75_{SpD}$	$Q75_{SpIn}$
H1	39.4±3.9	6.5±7.6	37.8±7.5	34.1±9.9	61.7±8.1	42.5±5.0	75.8±4.8	42.1±5.0
H2	44.1±7.2	20.3±9.0	28.4±5.5	56.7±5.9	52.0±6.3	64.3±7.1	75.0±11.3	82.3±15.9
H3$	36.4±14.0	25.0±18.1	41.0±8.7	41.4±12.8	64.6±8.5	54.0±11.5	76.7±13.4	65.8±18.8
H4	36.5±6.0	24.5±6.8	32.6±6.3	48.2±21.2	60.4±5.9	63.8±20.3	77.0±6.8	74.9±14.9
H5	43.4±28.7	33.8±32.3	26.3±6.6	46.4±20.3	46.8±9.1	64.0±26.4	72.5±22.5	80.8±21.0
H6	24.8±10.4	8.2±12.5	44.9±6.9	69.2±11.8	67.4±2.8	77.5±8.3	69.4±4.3	75.0±7.6
Mean	37.4	19.7	35.2	49.3	58.8	61.0	74.4	70.2
CV	38%	86%	20%	30%	12%	25%	16%	21%
CD	22%#	36%#	5%	8%	6%	11%	9%	12%
A1$	15.6±6.0	6.3±10.0	69.7±8.2	71.0±3.7	79.5±11.8	72.1±5.0	84.6±11.3	77.0±13.2
A2	27.0±6.2	13.7±9.4	33.3±8.6	30.5±5.6	51.5±7.1	35.5±5.5	60.7±8.8	42.6±12.4
A3	30.0±15.3	12.4±10.2	44.3±11.4	44.5±8.2	64.2±5.6	57.2±4.4	75.5±9.0	58.4±8.8
A4$	-14.1±10.9	-18.0±8.2	90.7±9.6	87.5±15.0	88.6±10.0	83.3±15.8	78.9±10.2	71.1±11.7
A5	17.2±5.8	6.9±6.4	50.3±4.3	45.3±4.8	59.2±7.0	42.5±5.0	67.9±5.4	48.5±6.3
A6	17.0±3.1	3.8±1.3	54.9±7.2	62.5±6.4	66.0±5.2	64.3±7.1	70.4±4.9	66.1±6.1
Mean	15.4	4.2	57.2	56.9	68.1	60.6	73.0	60.6
CV	44%	84%	15%	14%	12%	13%	12%	17%
CD	27%#	62%#	8%	8%	6%	7%	8%	11%
ANOVA								
$F_{(BG:WG)}$	10.1**	5.3*	5.8*	0.2	1.6	0.1	0.4	1.8
$F_{(BP:WP)}$	3.8***	2.8**	15.4***	8.7***	9.4***	6.4***	1.6	5.8***
ICC	0.600	0.399	0.847	0.628	0.687	0.521	0.098	0.522

$Sample size = 4. #$CV_{abs}$ (absolute CV) or CD_{abs} (absolute CD) are used. IQR: the depth range between the 25% and 75% quantile of the FeNO plateau. Q25: the depth at which the FeNO value reaches the 25% quantile of its plateau value. Q50: the depth at which the FeNO value reaches the 50% quantile of its plateau value. Q75: the depth at which the FeNO value reaches the 75% quantile of its plateau value. SpD: speed-dependent mode. SpIn: speed-independent mode. CV: coefficient of variance, calculated as the average of individual variance. CD: Coefficient of Dispersion, calculated as the average of individual CD. ICC: intraclass correlation coefficient. Errors are shown ±1SD. * p<0.05, **p<0.01, ***p<0.001.

5.2.3 Discussion

In this study, I first compared the FeNO plateau measured with the RFD with a commercial device, NIOX. Then, I scheduled repeated visits for participants to assess the repeatability and reliability of NO depth parameters.

The two FeNO measurement methods showed a strong correlation with each other. However, the two methods were distinct in their data collection and calculation. The primary purpose of NIOX is to measure the FeNO value. In contrast, the RFD is designed to estimate the location of NO production. NIOX calculates the FeNO value based on the last 3-second window in 10-second exhalation, while the RFD uses the last 25% of exhalation volume. In addition, the participants are required to wear a nose clip in RFD to avoid nasal contamination during inhalation (detailed in Chapter 3), while this is not required with the NIOX device. These protocol differences may contribute to discrepancies in final FeNO values.

Baseline physiological parameters confirmed that the participants were in stable condition during the five visits. All of them had spirometry and CCP results with CVs below 10%. Compared to Mountain *et al.*'s [187] study, which involved 18 participants, including young, healthy adults, older healthy adults and patients with chronic obstructive pulmonary disease (COPD), they reported that the CV for σlnC_L is ~8% across all groups. Our study has demonstrated a CV value for σlnC_L similar to that reported by Mountain *et al.*, indicating participant stability.

The FeNO measured by both devices gave a higher CV and CD compared to FEV_1% predicted and σlnC_L, which aligns with expectations that FeNO is more variable than other parameters. The variability is influenced by factors such as circadian rhythms and exogenous exposures[189-191].

The primary objective of this study was to assess whether the NO depth parameters were sufficient to distinguish between inter-individual variance and within-individual variance.

The results indicated that nearly all parameters demonstrated good repeatability and reliability. In particular, IQR_{SpD}, IQR_{SpIn} and $Q25_{SpD}$ demonstrate the ability to distinguish both inter-individual and differences across disease status. Furthermore, $Q25_{SpD}$ showed an ICC value comparable to that of commercial FeNO measurements, indicating it is a highly stable parameter. This study suggests that NO depth parameters were sufficient to detect biological differences among participants.

Although several NO depth parameters exhibited lower repeatability or reliability compared to established lung function measurements such as FEV_1 % predicted and σlnC_L, several factors may account for this:

(i) FeNO is a variable parameter influenced by multiple exogenous factors. It is reasonable to expect that the location of NO production in the conducting airways will also be affected by these factors. However, additional data are required to investigate this hypothesis.

(ii) NO depth estimation reflects the functional distribution of NO production, which is expected to be less stable than structure-based parameters (e.g. FEV_1%).

(iii) Lastly, this method is in a very early stage of development. There are several factors that could be optimised, including consideration of gas diffusion and improvements of the breathing hardware. However, given their proven repeatability and reliability, the next priority is to apply the test in a clinical setting to retrieve NO depth parameters and evaluate their application in disease detection and management.

I will continue to report all four depth parameters in the following Chapters. Even though $Q75_{SpD}$ may be similar among participants, leading it to show limited reliability, it still holds clear physiological meaning. Moreover, Q75 is necessary for calculating the IQR, which reveals the spread of the NO production region in the conducting airways. Given the limited

sample size and heterogeneity of the individual conditions in this study, all four parameters will be reported in clinical applications to further evaluate their value in disease assessment.

In one of the participants, IQR was negative, reflecting a limitation of this model. IQR is intended to represent the span of NO production regions. However, the assumptions in the DSP model may lead to negative IQR values. In the 'wallpaper' simulations, the DSP assumes that NO was produced at a fixed percentage of airways, whereas alternatively, it may occur at a fixed distance from the mouth. Under this alternative condition, the assignment of NO production sites proportionally cross airway pipes may result in a negative IQR. However, the CCP outputs do not contain an index describing the length of each pipe, making it challenging to recover a simulated NO expirogram based on distance from the mouth. On the biological side, several factors may underlie this limitation: some individuals may exhibit greater asymmetry in airway length, age-related distal airways collapse or mucus plug obstruction in distal airways[192, 193].

5.3 Determination of the DSP mode for future studies

To determine which mode should be used in further analysis, I summarised a comparison in **Table 5.5**. The comparison indicates that the SpD mode provides more insights for quality control and is more repeatable and reliable. Therefore, in future clinical studies, I will employ SpD modes to generate the NO depth parameters.

Table 5.5 Comparison between SpD and SpIn modes

	SpD mode	SpIn mode
Quality control		
Early rise due to nasal contamination.	A more accurate NO profile simulation increases sensitivity to the early rise.	Less sensitive to early rise due to ignoring speed variation.
Early peak occurrence	SpD mode simulates wallpaper using a speed profile and is unaffected by early peaks.	SpIn simulates NO profile at a constant speed. All early peaks require exclusion.
Overshoots	SpD mode adapts well to single overshoot and its 'wallpaper' reveals signs of multiple overshoots.	SpIn has limited ability to adapt to a single overshoot and no signs indicate the presence of multiple overshoots.
Repeatability	SpD mode generally shows lower CV and CD compared to SpIn mode.	
Reliability		
IQR, Q25, Q50	SpD mode shows higher F values and ICCs, with the F value and ICC of Q25 comparable to those of commercial FeNO measurements.	
Q75	The $F_{(BP:WP)}$ is less than one in the SpD mode, possibly due to Q75 being relatively fixed across individuals.	
Clinical significance	IQR and Q25 differentiate disease status.	Only IQR can differentiate.

5.4 Conclusion

This Chapter presents the quality assessment framework for NO depth measurements and the findings from repeatability and reliability tests. The quality assessment framework is established based on four core factors that lead to failure in generating accurate NO depth parameters. From these four factors, I developed a set of practical quality assessment criteria to facilitate implementation. The repeatability and reliability tests support the conclusion that the overall methodology can provide biological information among participants. Furthermore,

this Chapter summarises the advantages and disadvantages of the two modes in the DSP model and selects the SpD mode for future analysis.

Chapter 6

Novel measurement for locating the production location of nitric oxide (NO) in conducting airways - Clinical studies

In the previous three Chapters, I introduced the methodology of NO depth parameters estimation, including hardware, software and quality assessment, and also presented the findings from repeatability/reliability tests to support further clinical studies. This Chapter focuses on the implementation of NO depth measurements in various clinical scenarios to investigate the potential biological and clinical associations between NO depth parameters and clinical features in patients with asthma, and to examine the alterations in NO depth parameters following clinical interventions.

This Chapter begins with a cross-sectional study of healthy volunteers to establish reference values that reflect NO distribution in the conducting airways.

In patients with asthma, a cross-sectional study was conducted to detect the differences in NO depth parameters between disease severities, comparing treatment-naïve patients with mild asthma (TN group) to those with difficult-to-treat asthma receiving high-dose inhaled corticosteroids (ICS), referred to as the HD group. Two subsequent follow-up studies were

conducted based on this grouping: a portion of the TN group initiated low-dose ICS for two months, and a portion of the HD group began injection of anti-IL5/5R biologics for four doses. These follow-up studies aim to detect the impact of treatment (ICS or anti-IL5/5R biologics) on NO depth measurements in patients with asthma.

Lastly, I compared the patients before and after the administration of bronchodilators (BD) to evaluate the effects of salbutamol on NO depth parameters.

6.1 Methods

In this Chapter, participant recruitment primarily followed the standardised protocol, which is detailed below. Any deviations from this protocol will be mentioned separately.

All studies were conducted under ethical approval: Oxford Airway Study (OAS, Ref: 18/CS/0361). All participants provided written informed consent before participating in the study.

6.1.1 Study protocol

At each research visit, participants underwent the following assessments:

(i) Asthma control questionnaire (ACQ-5, only for asthmatic participants)

(ii) Fractional exhaled nitric oxide (FeNO, *NIOX, Sweden*)

(iii) Spirometry.

Parameters obtained include: the forced expired volume in 1s (FEV_1), the forced vital capacity (FVC), the expiratory flow between 25% and 75% of vital capacity (FEF_{25-75}%) and FEV_1/FVC ratio.

(iv) Standard RFD measurements, as described in Chapter 3. The NO depth simulation mode used was SpD, as detailed in Chapter 5.

Parameters obtained include: the depth range between the 25^{th} and 75^{th} percentiles of the FeNO plateau (IQR), the depth at which the FeNO value reaches the 25^{th}

percentile of its plateau value (Q25), the depth at which the FeNO value reaches the 50th percentile of its plateau value (Q50) and the depth at which the FeNO value reaches the 75th percentile of its plateau value (Q75).

(v) Standard CCP measurements, as described in Chapter 2.

Parameters obtained included: the functional residual capacity (FRC), deadspace volume (V_D), the standard deviation for the natural logarithm of the standardised lung compliance($\sigma \ln C_L$), the standard deviation for the standardised volume of deadspace(σV_D).

(vi) Blood collection for measuring full blood count.

6.1.2 Statistical analysis

For normally distributed continuous variables, two groups were compared by Student-t tests (paired or unpaired depending on related or unrelated samples). If the variable was not normally distributed, Mann-Whitney U test (unpaired) or Wilcoxon Signed Rank test (paired) was used. Proportions were compared using Chi-square test or Fisher's exact test, depending on the sampling size. Spearman correlation was used to assess the correlation between various parameters. The correlation analysis between CCP and NO depth parameters was not conducted, as CCP parameters were required to derive NO depth parameters. Any exceptions will be reported separately.

6.2 NO depth parameters in the Healthy (control) group

This section focuses on the NO depth parameters in healthy volunteers not diagnosed with chronic airway diseases but with elevated FeNO levels. Furthermore, I assess the correlation between NO depth parameters and other physiological parameters.

6.2.1 Participants

In this observational study, I recruited 24 healthy adults with elevated FeNO (≥ 25ppb) but without a diagnosis of asthma or any other chronic respiratory disease for a single research visit.

6.2.2 Results

6.2.2.1 Basic characteristics of healthy volunteers

Table 6.1 demonstrates the baseline characteristics of this group. There was an unbalanced gender ratio in this group, with more males than females. FeNO values were moderately elevated, and extremely high FeNO values (~ 100ppb) were rarely seen in healthy individuals.

Table 6.1 Baseline characteristics

	Healthy group
Number	24
Age /yr, mean ± SD	38 ± 18
Gender, Female (%)	4 (17%)
BMI /kg · m^{-2}, median (IQR)	23.0 (20.7, 25.6)
FeNO /ppb, median (IQR)	43 (33, 49)
BEC /10^{9}·L^{-1}, median (IQR)*	0.21 (0.13, 0.36)

* Limited sample size: 12. BMI: Body mass index, FeNO: fractional exhaled nitric oxide, BEC: blood eosinophil count.

6.2.2.2 Physiological parameters

The results of spirometry and CCP are listed in **Table 6.2**. All physiological and CCP parameters were within the normal range.

Table 6.2 Physiological parameters of healthy participants

Group	Healthy group (N = 24)
FEV_1 /L, mean ± SD	3.81 ± 1.04
FEV_1 % pred., mean ± SD	95.6 ± 11.9
FEV_1 z score., mean ± SD	-0.33 ± 0.91
FVC /L, mean ± SD	4.85 ± 1.18
FVC % pred., mean ± SD	99.6 ± 13.4
FVC z score, mean ± SD	-0.04 ± 1.00
FEV_1/FVC /%, mean ± SD	78.5 ± 8.5
FEV_1/FVC z score, mean ± SD	-0.41 ± 1.06
FEF_{25-75} % pred, mean ± SD*	83.3 ± 22.9
FEF_{25-75}% z score, mean ± SD*	-0.63 ± 0.94
σlnCL, mean ± SD	0.51 ± 0.09
σlnCL z score, mean ± SD	0.21 ± 0.87

* Limited sample size: 12. FEV_1: forced expiratory volume in 1 second, FVC: forced vital capacity, FEF_{25-75}%: forced expiratory flow between 25% and 75% of forced vital capacity, σlnCL: the standard deviation of lognormal distributions for normalised alveolar compliance.

6.2.2.3 NO Depth parameters in healthy volunteers

The NO depth parameters in the control group are shown in **Table 6.3**.

Table 6.3 NO depth parameters

Group	Healthy group (N = 24)
IQR % PDS, mean ± SD	21.8 ± 8.7
Q25 % PDS, mean ± SD	33.8 ± 20.1
Q50 % PDS, mean ± SD	48.3 ± 19.7
Q75 % PDS, mean ± SD	56.4 ± 19.9

IQR: interquartile range of FeNO plateau corresponding depth, Q25: the depth at 25% quantile of FeNO plateau value, Q50: the depth at 50% quantile of FeNO plateau value, Q75: the depth at 75% quantile of FeNO plateau value.

6.2.2.4 Correlations between depth parameters and other parameters

Table 6.4 demonstrates the correlations between depth parameters and other parameters.

The IQR was negatively correlated with age ($\rho = -0.415$, $p = 0.044$). Q25 showed a

nonsignificant trend toward correlation with FeNO (ρ = 0.345, p = 0.099). No other statistically significant correlations were observed.

Table 6.4 Correlation analysis between NO depth and other parameters

		IQR	Q25	Q50	Q75
Age /yrs	ρ	-0.415	-0.111	-0.263	-0.306
	p-value	**0.044**	0.607	0.214	0.146
Gender	ρ	-0.162	0.000	-0.097	-0.048
	p-value	0.451	1.000	0.652	0.822
BMI /kg·m^{-2}	ρ	-0.107	0.239	0.178	0.208
	p-value	0.620	0.261	0.405	0.329
FeNO /ppb	ρ	-0.157	0.345	0.327	0.258
	p-value	0.464	0.099	0.119	0.223
BEC /10^9 L^{-1} *	ρ	0.245	-0.259	-0.168	-0.266
	p-value	0.443	0.417	0.602	0.404
FEV_1 % pred.	ρ	-0.037	-0.056	-0.039	-0.016
	p-value	0.881	0.819	0.875	0.949
FEV_1 z score	ρ	-0.098	-0.119	-0.114	-0.089
	p-value	0.689	0.627	0.642	0.716
FEV_1/FVC	ρ	0.247	-0.100	-0.002	0.012
	p-value	0.307	0.684	0.994	0.960
FEV_1/FVC z score	ρ	0.225	-0.265	-0.225	-0.193
	p-value	0.355	0.273	0.355	0.429
FEF_{25-75} % pred.*	ρ	0.240	-0.073	-0.020	0.037
	p-value	0.409	0.805	0.946	0.899
FEF_{25-75} % pred. z score*	ρ	0.257	-0.116	-0.108	-0.033
	p-value	0.375	0.692	0.714	0.911

* Limited sample size: 12. FeNO: fractional exhaled nitric oxide, BEC: blood eosinophil count, FEV_1: forced expiratory volume in 1 second, FVC: forced vital capacity, FEF_{25-75}%: forced expiratory flow between 25% and 75% of forced vital capacity, ρ: Spearman's correlation coefficient.

6.2.3 Discussion

This section presents NO depth parameters in healthy volunteers, providing the first descriptions of NO production along the conducting airways.

On average, healthy participants had a Q25 at 33.8 % PDS and a Q75 at 56.4%, with a spread of NO production (IQR) of 21.8% PDS (see schematic diagram in **Figure 6.1**).

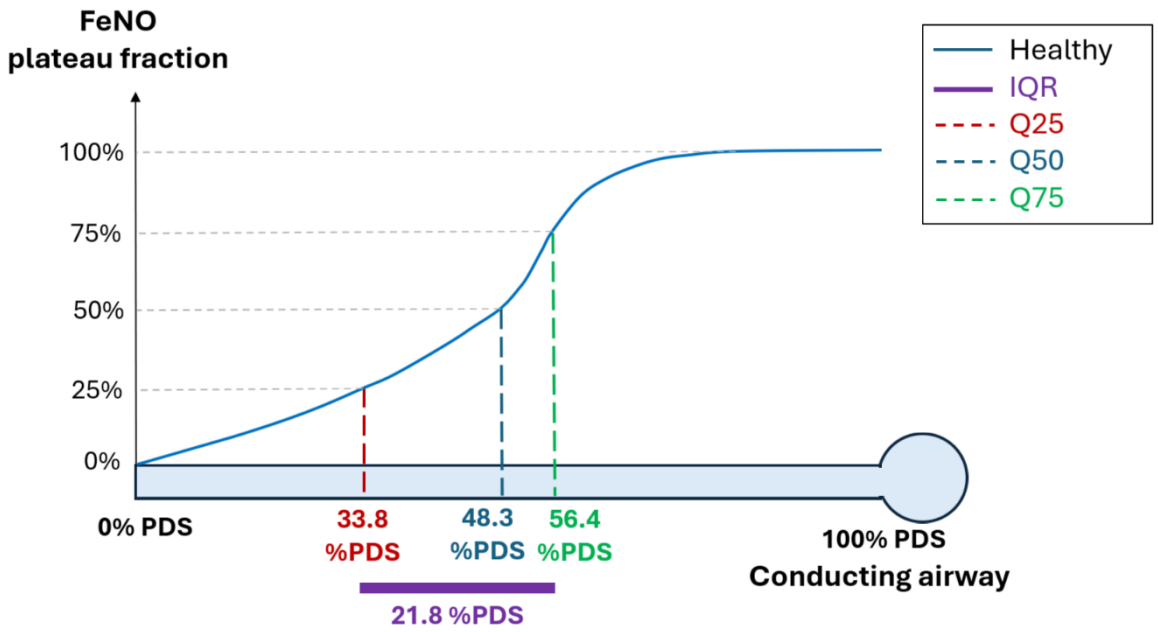


Figure 6.1 Schematic diagram of NO production in the airways. The X-axis lies along the airway, where the 0th generation of the airway is at 0% PDS depth, and the end of the 16th generation is at 100% PDS. The Y-axis represents the quantile of the FeNO plateau value. The blue curve shows how the cumulative NO production is distributed along the airways. Red number: Q25, blue number: Q50, green number: Q75, purple number: IQR. All parameters are extracted from the mean value of healthy volunteers.

These findings indicated that NO production is unevenly distributed along the length of the airways. If represented in a standardised human, 21.8% PDS (IQR) accounted for 50% of total NO production, spanning from 33.8% PDS (Q25) to 56.4% PDS (Q75). Further comparison between Q25-to-Q50 and Q50-to-Q75 revealed that the distal airways had a higher density of NO production, as indicated by a significantly smaller Q75 – Q50 compared to Q50 - Q25 (Q50 – Q25 vs Q75 – Q50, 14.4 ± 5.3 vs 8.1 ± 5.7 % PDS, $p < 0.001$). Biologically, these findings are consistent with the fact that distal airways had a larger surface area per unit volume than proximal airways, according to Weibel's lung morphology[82]. In addition, they also support the NO depth parameters calculation methods described in Chapter 4, where the median and IQR were preferred over the mean and standard deviation for representing NO depth parameters.

This study described the NO depth parameters in healthy volunteers, but several limitations should be noted. The sample was predominantly composed of young male participants, limiting its representativeness. Furthermore, the disease status was self-reported without clinical validation. Potential factors that might influence the NO production depth, such as seasonal variations and atopy conditions, were not accounted for. A larger cross-sectional study in a more diverse population is needed to provide a more comprehensive description of NO depth parameters.

6.3 Cross-sectional study of NO depth parameters in patients with asthma

6.3.1 Introduction

This study evaluated NO depth parameters in two groups of asthmatic patients: treatment-naïve patients with mild asthma (TN group) and patients with difficult-to-treat asthma on high-dose ICS (HD group). The TN group consisted of patients with newly diagnosed asthma who had not yet started regular ICS treatment, providing valuable insight into NO depth parameters in patients with asthma without the influence of ICS. The HD group offered insight into NO depth parameters in patients who have undergone high-dose ICS treatment but failed to achieve asthma control. The hypothesis is that NO depth parameters are influenced by disease severity or the administration of treatment and that the differences in these parameters can be identified between groups.

6.3.2 Participants

The TN group includes patients diagnosed with asthma who never received regular ICS treatment. The HD group consists of patients with difficult-to-control asthma who are on high-dose ICS, with beclomethasone dipropionate (BDP) equivalent doses ranging from 800mcg to 3200mcg.

6.3.3 Results

6.3.3.1 Baseline characteristics

Table 6.5 presents the baseline characteristics for the two groups. While they differed in ACQ-5 scores and duration since diagnosis, their FeNO and BEC values did not show significant variation, thereby controlling for the potential influence of these biomarkers. Other demographic information was similar between groups.

Table 6.5 Baseline characteristics and demographic information of TN and HD group

	TN group	**HD group**	**p**
Number	17	30	
Age /yr, mean ± SD	57 ± 16	56 ± 11	0.921
Gender Female (%)	6 (35)	17 (57)	0.307
BMI /kg · m^{-2}, median (IQR)	27.5 (24.7, 29.4)	25.9 (23.8,31.6)	0.816
Years diagnosed (yrs), median (IQR)	2 (0.8, 3)*	12 (3, 30)$^{\#}$	**0.002**
GINA step	0	IV-V	**-**
BDP equivalence (mcg), median (IQR)	0	2000(1000, 2000)	**-**
ACQ-5 value, mean ± SD	1.5 ± 0.9	2.2 ± 1.2	**0.026**
FeNO /ppb, median (IQR)	65 (48, 83)	68 (44, 102)	0.790
BEC /10^{9}·L^{-1}, median (IQR)	0.32 (0.25, 0.39)	0.41 (0.28, 0.54)	0.188

*Limited sample size: 11, $^{\#}$limited sample size:23. BMI: Body mass index, GINA: global initiate in asthma, BDP: Beclomethasone dipropionate, ACQ: Asthma Control Questionnaire, FeNO: fractional exhaled nitric oxide, BEC: blood eosinophil count.

6.3.3.2 Lung physiology parameters

HD group showed poorer lung function compared with TN group, as supported by worse values for FEV_1, FVC and σlnC_L (illustrated in **Table 6.6**).

Table 6.6 Physiological parameters at baseline visit between TN and HD group

Group	TN group	HD group	p
FEV_1 /L, mean ± SD	2.98 ± 0.93	2.26 ± 0.75	-
FEV_1 % pred., mean ± SD	90.4 ± 15.6	75.0 ± 21.6	**0.013**
FEV_1 z score., mean ± SD	-0.61 ± 1.03	-1.64 ± 1.40	**0.011**
FVC /L, mean ± SD	4.22 ± 1.06	3.45 ± 0.97	-
FVC % pred., mean ± SD	101.2 ± 12.3	89.5 ± 16.4	**0.013**
FVC z score, mean ± SD	0.08 ± 0.85	-0.74 ± 1.19	**0.015**
FEV_1/FVC /%, mean ± SD	70.0 ± 8.0	66.1 ± 14.6	0.318
FEV_1/FVC z score, mean ± SD	-1.16 ± 0.86	-1.61 ± 1.57	0.284
FEF_{25-75}% pred, mean ± SD	76.4 ± 27.1*	59.9 ± 32.6#	0.204
FEF_{25-75}% z score, mean ± SD	-0.85 ± 0.94*	-1.43 ± 1.23#	0.218
FRC /L, mean ± SD	2.94±0.58	2.95±0.98	-
FRC z score, mean ± SD	-0.44±1.21	0.13±1.32	0.164
V_D /L, mean ± SD	0.16±0.04	0.17±0.12	-
lnV_D z score mean ± SD	-0.73±1.02	-0.32±1.75	0.397
σV_D, mean ± SD	0.34±0.10	0.34±0.10	-
σV_D z score, mean ± SD	-0.44±1.21	0.13±1.32	0.164
σlnC_L, mean ± SD	0.64 ± 0.17	0.76 ± 0.21	-
σlnC_L z score, mean ± SD	1.21 ± 1.76	2.99 ± 2.78	**0.026**

*Limited sample size: 11, #limited sample size: 12. FEV_1: forced expiratory volume in 1 second, FVC: forced vital capacity, FEF_{25-75}%: forced expiratory flow between 25% and 75% of forced vital capacity. σlnC_L: the standard deviation of lognormal distributions for normalised alveolar compliance.

6.3.3.3 NO depth parameters

Table 6.7 shows the NO depth parameters in TN and HD groups. The p-values in the table indicated a comparison between the TN and HD groups with the control group

presented as a reference. It was excluded from the statistical comparison due to significant demographic differences with the TN and HD groups.

The TN group had a significantly higher IQR compared to the HD group, suggesting a wider spread of NO production, and a lower Q25 compared to the HD group, suggesting more proximal NO production in the TN group. The other parameters showed no significant differences.

Table 6.7 Depth parameters control, TN and HD group.

Parameter	Control group (N = 24)	TN group (N = 13)*	HD group (N = 30)	p[#]
IQR /% PDS, mean ± SD	21.8 ± 8.7	21.0 ± 13.0	4.8 ± 15.2	**0.002**
Q25 /% PDS, mean ± SD	33.8 ± 20.1	34.9 ± 12.6	49.2 ± 22.1	**0.038**
Q50 /% PDS, mean ± SD	48.3 ± 19.7	46.2 ± 15.6	53.6 ± 18.0	0.214
Q75 /% PDS, mean ± SD	56.4 ± 19.9	54.4 ± 19.9	53.7 ± 15.4	0.915

[#] comparison between the TN and HD groups. * limited sample size due to failure in generating NO depth parameters. IQR: interquartile range of FeNO plateau corresponding to depth, Q25: the depth at 25% quantile of FeNO plateau value, Q50: the depth at 50% quantile of FeNO plateau value, Q75: the depth at 75% quantile of FeNO plateau value.

6.3.3.4 Correlation between NO depth parameters and other variables

This section presents the correlation analysis in the TN group that remained unaffected by ICS, enabling the identification of the correlations without confounding effects of therapy (**Table 6.8**). What stands out in this table is that BEC levels were associated positively and strongly with Q25, Q50, and Q75. In addition, FeNO showed a positive correlation with only Q25. Furthermore, IQR showed a negative correlation with age, consistent with findings in the healthy control group. Q25 also showed a positive correlation with ACQ-5 scores. Other parameters did not exhibit any significant correlations.

Table 6.8 Spearman correlation analysis between NO depth and other parameters in the TN group

N=13		IQR	Q25	Q50	Q75
Age /yrs	ρ	-0.622	-0.289	-0.534	-0.622
	p-value	**0.023**	0.338	0.060	**0.023**
Gender	ρ	-0.338	-0.127	-0.127	-0.211
	p-value	0.259	0.680	0.680	0.488
BMI /kg·m^{-2}	ρ	-0.110	0.254	0.348	0.276
	p-value	0.719	0.402	0.244	0.361
FeNO /ppb	ρ	-0.247	0.593	0.407	0.165
	p-value	0.415	**0.033**	0.168	0.590
BEC /10^{9} L^{-1}	ρ	0.470	0.561	0.801	0.776
	p-value	0.105	**0.046**	**0.001**	**0.002**
ACQ5	ρ	0.003	0.635	0.566	0.472
	p-value	0.993	**0.020**	**0.044**	0.103
FEV_1 % pred.	ρ	-0.407	0.357	0.247	0.088
	p-value	0.168	0.231	0.415	0.775
FEV_1 z score	ρ	-0.522	0.264	0.110	-0.038
	p-value	0.067	0.384	0.721	0.901
FEV_1/FVC	ρ	0.000	0.220	0.330	0.253
	p-value	1.000	0.471	0.271	0.405
FEV_1/FVC z score	ρ	-0.319	0.049	0.071	-0.082
	p-value	0.289	0.873	0.817	0.789
FEF_{25-75} % pred.[#]	ρ	-0.509	0.000	-0.118	-0.273
	p-value	0.110	1.000	0.729	0.417
FEF_{25-75} % pred. z score[#]	ρ	-0.582	-0.073	-0.200	-0.355
	p-value	0.060	0.832	0.555	0.285
Diagnosed year /year[#]	ρ	-0.372	-0.179	-0.298	-0.482
	p-value	0.261	0.599	0.373	0.134

[#] limited sample size: 11. Spearman correlation is used here. BMI: Body mass index, FeNO: fractional exhaled nitric oxide, BEC: blood eosinophil count, ACQ: Asthma Control Questionnaire, FEV_1: forced expiratory volume in 1 second, FVC: forced vital capacity, FEF_{25-75}%: forced expiratory flow between 25% and 75% of forced vital capacity, ρ: Spearman correlation coefficient.

In correlations in the HD group, I excluded the correlation analysis between NO depth parameters and demographic data, considering the HD groups had undergone ICS-induced effects. IQR was negatively correlated with biomarkers and positively correlated with FEV_1 and FEV_1/FVC. The Q25 remains positively correlated with FeNO. At the same time, the association between Q25, as well as Q50 and Q75, was no longer observed with BEC,

although the correlation between Q25 and BEC has a small yet nonsignificant p-value (p = 0.075). Other NO depth parameters did not reveal significant correlations.

Table 6.9 Spearman correlation analysis between NO depth and physiological parameters in the HD group.

N=30		IQR	Q25	Q50	Q75
FeNO /ppb	ρ	-0.501	0.407	0.259	0.109
	p-value	**0.008**	**0.035**	0.192	0.589
BEC /10^9 L^{-1}	ρ	-0.442	0.349	0.282	0.167
	p-value	**0.021**	0.075	0.154	0.406
ACQ-5	ρ	-0.156	0.205	0.199	0.242
	p-value	0.446	0.315	0.329	0.233
FEV_1 % pred.	ρ	0.402	-0.299	-0.208	-0.134
	p-value	**0.038**	0.130	0.299	0.504
FEV_1 z score	ρ	0.371	-0.289	-0.216	-0.145
	p-value	0.057	0.144	0.280	0.470
FEV_1/FVC	ρ	0.476	-0.363	-0.333	-0.168
	p-value	**0.012**	0.063	0.089	0.401
FEV_1/FVC z score	ρ	0.417	-0.347	-0.362	-0.226
	p-value	**0.030**	0.076	0.064	0.256
FEF_{25-75} % pred.[#]	ρ	-0.115	0.139	-0.006	-0.018
	p-value	0.751	0.701	0.987	0.960
FEF_{25-75} % pred. z score[#]	ρ	-0.188	0.188	-0.042	0.018
	p-value	0.603	0.603	0.907	0.960

[#] Limited sample size: 12. Spearman correlation is used here. FeNO: fractional exhaled nitric oxide, BEC: blood eosinophil count, ACQ: Asthma Control Questionnaire, FEV_1: forced expiratory volume in 1 second, FVC: forced vital capacity, FEF_{25-75}%: forced expiratory flow between 25% and 75% of forced vital capacity, ρ: Spearman correlation coefficient.

6.3.4 Discussion

In the section above, I recruited two groups of patients with distinct asthma severity, as evidenced by FEV_1, FVC and σlnC_L, and receiving different doses of ICS therapy. Interestingly, both groups shared similar levels of type-2 high (T2H) biomarkers, FeNO and BEC. They presented with different NO production depths and widths, where Q25 was shallower (closer to the mouth) and had a wider spread (IQR) along the airways in the TN group. The correlation analysis demonstrated that Q25, Q50 and Q75 in the TN group, which

was not influenced by ICS, were positively associated with BEC levels. **Figure 6.2** illustrates a schematic graph of the NO production distribution in the conducting airways, where the green curve represents the TN group and the red curve represents the HD group.

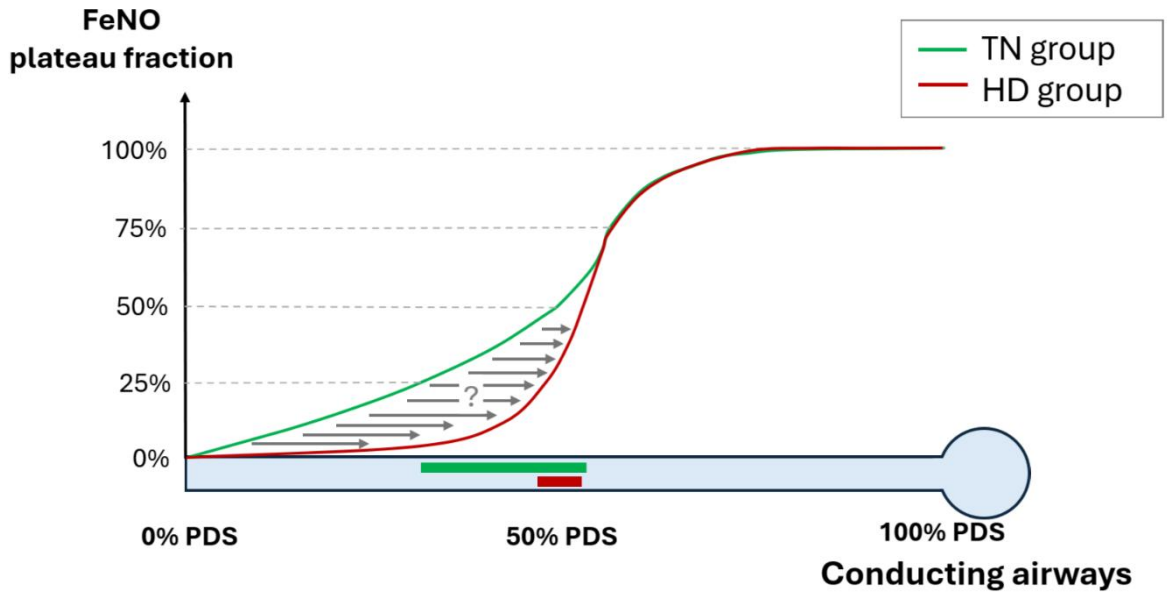


Figure 6.2 Schematic diagram of NO production distributions in the TN and HD groups. The axes are the same as Figure 6.1. The green curve represents the TN group, and the red curve represents the HD group. The significant difference in Q25 indicates distinct distributions of NO production locations in the conducting airways, while Q75 remains similar between the two groups. Consequently, the IQR becomes narrower in the HD group (the TN and HD group: green and red bars in conducting airways, respectively).

Several possible factors may drive these results. The first factor is the effects of ICS treatment and delivery patterns of ICS on the airways. The ICS, which had been administrated in the HD group, tends to suppress proximal airway inflammation due to their greater proximal disposition[194, 195], leaving the distal airways as the primary site of NO production. In the HD group, their NO production depth showed a distal distribution consistent with the spatial pattern of ICS suppression. In addition, this group of patients had been identified in a FeNO suppression test as non-suppressors and/or assessed by a specialist pharmacist, confirming adequate usage of ICS to the airways.

An alternative explanation for the distinct NO depth parameters between the two groups is that these parameters may be driven by disease severity. The HD group had a deeper Q25 value, indicating that the inflammation is more focused on distal airways. A more distal location of inflammation is associated with more severe asthma[47, 48], which is consistent with findings in this group, as supported by other physiological assessments. Furthermore, although FeNO levels in the two groups were statistically similar, a significantly narrower production region, as indicated by a smaller IQR, may contribute to more pronounced airway obstruction and symptoms.

It is possible that both factors simultaneously contribute to disease progression, leading to a deeper and narrower NO production profile in the HD group.

Another important finding is the positive correlation between Q25, Q50, Q75 and BEC in the TN group. Although the correlation between Q25 and BEC did not reach statistical significance in the HD group, it still showed a p-value of less than 0.1. To better understand this relationship, the correlation between BEC and Q25 in both groups is illustrated in **Figure 6.3**.

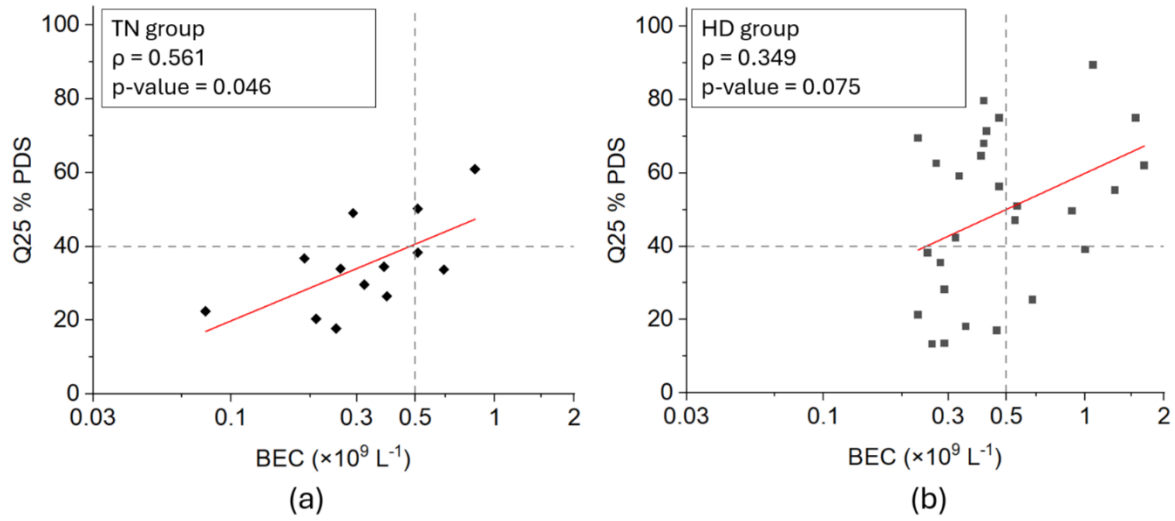


Figure 6.3 BEC and Q25 correlations in (a) TN group and (b) HD group. The TN group shows a significant correlation between Q25 and BEC, while the HD group shows only a nonsignificant trend. The HD group has more 'low BEC – deep Q25' points, while the 'high BEC – shallow Q25' remains similar to that in the TN group. Horizontal auxiliary line: Q25 = 40% PDS, vertical auxiliary line:

BEC = 0.5×10^9 L^{-1}. Red lines represent linear regression lines. Q25: the depth at 25% quantile of FeNO plateau value. BEC: blood eosinophil count.

One important confounding factor to consider is the administration of ICS, which the HD group had received at high doses over the long term. The use of ICS may weaken this correlation with BEC in the HD group compared with the TN group. In the HD group, the patients are FeNO suppression non-responders with confirmed adherence. Several studies have found that BEC levels in this group of patients remain unchanged[196-198]. However, the prolonged ICS exposure may cause Q25 to shift deeper, with this effect more likely to occur in originally shallower Q25 values, given the ICS distribution pattern and the likelihood that the deeper Q25 values are approaching their physiological limit.

In the current study, Q25 is a direct parameter reflecting the depth of inflammation in conducting airways. Its correlation with BEC supports its correlation to small airway inflammation. Multiple existing studies have revealed that BEC levels are positively associated with disease severity[199, 200] and small airway dysfunction (SAD), as reflected by various small airway function parameters, including R5-20 from impulse oscillometry[72, 201], FEF_{25-75}% from spirometry[202, 203], and σlnC_L from CCP[73]. While the correlation between Q25 and FEF_{25-75}% did not show any significance, the uncertainty in defining small airway function and the limited sample size here (only 12 of the participants had FEF_{25-75} measurements done in the HD group) indicate that a larger-scale and comprehensive study is needed.

To further observe the effects of treatment, the next two sections present subsequent cohort studies in the TN and HD groups, examining changes in NO depth parameters.

6.4 Effects of ICS treatment on NO depth parameters in the TN group

6.4.1 Introduction

Previously, I demonstrated that the HD group (high-dose ICS) has a narrower IQR and higher Q25 (indicating deeper NO production) than the TN group. One possible explanation is that ICS primarily suppresses inflammation in the central airways while leaving peripheral airways unaffected. To further investigate this hypothesis, low-dose ICS treatment was initiated in patients in the TN group for 8 weeks, and a follow-up visit was conducted to assess changes in their NO depth parameters.

6.4.2 Methods

Each participant in the TN group completed two visits: a baseline visit on the day they started ICS treatment and a follow-up visit after eight weeks. The standardised therapy was ICS at a BDP equivalent dose of 400mcg per day. Of 13 patients from the previous section, 2 were excluded: 1 for non-adherence based on self-report, and 1 due to oral corticosteroids prescribed for the management of chronic rhinosinusitis. As a result, 11 patients completed both visits, and their follow-up assessments were conducted according to the standard assessment protocol.

6.4.3 Results

6.4.3.1 Changes in biomarkers and physiological parameters

Figure 6.4 illustrates the changes in biomarkers and ACQ-5 scores following the administration of ICS.

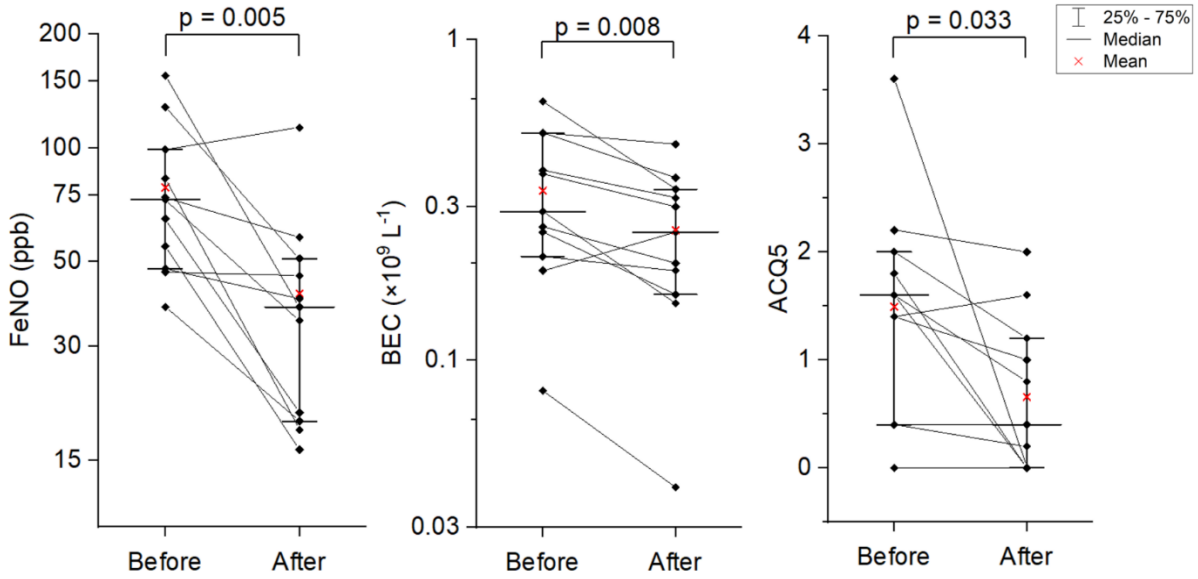


Figure 6.4 Biomarkers and ACQ-5 changes during ICS therapy. FeNO, BEC and ACQ-5 all show a significant decrease after the start of ICS therapy. The red cross indicates the mean value. The I-shaped line outlines the 25% percentile, median and 75% percentile.

Figure 6.4 shows a significant reduction in FeNO following ICS treatment (Before vs After: 73[48, 99] vs 38[19, 51], p = 0.005), as well as a decrease in BEC (Before vs After: 0.29[0.21, 0.51] vs 0.25[0.16, 0.34], p = 0.008). Alongside these biomarker reductions, ACQ-5 scores showed significant improvement (Before vs After: 1.5 ± 1.0 vs 0.7 ± 0.7, p = 0.033). However, none of the lung function parameters (FEV_1, FVE1/FVC and FVC) showed improvement during 8 weeks of ICS therapy (illustrated in **Figure 6.5**).

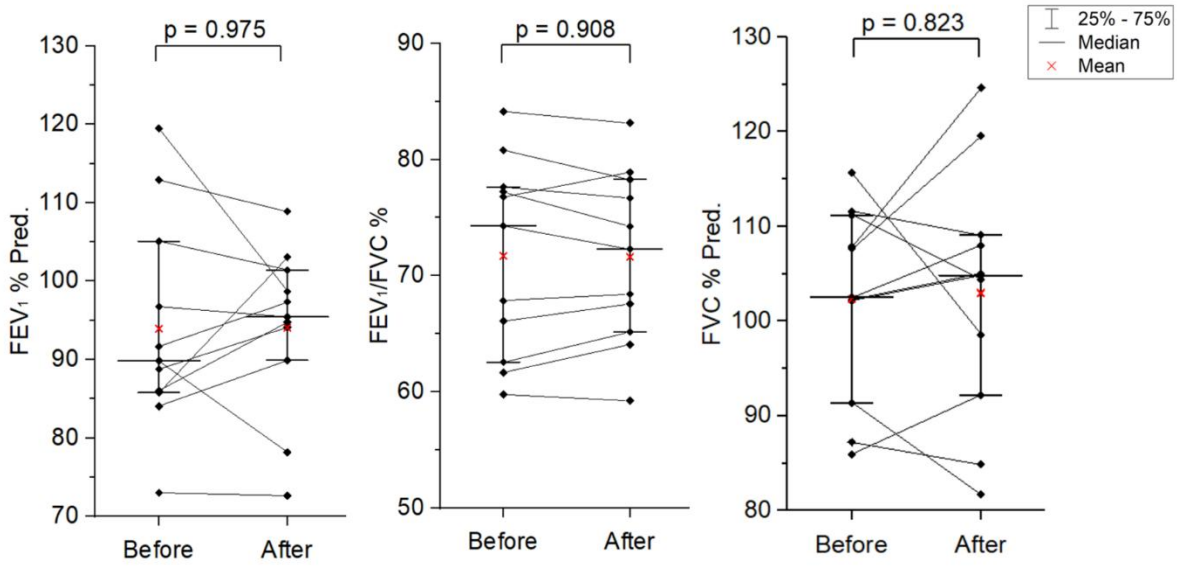


Figure 6.5 Spirometry changes before and after administration of low-dose ICS in the TN group. FEV_1 % predicted, and FEV_1/FVC remained similar before and after the test. FEV_1 % predicted before vs after: 93.9 ± 13.6 vs 94.0 ± 10.6, p = 0.975. FEV_1/FVC before vs after 71.7 ± 8.4 vs 71.6 ± 7.3, p = 0.908. FVC % predicted before vs after 102.3 ± 10.1 vs 103.0 ± 13.2, p = 0.823.

6.4.3.2 Depth parameters change

The depth parameters before and after treatment are summarised in **Table 6.10**. The statistical test compares values before and after low-dose ICS treatment. None of the NO depth parameters showed significant changes.

Table 6.10 NO depth parameter changes during ICS treatment

Parameter	Healthy Control (N = 24)	TN-group (N = 11) Before ICS	TN-group (N = 11) After ICS	p
IQR %PDS, mean ± SD	21.8 ± 8.7	18.4±12.4	29.0±18.7	0.096
Q25 %PDS, mean ± SD	33.8 ± 20.1	33.0±10.7	28.6±16.2	0.207
Q50 %PDS, mean ± SD	48.3 ± 19.7	43.2±13.2	46.9±13.0	0.444
Q75 %PDS, mean ± SD	56.4 ± 19.9	49.9±15.6	58.9±16.4	0.163

IQR: interquartile range of FeNO plateau corresponding to depth, Q25: the depth at 25% quantile of FeNO plateau value, Q50: the depth at 50% quantile of FeNO plateau value, Q75: the depth at 75% quantile of FeNO plateau value.

However, the change in Q25 was positively correlated with the change in BEC (ρ = 0.755, p = 0.007, illustrated in **Figure 6.6**), suggesting that a proximal shift in Q25 accompanies a reduction in BEC.

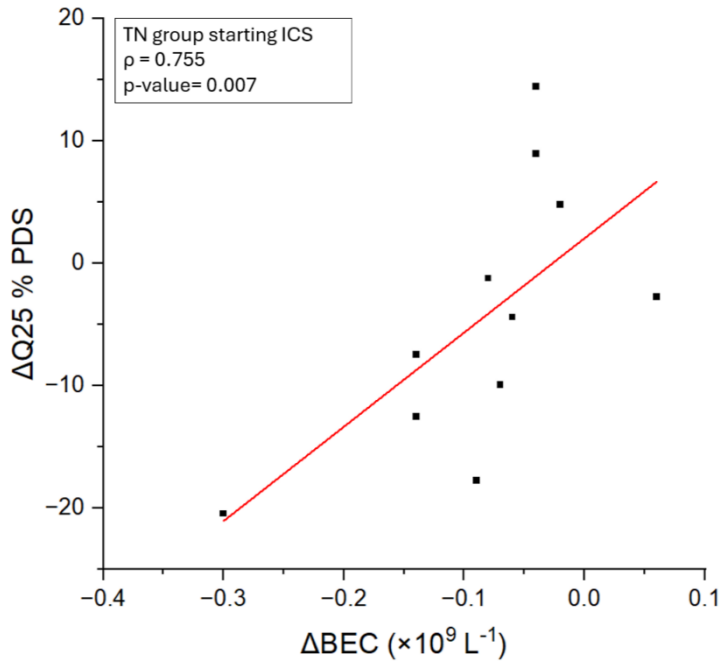


Figure 6.6 ΔQ25 and ΔBEC relationship in the TN group receiving ICS treatment. The red line represents the linear regression line. The decrease in BEC indicates that Q25 is simultaneously decreasing. BEC: blood eosinophil count, Q25: the depth at 25% quantile of FeNO plateau value.

6.4.4 Discussion

In this group, there was no significant change in NO depth parameters following treatment with low-dose ICS. However, the change of Q25 displayed a consistent correlation with the change of BEC values, consistent with the baseline correlation in the TN group.

The unchanged NO production distribution along the airways may suggest that ICS particles are distributed along the axial axis of airways in a relatively even way. As the TN group consists of patients with mild disease, the deposition pattern of ICS is less influenced by factors such as mucus accumulation[204], inflammation[205]and ventilation inhomogeneity[206], thereby allowing sufficient deposition in the distal airways. In this case, the inflammation is

suppressed simultaneously in both the central and distal airways, resulting in unchanged NO production sites despite a reduction in FeNO levels.

Notably, among these 11 patients, 7 were "FeNO suppression responders" – meaning they reduced their FeNO by more than 42% following ICS – while 4 did not (FeNO stayed high). I examined whether there was a difference in how NO depth parameters changed between FeNO suppression responders versus non-responders. The responder group had a nonsignificant more increase in IQR compared with the non-responder group (Responder vs Non-responder: 15.4 vs 2.2% PDS IQR change, $p = 0.295$). Determining the clinical significance of this observation requires a larger sample size and a more balanced recruitment of responders and non-responders.

The correlation analysis of the changes in parameter values is consistent with the findings from the previous section, where the Q25 value was significantly correlated with BEC levels. This finding further supports the association between NO production depth and BEC levels.

The most significant limitation of this study is the small sample size available for analysis. Additionally, the mixed composition of FeNO suppression responders and non-responders may pose a potential issue, as they may respond differently in terms of NO depth parameters.

6.5 Effects of biologics (anti-IL5/5R) therapy on NO depth parameters in the HD group

6.5.1 Introduction

A subset of HD patients from the previous baseline comparison started biologic therapy(anti-IL5/5R, mepolizumab or benralizumab) due to persistent, difficult-to-control asthma, in accordance with NICE guidelines [77, 78]. While anti-IL5/5R therapy has not shown clear suppression of FeNO[80, 207], its effects on NO production location remain unclear,

particularly given potential interactions between T2H cytokines and their receptors. This study examines the effects of receiving anti-IL5/5R therapy on NO depth parameters.

6.5.2 Methods

In total, 10 patients were recruited for a follow-up visit after initiating anti-IL5/5R treatment. Two of these were excluded: one was tapering his regular OCS for eosinophilic granulomatosis with polyangiitis (EGPA) during the study period, and another was excluded due to an exacerbation occurring around the time of biologics therapy initiation.

Thus, 8 participants were studied on the day they received their first injections of anti-IL5/5R therapy (baseline visit) and at a follow-up visit after the fourth injection of anti-IL5/5R (3 or 4 months after, depending on the type of biologic).

6.5.3 Results

6.5.3.1 Basic characteristics of anti-IL5/5R group

Table 6.11 presents the demographic characteristics of patients recruited in the anti-IL5/5R cohort. The patients exhibited T2H inflammation at the initiation of biologics therapy, with elevated FeNO or BEC.

Table 6.11 Demographic characteristics of the anti-IL5/5R group

Group	BI group
Number	8
Age /yr, mean ± SD	63 ± 9
Gender Female (%)	2 (25)
BMI /kg · m^{-2}, median (IQR)	30.0 (27.0, 32.0)
FeNO /ppb, Median (IQR)	54(26, 88)
BEC /10^{9}·L^{-1}, median (IQR)	0.54(0.33, 1.30)
Asthma diagnosed years, median(IQR)	5(2,15)

BMI: Body mass index, FeNO: fractional exhaled nitric oxide, BEC: blood eosinophil count.

6.5.3.2 Changes in physiological parameters during biologics therapy

The biomarkers and ACQ5 changes are illustrated in **Figure 6.7**.

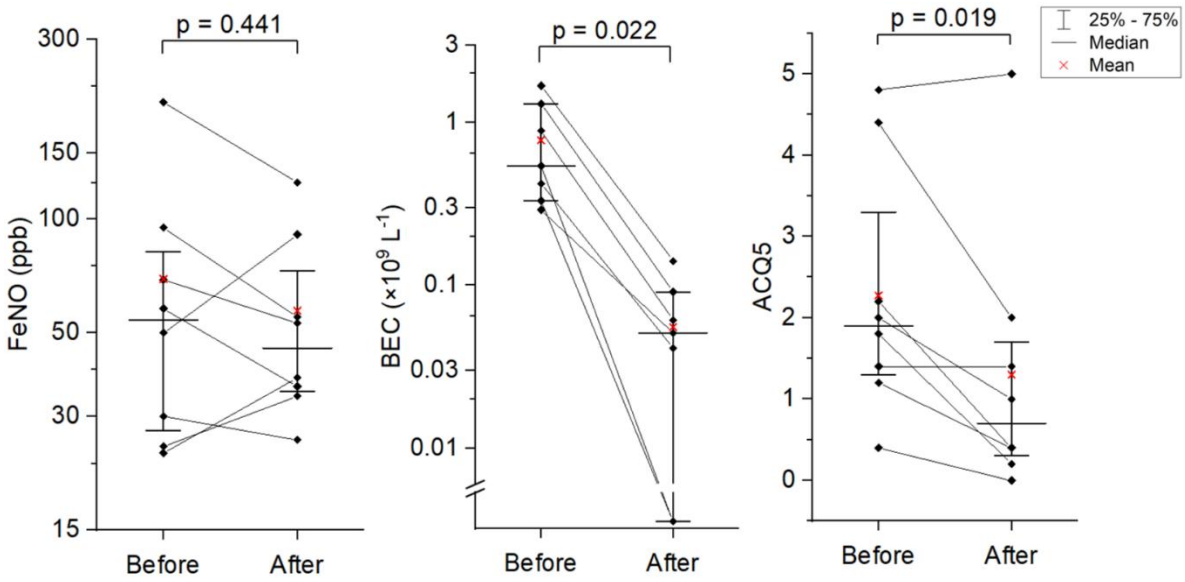


Figure 6.7 Biomarkers and ACQ-5 changes in patients receiving anti-IL5/5R therapy. FeNO does not change significantly, while BEC decreases significantly. The red cross indicates the mean value. The I-shaped line outlines the 25% percentile, median and 75% percentile. ACQ-5 also shows significant improvement. FeNO: fractional exhaled nitric oxide, BEC: blood eosinophils count, ACQ: asthma control questionnaire.

FeNO did not show significant change, while BEC decreased significantly (Before vs After: 0.54[0.33, 1.30] vs 0.05[0, 0.09], p = 0.044). Symptoms also improved significantly, as indicated by ACQ-5 scores (Before vs After: 2.3 ± 1.5 vs 1.3 ± 1.6, p = 0.019).

Figure 6.8 illustrates spirometry results comparing values before and after anti-IL5/5R treatment, showing a significant improvement in FVC, while other parameters remained largely unchanged.

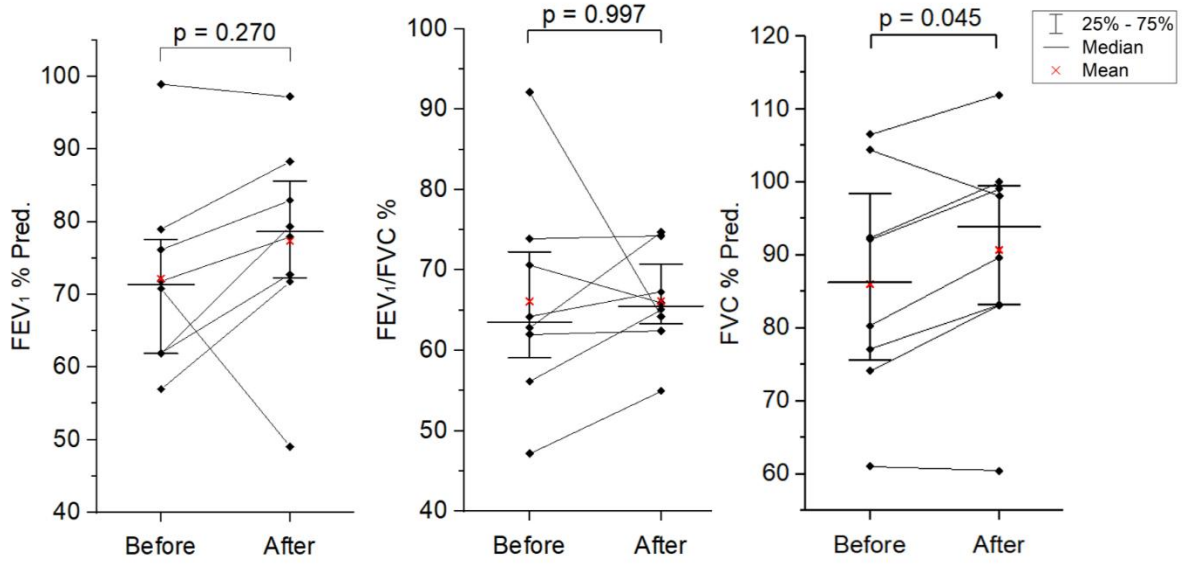


Figure 6.8 Spirometry results before and after treatment in the BI group. FEV_1 % predicted Before vs After 72.2 ± 13.2 vs 77.4 ± 14.1, p = 0.270, FEV_1/FVC Before vs After 66.1 ± 13.4 vs 66.1 ± 6.4, p = 0.997, FVC % predicted Before vs After 86.0 ± 15.6 vs 90.1 ± 15.6, p = 0.045. The I-shaped line outlines the 25% percentile, median and 75% percentile.

6.5.3.3 Depth parameters change

Table 6.12 demonstrates that Q25 decreased significantly, and Q75 showed a nonsignificant decreasing trend following anti-IL5/5R treatment. This parallel reduction resulted in the IQR remaining comparable to the baseline.

Table 6.12 NO depth parameter changes during anti-IL5/5R therapy

Group	Before	After	p
IQR %PDS, mean ± SD	3.3 ± 15.5	8.6 ± 12.0	0.349
Q25 %PDS, mean ± SD	53.7 ± 12.7	42.3 ± 13.8	**0.028**
Q50 %PDS, mean ± SD	57.1 ± 10.8	47.5 ± 19.4	0.133
Q75 %PDS, mean ± SD	56.9 ± 7.7	47.7 ± 18.4	0.196

IQR: interquartile range of FeNO plateau corresponding depth, Q25: the depth at 25% quantile of FeNO plateau value, Q50: the depth at 50% quantile of FeNO plateau value, Q75: the depth at 75% quantile of FeNO plateau value.

Figure 6.9 illustrates changes in Q25 and Q75 during the treatment, highlighting the two patients who showed increased Q25 after treatment using markers in both plots. However,

most patients exhibited a consistent decrease in both Q25 and Q75 following biologics therapy.

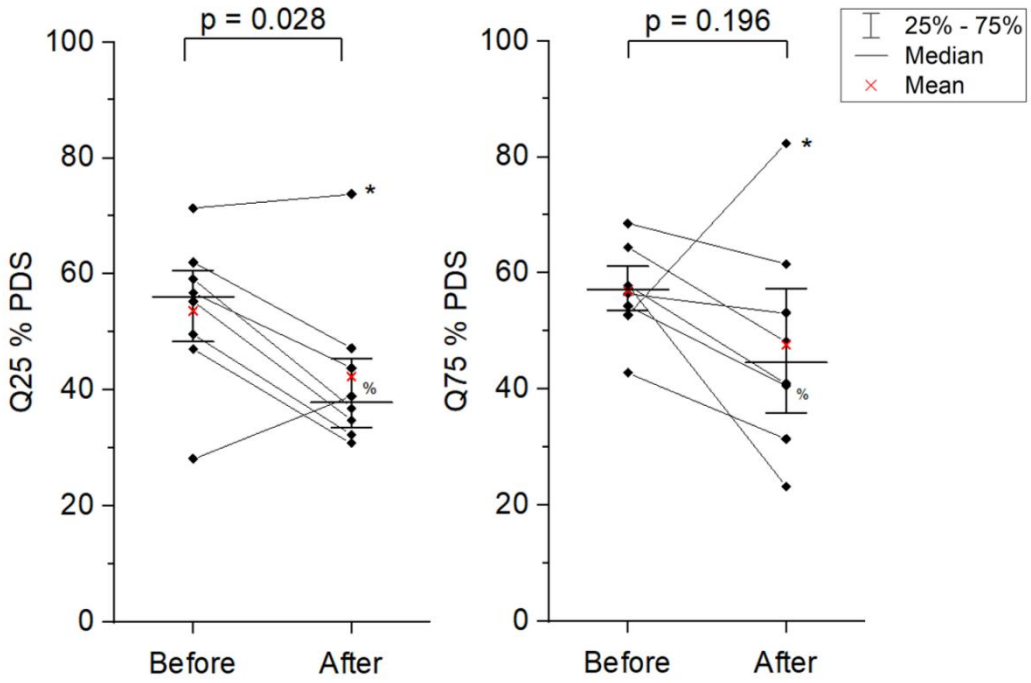


Figure 6.9 Q25 and Q75 before and after receiving anti-IL5/5R biologics. Q25 shows a significant decrease during the application of biologics, while Q75 shows only a nonsignificant trend. * and % indicate the same patients. The red cross indicates the mean value, and the I-shaped line outlines the 25% percentile, median and 75% percentile.

6.5.4 Discussion

As shown in **Figure 6.10**, a schematic figure, a proximal shift in NO production location occurred after receiving anti-IL5/5R biologic therapy. The only lung physiological parameter that changed significantly was an increase in FVC increases after receiving anti-IL5/5R therapy.

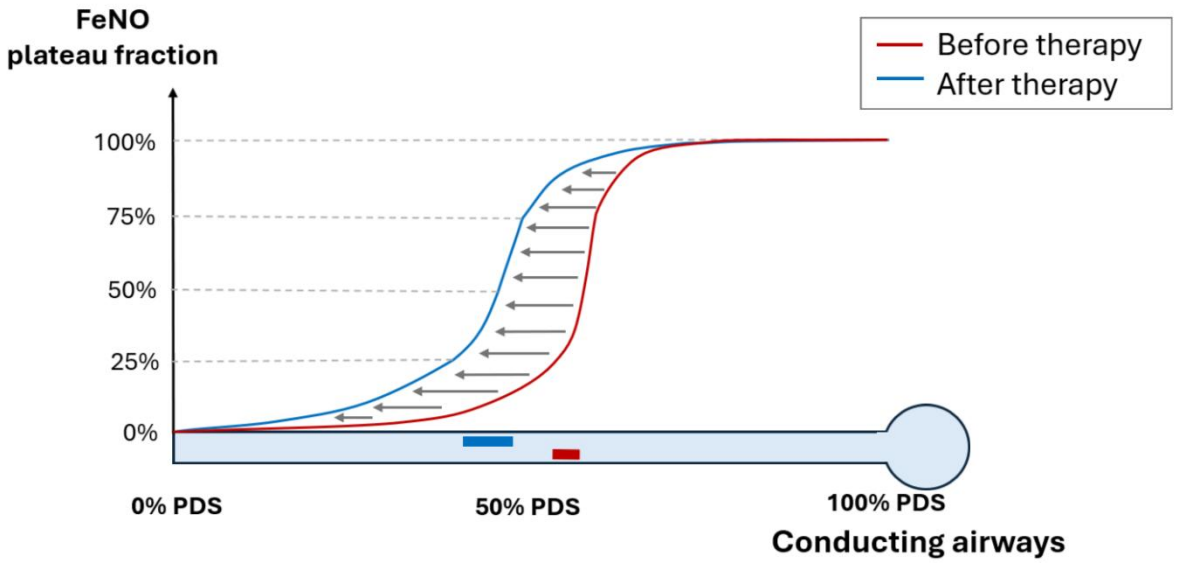


Figure 6.10 Schematic diagram showing the change of NO production location during anti-IL5/5R therapy. The axes are the same as Figure 6.1. Red curve: NO production cumulative distribution before anti-IL5/5R therapy, blue curve: NO production cumulative distribution after anti-IL5/5R therapy.

The shift in NO depth parameters possibly indicates that anti-IL5/5R therapy has induced a reduction in distal airway inflammation. The previous section found that Q25 was deeper in patients with more severe disease, suggesting it reflects distal airway involvement. This finding provides an example of opposite movement in Q25, potentially reflecting relief in small airway involvement. This is further supported by the improved FVC, an indicator of air trapping, which can reflect closure or narrowing of the distal airways[208, 209]. However, previous studies have shown mixed results in examining anit-IL5/IL5R therapy for improving small airway function. While FEF_{25-75}% has shown improvements[210, 211], findings from lung inhomogeneity and oscillometry have been more inconsistent[73, 212, 213]. A possible explanation for these inconsistent findings is the lack of a clear definition of small airway function. Various tests address specific aspects of small airway function, yet a comprehensive definition and categorization remain lacking.

This study, meanwhile, has provided a potential new perspective on assessing small airway function, focusing on the evaluation of inflammatory activity to capture small airway involvement, with or without associated structural changes in the lung. This hypothesis indicates that NO depth parameters may serve as a more sensitive measure of small airway function by detecting the functional changes prior to structural changes, which may explain why physiological parameters remain relatively stable.

The alterations in NO depth parameters might be attributed to their association with BEC levels, which were nearly eliminated following anti-IL5/5R therapy. Given that asthma involves both proximal and distal airways[48], several studies have examined differences between these airway regions. Previous findings suggested that the distal airways underwent increased eosinophil recruitment[49] and contained elevated levels of IL-5 or its gene expression products, which regulated the eosinophil recruitment process[50]. These results were supported by clinical studies, which reveal a positive association between BEC levels and distal airway dysfunction[72, 73, 201-203]. These findings, in combination with our results showing an association between Q25 and BEC, suggest that BEC or its upstream mediator, IL-5, may play an essential role in regulating the location of airway inflammation, thereby being associated with NO production sites in the conducting airways.

Beyond the associations, one possible link between BEC and distal airway function is the effects on ICS deposition in distal airways. Ragunayakam *et al.* used CT scans to simulate the ICS deposition in 28 patients with severe asthma. They found that the higher sputum eosinophil group showed a less peripheral distribution of ICS particles while the higher blood eosinophil group exhibited a similar but insignificant trend[205]. An alternative interpretation of our findings is that the observed shallowing of NO production sites may result from more effective deposition of ICS in the distal airways rather than being a direct consequence of anti-IL5/5R therapy.

The primary limitation of this study is the small sample size of the group of patients receiving biologics therapy. Additionally, differences between mepolizumab and benralizumab should be considered in future designs. The relatively short study period restricts its ability to assess associations with clinical outcomes.

6.6 Summary

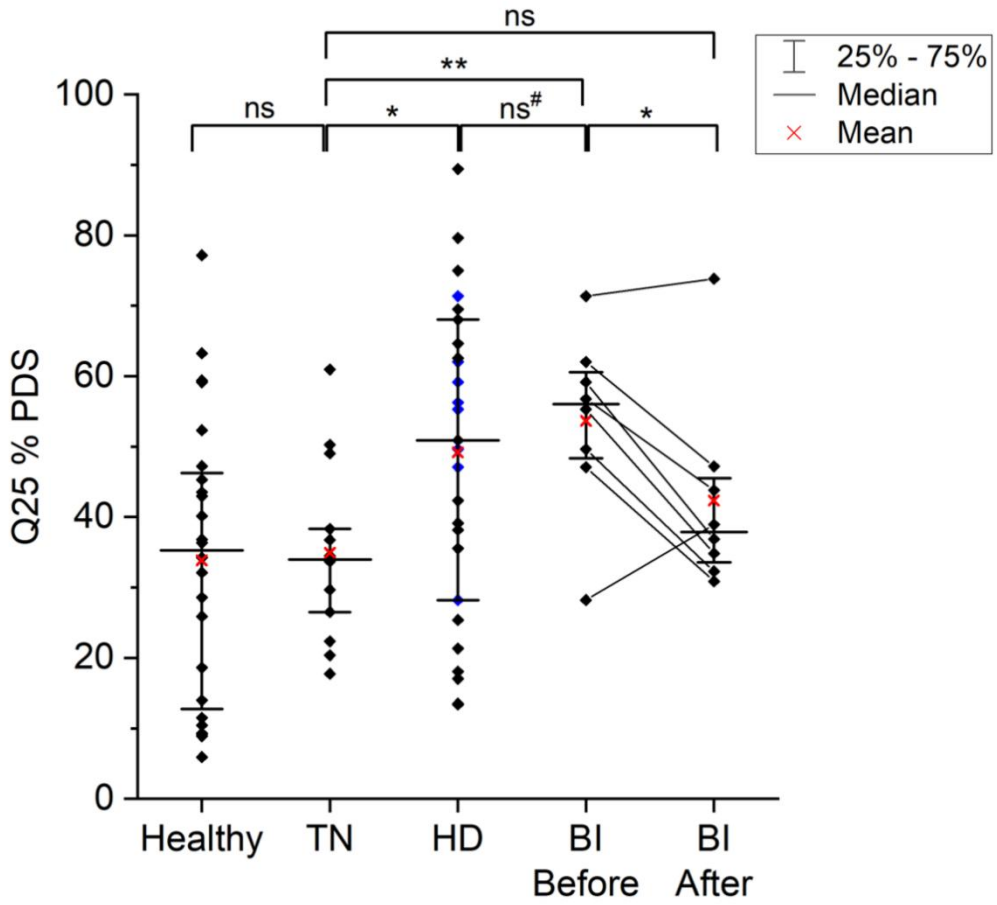


Figure 6.11 Q25 in Healthy, TN, HD and BI groups. Due to differences in baseline characteristics between the Healthy group and other groups, all comparisons are made against the TN group. The blue dot marks the individual who continues to receive biologics treatment (anti-IL5/5R). The red crosses indicate the mean value. The I-shaped lines outline the 25% percentile, median and 75% percentile. # comparison between the BI group and the remaining HD group. TN: treatment-naïve group, HD: high-dose ICS treatment group, BI: biologics (anti-IL5/5R) group, Q25: the depth at 25% quantile of FeNO plateau value. ns: nonsignificant, * <0.05, ** <0.01, *** <0.001.

Figure 6.11 illustrates the variation in Q25 across different groups. Q25 appears similar between the control and TN groups (who have mild disease), although this result may be

somewhat biased due to significant differences in demographic characteristics between these two groups.

Q25 is more distal in the HD group compared with the TN group, potentially due to either the effects of ICS therapy or disease progression. The TN group that initiated low-dose ICS was not displayed in this figure, as the change in Q25 was nonsignificant. Patients in the HD group who started biologic therapy (anti-IL5/5R) were marked in blue and referred to as the BI group. Their Q25 values were comparable to those of the remaining patients in the HD group, which is still significantly more distal compared with the TN group. After receiving biologics treatment, Q25 returned to a level similar to that of the TN group, possibly reflecting a reduction in small airway involvement and an overall improvement in disease severity. The whole process highlights the potential of Q25 to serve as a marker of inflammatory activity with promise in detecting functional alterations before structural changes occur in the lung.

Another interesting finding was the association between BEC and Q25. BEC levels or their upstream regulating cytokine, IL-5, appear to play a key role in the process described above. This series of studies found that Q25 is positively associated with BEC levels when patients were treatment-naïve and that initiation of ICS also showed a significant association between changes in BEC and Q25 levels. When a stronger reducer of BEC, anti-IL5/5R, was administered, Q25 displayed a significant proximal shift. These findings underscored the important role of eosinophils and/or IL-5 in distal airway function.

6.7 BD effects on NO depth parameters

In previously presented studies, participants also undertook bronchodilation (BD) with salbutamol and had spirometry and NO depth measurements repeated to assess the effects of BD on NO depth parameters.

6.7.1 Participants

I show the results of 27 participants who underwent BD, 10 of whom were from the TN group and 17 from the HD group.

6.7.2 Results

6.7.2.1 Basic characteristics

Table 6.13 provides an overview of the basic characteristics of patients who underwent BD intervention.

Table 6.13 Demographic characteristics of participants receiving BD.

	Patient group
Number	27
Age /yr, mean ± SD	55 ± 12
Gender, Female (%)	16(60%)
BMI /kg · m^{-2}, median (IQR)	25.8(24.5, 29.7)
GINA step	
0	10 (37%)
IV - V	17(63%)
Years diagnosed (yrs), median (IQR)	4(1,16)
ACQ-5 value, mean ± SD	2.1 ± 1.2
FeNO /ppb, median (IQR)	73(50, 125)
BEC /10^{9}·L^{-1}, median (IQR)	0.40(0.29, 0.54)

BMI: Body mass index, GINA: global initiative in asthma, BDP: Beclomethasone dipropionate, ACQ: Asthma Control Questionnaire, FeNO: fractional exhaled nitric oxide, BEC: blood eosinophil count.

6.7.2.2 Physiological parameters and CCP parameters

Table 6.14 provides the spirometry and CCP measurement results of the whole group of patients. Following BD, improvements were observed in FEV_1, FEV_1/FVC, and V_D, which was consistent with expectations. An improved V_D indicates that the patients have limited airway remodelling, as their dead space responds to BD.

Table 6.14 Physiological parameters of BD receiving patients

Group	Pre-BD	Post-BD	p
FEV_1 /L, mean ± SD	2.55 ± 0.96	2.68±0.88	-
FEV_1 % pred., mean ± SD	80.8 ± 20.7	85.2 ± 18.6	**0.003**
FEV_1 z score., mean ± SD	-1.27 ± 1.36	-0.98 ± 1.24	**0.004**
FVC /L, mean ± SD	3.68 ± 1.12	3.66 ± 1.10	-
FVC % pred., mean ± SD	92.5 ± 15.0	92.1 ± 14.7	0.659
FVC z score, mean ± SD	-0.52±1.07	-0.55 ± 1.06	0.635
FEV_1 /FVC /%, mean ± SD	68.8 ± 13.1	73.3 ± 12.7	**0.001**
FEV_1 /FVC z score, mean ± SD	-1.32 ± 1.51	-0.71 ± 1.66	**0.001**
Reversibility %	7.1 ± 11.8		-
V_D /L, mean ± SD	0.12 ± 0.04	0.13 ± 0.04	-
lnV_D z score mean ± SD	-0.59 ± 1.17	-0.11 ± 1.13	**0.001**
σV_D, mean ± SD	0.34 ± 0.10	0.32 ± 0.07	-
σV_D z score, mean ± SD	0.20 ± 1.81	-0.06 ± 1.33	0.347
σlnC_L, mean ± SD	0.72 ± 0.22	0.61 ± 0.18	-
σlnC_L z score, mean ± SD	2.46 ± 2.83	0.97 ± 2.20	**<0.001**

FEV_1: forced expiratory volume in 1 second, FVC: forced vital capacity, FEF_{25-75}%: forced expiratory flow between 25% and 75% of forced vital capacity. V_D: volume of dead space, lnV_D: natural logarithm of V_D, σV_D: The standard deviation of normal distribution for normalised deadspace across lung volume. σlnC_L: the standard deviation of lognormal distributions for normalised alveolar compliance.

6.7.2.3 Depth parameters

All NO depth parameters showed no significant change between Pre- and Post-BD (**Table 6.15**).

Table 6.15 NO production location parameters

Group	Pre-BD	Post-BD	p
IQR /% PDS, mean ± SD	10.4 ± 17.4	13.4 ± 11.6	0.301
Q25 /% PDS, mean ± SD	46.0 ± 20.9	41.4 ± 17.7	0.146
Q50 /% PDS, mean ± SD	52.1 ± 18.6	51.9 ± 16.7	0.933
Q75 /% PDS, mean ± SD	55.4 ± 18.1	54.8 ± 17.0	0.843

IQR: interquartile range of FeNO plateau corresponding depth, Q25: the depth at 25% quantile of FeNO plateau value, Q50: the depth at 50% quantile of FeNO plateau value, Q75: the depth at 75% quantile of FeNO plateau value.

6.7.2.4 Correlation analysis

To investigate the potential link between NO production depth and airway reversibility, we analysed the correlation between changes in NO production depth and the degree of reversibility. **Table 6.16** shows that NO depth parameters were not associated with airway reversibility.

Table 6.16 NO depth parameters correlation analysis with reversibility

		Delta IQR	Delta Q25	Delta Q50	Delta Q75
Reversibility %	Spearman Corr.	-0.022	0.175	0.170	0.346
	p-value	0.913	0.382	0.397	0.078

IQR: interquartile range of FeNO plateau corresponding depth, Q25: the depth at 25% quantile of FeNO plateau value, Q50: the depth at 50% quantile of FeNO plateau value, Q75: the depth at 75% quantile of FeNO plateau value.

6.7.3 Discussion

In this part, I evaluate the effects of BD on NO depth parameters and the correlation between NO depth parameters and airway reversibility. The findings indicate that BD does not affect NO depth parameters and no correlation was observed between NO depth parameters and reversibility.

Salbutamol, an β_2-androgenic agonist, does not have a known direct influence on the site of NO production, although it is expected to alter the lung structure. The physiological

parameters support the observation of an alteration in the lung structure after administration of BD. BD effectively reduces airway obstruction, reflected by increased FEV_1, FEV_1/FVC. CCP also shows that the inhomogeneity has been improved. The results demonstrated that BD does not alter the NO depth parameters. More importantly, the correlation analysis further validated that the measured CCP accurately reflects lung physiology, eliminating the influence of airway structure changes while keeping NO depth parameters unchanged.

6.8 Summary

The series of studies presents NO depth parameters across different participant groups. The healthy group provides reference values for NO depth parameters. Comparisons between TN and HD groups, along with two follow-up studies involving low-dose ICS and anti-IL5/5R, suggest that Q25 is associated with disease severity and linked to BEC levels. The absence of association between reversibility from BD and NO depth parameters validates the ability of CCP to capture accurate lung physiology through measurements of NO production depth.

Chapter 7

Assessment of Ventilation-perfusion ($\dot{V}/\dot{Q}$) in patients with severe COVID-19

The COVID-19 pandemic, which emerged in 2020, posed a significant threat to public health and caused substantial personal, societal and economic disruption[214]. Personally, this prevented me from starting the experimental work for my DPhil project. However, during this time, Busana *et al.* published a study that attempted to identify ventilation-perfusion ($\dot{V}/\dot{Q}$) distributions in patients with severe COVID-19[215]. Their $\dot{V}/\dot{Q}$ distributions were identified numerically, but these did not fit the data particularly well. I developed a more analytical approach to identifying the potential distribution, and the resulting publication, jointly with my two supervisors, is provided in Appendix C[216]. In addition, we also published a comment in response to the original paper[217].

Chapter 8

Conclusions and Future Work

This thesis presents a novel methodology for identifying the location of NO production within the conducting airways. The research incorporates the use of the Rapid FeNO Device (RFD; FeNO: fractional exhaled nitric oxide), the introduction of a standardised protocol, the development of the underlying model, the establishment of quality control assessments and clinical implementation of this methodology in both healthy individuals and those with asthma. Additionally, two clinical studies are presented to demonstrate the sensitivity of evaluating pulmonary function using lung inhomogeneity measured by Computed Cardiopulmonography (CCP). An extra project conducted during the COVID-19 pandemic employed a mathematical model to reveal abnormal ventilation-perfusion ($\dot{V}/\dot{Q}$) distributions in patients with COVID-19.

8.1 Location of NO production within conducting airways

The framework for obtaining NO production locations consists of three key components: hardware — RFD and its accompanying process for raw data, software — DSP and derivation of NO depth parameters, and quality assessments. This framework is subsequently applied in clinical studies to demonstrate its potential clinical significance.

The hardware enables accurate and rapid measurement of gas concentrations and associated parameters, as demonstrated in Chapter 3. The RFD employs laser-based spectroscopy and features a hybrid design that combines both mainstream and sidestream laser-based compartments to measure CO_2 and NO concentrations. Based on Cavity Enhanced Absorption Spectroscopy (CEAS), the sidestream compartment achieves NO concentration (and CO_2 concentration) measurements by extending the optical path length and operating at a reduced pressure. Simultaneously, the mainstream compartment (Direct Absorption Spectroscopy, DAS) provides real-time CO_2 readings. Pressure and temperature are measured concurrently with gas concentrations. To reconstruct NO levels in the mainstream flow, the time delay and dynamics of RFD are modelled as a first-order system, validated by observing changes in CO_2 levels following the cut-off of the CO_2 supply to the CEAS. The fitted first-order system parameters from sidestream and mainstream CO2 expirograms enable the accurate reconstruction of the mainstream NO expirogram from the sidestream NO expirogram. As a result, the RFD outputs volumetric CO_2 and NO expirograms.

The software for NO location measurement relies on combining the simulation of the NO expirogram by the Dead Space Pipes (DSP) model with the derivation of NO depth parameters to overcome the challenge of reconstructing the complete distribution within the conducting airways. Chapter 4 shows how the model is constructed from CCP outputs, which capture lung physiology during tidal breathing and multiple-breath nitrogen washout. This Chapter also presents two modes of the DSP model, depending on whether the speed variation is considered: the speed-independent (SpIn) mode and the speed-dependent (SpD) mode. The SpIn mode provides a more straightforward simulation, whereas the SpD mode more accurately reflects real-world conditions, as the NO concentration is a speed-dependent

variable. The statistical analysis derives four parameters, which can be generated in both SpIn and SpD modes:

(1) IQR: a description of the depth range between the 25th and 75th percentiles of the FeNO plateau,

(2) Q25: the depth at which the FeNO value reaches the 25th percentile of its plateau value,

(3) Q50: the depth at which the FeNO value reaches the 50th percentile of its plateau value,

(4) Q75: the depth at which the FeNO value reaches the 75th percentile of its plateau value.

The quality assessment system generates a matrix to evaluate individual breath in NO depth measurements. It ensures that all accepted breaths are accurately measured and modelled. The repeatability/reliability test confirms that the NO depth parameters are both repeatable and reliable. Despite these findings, the SpD mode was selected for future clinical studies because of its advantages in quality control, repeatability, reliability, and potential clinical application.

The clinical application of this novel methodology presents the NO depth parameters in healthy volunteers, demonstrating an unbalanced distribution in conducting airways. The comparison between the treatment-naïve (TN) patients group and the difficult-to-treat, high-dose ICS receiver group (HD) with asthma revealed distinct differences in Q25 and IQR, indicating that NO is produced more proximally and over a wider region in the TN group. A portion of TN group patients continued to have a follow-up after being administered with low-dose ICS. They did not show any changes in NO depth parameters, even though their biomarkers, including both FeNO and blood eosinophil count (BEC), were significantly reduced. In contrast, administration of anti-IL5/5R to a subset of the HD group resulted in a

clearly shallower effect on Q25, indicating that distal inflammation was reduced by biologics therapy either directly or indirectly. These clinical studies also demonstrate a clear positive correlation between Q25 and BEC, suggesting potential involvement of distal airways.

The bronchodilator study showed no change in NO depth parameters before and after bronchodilator administration, while spirometry parameters changed significantly. These findings support the hypothesis that CCP outputs provide highly accurate physiological descriptions of the lung, allowing the influence of structural alterations to be eliminated.

Future developments of this methodology are summarised as follows:

(1) Theoretical development.

'Backdiffusion', which occurs when NO diffuses from the conducting airway back to the alveolars during exhalation, can be accounted for in the next model. As reviewed in Chapter 1, 'backdiffusion' affects FeNO measurements. Developing an adaptive model that incorporates 'backdiffusion' may provide more accurate measurements in NO production locations.

As discussed in Chapter 5, the current model, based on CCP outputs, offers an accessible approach to estimating NO production locations. However, it relies on several fundamental assumptions that may need revision as more evidence becomes available. These assumptions include axial and inter-branch homogeneity in the NO production rate. Beyond this, a different model independent of CCP outputs could be investigated in future work. Revisions to these assumptions may be required as additional evidence emerges from clinical or experimental studies.

Moreover, the bronchoscopy may provide an opportunity to biopsy epithelial tissues and assess the expression intensity of inducible nitric oxide synthase (iNOS). After collecting NO depth parameters, using bronchoscopy to acquire samples could offer valuable insights into

the spatial distribution of NO production and provide supporting evidence for refining model assumptions.

(2) Clinical study

A large-scale cross-sectional study of healthy volunteers with high FeNO may provide a more accurate reference value for NO depth parameters. Such a study would enable more detailed subgroup analyses. Apart from examining the relationship between demographic information and NO production depth, exploring seasonal variation could help reveal the relationship between seasonal changes and NO production sites. Similarly, NO depth measurements at different times of the day could provide evidence for the circadian rhythm of NO production locations.

An expanded cohort of treatment-naïve patients would enable a more detailed observation of differential responses to low-dose ICS. As discussed in Chapter 6, a larger sample size could not only reveal more statistically significant findings but also improve the ability to distinguish between responders and non-responders at the FeNO level. Moreover, a cohort of patients with difficult-to-treat asthma initiating oral corticosteroid (OCS) may help elucidate the reasons for their non-responsive to ICS, including whether depth of NO production contributes to limited ICS effectiveness and results in treatment failure. Furthermore, NO depth measurement in patients with asthma exacerbation may provide insight into the relationship between NO depth parameters and disease severity.

Additionally, studying patients administered anti-IL4Rα allows assessment of changes in NO production location before and after direct iNOS suppression induced by anti-IL4Rα.

8.2 Lung inhomogeneity measured by the CCP

This thesis presents two studies that assess structural alterations in the lungs using inhomogeneity parameters. The first group consisted of apparently healthy volunteers. The findings indicate that elevated biomarkers (FeNO and/or BEC) suggest subclinical

physiological changes in the lung, which are even detectable using traditional methods such as spirometry, although lung inhomogeneity may offer the most sensitive results. The second group includes patients undergoing treatment with low-dose ICS or systemic corticosteroid (SCS). The findings show that lung inhomogeneity changed during the interventions in both groups, whereas spirometry failed to detect these alterations in the ICS group, underscoring the potential of lung inhomogeneity for more sensitive disease monitoring.

A large sample study is needed to confirm the relationship between lung function, particularly lung inhomogeneity, and biomarkers. Moreover, a longitudinal study is needed to examine whether elevated biomarkers are associated with airway morbidities while simultaneously identifying the most effective lung function test for detecting and predicting the presence of these morbidities.

8.3 Concluding remarks

This thesis presents a novel methodology for determining NO production sites in the conducting airways, highlighting its advantage in highly accurate measurements, precise computation and potential clinical implementations. It also contributes to the development of lung inhomogeneity parameters, particularly in identifying subclinical airway physiological alterations.

Appendix A

Standard Operating Procedure (SOP) for the Rapid FeNO Device (RFD)

This document is a copy of the SOP for the Rapid FeNO Device (RFD; FeNO: fractional exhaled nitric oxide), which provides detailed and practical instructions for using the RFD to collect NO depth data. The SOP reflects the challenges and solutions associated with operating the RFD, a completely new device transitioning from laboratory to clinic applications. While this thesis presents a well-structured framework for measuring NO depth parameters, daily applications are instructed by this step-by-step SOP. This SOP integrates the relevant contents from Chapter 2, Chapter 3 and Chapter 4, reorganises them to follow the temporal sequence within NO depth measurement, and ultimately enables standardised and precise data collection.

Standard Operating Procedure (SOP) for the Rapid FeNO Device (RFD)

Pre-heating the machine

- Start the power supply: turn on all the power switches.
- Position the RFD in a suitable location for conducting the test.
- Start the laptop.
    - The laptop is labelled with the 'FeNO LGA'.
    - Connect the two leads to the USB ports on the laptop
    - Start the laptop (Username: g****** and Password: h******) and start the software (FeNO.exe, in the middle of the Desktop)
    - Wait until the QCL reaches 450 mA (**please wait for this step to complete before continuing to the next step**)
- Start the pump (**please follow the order of steps**)
    - The pump is located in the locked cupboard of the RFD. Use the key to unlock the cupboard.
    - Step 1: turn on the switch of the pump (Figure 1, Green circle)
    - Step 2: Wait 5 seconds, then turn on the manual valve at the pump (red circle), and close the RFD cupboard.
    - Step 3: turn on the manual valve near the head, in the connecting tube between the head and cavity.

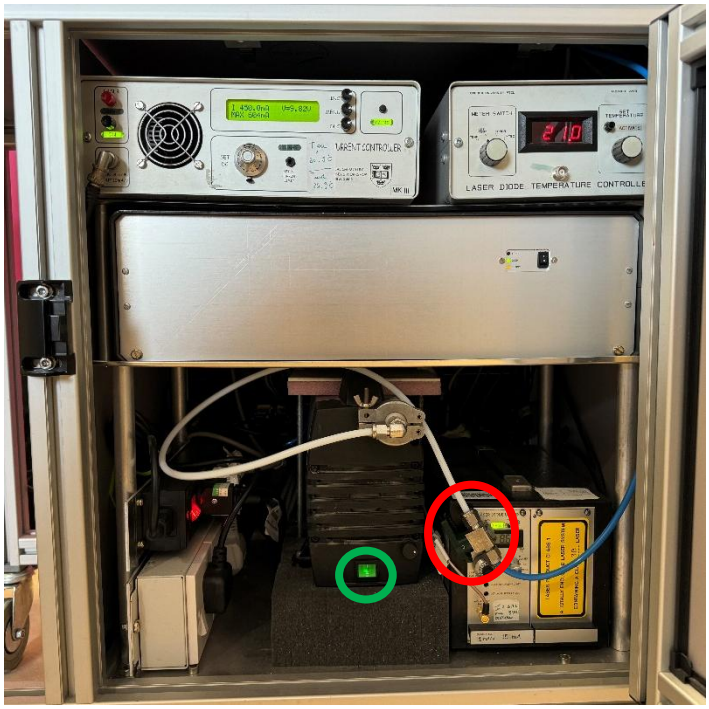


Figure 1 The structure inside the trolley

- Locate the 'Write data to file' option in the software and deselect it(see **Figure 2)**. It is located under 'gear icon' (red box in **Figure 2**) and the tab 'Other' (purple box). The

home screen will display ‘Not saving data’. Run the software (click the green arrow to start, blue box) without recording data for about 45 minutes.

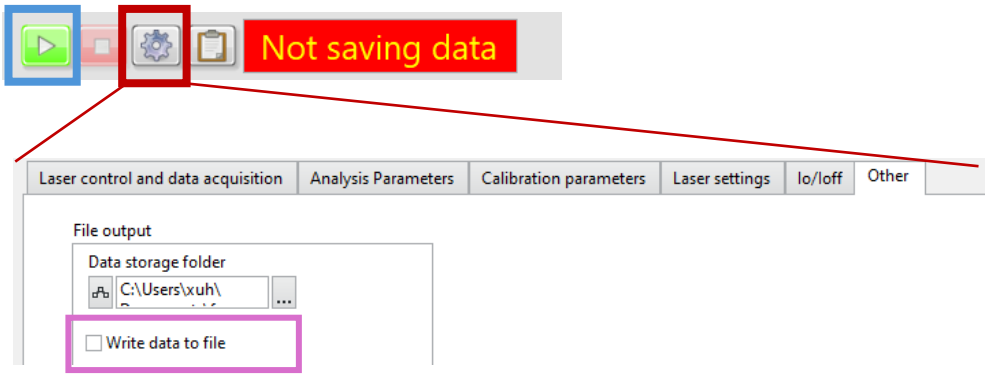


Figure 2 Partial interface of FeNO software

- Check the peak of the laser 15 minutes after starting the run(**Figure 3**, green box). The H_2O peak should lie between 300 – 400 ms. If it is not within this range, increase or decrease the QCL current (Red box) by 1 mA. The option is located at the bottom left of the page (see **Figure 3** below). The adjustment of QCL direction is opposite to the peak's movement)

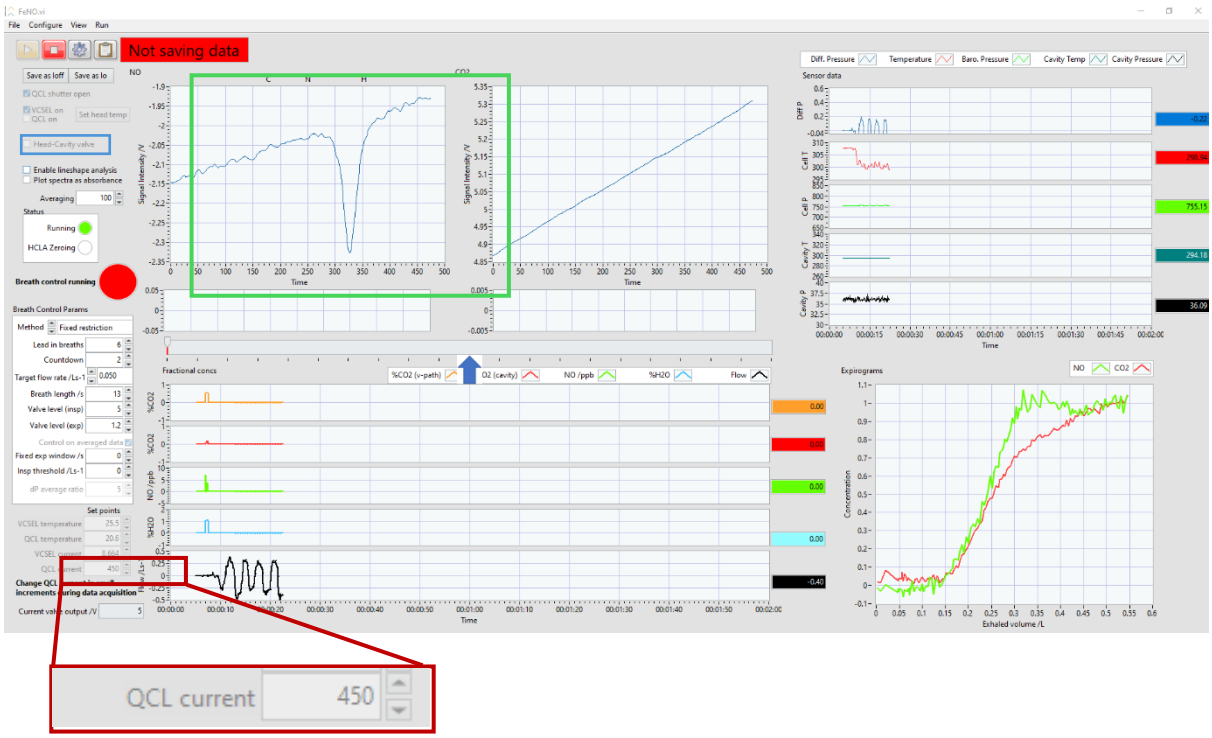


Figure 3 Full interface of FeNO software

Calibration of the RFD

- Locate the ‘Write data to file’ option again and select it to record data for calibration and measurement.

- Click ‘Calibration’ in the ‘Configuration’ tab.
- Ventilate with N_2 at a flow rate of 5 L/min.
- Wait until the dialogue box pops up, then ventilate with 5% CO_2 mixed gas before clicking ‘Continue’ in the dialogue. Give a low flow to calibrate with CO_2 flow. Wait until the dialogue box pops up, indicating that calibration is finished. Press the ‘OK’ button to close the dialogue.
- Test of calibration results
    - Starting running the software
    - Select ‘Head-cavity valve’ (**Figure 3**, blue box, left panel of interface)



    - Open the CO_2 mixed-gas valve and check whether the measurement and regression curves align. Also, check whether the cavity CO_2 and head CO_2 are at a similar level.
    - Stop the running program.
- If calibration is not successful, repeat the calibration process again.

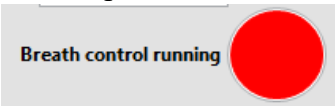
Performing the RFD Test

- Explain the use of a mouthpiece, nose clip, etc.
- Let participants sit in a position that is as comfortable as possible. The head of RFD can be adjusted vertically and horizontally, although with a limited horizontal range. To adjust vertically, release the handle (red circle) first, then adjust the location and tighten the handle again.

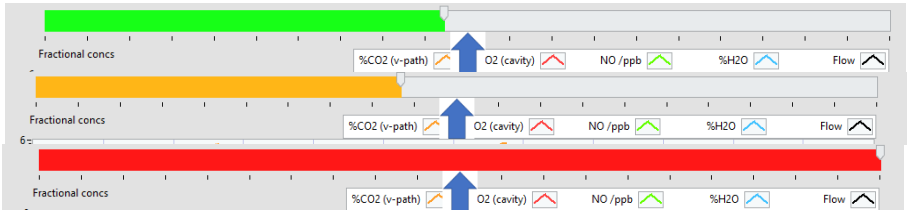


- Start by running the program. Wait until the peak occurs before instructing the participant to bite on the mouthpiece.

- In RFD, the participant will breathe in two ways: normal breathing and special breathing. Normal breathing is a breath without any restriction. Though with normal inhalation, special breathing will make the participants feel restricted in exhalation because of the restrictive valve, which aims to control the exhalation flow rate.
- Start with a normal breath. After every 5 breaths, a special breath will occur.
- When the light (Figure below) becomes amber, remind participants that the next breath is a special breath.



- When the light above becomes green, it indicates that this breath is a special breath. Try to maintain the optimised flow rate (green bar on the indicator, Figure below). If the flow rate is far from the arrow, the bar will show amber or red(Figure below). Remind the participants to resume normal breathing when the light (above) returns to red, as the restrictive valve has turned off. Use the 5 times normal breathing period to check the expirogram to make sure the special breath is roughly correct (both NO and CO_2 curves should be continuous and smooth curves).



- Stop the test by clicking the stop icon (red box) and write in the note (blue box, click the note icon to open a .txt file) the subject ID, FeNO number (from NIOX test), pre/post-BD and time of the test.



- Repeat 7 special breaths in each test, and repeat the test twice, with a short break between the two tests. Typically, one test takes 5-7 minutes.
- Tips (I prefer not telling participants any of the information below, but it can help identify issues when a participant meets problems in creating a qualified breath).
    - Usually, the special breath time for each test should be fewer than 10 times. Some of the participants find this process quite exhausting. Feeling a little light-headed after a test is normal, and rest usually helps with recovery.
    - Sometimes, during the 1st special breath, the software may not correctly regress the NO signal, but most of the time, it returns to normal during the following special breath.
    - Ask participants to try once or twice before officially starting the test
    - As the restricted exhalation flow rate is low, ask participants not to inhale too deeply.

- Adjust the ‘Breaths length /s’ (left panel on screen). It shows the total time length for each special breath (usually starting with 15s). If it is hard to maintain 15s, reduce it; if the CO_2 plateau does not appear, extend the period. I usually adjust it to an increase of 2 s.
- Consider asking participants to keep their tongues still during the special breath.

After measurement

- Deselect ‘QCL On’ in the software to shut down QCL, and wait until the current reads 0 mA.
- Turn off the pump in this order: manual valve near the LGA head, manual valve near the pump and the pump itself.
- Make sure the QCL has already been turned off before switching off the rest of the machine. Push the machine back to the wall and press the brake.
- Ensure all gas cylinders are closed.

Appendix B

Dead Space Pipes (DSP) Model

The goal of the Dead Space Pipes (DSP) model is to generate a series of simulated NO expirograms. The simulation is based on data measured by the Computed Cardiopulmonograph (CCP) and the Rapid FeNO Device (RFD; FeNO: fractional exhaled nitric oxide), under the assumption that NO is produced only at a single point along the conducting airways.

In this Appendix, I present the detailed calculations for the DSP model. I first list all input parameters, output parameters and configuration parameters as a reference in **Table B.1 (Section B.1)**. Following the reference table, I introduce the structure of the DSP model and its associated setups**(Section B.2)**. Then, I describe in detail the steps of this model to simulate the NO expirograms. The model operates in two separate modes, distinguished by whether they account for breath speed variations. I start with a simpler mode, which assumes breath speed is a constant of 50 mL/s (**Section B.3**). This version is referred to as the Speed-independent(SpIn) mode. After becoming familiar with SpIn modes, I then extend the model to account for variations in breath speed, naming this version as the Speed-dependent (SpD) mode (**Section B.4**).

B.1 Input, output and configuration parameters

For clarity, all parameters and their sources are summarised in a reference chart in **Table B.1**. All parameters are arranged in the form of a matrix during calculation, with rows and columns, while calculations involve only elementwise operations.

Table B.1 Parameter settings of the model

Parameters	Shape (rows × columns)	Source	Contents
Input parameters			
C_{p_PDS,CO_2}	1×1	Calculation	CO_2 concentrations at production site (alveolar CO_2).
V_{d,CO_2}	1×1	Calculation	CO_2 production depth, equals V_{PDS_EI}.
$C_{plateau,NO}$	1×1	Calculation	NO concentration at plateau stage. $C_{plateau,NO}$ is acquired by the average of NO concentration in the last 25% of exhaled volume.
$V_{d,NO}$	1×1	User setting	NO production depth occupying volume, ranging from 0% to 100% of V_{PDS_EI}. 0% indicates the NO production location is the same as the top of PDS.
Vol_data_In	$1 \times N_{in}$	Measurement	Inhalation volume data N_{in}, number of inhalation time points
Vol_data_Ex	$1 \times N_{ex}$	Measurement	Exhalation volume data N_{ex}, number of exhalation time points
Fitting parameters			
dV	1×1	Fitting	The dead space volume correction accounts for the expansion of the PDS volume during inhalation. It is obtained by fitting the CO_2 expirograph.
Output parameters			
$C_{s,gas}$	$1 \times N_{ex}$	Calculation	Target gas concentration at the sensor level
Configuration parameters			
ΔT	1×1	RFD setup	The time interval for measurement, 0.1s
F_{V_DDS}	$N_j \times 1$	CCP*	Fraction of volume for pipes in DDS. $Nj = 11$, number of DDS pipes.
F_{f_DDS}	1×1	CCP	Fraction of flow for pipes in DDS.
F_{V_PDS}	$N_i \times 1$	CCP	Fraction of volume for pipes in PDS. $Ni = 125$, number of PDS pipes.
F_{f_PDS}	$N_i \times 1$	CCP	Fraction of flow for pipes in PDS
V_{DDS}	1×1	CCP	Total volume of DDS
V_{PDS_FRC}	$N_i \times 1$	CCP	Volume of each PDS pipe at FRC
V_{PDS_EI}	$N_i \times 1$	CCP	Volume of each PDS pipe at end-inspiration.

*CCP: Computed Cardiopulmonography.

B.2 General principles of the DSP model.

This section starts with an introduction to the structure of the DSP model and its configurations, followed by assumptions made for the model. The gas column and the Reference Point selection are two key concepts that aid in understanding the following calculation steps. After clarifying these concepts, I will define the general function *g()*, which resolves the gas concentration array(i.e., expirogram) based on the independent variables.

B.2.1 Structure of DSP

B.2.1.1 Structure at FRC status

From top to bottom, the DSP model includes the following components in sequence: the sensor layer, the device dead space (DDS), the mixing layer, the personal dead space (PDS) and the alveoli (not modelled). **Figure B.1** illustrates the structure of the DSP.

(1) The sensor layer: This is where the sensor obtains parameters such as gas concentration, volume, pressure, and temperature every 100ms. The gas concentration expirograph is the gas concentration at this level ($C_{s,gas}$) with the variation with exhaled volume (*Vol_data_Ex*).

(2) The DDS: Composed of $Nj = 11$ pipes with a total volume of V_{DDS}. The j^{th} DDS pipe has its own fraction of volume ($F_{V_DDS}(j)$) but shares the uniform fraction of flow (F_{f_DDS}).

(3) The mixing layer: Enables a full mixing status of gases from PDS and occupies no volume.

(4) The PDS: Consists of $Ni = 125$ pipes, i^{th} pipe has a volume of $V_{PDS_FRC}(i)$ at FRC. It has its own fraction of volume ($F_{V_PDS}(i)$) at FRC and its own fraction of flow ($F_{f_PDS}(i)$).

(5) The alveoli: It is a chamber that provides a homogenous gas mixture, while its volume is not considered in this model. CO_2 concentration will remain fixed in the alveoli within each breath. The NO concentration will be assumed to be zero in the alveoli.

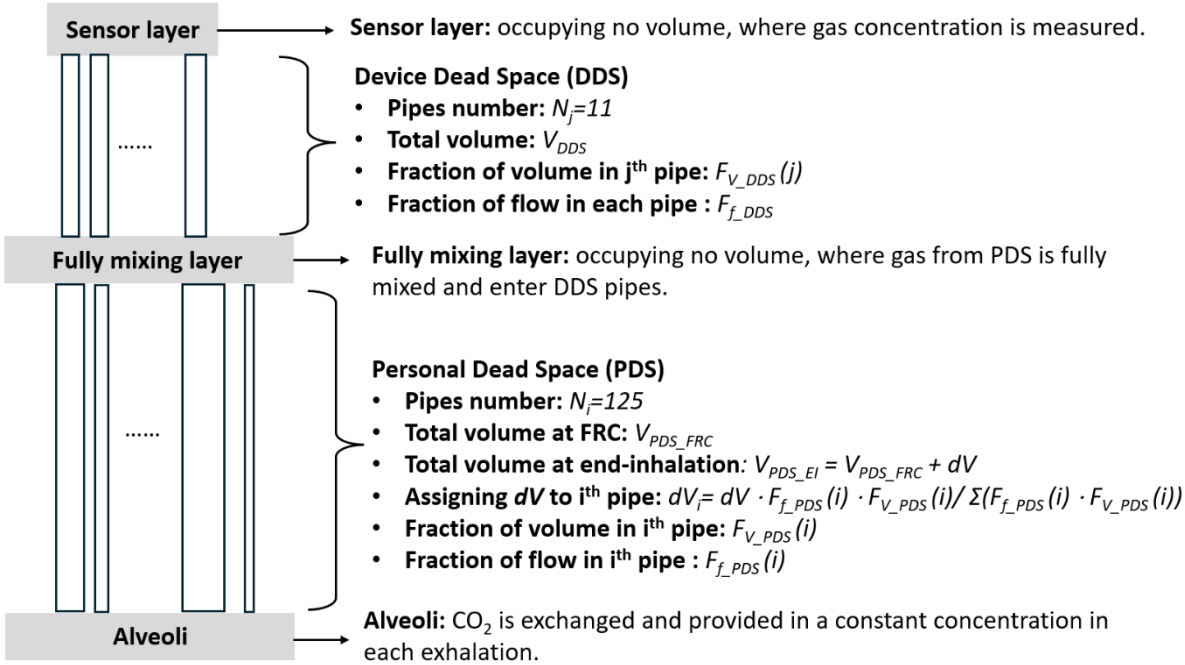


Figure 8.1 The structure of DPS model. From top to bottom, the DSP model includes the following components in sequence: the sensor layer, the device dead space (DDS), the mixing layer, the personal dead space (PDS) and the alveoli (not modelled).

B.2.1.2 Structure of DPS model at end-inhalation status

When a participant inhales, the PDS expands, while the volume of the DDS remains in the same as at FRC. The PDS volume at the end of inspiration is defined as the sum of the PDS volume at FRC status and *dV*, a correction to the dead space volume during inhalation. The *dV* value is assigned to each PDS pipe by the following equation, indicating that it is proportional to both the exhalation speed and volume of each pipe,

$$dV_i = dV \cdot F_{f_PDS}(i) \cdot F_{V_PDS}(i) / \Sigma(F_{f_PDS}(i) \cdot F_{V_PDS}(i)). \quad \text{(B.1)}$$

The volume of i^{th} PDS pipe at the end-inspiration point is

$$V_{PDS_EI}(i) = V_{PDS_FRC}(i) + dV_i \quad \text{(B.2)}$$

The purpose of defining a parameter dV is to adjust breath-specific expansion of dead space. The V_{PDS_FRC} originates from the outputs from CCP, which estimates the dead space volume at FRC. However, consciously or unconsciously altered breathing behaviour is expected during the special breath manoeuvre performed with the RFD, making the value inaccurate if we directly use the end-inspiration dead space volume provided by the fitted CCP outputs.

B.2.2 Assumptions on NO production site

In participants' airways, it is expected that the NO is produced across a range of regions rather than from one point. However, as mentioned in the main text, the modelling approach simulates NO expirograms by assuming that NO is produced only from a single point in the PDS. Therefore, the NO is assumed to be produced at $V_{d,NO}$, where $V_{d,NO}$ varies from 0 to $\sum V_{PDS_EIN}$. In **Figure B.1**, the NO production location should be located within the PDS range (between the mixing layer and alveoli). If NO production location is at the edge closest to the mixing layer, $V_{d,NO}$ equals 0% of the PDS.

B.2.3 Gas column and selection of Reference Point

The DSP model assumes plug flow within each DDS and PDS pipe, neglecting gas diffusion. Based on this assumption, the gas exhaled from each pipe can be visualised as a gas column that can be divided into segments according to time intervals (100ms in the DSP model), as shown in **Figure B.2**. The gas column index is a sequential numbering for these segments, starting from 0. The indices enable us to track and account for the segments. Since each segment forms over a fixed time interval (0.1s), the gas column index is proportional to time. For example, 2nd segment which has an index of 2, is the segment of gas that emerged from the pipe during the interval from 0.1s to 0.2s.

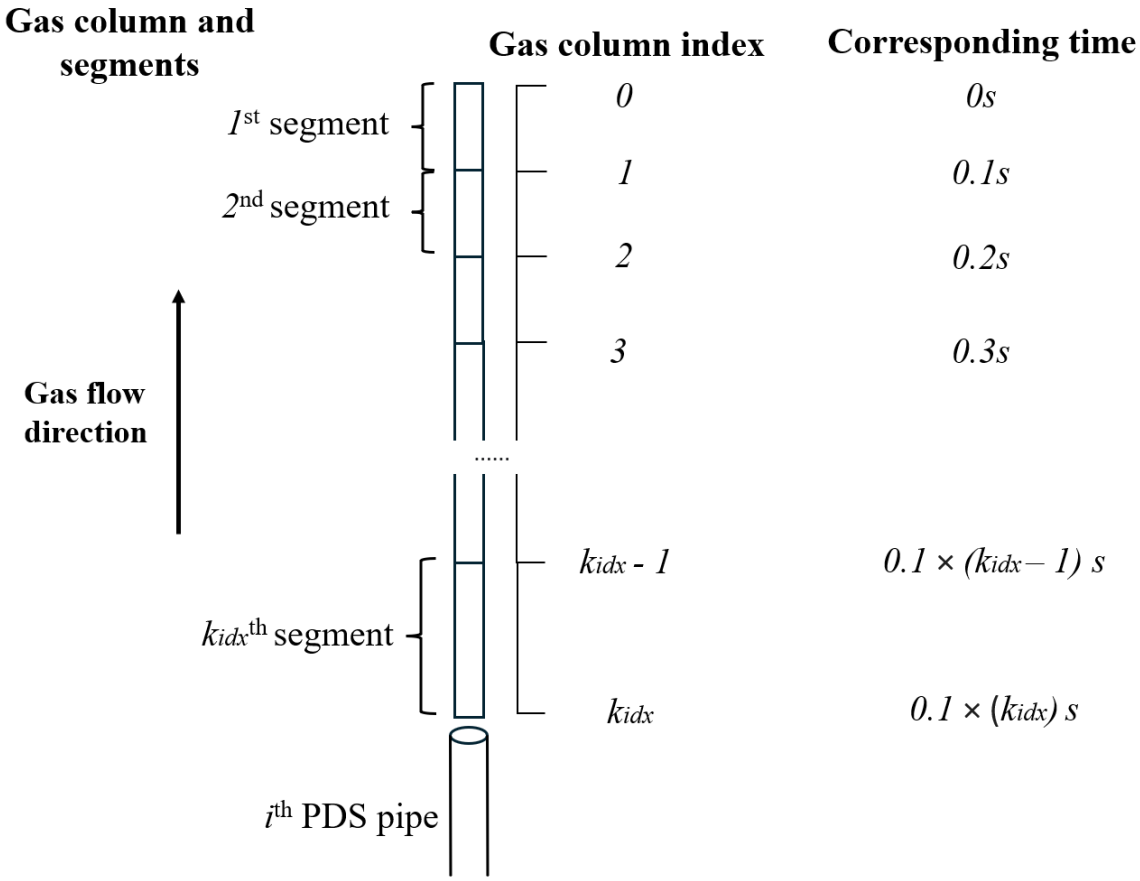


Figure 8.2 Gas column and segments. The gas column index accounts for the number of segments, which is proportional to the time scale. Each segment contains the gas flow through during 0.1s time. Therefore, it has its own volume, CO_2 amount and NO amount. From the attributes listed above, the cumulative volume and gas concentration can also be calculated.

However, selecting a Reference Point is necessary to determine how much gas is exhaled and which segment it belongs to. A Reference Point specifies the location and time from which exhaled gas is measured or defines the zero point for the index. I uses underline to underscore the selected Reference Point location and times, The cumulative volume means the total volume of gas that has flowed through the Reference Point location after the Reference Point time. Suppose we used the notation of k_{idx} as an index for a segment of gas based on a defined Reference Point. $k_{idx} = 1$ represents the first segment flow through the Reference Point location after Reference Point time (i.e., at $1 \cdot \Delta T$). Sequentially, the $k_{idx} = 5$ is the fifth segment going through the Reference Point location after Reference Point time

(i.e., at 5 $\cdot \Delta T$). Changing the Reference Point time or location alters the segment index accordingly, as detailed in the following sections.

B.2.3.1 Shift of Reference Point time

One example is demonstrated in **Figure B.3**, in which we have selected the start of exhalation (time) and the NO production site (location) as the Reference Point (Reference Point A).

If we shift the Reference Point to 0.3s after the start of the exhalation while keeping the location at the NO production site (Reference Point B), the cumulative volume will only include exhaled volume from 0.3s onwards until $k_{idx} \cdot \Delta T$(the greyed segments under Reference point B are excluded as they occur before Reference Point time). The newly defined index, k_{idx}', will set the NO production site and 0.3s after the start of the exhalation as 0 ($k_{idx}' = 0$). The relationship between indices is $k_{idx} = k_{idx}' + 3$.

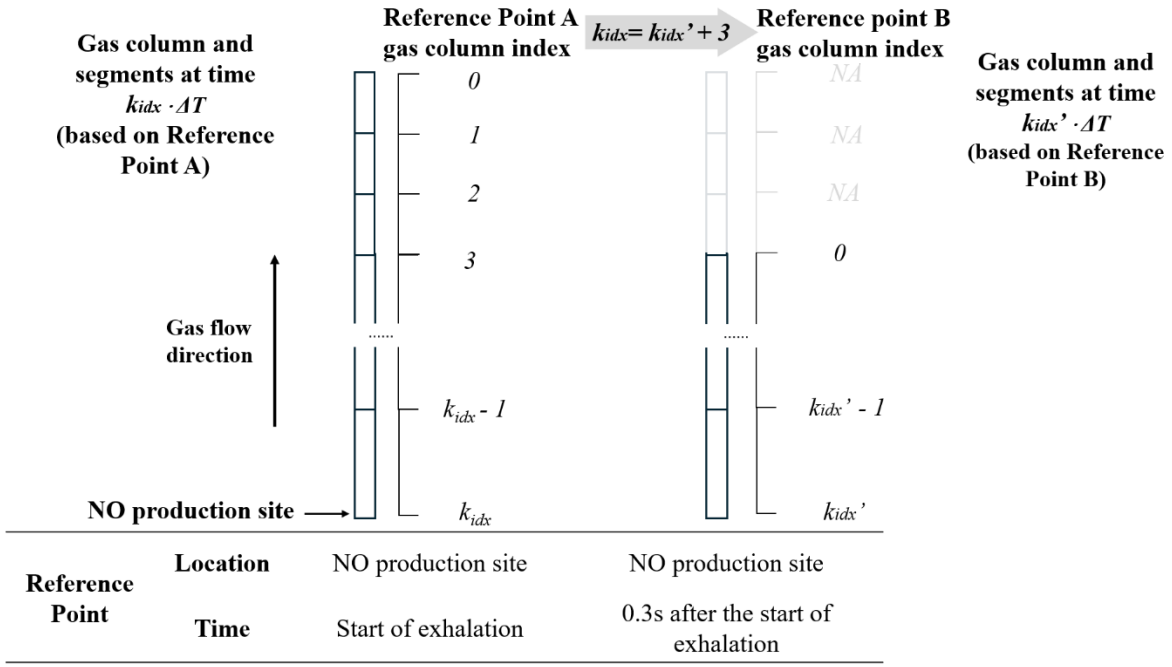


Figure 8.3 Schematic diagram of segments in exhalation in a certain pipe. This Figure shows when time equals $k_{idx} \cdot \Delta T$ after Reference Point 1 time *or* $k_{idx}' \cdot \Delta T$ after Reference Point 2 time gas segments distributions. Each segment is the gas going through the Reference Point location during ΔT time. The cumulative volume count starts at Reference Point time. The index marks the number of segments counting from Reference Point time, while the actual number equals index + 1. The calculation of volume, cumulative volume, as well as gas concentration depends on the selection of

the Reference Point. k_{idx}: index based on Reference Point A, k_{idx}' : index based on Reference Point B. The selection of a Reference Point, even when the location is unchanged, will affect the calculation of cumulative volume and gas amount. ,

B.2.3.2 Shift of Reference Point location

Alternatively, as demonstrated in **Figure B.4**, if a change in Reference Point location is involved, the relationship between the indices of these two gas columns becomes more complex. Suppose we choose a point ΔV above the NO production site as Reference Point C, while maintaining the Reference Point time the same as Reference Point A, which means $k_{idx} = k_{idx}'$. At Reference Point C, the gas column index, segments' volume and cumulative volume are expected to be the same as NO production site.

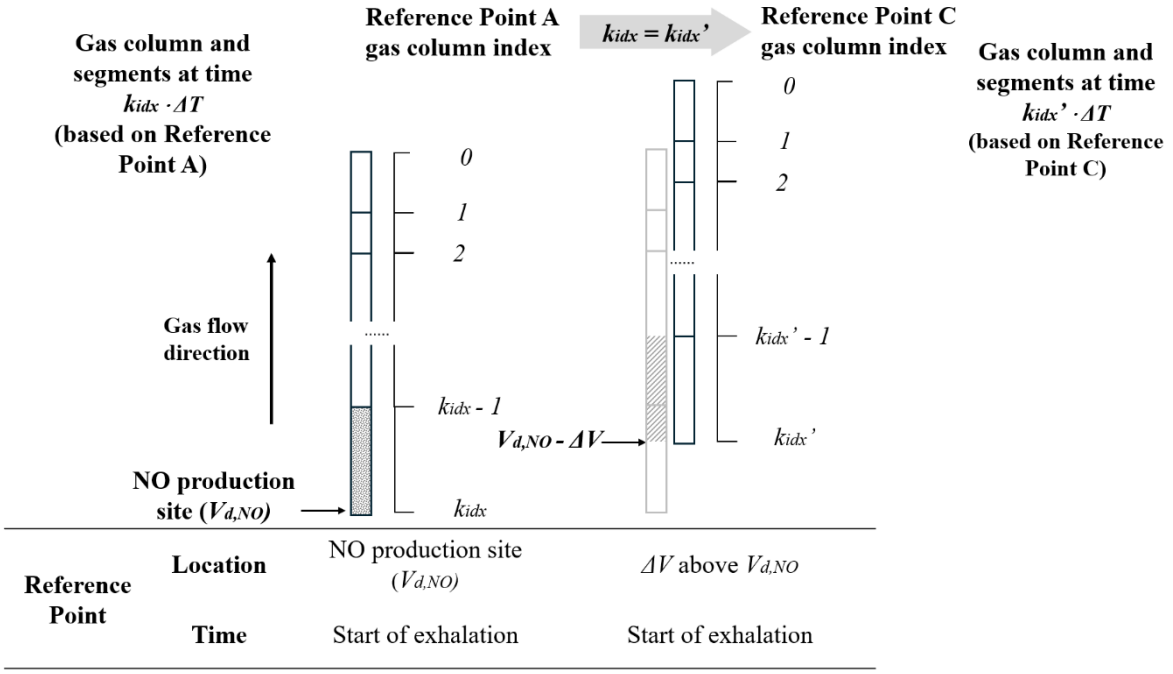


Figure 8.4 Shift of Reference Point location and its effects on the attributes of gas column segments. The Reference Point location has been shifted from NO production site to ΔV above the NO production location. The index has been maintained the same due to Reference Points time has kept the same. The attributes change has been demonstrated in **Table B.2**. The black-lined gas columns are gas columns based on two different Reference Points. The grey-edged gas column shows a parallel gas column from Reference Point A reflecting its NO distribution on Reference Point C, with the slash-shaded area being the amount of NO in the segment k_{idx}'.

However, the NO amount in segments needs to be adjusted when a different Reference point is chosen, as shown in **Figure B.4**. At the k_{idx}^{th} and $k_{idx}{}'^{th}$ segment, the amount of NO molecules represented by dot-shaded part when using Reference Point A, while it is represented by slash-shaded part from the grey-edged gas column if using the Reference point C. The relationship between the NO amounts when different Reference points are chosen will be discussed in the following section. To clarify the attributes associated with the two Reference Points, I have listed them in **Table B.2** to provide a comprehensive overview.

Table B.2 Attributes based on Reference Point A and Reference Point C.

Attributes	Reference Point A	Reference point C	Relation between A and C
Segment's volume	$V_A(k_{idx})$	$V_C(k_{idx}')$	Equal
Segment's cumulative volume	$V_{A,cum}(k_{idx})$	$V_{C,cum}(k_{idx}')$	Equal
Amount of NO	$A_{A,NO}(k_{idx})$	$A_{C,NO}(k_{idx}')$	$A_{C,NO}(k_{idx}')$ equals slash-shaded area in **Figure B.4**
Concentration of NO	$C_{A,NO}(k_{idx})$	$C_{C,NO}(k_{idx}')$	Calculated from amount and volume

B.2.4 Definition of gas concentration with exhaled volume function

I define the function to show what input values are required to output the gas concentration array. The established concepts of gas columns and Reference Points facilitate the calculation process of the function.

For CO_2 the concentration at the sensor layer ($C_{s,NO}$) can be written as,

$$C_{s,CO_2} = g_{CO_2}(C_{plateau,CO_2}, V_{d,CO_2}, Vol_data_In, Vol_data_Ex), \quad \text{(B.3)}$$

with notations are listed in **Table B.1.**

In ***Eq. B.3***, the $C_{plateau,CO_2}$ is the same as the alveolus CO_2 value and V_{d,CO_2} is a constant equal to ΣV_{PDS_EIN}. The ΣV_{PDS_EIN} is the sum of dV and V_{PDS_FRC}, where dV is the only unknown variable in ***Eq. B.3.*** The fitting of the simulated CO_2 expirograph with the measured CO_2 expirograph will provide the value for dV.

For NO, the concentration at the sensor layer ($C_{s,NO}$) can be written as,

$$C_{s,NO} = g_{NO}(C_{plateau,NO}, V_{d,NO}, Vol_data_In, Vol_data_Ex) \quad \text{(B.4)}$$

where the notation is listed in **Table B.1**.

The $C_{plateau,NO}$ is the NO concentration average of the last 25% exhaled volume. The $V_{d,NO}$ ranges from 0% to 100% of ΣV_{PDS_EIN}. With all independent variables determined, the $C_{s,NO}$ can be calculated.

In the following section, I will use NO as an example to explain the calculation process, both in SpIn and SpD modes. The model for CO_2 follows the same process as SpIn modes with V_{d,CO_2} is a constant in the calculation.

B.3 SpIn mode

To distinguish SpIn and SpD modes, I substitute $g_{NO}()$ with $g_{SpIn}()$ in the ***Eq. B.4***

$$C_{s,NO} = g_{SpIn}(C_{plateau,NO}, V_{d,NO}, Vol_data_In, Vol_data_Ex). \quad \text{(B.5)}$$

During the plateau phase, all PDS pipes contribute to the NO molecules. The NO production site concentration ($C_{p_PDS,NO}$) in each pipe can be expressed as, if we assume each pipe NO production rate is identical,

$$C_{p_PDS,NO} = C_{plateau,NO} \quad \text{(B.6)}$$

For i^{th} PDS pipe, its top end (where the exhalation gas flows to the mixing layer) NO concentration ($C_{top_PDS,NO}$) can be expressed as a step function,

$$C_{top_PDS,NO}(i) = \begin{cases} 0, & \text{if } V_{top_PDS,cum} < V_{PDS_EI}(i), \\ C_{p_PDS,NO}, & \text{if } V_{top_PDS,cum} \geq V_{PDS_EI}(i). \end{cases} \quad \text{(B.7)}$$

where $V_{top_PDS,cum}$ is the cumulative volume at the top of PDS, V_{PDS_EI} is the volume of that PDS pipe at end-inspiration.

The mixing process is represented as,

$$C_{mix,NO} = \sum F_{f_PDS}(i) \cdot C_{top_PDS,NO}(i). \quad \text{(B.8)}$$

where $C_{mix,NO}$ is the mixing layer NO concentration.

Following full mixing at the mixing layer, each DDS pipe is assigned with the same concentration of NO, meaning there is a constant centration of gas (C_{p_DDS}) gas enters the DDS,

$$C_{p_DDS} = C_{mix,NO} \tag{B.9}$$

Similarly, the concentration at j^{th} DDS pipe top ($C_{top_DDS,NO}$) can be expressed as

$$C_{top_DDS,NO}(j) = \begin{cases} 0, & \text{if } V_{top_DDS,cum} < V_{DDS} \cdot F_{V_DDS}(j), \\ C_{p_DDS,NO}, & \text{if } V_{top_DDS,cum} \geq V_{DDS} \cdot F_{V_DDS}(j). \end{cases} \tag{B.10}$$

where $V_{top_DDS,cum}$ is the cumulative volume at the top of DDS, V_{DDS} is the total volume of DDS, F_{V_DDS} is the fraction of volume in pipes of DDS.

Sequentially, the sensor level concentration is calculated as,

$$C_{s,NO} = \sum F_{f_DDS}(j) \cdot C_{top_DDS,NO}(j). \tag{B.11}$$

In SpIn modes, the $C_{s,NO}$ is independent of Vol_data_Ex(t) and Vol_data_In(t). We can see that the volume profile is not involved in the calculation of $C_{s,NO}$ in ***Eq. B.7*** to ***B.11***.

B.4 SpD mode

In SpD mode, when breath speed is takin into consideration, the equation can be expressed as follows,

$$C_{s,NO} = g_{SpD}(C_{plateau,NO}, V_{d,NO}, Vol_data_In, Vol_data_Ex) \tag{B.12}$$

The process is composed of four steps:

(1) Step 0: Calculation of the NO production rate, r_0.

(2) Step 1: At the end of inhalation, a portion of NO molecules remains stored in the conducting airways, not eliminated by alveolar perfusions, also contributing to the NO concentration in the exhaled gas. This step estimates the influence of residual NO

from inhalation on the exhaled NO concentration. It involves switching the Reference Point time from the start of inhalation to the start of exhalation.

(3) Step 2: Calculate the NO concentration at the production site in exhalation gas segments, including contributions from epithelial NO production and residual NO from Step 1. The Reference Point is selected at the NO production site at the start of exhalation.

(4) Step 3: Switching the Reference Point location from the NO production site to the top of the DDS, accompanied by re-assigning the NO-containing segments. Re-assignment is conducted at the top of the PDS, the bottom of the DDS, and the top of the DDS.

The goal of each step is to determine the corresponding volume, cumulative volume, NO amount, and NO concentration based on the selected Reference Point.

B.4.1 Step 0: Calculation of NO production rate, r_0

The NO production rate is calculated from the plateau concentration of NO, as we assume that at the plateau stage, NO produced from all pipes has emerged at the sensor layer. Thus, the total production rate across all PDS pipes, $r_{0,sum}$, can be expressed as,

$$r_{0,sum} = C_{plateau,NO} \cdot V_{plateau} / t_{plateau} \quad \text{(B.13)}$$

where $V_{plateau}$ is the last 25% of exhaled volume, and $t_{plateau}$ is the corresponding time.

We also assume that each PDS pipe produces NO at the same rate,

$$r_0 = r_{0,sum} / N_i, \quad \text{(B.14)}$$

where N_i is the pipe number of PDS. Currently, N_i =125.

B.4.2 Step 1: Estimation of the effect of inhalation residual NO on exhaled gas

B.4.2.1 Construction of inhalation gas column

When the Reference Point is selected at the NO production site at the start of inhalation, the indexes of inhalation gas columns are represented as h_{idx}. Only gas segments that remain between the NO production site and the bottom of the PDS at end-inhalation contain NO molecules, as illustrated in **Table B.5**. Segments above the NO production site have not encountered NO, and segments below the bottom of the PDS have entered the alveoli, where NO is diminished by blood flow, as mentioned in the model assumptions. **Figure B.5** illustrates residual gas stored in conducting airways, which contains NO molecules.

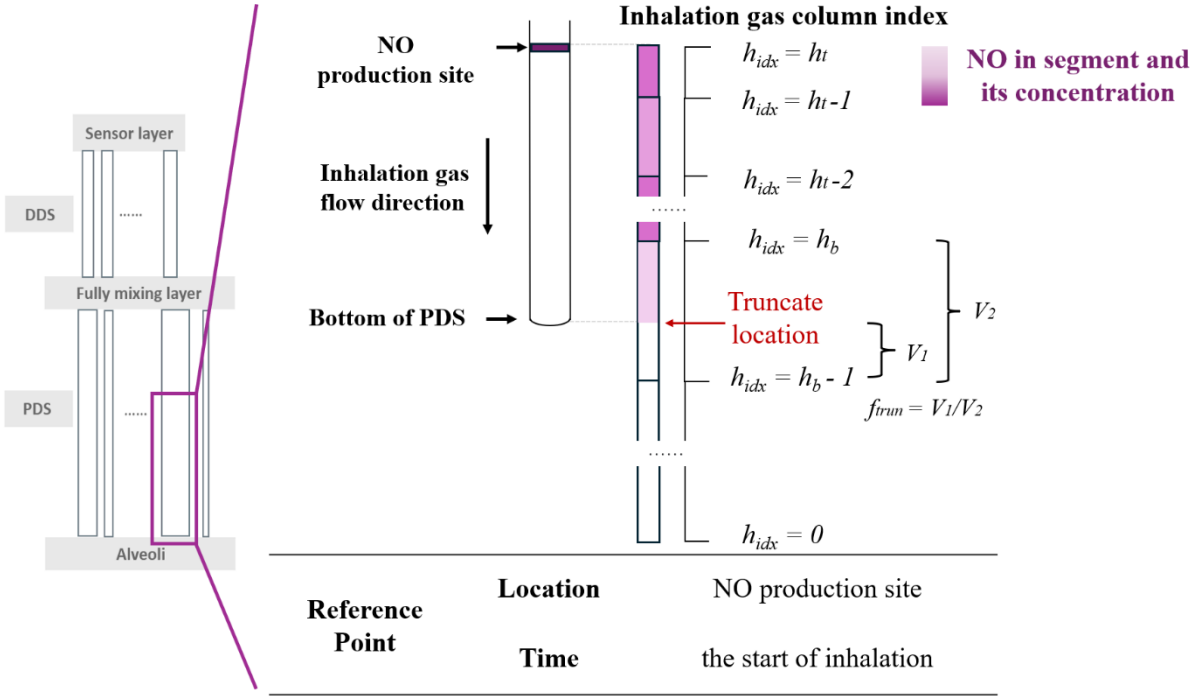


Figure 8.5 Inhalation residual gas column determination. The purple colour indicates the NO molecules in the gas segments. Due to variations in inhalation speed, different segments have different concentrations of NO, while the amount of NO is the same in each segment. The truncate point marks the boundary between deadspace and alveolus(not shown in the Figure). If a gas segment enters the alveolus, the entered part will have zero for NO concentration.

The volume of h_{idx}^{th} segment in i^{th} pipe ($V_{in}\ (i,h_{idx})$) can be defined as,

$$V_{in}\ (i,h_{idx}) = Ff_{_PDS}(i) \cdot (Vol_data_In(h_{idx}) - Vol_data_In(h_{idx} - 1)) \quad \text{(B.15)}$$

where $h_{idx} = 1,2,3\ to\ h_t$, with h_t being the last index of h_{idx} , when the inhalation is finished.

Sequentially, the cumulative volume of h_{idx} th timepoint in i^{th} pipe ($V_{in,cum}(i,hidx)$) is,

$$V_{in,cum}(i,h_{idx}) = \Sigma V_{in}(i,n)\ (n=1,2,3,\ \dots\ ,h_{idx}) \tag{B.16}$$

However, estimating the amount of NO in each segment is more challenging when the bottom of the PDS truncates a segment partway. To accurately account for the truncated segment, the fractional volume of the segment that remains within the PDS must be calculated. In that segment, the upper portion retains the NO molecules, while the lower portion has lost NO to the alveoli. This approach ensures the conservation of mass.

To facilitate this, we define a function $f()$ to find the adjacent index (idx_{target}) in an original sorted array ($Y_{original}$), under the condition that the target value (X_{target}) satisfies the following equation:

$$Y_{original}(idx_{target}-1) < X_{target} <= Y_{original}(idx_{target}). \tag{B.17}$$

The function can be written as

$$idx_{target} = f(Y_{original}(:), X_{target}), \tag{B.18}$$

where the symbol ' $:$ ' represents all elements of the array, the same as follows.

Using the NO production site and the start of inhalation as the Reference Point, we can apply ***Eq. B.18*** to find the target index, h_b (illustrated in **Figure B.5**), in i^{th} pipe of PDS,

$$h_b = f(V_{in,cum}(i,\ :\ ),\ V_{res}), \tag{B.19}$$

where $V_{res} = V_{in,cum}(i,\ h_t\ ) - (V_{PDS_EI}(i) - V_{d,NO})$ gives the different volume between index = 0 location to the bottom of PDS.

The fraction of truncation in h_b *-1* to h_b segment (f_{trun}) can be calculated as

$$f_{trun} = 1 - (V_{res} - V_{in,cum}(i,h_t) + V_{in,cum}(i,h_b)\ )/V_{in}(i,h_b). \tag{B.20}$$

The NO amount in h_{idx} th segment of i^{th} pipe is,

$$A_{in,NO}(i,h_{idx}) = \begin{cases} r_0 \cdot \Delta T, \text{ if } h_b < h_{idx} \leq h_t, \\ (1 - f_{trun}) \cdot r_0 \cdot \Delta T, \text{ if } h_{idx} = h_b, \\ 0, \text{ if } h_{idx} < h_b. \end{cases} \tag{B.21}$$

The NO concentration in this segment is

$$C_{in,NO}(i,h_{idx}) = -A_{in,NO}(i,h_{idx}) / V_{in}(i,h_{idx}), \quad \text{(B.22)}$$

and the negative sign is because inhalation is recorded as a negative value.

With an established inhalation gas column and identified residual gas segments in the conducting airways, the gas segments can now be re-indexed to align with exhalation. The Reference Point is set at the NO production site and the start of inhalation, while the index is reversed. **Figure B.6** illustrates the transition from the inhalation gas index to the reversed inhalation gas index, as during exhalation, the gas segments move in the opposite direction compared to inhalation. Suppose l_{idx} is used to demote the index of exhalation gas segments, with $l_{idx} = 0$ indicating the start of exhalation.

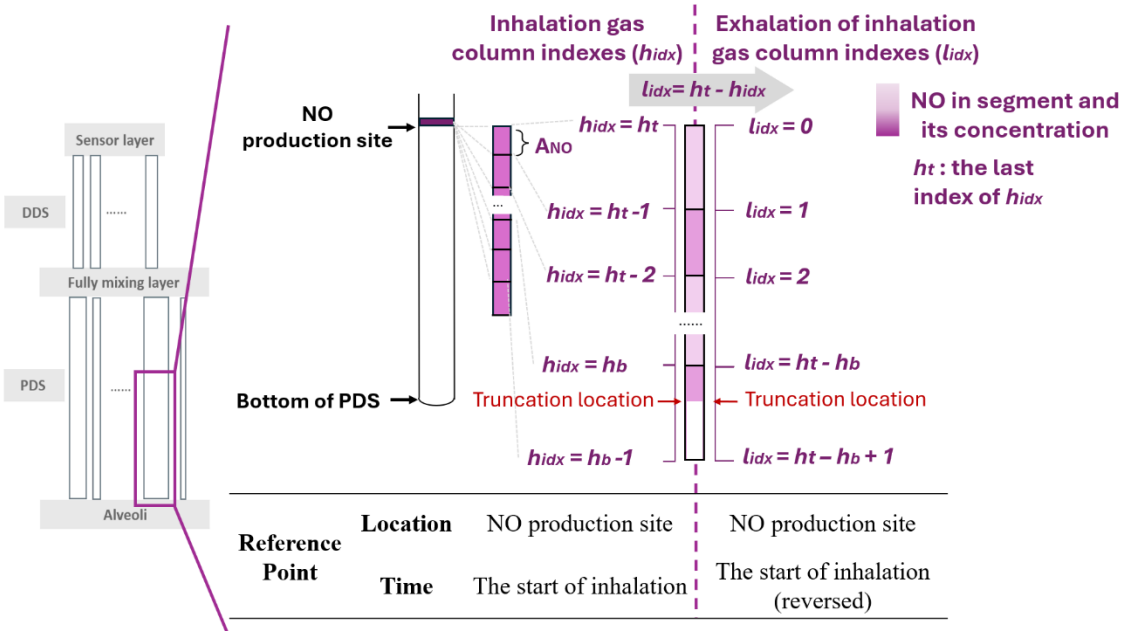


Figure 8.6 Inhalation gas column transition to exhalation gas column. Inhalation gas column index(h_{idx}): the indexes of inhalation gas column. Exhalation of inhalation gas column indexes(l_{idx}): the indexes transitioned from h_{idx} due to transition between inhalation to exhalation. The inhalation volume and NO concentration is $V_{in}(i,h_{idx})$, $C_{in,NO}(i,h_{idx})$. The exhalation stage volume and NO concentration are $V_{in_ex}(i,l_{idx})$ and $C_{in_ex,NO}(i,l_{idx})$. They can be defined if there is known volume profile(Vol_data_In and Vol_data_Ex), as any certain segment's volume and concentration can be found from this profile with an known index. * the two Reference Point times are actually the same time.

The reversion equation between the index of gas is,

$$l_{idx} = h_t - h_{idx}. \tag{B.23}$$

Based on ***Eq. B.23***, the corresponding volume, NO concentration and NO amount for exhalation of the inhalation gas column are, respectively,

$$V_{in_ex}(i,l_{idx}) = -V_{in}(i,h_t - h_{idx}), \tag{B.24}$$

$$C_{in_ex,NO}(i,l_{idx}) = C_{in,NO}(i, h_t - h_{idx}), \tag{B.25}$$

and

$$A_{in_ex,NO}(i,l_{idx}) = A_{in,NO}(i, h_t - h_{idx}). \tag{B.26}$$

The cumulative exhalation volume of the inhalation gas column can be written as,

$$V_{in_ex,cum}(i,l_{idx}) = \Sigma V_{in_ex}(i,n)\ (n= 1, 2, 3, \dots, l_{idx}). \tag{B.27}$$

Table 1.3 presents the parameters and their corresponding calculations, showing the transition between the inhalation gas column and the exhalation gas stage. This process ensures that the calculation accounts for the residual NO from inhalation.

Table B.3 Gas attributes and their calculation equations

Reference Point	**Location**	**NO production site**	**NO production site**
	Time	**The start of inhalation**	**The start of inhalation (reversed)**
Index nomination		h_{idx}	l_{idx}
Segment's volume		$V_{in}(i,h_{idx})$ *Eq. B.15*	$V_{in_ex}(i,l_{idx})$ *Eq. B.24*
Segment's cumulative volume		$V_{in,cum}(i,h_{idx})$ *Eq. B.16*	$V_{in_ex,cum}(i,l_{idx})$ *Eq. B.27*
Segment's NO amounts		$A_{in,NO}(i,h_{idx})$ *Eq. B.21*	$A_{in_ex,NO}(i,l_{idx})$ *Eq. B.26*
Segment's NO concentration		$C_{in,NO}(i,h_{idx})$ *Eq. B.22*	$C_{in_ex,NO}(i,l_{idx})$ *Eq. B.25*
Relationship between indexes		$l_{idx} = h_t - h_{idx}$ *Eq. B.23*	

h_t: last index of h_{idx}.

B.4.2.2 Construction of exhalation gas column

Although the reversed index (l_{idx}) provides the correct occurrence order of gas segments during exhalation, the division of segments changes due to variations in exhalation speed compared to inhalation speed. Therefore, it is necessary to account for the change in speed when calculating gas concentrations. To assist in determining the exact values, the Reference Point is now set at the NO production site and the time at the start of exhalation.

Based on the Reference Point, the aim is to obtain the related attributes, including volume, cumulative volume, the amount of NO molecules and the NO concentration in each gas segment. **Figure B.7** captures a snapshot at $k_{idx} \cdot \Delta T$ time point, where k_{idx} is the index assigned to the blue gas column in the Figure. In k_{idx} th segment, which forms during the most recent ΔT, we denote the volume at NO production site as $V_{p_PDS}(i,k_{idx})$, the cumulative volume as $V_{p_PDS,cum}(i,k_{idx})$, its NO molecule amount as $A_{p_PDS,NO}(i,k_{idx})$ and its concentration as $C_{p_PDS,NO}(i,k_{idx})$.

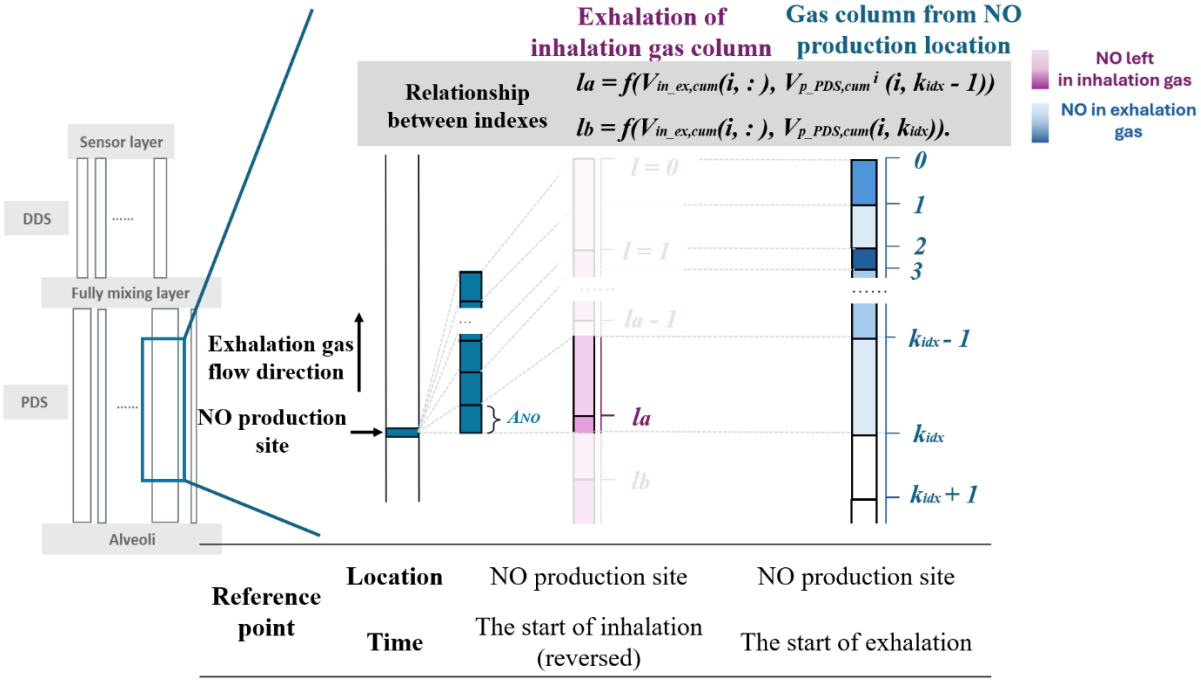


Figure 8.7 Re-assignment of inhalation gas column to exhalation gas column. For both columns of gas, the Reference Point location is the NO production site. But the Reference Point time is different. The purple gas column (index l_{idx}) uses reversed inhalation start as the Reference Point time, while the blue gas column (index k_{idx}) uses the start of exhalation. The non-shaded part in the purple gas column shows the parts of purple gas column segments that should be re-assigned to (k_{idx} -1) $\cdot \Delta T$ to $k_{idx} \cdot \Delta T$ blue gas column segments. The relationship between indexes is constructed by applying

the function $f()$. With l_a and l_b determined, the subsequent attributes, NO amount and NO concentration, can be calculated.

Similar to previous step, $V_{p_PDS}(i,k_{idx})$ is defined by exhalation volume,

$$V_{p_PDS}(i,k_{idx}) = F_{f_PDS}(i) \cdot (Vol_data_Ex(k_{idx}) - Vol_data_Ex(k_{idx} - 1)) \quad \text{(B.28)}$$

where $k_{idx} = 1,2,3, \ldots N_t$, N_t is the last index of exhalation timepoints, with $V_{p_PDS}(i,0) = 0$.

The cumulative volume can be calculated as,

$$V_{p_PDS,cum}(i,k_{idx}) = \Sigma\, V_{p_PDS}(i,n)\ (n = 0, 1, 2, 3 \ldots, k_{idx}). \quad \text{(B.29)}$$

The amount of NO molecules in each segment is the sum of the residual NO from the inhalation gas, $A_{res,NO}(i,k_{idx})$, and the newly produced NO, $A_{new,NO}(i,k_{idx})$,

$$A_{p_PDS,NO}(i,k_{idx}) = A_{res,NO}(i,k_{idx}) + A_{new,NO}(i,k_{idx}). \quad \text{(B.30)}$$

In the above equation, $A_{new,NO}(i,k_{idx})$ is a constant, as NO is assumed to be produced at the same rate:

$$A_{new,NO}(i,k_{idx}) = r_0 \cdot \Delta T. \quad \text{(B.31)}$$

For $A_{res,NO}(i,k_{idx})$, a fluctuating flow rate means the segmentations based on the original Reference Point do not align with the exhalation of inhaled gas column segments. Therefore, re-segmentation is required to match exhalation segments with inhaled gas segmentation. If we only look at one exhalation segment, the $A_{res,NO}(i,k_{idx})$ may include fractions of inhaled gas segments, with or without some entire segments. This process is similar to the truncation from the bottom of PDS in inhalation gas in the previous section, illustrated in **Figure B.7**.

We use the function $f()$ to find the indices l_a and l_b, which correspond to the start and end of the last section of the exhalation gas column, such that:

$$l_a = f(V_{in_ex,cum}(i, :), V_{p_PDS,cum}(i, k_{idx} - 1)), \quad \text{(B.32)}$$

and

$$lb = f(V_{in_ex,cum}(i, :) , V_{p_PDS,cum}(i, k_{idx})). \quad \text{(B.33)}$$

After linking the indices of the two gas columns (purple column and blue column in **Figure B.7**), we can calculate the amount of NO molecule remaining from the inhalation gas column under the exhalation-based segmentation, as follows:

$$\begin{aligned} &A_{res,NO}(i,k_{idx}) = \\ &A_{in_ex,NO}(i,la) \cdot [V_{in_ex,cum}(i,la) - V_{p_PDS,cum}(i, k_{idx} - 1)] / V_{in_ex}(i,la) && Seg.1 \\ &+ A_{in_ex,NO}(i,la+1) + \ldots && Seg.2 \\ &+ A_{in_ex,NO}(i,lb) \cdot [V_{p_PDS,cum}(i, k_{idx}) - V_{in_ex,cum}(i,lb-1)] / V_{in_ex}(i,lb)]. && Seg.3 \end{aligned} \quad \text{(B.34)}$$

where $A_{in_ex,NO}(i,la)$, $A_{in_ex,NO}(i,la+1)$ and $A_{in_ex,NO}(i,lb)$ are given by ***Eq. B.26***, $V_{in_ex,cum}(i,la)$ and $V_{in_ex,cum}(i,lb-1)$ are given by ***Eq. B.27*** and $V_{in_ex}(i,la)$ and $V_{in_ex}(i,lb)$ are given by ***Eq. B.24*** and ***Eq. B.27***.

In ***Eq. B.34***, *Seg.1* represents the NO amount from the la^{th} inhalation gas segment, *Seg.3* represents NO amount from lb^{th} inhalation gas segment and *Seg.2* represents the segments between the la^{th} and the lb^{th} inhalation gas segments. Two special conditions can arise:

(1) if $la = lb$, *Seg.2* does not exist, and the remaining NO in the exhalation gas segment k_{idx} comes entirely from a single inhalation gas segment.

(2) If $Ia+1 = lb$, *Seg.2* also does not exist, and the remaining NO in the k_{idx}^{th} exhalation segment comes from two adjacent inhalation gas segments.

The NO concentration in the $k_{idx}{}^{th}$ segment is given by,

$$C_{p_PDS,NO}(i,k_{idx}) = A_{p_PDS,NO}(i,k_{idx}) / V_{p_PDS}(i,k_{idx}). \quad \text{(B.35)}$$

Similar to the previous section, **Table B.4** gives the attributes of segments based on two Reference Points.

Table B.4 Gas attributes from exhalation of residual inhalation gas and exhalation gas

Reference Point	Location	NO production site	NO production site
	Time	The start of inhalation (reversed)	The start of exhalation
Index nomination		l_{idx}	k_{idx}
Segment's volume		$V_{in_ex}(i,l_{idx})$ Eq. B.24	$V_{p_PDS}(i,k_{idx})$ Eq. B.28
Segment's cumulative volume		$V_{in_ex,cum}(i,l_{idx})$ Eq. B.27	$V_{p_PDS,cum}(i,k_{idx})$ Eq. B.29
Segments NO amounts		$A_{in_ex,NO}(i,lidx)$ Eq. B.26	$A_{p_PDS,NO}(i,kidx)$ Eq. B.30
Segment's NO concentration		$C_{in_ex,NO}(i,lidx)$ Eq. B.25	$C_{p_PDS,NO}(i,kidx)$ Eq. B.35
Relationship between indexes		$la = f(V_{in_ex,cum}(i,:), V_{p_PDS,cum}(i, kidx - 1))$, $lb = f(V_{in_ex,cum}(i,:), V_{p_PDS,cum}(i, kidx))$. Eq. B.32 and Eq. B.33	

B.4.3 Step 2: Re-assignment with a shift in the Reference Point location

B.4.3.1 Re-assignment in segments at the top of PDS pipes

The previous step gives the exhalation gas' attributes when the Reference Point is set at the location of NO production. If we select the Reference Point at the top of the PDS pipes, while keeping the Reference point time at the start of exhalation, the new gas attributes can be expressed as the attributes of the old Reference point plus the time delay between the new and old Reference locations, i.e., the top of PDS pipes and the NO production location.

Most of the attributes are the same between old and new Reference point, as explained in the shift of Reference point location. However, the NO amount in each segment needs to be adjusted as the division of segments has changed when using a different Reference point. m_{idx} is used as the index for the new Reference Point.

We start by writing out the volume and cumulative volume based on the top of PDS pipes as the Reference Point. The cumulative volume is given by,

$$V_{top_PDS,cum}(i,m_{idx}) = Ff_{PDS}(i) \cdot Vol_data_Ex(m_{idx}), \quad \text{(B.36)}$$

The volume of $midx^{th}$ segment is:

$$V_{top_PDS}(i,midx) = V_{top_PDS,cum}(i,midx) - V_{top_PDS,cum}(i,midx - 1), \quad \text{(B.37)}$$

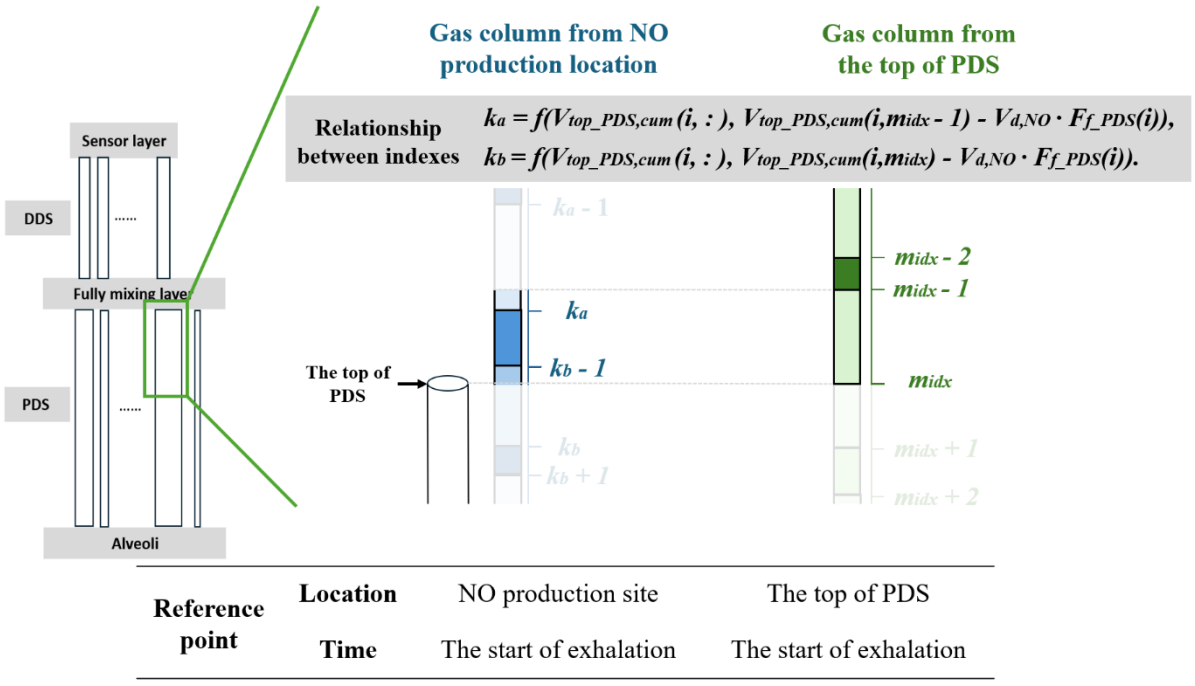


Figure 8.8 Re-assignment of the gas column at the top of PDS. The blue gas column uses the Reference Point at the NO production site (index k_{idx}), and the green gas column uses the Reference Point at the top of PDS(index m_{idx}). The non-shaded part in the blue gas column shows the parts of blud gas column segments that should be assigned to $(m_{idx} - 1) \cdot \Delta T$ to $m_{idx} \cdot \Delta T$ green gas column segments. The relationship between indexes is constructed by applying the function $f()$. With k_a and k_b determined, the subsequent attributes, such as NO amount and NO concentration, can be calculated.

Although volume and cumulative volume remain the same, the NO amount of each segment changes with the shift of Reference Point. When a new Reference Point at the top of the PDS pipes is selected, a difference in the distributions of $V_{d,NO}$ occurs compared to the old Reference Point. We use $f()$ again to identify the index relationship between the old and new Reference Points. Suppose that at the time corresponds to m_{idx} as index based on the new Reference Point, the gas segments of m_{idx} start in $k_a{}^{th}$ segments and end in $k_b{}^{th}$ segment using the old Reference Point, as blue and green columns shown in **Figure B.8**. The relationship

between m_{idx} to k_a or k_b should be, indicating the NO segments is re-assigned based on the Reference Point,

$$k_a = f(V_{top_PDS,cum}(i, :), V_{top_PDS,cum}(i,m_{idx} - 1) - V_{d,NO} \cdot F_{f_PDS}(i)), \quad \text{(B.38)}$$

and

$$k_b = f(V_{top_PDS,cum}(i, :), V_{top_PDS,cum}(i,m_{idx}) - V_{d,NO} \cdot F_{f_PDS}(i)). \quad \text{(B.39)}$$

Thus, the NO molecule amount at the top of PDS is

$$\begin{aligned} &A_{top_PDS,NO}(i, m_{idx}) = \\ &A_{p_PDS,NO}(i,k_a) \cdot [V_{p_PDS,cum}(i,k_a) - V_{top_PDS,cum}(i,m_{idx} - 1) + V_{d,NO} \cdot F_{f_PDS}(i)] / \\ &V_{p_PDS}(i,k_a) && seg.1 \\ &+ A_{p,NO}(i,k_a+1) + \ldots && seg.2 \\ &+ A_{p,NO}(i,k_b) \cdot [V_{top_PDS,cum}(i,m_{idx}) - V_{d,NO} \cdot F_{f_PDS}(i) - V_{p_PDS,cum}(i,k_b - 1)] / \\ &V_{p_PDS}(i,k_b). && seg.3 \end{aligned} \quad \text{(B.40)}$$

where $A_{p,NO}(i,k_a)$ is given by ***Eq. B.30***.

In ***Eq. B.40***, *Seg.1* represents the NO amount from the k_a^{th} inhalation gas segment, *Seg.3* represents NO amount from k_b^{th} inhalation gas segment and *Seg.2* represents the segments between the k_a^{th} and the k_b^{th} inhalation gas segments.

The NO concentration at the top of PDS is

$$C_{top_PDS,NO}(i, m_{idx}) = A_{top_PDS,NO}(i,m_{idx}) / V_{top_PDS}(i,m_{idx}). \quad \text{(B.41)}$$

The gas attributes and index relationship are summarised in **Table B.5**.

Table B.5 Gas attributes and the relationship between NO production site and the top of PDS.

Reference Point	Location	NO production site	the top of PDS
	Time	The start of inhalation	The start of exhalation
Index nomination		k_{idx}	m_{idx}
Segment's volume		$V_{p_PDS}(i,k_{idx})$ *Eq. B.28*	$V_{top_PDS}(i,m_{idx})$ *Eq. B.37*
Segment's cumulative volume		$V_{p_PDS,cum}(i,k_{idx})$ *Eq. B.29*	$V_{top_PDS,cum}(i,m_{idx})$ *Eq. B.36*
Segments NO amounts		$A_{p_PDS,NO}(i,k_{idx})$ *Eq. B.30*	$A_{top_PDS,NO}(i,m_{idx})$ *Eq. B.40*
Segment's NO concentration		$C_{p_PDS,NO}(i,k_{idx})$ *Eq. B.35*	$C_{top_PDS,NO}(i,m_{idx})$ *Eq. B.41*
Relationship between indexes		$k_a = f(V_{top_PDS,cum}(i,:), V_{top_PDS,cum}(i,m_{idx}-1) - V_{d,NO} \cdot Ff_{_PDS}(i))$, $k_b = f(V_{top_PDS,cum}(i,:), V_{top_PDS,cum}(i,m_{idx}) - V_{d,NO} \cdot Ff_{_PDS}(i))$. *Eq. B.38 and Eq. B.39*	

B.4.3.2 The bottom of DDS share of NO molecules

At the end of the previous section, the gas flows past the top of PDS, mixes in the mixing layer and enters the bottom of DDS. The mixing layer reaches a fully mixed status of gas from PDS, resulting in the NO concentration in the mixing layer being a single value equal to the flow-weighted average from various pipes of the PDS. At the same time, the mixing layer does not occupy any volume, so it has no effect on the total gas volume. The NO concentration at the mixed layer $C_{mix,NO}(m_{idx})$, can be expressed as,

$$C_{mix,NO}(m_{idx}) = Ff_{_PDS}(i) \cdot C_{top_PDS,NO}(i,m_{idx}). \quad \text{(B.42)}$$

When it comes to the bottom of DDS, the index is designated as n_{idx}. Different DDS pipes share the same NO concentration from the mixing layer. The NO concentration at the bottom of DDS ($C_{p_DDS,\,NO}(n_{idx})$),

$$C_{p_DDS,\,NO}(n_{idx}) = C_{mix,NO}(m_{idx}) \quad \text{(B.43)}$$

The cumulative volume of gas passes through the bottom of DDS, $V_{p_DDS,cum}(i,n_{idx})$, can be written as,

$$V_{p_DDS,cum}(n_{idx}) = Ff_{_DDS} \cdot Vol_data_Ex(n_{idx}), \tag{B.44}$$

The volume of the segment can be written as $V_{p_DDS}(n_{idx})$,

$$V_{p_DDS}(n_{idx}) = V_{p_DDS,cum}(n_{idx}) - V_{p_DDS,cum}(n_{idx} - 1) \tag{B.45}$$

The amount of NO molecules is,

$$A_{p_DDS,\,NO}(n_{idx}) = C_{p_DDS,\,NO}(n_{idx}) \cdot V_{p_DDS}(n_{idx}) \tag{B.46}$$

B.4.3.3 The top of the DDS output

As the gas flows to the top of the DDS, the Reference Point moves to the top of DDS, marking it as reaching the sensor layer. While the Reference Point time is still at the start of exhalation. This process is identical to the gas transport in the PDS, except the number of pipes needs to be adjusted to 11.

The top of DDS cumulative volume ($V_{top_DDS,cum}$) at p_{idx} timepoint can be written as,

$$V_{top_DDS,cum}(p_{idx}) = Ff_{_DDS} \cdot Vol_data_Ex(p_{idx}), \tag{B.47}$$

p_{idx}^{th} segment volume at the top of DDS is

$$V_{top_DDS}(p_{idx}) = V_{top_DDS,cum}(p_{idx}) - V_{top_DDS,cum}(p_{idx} - 1) \tag{B.48}$$

The corresponding relationship between the NO gas column and the top of DDS can be written as, if we assume the index marking the start and end of p_{idx}^{th} segment are n_a and n_b ,

$$n_a = f(V_{top_DDS,cum}(j, :), V_{top_DDS,cum}(i,p_{idx} - 1) - V_{DDS} \cdot Ff_{_DDS}(j)), \tag{B.49}$$

and

$$n_b = f(V_{p_DDS,cum}(j, :), V_{top_DDS,cum}(i,p_{idx}) - V_{DDS} \cdot Ff_{_DDS}(j)). \tag{B.50}$$

The NO molecule amount is,

$$A_{top_DDS,NO}(j,p_{idx}) = C_{p_DDS,NO}(j,n_a) \cdot [V_{p_DDS,cum}(j,n_a) - V_{top_DDS,cum}(i,p_{idx} - 1) + V_{DDS} \cdot Ff_{_DDS}(j)] \tag{B.51}$$

$$+ C_{p_DDS,NO}(j,n_a) \cdot V_{p_DDS,cum}(j,n_a+1) + \ldots \quad \text{seg.1}$$

$$+ C_{p_DDS,NO}(j,n_b) \cdot [V_{top_DDS,cum}(i,p_{idx}) - V_{DDS} \cdot F_{f_DDS}(j) - V_{p_DDS,cum}(j,n_b-1)]. \quad \text{seg.2}$$

$$\text{seg.3}$$

The three segments have similar function as previously stated.

The NO concentration at the top of DDS is,

$$C_{top_DDS,NO}(j,k_{idx}) = A_{top_DDS,NO}(j,k_{idx}) / V_{top_DDS}(j,k_{idx}). \quad \text{(B.52)}$$

Table B.6 gives the gas attributes from the bottom of DDS and the top of DDS, as well as the relationship between their index (n_{idx} and p_{idx}).

Table B.6 Gas attributes and relationship between the bottom and the top of DDS.

Reference Point	Location	the bottom of DDS	the top of DDS
	Time	The start of exhalation	The start of exhalation
Index nomination		n_{idx}	p_{idx}
Segment's volume		$V_{p_DDS}(i,n_{idx})$ *Eq. B.45*	$V_{top_DDS}(i,p_{idx})$ *Eq. B.48*
Segment's cumulative volume		$V_{p_DDS,cum}(i,n_{idx})$ *Eq. B.44*	$V_{top_DDS,cum}(i,p_{idx})$ *Eq. B.47*
Segments NO amounts		$A_{p_DDS,NO}(i,n_{idx})$ *Eq. B.46*	$A_{top_DDS,NO}(i,p_{idx})$ *Eq. B.51*
Segment's NO concentration		$C_{p_DDS,NO}(i,n_{idx})$ *Eq. B.43*	$C_{top_DDS,NO}(i,p_{idx})$ *Eq. B.52*
Relationship between indexes		$n_a = f(V_{top_DDS,cum}(j,:), V_{top_DDS,cum}(i,p_{idx}-1) - V_{DDS} \cdot F_{f_DDS}(j))$, $n_b = f(V_{p_DDS,cum}(j,:), V_{top_DDS,cum}(i,p_{idx}) - V_{DDS} \cdot F_{f_DDS}(j))$. *Eq. B.49 and Eq. B.50*	

When the gas enters the sensor layer, it is fully mixed in the layer. So, the sensor measured gas concentration ($C_{s,NO}(p_{idx})$) can be written as,

$$C_{s,NO}(p_{idx}) = F_{f_DDS} \cdot C_{top_DDS,NO}(j,p_{idx}). \quad \text{(B.53)}$$

Appendix C

Identifying putative ventilation-perfusion distributions in COVID-19 pneumonia (published)

Adapted for this thesis, the original file can be found at

https://doi.org/10.1371/journal.pone.0273214

Identifying putative ventilation-perfusion distributions in COVID-19 pneumonia

Haopeng Xu[1], Nayia Petousi[1] and Peter A. Robbins[2a*]

[1]Nuffield Department of Medicine, University of Oxford, Oxford, UK

[2]Department of Physiology, Anatomy and Genetics, University of Oxford, UK

[a]ORCID ID: 0000-0002-4975-0609

*Correspondence to:

Peter A Robbins

Department of Physiology, Anatomy and Genetics

Sherrington Building

Parks Road

Oxford OX1 3PT

Tel: +44 1865 272490

Email: peter.robbins@dpag.ox.ac.uk

Short title: Ventilation-perfusion inequality in COVID-19

Abstract

Busana *et al.* (doi.org/10.1152/japplphysiol.00871.2020) published 5 patients with COVID-19 in whom the fraction of non-aerated lung tissue had been quantified by computed tomography. They assumed that shunt flow fraction was proportional to the non-aerated lung fraction, and, by randomly generating 10^6 different bimodal distributions for the ventilation-perfusion ($\dot{V}/\dot{Q}$) ratios in the lung, specified as sets of paired values $\{\dot{V}i, \dot{Q}i\}$, sought to identify as solutions those that generated the observed arterial partial pressures of CO_2 and O_2 (Pa_{CO2} and Pa_{O2}). Our study sought to develop a direct method of calculation to replace the approach of randomly generating different distributions, and so provide more accurate solutions that were within the measurement error of the blood-gas data. For the one patient in whom Busana *et al.* did not find solutions, we demonstrated that the assumed shunt flow fraction led to a non-shunt blood flow that was too low to support the required gas exchange. For the other four patients, we found precise solutions (prediction error < $1x10^{-3}$ mmHg for both Pa_{CO2} and Pa_{O2}), with distributions qualitatively similar to those of Busana *et al*. These distributions were extremely wide and unlikely to be physically realisable, because they predict the maintenance of very large concentration gradients in regions of the lung where convection is slow. We consider that these wide distributions arise because the assumed value for shunt flow is too low in these patients, and we discuss possible reasons why the assumption relating to shunt flow fraction may break down in COVID-19 pneumonia.

INTRODUCTION

COVID-19 pneumonia is unusual in the severity of the hypoxaemia relative to the degree of atelectasis or consolidation observed in the lung [1]. To explore gas exchange in COVID-19 pneumonia further, *Busana et al.* [2] enrolled 5 patients with the disease who were undergoing mechanical ventilation in an intensive care unit, who had a pulmonary artery catheter in place for clinical reasons, and for whom there was a complete set of data for gas exchange, haemodynamics and lung mechanics together with a near-contemporaneous chest CT scan.

Busana *et al.* sought to interpret their data in terms of the associated ventilation-perfusion ($\dot{V}/\dot{Q}$) distribution in the lung. In order to do this, it was necessary to assign a shunt fraction (the fraction of the cardiac output that passes through the lungs without coming into contact with any fresh gas) for each patient. Busana *et al.* assigned this shunt fraction as equivalent to the fraction of non-aerated lung tissue observed with quantitative computed tomography for each of five patients with severe COVID-19 pneumonia. This assumption is important and we refer to it henceforth as the 'shunt fraction assumption'. The remainder of the cardiac output perfused the aerated lung tissue, and with this Busana *et al.* sought to find solutions to their problem in form of ventilation-perfusion ($\dot{V}/\dot{Q}$) distributions that would reproduce the arterial partial pressures of CO_2 and O_2 (Pa_{CO2} and Pa_{O2}, respectively) observed in the patients.

Busana *et al.*'s model of gas exchange had 498 compartments that were both perfused and ventilated, with values for $\dot{V}/\dot{Q}$ ranging from between ~10^{-2} to ~10^{2}. Any particular $\dot{V}/\dot{Q}$ distribution is then specified as a set of paired values for ventilation and perfusion $\{\dot{V}i, \dot{Q}i\}$, where i is the index for the compartment. Each compartment has a single value for Pa_{CO2} and Pa_{O2} associated with it that is determined by its $\dot{V}/\dot{Q}$ ratio, and the compartments taken together represent the variation in Pa_{CO2} and Pa_{O2} across the lungs. The Pa_{CO2} and Pa_{O2} for the whole lung can be calculated by mixing together all of the blood leaving the compartments.

Thus the putative or candidate $\dot{V}/\dot{Q}$ distributions for any particular patient are those that, when the blood is combined from all the compartments, result in Pa_{CO2} and Pa_{O2} values that match those of the patient.

Busana *et al.* used an approach of randomly generating many different $\dot{V}/\dot{Q}$ distributions to identify candidate distributions that may approximate the underlying distribution within each patient. For each patient, 10^6 bimodal distributions were randomly generated, based on five underlying parameters. For each distribution, an associated Pa_{CO2} and Pa_{O2} value were calculated. Distributions were considered as potentially acceptable solutions for the underlying $\dot{V}/\dot{Q}$ distribution of the patient if the resultant Pa_{CO2} and Pa_{O2} values were within 10% of the measured values.

Busana *et al.* found potential solutions for four out of the five patients. The predicted values for Pa_{CO2} and Pa_{O2} from all the potential solutions for the $\dot{V}/\dot{Q}$ distribution for each patient together with the patient's actual Pa_{CO2} and Pa_{O2} are illustrated in Fig. 6 of their paper. For no patient did their approach generate any candidate $\dot{V}/\dot{Q}$ distribution where the model value for either Pa_{CO2} or Pa_{O2} fell within 1 mmHg of the measured value, which is a reasonable estimate for the error associated with a blood-gas measurement. Furthermore, for no patient did the cloud of potential solution points surround the patient's measured value. Instead the cloud was always located away from the true value in the direction of higher Pa_{CO2} and higher Pa_{O2}. It is not clear whether these features arise because of the limited accuracy of the random simulation approach or whether there are other, more fundamental factors involved.

The purpose of the present study was to improve the accuracy with which candidate $\dot{V}/\dot{Q}$ distributions could be identified. In particular we sought to replace the random simulation approach by developing a method that would allow the direct calculation of the parameter set(s) for a $\dot{V}/\dot{Q}$ distribution that would reproduce a given patient's Pa_{CO2} and Pa_{O2}. Three

different types of $\dot{V}/\dot{Q}$ distribution were explored in increasing order of complexity: 1) the well-known three-compartment model; 2) a model with one low and one high $\dot{V}/\dot{Q}$ compartment; and 3) a continuous $\dot{V}/\dot{Q}$ distribution based on the beta distribution.

METHODS

Overview

In this study, a set of paired values for ventilation and perfusion, $\{\dot{V}i, \dot{Q}i\}$, is referred to as a $\dot{V}/\dot{Q}$ distribution and reflects the ventilation and perfusion going to different regions (indexed by i) in the lung. A particular choice of the number of elements within $\{\dot{V}i, \dot{Q}i\}$, or a particular choice of the distribution of the ratios $\dot{V}i/\dot{Q}i$ within the set, is referred to as a compartmental model. Also referred to as a model within this study, is a set of equations, based on mass balance and blood gas chemistry, that reflect the processes of gas exchange within the lung. When supplied with the particular inspiratory and mixed venous blood gas compositions pertaining to a patient, this model maps $\{\dot{V}i, \dot{Q}i\}$ to an associated arterial blood gas composition. Solutions are sets $\{\dot{V}i, \dot{Q}i\}$ for which this calculated arterial blood gas composition matches the measured arterial blood gas composition of the patient to within experimental error. In this study, the problem is to find solutions that are also consistent with additional constraints relating to the patient, in particular the value for the cardiac output (the sum of all the elements, $\dot{Q}i$), the shunt flow (the value for $\dot{Q}i$, for which $\dot{V}i = 0$) and the measured rate of oxygen uptake.

The methods are split into three main sections. The first section is a statement of the governing equations for compartmental models of gas exchange. The second section develops a set of useful functions, based on the governing equations of the model, that map between $\dot{V}/\dot{Q}$ ratios, respiratory quotient (R) values and compartmental partial pressures for CO_2 and

O_2 (P_{CO2} and P_{O2}, respectively). The third section develops the methodology to calculate parameter sets that will reproduce the Pa_{CO2} and Pa_{O2} values for each of three types of compartmental model under consideration. A flow chart to illustrate the overall process is given in Fig. 1. The accuracy we sought was for the model values for Pa_{CO2} and Pa_{O2} to be within 1 mmHg of the patient's measured values, although in practice the errors were less that $1x10^{-2}$ mmHg or even $1x10^{-3}$ mmHg.

All calculations were performed in Matlab version 9.9.0. Where numerical solutions were required, Matlab's inbuilt solvers fsolve and fminbnd were used.

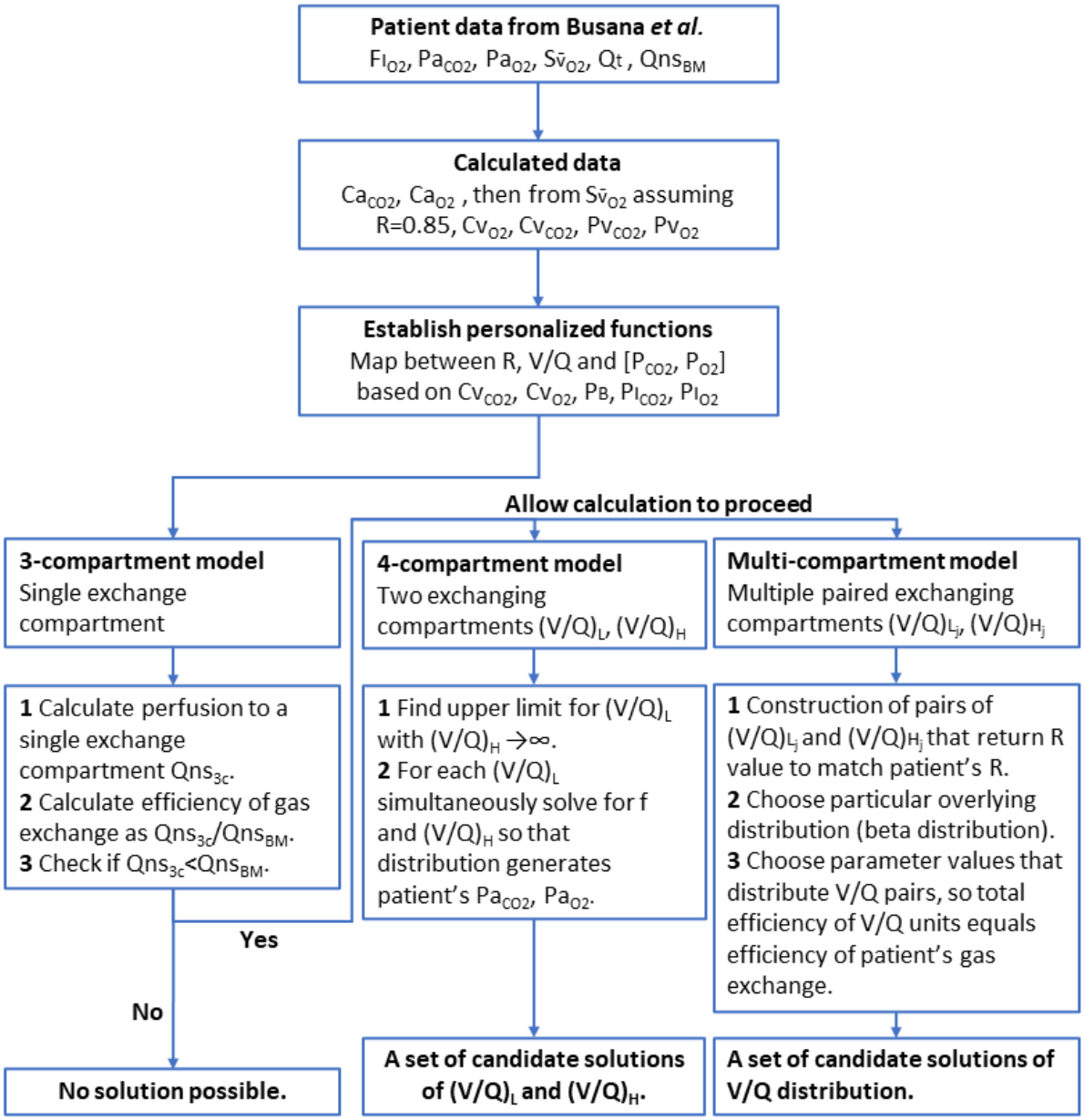


Figure 1. Flow chart of the overall process. The flow chart illustrates the source of data, the analytic approach taken, and the expected results. FI_{O2}, inspired O_2 fraction; Pa_{CO2} & Pa_{O2}, arterial partial pressures for CO_2 and O_2, respectively; $S\bar{v}_{O2}$, O_2 saturation of mixed venous blood; $\dot{Q}t$, total cardiac output; $\dot{Q}ns_{BM}$, non-shunt flow from Busana et al.; Ca_{CO2} & Ca_{O2}, arterial gas contents for CO_2 and O_2, respectively; R, respiratory quotient; $C\bar{v}_{O2}$ & $C\bar{v}_{CO2}$, mixed venous gas contents for O_2 and CO_2, respectively; $P\bar{v}_{CO2}$ & $P\bar{v}_{O2}$, mixed venous partial pressures for CO_2 and O_2, respectively; P_B, barometric pressure; PI_{CO2} & PI_{O2}, inspired partial pressures for CO_2 and O_2, respectively; $\dot{Q}ns_{3c}$, non-shunt flow calculated for 3-compartment model; $(\dot{V}/\dot{Q})_L$, $\dot{V}/\dot{Q}$ ratio for the low $\dot{V}/\dot{Q}$ compartment; $(\dot{V}/\dot{Q})_H$, $\dot{V}/\dot{Q}$ ratio for the high $\dot{V}/\dot{Q}$ compartment; $(\dot{V}/\dot{Q})_{Lj}$ & $(\dot{V}/\dot{Q})_{Hj}$, j^{th} pair of $\dot{V}/\dot{Q}$ ratios for the low and high $\dot{V}/\dot{Q}$ compartments, respectively.

Governing equations

The lung is heterogenous, with different partial pressures for alveolar CO_2 and O_2 occurring in different locations. One way of modelling this is to consider the lung as if it were constructed from a set of compartments, with each individual compartment having its own unique values for alveolar P_{CO2} and P_{O2}. The governing equations for the model of compartmental gas exchange arise from the conservation of mass and are essentially those from the classical studies surrounding $\dot{V}/\dot{Q}$ developed by Fenn, Rahn and Otis [3, 4] and by Riley and Cournand [5, 6].

In any given compartment, the rates at which CO_2, O_2 and N_2 enter or leave the compartment from the blood have to equal to the rates that they enter or leave from the gas phase. This yields the following equations:

$$\dot{V}_{CO2} = \dot{Q}(C\bar{v}_{CO2} - C_{CO2}) = \dot{V}_E P_{CO2}/P_B - \dot{V}_I P_{ICO2}/P_B, \quad (1)$$

$$\dot{V}_{O2} = \dot{Q}(C_{O2} - C\bar{v}_{O2}) = \dot{V}_I P_{IO2}/P_B - \dot{V}_E P_{O2}/P_B, \text{ and} \quad (2)$$

$$\dot{V}_{N2} = 0 = \dot{V}_I P_{IN2}/P_B - \dot{V}_E P_{N2}/P_B. \quad (3)$$

where $\dot{V}_{CO2}$, $\dot{V}_{O2}$ and $\dot{V}_{N2}$ are the compartmental rates of gas production or consumption for CO_2, O_2 and N_2, respectively; $\dot{Q}$ is perfusion of the compartment; $C\bar{v}_{CO2}$ and $C\bar{v}_{O2}$ are mixed venous contents of CO_2 and O_2, respectively; C_{CO2} and C_{O2} are the compartmental end-capillary blood contents for CO_2 and O_2, respectively; P_{CO2} and P_{O2} are the compartmental partial pressures for CO_2 and O_2, respectively; P_{ICO2} and P_{IO2} are inspired partial pressures for CO_2 and O_2, respectively; $\dot{V}_I$ and $\dot{V}_E$ are inspired and expired ventilations, respectively; and P_B is barometric pressure. In the gas phase, there is the additional constraint:

$$P_B = P_{N2} + P_{CO2} + P_{O2} + P_{H2O}, \quad (4)$$

where P_{H2O} is the saturated water vapour pressure at 37 degrees C.

It is worth noting that, apart from the diffusional equilibration for CO_2 and O_2 between blood and gas, these equations assume that convection is completely dominant over diffusion

so that diffusion within the gas (or blood) phase can be neglected. The model also assumes that, because N_2 is not metabolised and does not reversibly react with blood in large quantities like CO_2 and O_2, the N_2 exchange between blood and gas can be set to zero.

Apart from these relations, the only other one required is a model of the dissociation curves for blood that relates paired values for P_{CO2} and P_{O2} to values for blood gas contents (C_{CO2} and C_{O2}). Various approaches have been adopted by different authors over time, and the current study makes use of a recent numerical model of the oxygen and carbon dioxide dissociation curves for blood [7]. In each case, the patient's reported haemoglobin concentration was used in the model together with an assumed albumin concentration at the lower end of the normal range at 30 gm/L. The Pa_{CO2}, Pa_{O2} and pH were then used to construct the blood model with the correct acid-base status. Standard values for electrolytes were used as described by [7] except that the plasma chloride concentration was adjusted to provide for electroneutrality. The model described in [7] is represented here by the vector function **g**:

$$\mathbf{c} = \mathbf{g}(\mathbf{p}) \qquad (5)$$

where $\mathbf{c} = [C_{CO2}, C_{O2}]$ and $\mathbf{p} = [P_{CO2}, P_{O2}]$.

Functions

These functions are required to map between values for $\dot{V}/\dot{Q}$, values for the respiratory quotient (R), and paired values for blood gas partial pressures/ contents.

The functions require that the composition of the mixed venous blood is known, that the composition of the inspired gas is known, and that the barometric pressure is known. Busana *et al.* [2] provided the patients' mixed venous oxygen saturations, but no directly measured mixed venous partial pressures or contents. In order to obtain these, we calculated a value for $C\bar{v}_{O2}$ based on the reported haemoglobin concentration, the reported mixed venous oxygen

saturation, and an estimate for the small amount of O_2 physically dissolved based on an approximate value for $P\bar{v}_{O2}$. In the absence of measured mixed venous blood gas contents, Busana *et al.* assumed a respiratory quotient of 0.85 for all patients. The blood gas function, **g**, allowed the estimation of Ca_{CO2} and Ca_{O2} from the reported values for Pa_{CO2} and Pa_{O2}. From this, for each patient we estimated:

$$C\bar{v}_{CO2} = 0.85(Ca_{O2} - C\bar{v}_{O2}) + Ca_{CO2}. \quad (6)$$

Function for mapping $\dot{V}/\dot{Q}$ to corresponding respiratory quotient, R.

This section constructs a function, h, of the form:

$$R = h(\dot{V}/\dot{Q}). \quad (7)$$

The function has a domain of $[0,\infty]$ and a codomain of $[R_{min}, R_{max}]$, where R_{min} is obtained when $\dot{V}/\dot{Q} = 0$ and R_{max} is obtained when $\dot{V}/\dot{Q} \rightarrow \infty$. To construct the function, values are required for P_B, P_{ICO2}, P_{IO2}, $C\bar{v}_{CO2}$ and $C\bar{v}_{O2}$. The function was derived as follows:

Applying mass balance for N_2 yields:

$$\dot{V}_I(P_{IN2}/P_B) = \dot{V}_E(P_{EN2}/P_B), \quad (8)$$

where P_{IN2} is the inspired N_2 partial pressure and P_{EN2} is the expired N_2 partial pressure.

Defining alveolar ventilation as the inspiratory value, $\dot{V} = \dot{V}_I$, and rearranging yields:

$$\dot{V}_E = (P_{IN2}/P_{EN2})\dot{V}. \quad (9)$$

Substitution for $\dot{V}_E$ according to *Eq. 9* and defining $\dot{V} = \dot{V}_I$, allows *Eqns 1 & 2* to be rewritten as:

$$\dot{V}_{CO2} = \dot{Q}(C\bar{v}_{CO2} - Ca_{CO2}) = (P_{IN2}/P_{EN2})\dot{V}P_{CO2}/P_B - \dot{V}P_{ICO2}/P_B, \text{ and} \quad (10)$$

$$\dot{V}_{O2} = \dot{Q}(C_{O2} - Ca\bar{v}_{O2}) = \dot{V}P_{IO2}/P_B - (P_{IN2}/P_{EN2})\dot{V}P_{O2}/P_B. \quad (11)$$

Rearranging each yields:

$$(\dot{V}/\dot{Q})((P_{IN2}/P_{EN2})P_{CO2} - P_{ICO2})/P_B - (C\bar{v}_{CO2} - \mathbf{g}(Pa_{CO2}, P_{O2})[1, 0]^T) = 0, \text{ and} \quad (12)$$

$$(\dot{V}/\dot{Q})(P_{IO2} - (P_{IN2}/P_{EN2})P_{O2})/P_B - (\mathbf{g}(Pa_{CO2}, P_{O2})[0, 1]^T - C\bar{v}_{O2}) = 0, \quad (13)$$

where the blood gas dissociation function, **g**, has been used to express Ca_{CO2} and Ca_{O2} (*Eqns 5*) in terms of Pa_{CO2} and Pa_{O2}, and we assume that alveolar P_{CO2} and P_{O2} equal to Pa_{CO2} and Pa_{O2}. In order to obtain expressions for P_{IN2} and P_{EN2}, the following relationship was used:

$$P_{N2} = P_B - P_{CO2} - P_{O2} - P_{H2O}, \quad (14)$$

where P_{IN2} can then be evaluated from P_{ICO2} and P_{IO2}, and P_{EN2} expressed in terms of P_{CO2} and P_{O2}. These relations now allow *Eq. 12* and *Eq. 13* to be solved simultaneously for P_{CO2} and P_{O2} by use of a numerical method. Finally, a value for R can be calculated from the relationship:

$$R = (C\bar{v}_{CO2} - \mathbf{g}(P_{CO2}, P_{O2})[1, 0]^T)/(\mathbf{g}(P_{CO2}, P_{O2})[0, 1]^T - C\bar{v}_{O2}), \quad (15)$$

where the blood gas dissociation function, **g**, was used to calculate C_{CO2} and C_{O2} from P_{CO2} and P_{O2}. Alternatively, R may be calculated from the gas phase relationships as:

$$R = ((P_{IN2}/P_{EN2})P_{CO2} - P_{ICO2})/(P_{IO2} - (P_{IN2}/P_{EN2})P_{O2}). \quad (16)$$

Function for mapping R to P_{CO2} and P_{O2}.

This section describes a vector-valued function, **j**, of the form:

$$\mathbf{p} = \mathbf{j}(R), \quad (17)$$

where, as previously, $\mathbf{p} = [P_{CO2}, P_{O2}]$. As for the function h, values need to be specified for P_B, P_{ICO2}, P_{IO2}, $C\bar{v}_{CO2}$ and $C\bar{v}_{O2}$. The evaluation of this function then simply involves the simultaneous numerical solution of *Eq. 15* and *Eq. 16* for P_{CO2} and P_{O2}. As for the construction of function h, the expressions for P_{IN2} (in terms of P_{ICO2} and P_{IO2}) and P_{EN2} (in terms of P_{CO2} and P_{O2}) in *Eq. 16* are obtained by use of *Eq. 14*.

Calculation of the candidate $\dot{V}/\dot{Q}$ distributions

Three different types of $\dot{V}/\dot{Q}$ distribution were explored to determine whether specific parameter set(s) could be calculated for them so that they would reproduce the Pa_{CO2} and Pa_{O2} for each patient individually. These are each considered in increasing order of complexity under their individual sections below.

Estimation of shunt in three-compartment model.

The three-compartment lung model of Riley and Cournand [5, 6] consists of just one perfused and ventilated compartment that is called the ideal compartment, together with two other compartments consisting of pure shunt (blood flow but not ventilation) and pure deadspace (ventilation but no blood flow), respectively. The model's special theoretical importance is that for any real $\dot{V}/\dot{Q}$ distribution, no matter how complex, there always exists a corresponding three-compartment model that can exactly replicate the patient's Pa_{CO2} and Pa_{O2}. A particular parameter of interest is the non-shunt flow for the three-compartment model, $\dot{Q}ns_{3CM}$. This is the blood flow to the ideal compartment.

First, $\dot{V}_{CO2}$ and $\dot{V}_{O2}$ were calculated directly as:

$$\dot{V}_{CO2} = \dot{Q}t(C\bar{v}_{CO2} - Ca_{CO2}), \text{ and} \quad (18)$$

$$\dot{V}_{O2} = \dot{Q}t(Ca_{O2} - C\bar{v}_{O2}). \quad (19)$$

Next, using function **j**, we calculated the P_{CO2} and P_{O2} of the ideal compartment of the three-compartment model, Pi_{CO2} and Pi_{O2}, as:

$$[Pi_{CO2}, Pi_{O2}] = \mathbf{j}(0.85). \quad (20)$$

We then calculated the associated blood-gas contents through function **g**:

$$[Ci_{CO2}, Ci_{O2}] = \mathbf{g}([Pi_{CO2}, Pi_{O2}]), \quad (21)$$

where Ci_{CO2} and Ci_{O2} are blood contents of ideal compartment.

From these values, $\dot{Q}ns_{3CM}$ was estimated by either of the following two relations:

$\dot{Q}ns_{3CM} = \dot{V}_{CO2}/(C\bar{v}_{CO2} - Ci_{CO2})$, or (22)

$\dot{Q}ns_{3CM} = \dot{V}_{O2}/(Ci_{O2} - C\bar{v}_{O2})$. (23)

Importantly, $\dot{Q}ns_{3CM}$ forms a minimum value for the non-shunt flow, as it is all used optimally to perfuse the ideal compartment of the model. From this, the shunt flow for the three-compartment model, $\dot{Q}s_{3CM}$, can be calculated by subtracting the shunt flow from the total cardiac output, $\dot{Q}t$.

The shunt fraction assumption proposed by Busana *et al.*, $\dot{Q}s_{BM}$ (subscript 'BM' refers to the model of Busana *et al.*), is *not* that associated with the three-compartment model, but instead is proportional to the non-aerated lung fraction as quantified by computer tomography (CT). Subtraction of $\dot{Q}s_{BM}$ from $\dot{Q}t$ yields the non-shunt flow that perfuses the remaining aerated lung, $\dot{Q}ns_{BM}$. The distinction between $\dot{Q}ns_{BM}$ and $\dot{Q}ns_{3CM}$ allowed an overall efficiency for the use of the perfusion, $E_{\dot{Q}ns_{BM}}$, for the ventilated and perfused compartments to be defined as $\dot{Q}ns_{3CM}/\dot{Q}ns_{BM}$. As $\dot{Q}ns_{3CM}$ is the minimum possible non-shunt flow, this ratio may be seen as the ratio of the minimum-to-actual blood flow required to deliver the gas exchange, and therefore should be less than, or equal to, one. (It is also equivalent to the ratio of the actual-to-maximum O_2 consumption or CO_2 production that is possible with a blood flow of $\dot{Q}ns_{BM}$.) From this, it follows immediately that, if $\dot{Q}ns_{3CM} > \dot{Q}ns_{BM}$, then $\dot{Q}ns_{BM}$ is too low to support the gas-exchange required to produce the patient's measured Pa_{O2} and Pa_{CO2}. This provides a basis for our test of whether $\dot{V}/\dot{Q}$ distributions exist for the shunt flows proposed by Busana *et al*.

Estimation of $\dot{V}/\dot{Q}$ values for model with two perfused compartments.

This section explored whether a pair of $\dot{V}/\dot{Q}$ compartments, one with low $\dot{V}/\dot{Q}$, $(\dot{V}/\dot{Q})_L$, and one with high $\dot{V}/\dot{Q}$, $(\dot{V}/\dot{Q})_H$, could reproduce a patient's values for Pa_{CO2} and Pa_{O2}, assuming that the combined total perfusion of the two compartments was equal to $\dot{Q}ns_{BM}$,

(the shunt fraction assumption) which was calculated from the non-aerated lung fraction, F_{NAL}, as follows:

$$\dot{Q}ns_{BM} = (1 - F_{NAL})\dot{Q}t, \qquad (24)$$

where the values for F_{NAL} are those provided by Busana *et al* [2]. Expressions for total $\dot{V}_{CO2}$ and $\dot{V}_{O2}$ may be written by summing the CO_2 production from the low and high $\dot{V}/\dot{Q}$ compartments, and the O_2 consumption from the low and high $\dot{V}/\dot{Q}$ compartments, respectively, as follows:

$$\dot{V}_{CO2} = (\dot{Q}ns_{BM}f)(C\bar{v}_{CO2} - \mathbf{g}(\mathbf{j}(h((\dot{V}/\dot{Q})_L)))[1, 0]^T) + (\dot{Q}ns_{BM}(1 - f))(C\bar{v}_{CO2} - \mathbf{g}(\mathbf{j}(h((\dot{V}/\dot{Q})_H)))[1, 0]^T), \text{ and} \qquad (25)$$

$$\dot{V}_{O2} = (\dot{Q}ns_{BM}f)(\mathbf{g}(\mathbf{j}(h((\dot{V}/\dot{Q})_L)))[0, 1]^T - C\bar{v}_{O2}) + (\dot{Q}ns_{BM}(1 - f))(\mathbf{g}(\mathbf{j}(h((\dot{V}/\dot{Q})_H)))[0, 1]^T - C\bar{v}_{O2}), \qquad (26)$$

where f is the fraction of blood flow to the low $\dot{V}/\dot{Q}$ compartment, and (1 – f) is the fraction of blood flow to the high $\dot{V}/\dot{Q}$ compartment.

Eqns 25 and *26* have three unknown variables: $(\dot{V}/\dot{Q})_L$, $(\dot{V}/\dot{Q})_H$ and f. Thus, the general approach taken was to choose a value for $(\dot{V}/\dot{Q})_L$ and then solve the equations simultaneously to obtain values for $(\dot{V}/\dot{Q})_H$ and f that are associated with the particular value for $(\dot{V}/\dot{Q})_L$. However, for any particular choice for $(\dot{V}/\dot{Q})_L$, in general there is no guarantee that a solution will exist.

In order to establish possible bounds for $(\dot{V}/\dot{Q})_L$ within which solutions for *Eqns 25* and *26* may exist, it is first worth noting that, if $(\dot{V}/\dot{Q})_L = 0$, then all gas exchange has to arise from the $(\dot{V}/\dot{Q})_H$ compartment. In this scenario $(\dot{V}/\dot{Q})_H$ must equal the value for the ideal compartment from the associated three-compartment model (and $\dot{Q}ns_{BM}(1 - f) = \dot{Q}ns_{3CM}$). As $(\dot{V}/\dot{Q})_L$ is increased above zero, it will start to contribute to gas exchange with a value for R that is below the overall R value for the patient. Consequently gas exchange from the $(\dot{V}/\dot{Q})_H$

compartment will require a value for R above that for the overall patient. Therefore the value for $(\dot{V}/\dot{Q})_H$ must increase above the that of the ideal compartment from the associated three-compartment model. This reasoning suggests that a possible maximum for $(\dot{V}/\dot{Q})_L$ may arise as the value for $(\dot{V}/\dot{Q})_H \rightarrow \infty$. Consequently, we first solved *Eqns 25* and *26* for $(\dot{V}/\dot{Q})_L$ and f under the condition $(\dot{V}/\dot{Q})_H \rightarrow \infty$, and subsequently sought solutions for *Eqns 25* and *26* (in terms of $(\dot{V}/\dot{Q})_H$ and f) for values of $(\dot{V}/\dot{Q})_L$ between 0 and this putative maximum.

Estimation of $\dot{V}/\dot{Q}$ distributions for model with multiple perfused compartments.

The final step is to attempt to construct models with multiple perfused units that could replicate the gas exchange of the patient. The preceding section suggests one possible way forward is to construct them from pairs of $\dot{V}/\dot{Q}$ compartments, where each pairing has one value below and one value above the ideal $\dot{V}/\dot{Q}$, $(\dot{V}/\dot{Q})i$. Symmetry suggests a natural pairing between the j^{th} low, $(\dot{V}/\dot{Q})_{Lj}$, and the j^{th} high, $(\dot{V}/\dot{Q})_{Hj}$, compartments of the form:

$$(\dot{V}/\dot{Q})_{Lj}/\ (\dot{V}/\dot{Q})i = (\dot{V}/\dot{Q})i/(\dot{V}/\dot{Q})_{Hj}, \qquad (27)$$

which, when rearranged gives:

$$(\dot{V}/\dot{Q})_{Hj} = ((\dot{V}/\dot{Q})i)^2/(\dot{V}/\dot{Q})_{Lj}. \qquad (28)$$

Following the approach of Busana *et al.* [2], we constructed a set of N evenly-spaced sub-intervals on a logarithmic basis within an interval $[(\dot{V}/\dot{Q})i/k\ ,\ (\dot{V}/\dot{Q})i]$ for the low $\dot{V}/\dot{Q}$ units, and a further N evenly-spaced sub-intervals on a logarithmic basis within an interval $[(\dot{V}/\dot{Q})i\ ,\ k(\dot{V}/\dot{Q})i]$ for the high $\dot{V}/\dot{Q}$ units. We chose a value of 50 for N and 100 for k. Values for $(\dot{V}/\dot{Q})_{Lj}$ and $(\dot{V}/\dot{Q})_{Hj}$ were then allocated as the (logarithmically) central values for each of the sub-intervals below and above $(\dot{V}/\dot{Q})i$, respectively.

For each $\dot{V}/\dot{Q}$ unit, function h (*Eq. 7*) provides the associated value for R; for each value of R, function **j** (*Eq. 17*) provides the unit's associated P_{CO2} and P_{O2}; and for each pair of P_{CO2} and P_{O2} values, function **g** (*Eq. 5*) provides the unit's associated blood gas contents, C_{CO2} and

C_{O2}. For each pair of units, we can solve for the fractional blood flow to the lower unit, f_j, in relation to the combined blood flow to both units that generates the overall R value for the patient:

$$R = (f_j (C\bar{v}_{CO2} - C_{LCO2,j}) + (1 - f_j)(C\bar{v}_{CO2} - C_{HCO2,j}))/(f_j (C_{LO2,j} - C\bar{v}_{O2}) + (1 - f_j)(C_{HO2,j} - C\bar{v}_{O2})), \quad (29)$$

where $C_{HCO2,j}$ and $C_{LCO2,j}$ are the j^{th} pair of blood CO_2 contents for the jth pair of high and low $\dot{V}/\dot{Q}$ units, respectively; and $C_{HO2,j}$ and $C_{LO2,j}$ are the j^{th} pair of blood O_2 contents for the jth pair of high and low $\dot{V}/\dot{Q}$ units, respectively.

By considering the O_2 consumption per unit of blood flow for the pair of units relative to that which would occur per unit of blood flow to the ideal compartment of the three-compartment model, an efficiency for the use of the perfusion to the j^{th} pair of units ($E_{\dot{Q}j}$) may be calculated as:

$$E_{\dot{Q}j} = (f_j (C_{LO2,j} - C\bar{v}_{O2}) + (1 - f_j)(C_{HO2,j} - C\bar{v}_{O2}))/(Ci_{O2} - C\bar{v}_{O2}). \quad (30)$$

From this construction, any distribution that obeys the relationship:

$$E_{\dot{Q}ns_{BM}} = \sum^{j}(\dot{Q}_j E_{\dot{Q}j})/\dot{Q}ns_{BM}, \quad (31)$$

where $E_{\dot{Q}ns_{BM}}$ is the overall circulatory efficiency for the patient given by $\dot{Q}ns_{3CM}/\dot{Q}ns_{BM}$, should reproduce the patient's arterial blood gas values precisely.

One approach to finding solutions to *Eq. 31* is to apply a parameterised probability distribution over the interval containing the values for $(\dot{V}/\dot{Q})L_j$ to distribute $\dot{Q}ns_{BM}$ over the pairs of values for $\dot{V}/\dot{Q}$. We chose a bounded probability function, the beta distribution, and partitioned it into N equal divisions on the interval [0,1]. The beta distribution has two shape parameters, α and β, where $\alpha>0$ and $\beta>0$. For our purposes, it was convenient to reparameterise this in the form:

$$\alpha = \theta, \text{ and} \quad (32)$$

$$\beta = \mu - \theta, \quad (33)$$

where μ is a constant greater than zero, a value of 10 was initially chosen, and $0 < \theta < \mu$. This parameterisation ensured that the peak for the probability distribution gradually migrated rightwards on the interval [0,1] as θ increased. The values for $\dot{Q}_j$ could then be written using the cumulative density function for the beta distribution, $\text{beta}_{\text{cdf}}(\alpha, \beta, x)$, as follows:

$$\dot{Q}_j = (\text{beta}_{\text{cdf}}(\theta, (\mu - \theta), j/N) - \text{beta}_{\text{cdf}}(\theta, (\mu - \theta), (j - 1)/N))\dot{Q}\text{ns}_{\text{BM}}. \quad (34)$$

These may be substituted into *Eq. 31* to yield:

$$E_{\dot{Q}\text{ns}_{\text{BM}}} = \sum^{j}(\text{beta}_{\text{cdf}}(\theta, (\mu - \theta), j/N) - \text{beta}_{\text{cdf}}(\theta, (\mu - \theta), (j - 1)/N))E_{\dot{Q}j}. \quad (35)$$

Setting $E_{\dot{Q}\text{ns}_{\text{BM}}}$ equal to the overall efficiency of gas exchange for the patient, the equation could be solved for θ to provide a possible multi-compartment $\dot{V}/\dot{Q}$ distribution for the patient. Other distributions could be calculated by varying the value of μ for the beta distribution, or potentially could be obtained by employing other distributions in place of the beta distribution.

RESULTS

Shunt flow calculation for each patient using the three-compartment model

The essential patient data from Busana *et al.* [2] are given in Table 1 together with the results obtained for each patient from fitting a three-compartment model to their gas exchange data. Patients 2, 3 and 5 were relatively similar in terms of their blood gases. Patient 1 had a substantially higher Pa_{O2} than the other patients, and patient 4 had a substantially lower Pa_{CO2} than the other patients. The P_{CO2} and P_{O2} values for the ideal compartment for each patient reflected these initial differences.

Table 1. Patient data and results from fitting three-compartment model of gas exchange

Patient	1	2	3	4	5
Hb /g·L^{-1}	95	100	117	86	114
Inspired gas					
P_{ICO_2} /mmHg(kPa)	0.0(0.0)	0.0(0.0)	0.0(0.0)	0.0(0.0)	0.0(0.0)
P_{IO_2} /mmHg(kPa)	641.7(85.5)	606.1(80.8)	570.4(76.0)	570.4(76.0)	427.8(57.0)
Arterial blood					
Pa_{CO_2} /mmHg(kPa)	71.0(9.5)	79.0(10.5)	69.5(9.3)	42.0(5.6)	83.3(11.1)
Pa_{O_2} /mmHg(kPa)	105.0(14.0)	62.0(8.3)	65.3(8.7)	64.0(8.5)	62.5(8.3)
Ca_{CO_2} /L_{STPD}·L^{-1}	0.8685	0.8148	0.7759	0.5673	0.8097
Ca_{O_2} /L_{STPD}·L^{-1}	0.1299	0.1231	0.1479	0.1107	0.1395
pHa	7.390	7.310	7.360	7.430	7.290
Mixed Venous blood					
$P\bar{v}_{CO_2}$ /mmHg(kPa)	79.1(10.5)	84.8(11.3)	74.7(10.0)	46.7(6.2)	89.3(11.9)
$P\bar{v}_{O_2}$ /mmHg(kPa)	38.4(5.1)	41.0(5.5)	42.5(5.7)	35.3(4.7)	42.6(5.7)
$C\bar{v}_{CO_2}$ /L_{STPD}·L^{-1}	0.9019	0.8383	0.7999	0.5926	0.8346
$C\bar{v}_{O_2}$ /L_{STPD}·L^{-1}	0.0906	0.0954	0.1196	0.0809	0.1102
Ideal compartment in a three-compartment model					
Pi_{CO_2} /mmHg(kPa)	67.6(9.0)	71.8(9.6)	63.2(8.4)	37.3(5.0)	76.1(10.1)
Pi_{O_2} /mmHg(kPa)	572.1(76.3)	531.8(70.9)	504.9(67.3)	531.8(70.9)	348.0(46.4)
Ci_{CO_2} /L_{STPD}·L^{-1}	0.8587	0.7917	0.7530	0.5479	0.7852
Ci_{O_2} /L_{STPD}·L^{-1}	0.1470	0.1525	0.1749	0.1335	0.1659
Perfusion					
$\dot{Q}t$ /L·min^{-1}	8.060	9.490	10.400	9.450	10.550
$\dot{Q}s_{BM}$ /L·min^{-1}	3.224	3.701	3.744	2.552	2.743
$\dot{Q}ns_{BM}$ /L·min^{-1}	4.836	5.789	6.656	6.899	7.807
$\dot{Q}s_{3CM}$ /L·min^{-1}	2.447	4.897	5.079	4.086	5.001

$\dot{Q}ns_{3CM}$ /L·min^{-1}	5.613	4.593	5.321	5.364	5.549
$E_{\dot{Q}ns_{BM}}$	(1.161)	0.793	0.799	0.778	0.711

PI_{CO2} & PI_{O2}, inspired P_{CO2} & P_{O2}, respectively; Hb, haemglobin concentration; Pa_{CO2} & Pa_{O2}, arterial P_{CO2} and P_{O2}, respectively; Ca_{CO2} & Ca_{O2}, arterial gas contents for CO_2 and O_2, respectively; pHa, arterial pH; $P\bar{v}_{CO2}$ & $P\bar{v}_{O2}$, mixed venous P_{CO2} and P_{O2}, respectively; $C\bar{v}_{CO2}$ & $C\bar{v}_{O2}$, mixed venous gas contents for CO_2 and O_2, respectively; Pi_{CO2} & Pi_{O2}, P_{CO2} and P_{O2} for ideal compartment of three-compartment model, respectively; Ci_{CO2} & Ci_{O2}, blood gas contents for CO_2 and O_2 for ideal compartment of three-compartment model, respectively; $\dot{Q}t$, total cardiac output; $\dot{Q}s_{BM}$ & $\dot{Q}ns_{BM}$ shunt flow to non-aerated lung and corresponding non-shunt flow from Busana *et al.*, respectively; $\dot{Q}s_{3CM}$ & $\dot{Q}ns_{3CM}$ shunt flow for three-compartment model of lung and corresponding non-shunt flow, respectively; $E_{\dot{Q}ns_{BM}}$, perfusion efficiency relative to maximal value associated with three-compartment model.

In the case of patient 1, the required perfusion to the ideal compartment of the three-compartment model, $\dot{Q}ns_{3CM}$, exceeded the hypothesised value, $\dot{Q}ns_{BM}$, as obtained from the total cardiac output and fraction of non-ventilated lung (F_{NAL} estimated from CT in Busana *et al*). Given that $\dot{Q}ns_{3CM}$ is the minimum possible value for perfusion for the required gas exchange, this finding means that, for this particular patient, the assumption that the shunt fraction is equivalent to fraction of non-aerated lung quantified by CT cannot be valid. The true shunt fraction for this particular patient has to be below that calculated from the fraction of non-ventilated lung. For all other patients $\dot{Q}ns_{BM}$ substantially exceeded $\dot{Q}ns_{3CM}$, allowing the exploration of possible $\dot{V}/\dot{Q}$ distributions to proceed. The ratio of $\dot{Q}ns_{3CM}$:$\dot{Q}ns_{BM}$ is shown as an efficiency, $E_{\dot{Q}ns_{BM}}$, for the use of the blood flow that is being used to support gas exchange, and was less than 1 for patients 2-5.

Estimation of $\dot{V}/\dot{Q}$ pairs (two perfused compartment model) when total perfusion is equal to $\dot{Q}ns_{BM}$

Figures 2 and 3 illustrate the results for estimating pairs of low and high values for $\dot{V}/\dot{Q}$ that will replicate the Pa_{CO2} and Pa_{O2} values for each patient. For all pairs, the numerical error between the calculated and actual values for Pa_{CO2} and Pa_{O2} in the patients was very low, and always < $1x10^{-2}$ mmHg. This is a very major improvement in precision (2-3 orders of magnitude) compared with the multiple random simulations approach that was employed by Busana *et al,* and it demonstrates that, assuming $\dot{Q}ns_{BM}$ is the non-shunt blood flow for the aerated lung, there are multiple (infinite) solutions for $\dot{V}/\dot{Q}$ distributions that match the patients' Pa_{CO2} and Pa_{O2} precisely. Figure 2 illustrates that as the $\dot{V}/\dot{Q}$ for the low $\dot{V}/\dot{Q}$ compartment increased, there was a progressive increase in the low $\dot{V}/\dot{Q}$ compartment's share of total blood flow (left-axis) and a progressive rise in $\dot{V}/\dot{Q}$ for the high $\dot{V}/\dot{Q}$ compartment (right-axis). As a higher $\dot{V}/\dot{Q}$ value for the low $\dot{V}/\dot{Q}$ compartment was associated with a higher $\dot{V}/\dot{Q}$ value for the high $\dot{V}/\dot{Q}$ compartment, we calculated putative maximal values of $\dot{V}/\dot{Q}$ for the low $\dot{V}/\dot{Q}$ compartment by assuming that, in the high $\dot{V}/\dot{Q}$ compartment, the blood was maximally oxygenated and had all the CO_2 removed (i.e. $(\dot{V}/\dot{Q})_H \rightarrow \infty$). The maximal values for $\dot{V}/\dot{Q}$ obtained for the low $\dot{V}/\dot{Q}$ compartment in this manner were 0.060, 0.064, 0.084 and 0.078, for patients 2, 3, 4 and 5, respectively.

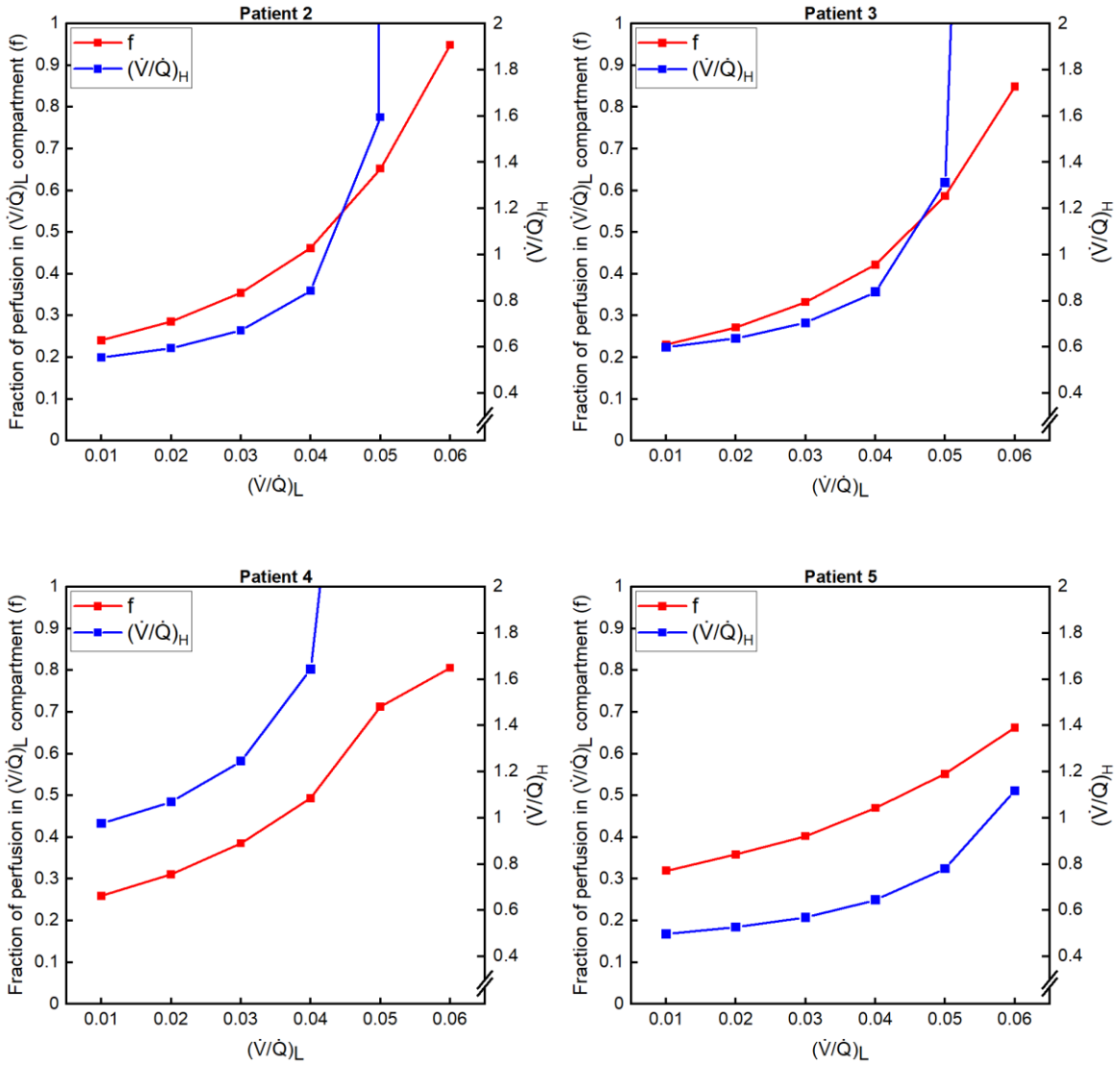


Figure 2. Fraction of total perfusion to the low ventilation-perfusion ($\dot{V}/\dot{Q}$) compartment and $\dot{V}/\dot{Q}$ value for high $\dot{V}/\dot{Q}$ compartment in relation to $\dot{V}/\dot{Q}$ value for low $\dot{V}/\dot{Q}$ compartment. Results shown for patients 2-5. Some values off-scale for higher values of $\dot{V}/\dot{Q}$ for the low $\dot{V}/\dot{Q}$ compartment. Differences between measured and calculated arterial partial pressures for CO_2 and O_2 < $1x10^{-2}$ mmHg for all distributions illustrated. f, fraction of total perfusion to the low $\dot{V}/\dot{Q}$ compartment; $(\dot{V}/\dot{Q})_L$, $\dot{V}/\dot{Q}$ ratio for the low $\dot{V}/\dot{Q}$ compartment; $(\dot{V}/\dot{Q})_H$, $\dot{V}/\dot{Q}$ ratio for the high $\dot{V}/\dot{Q}$ compartment.

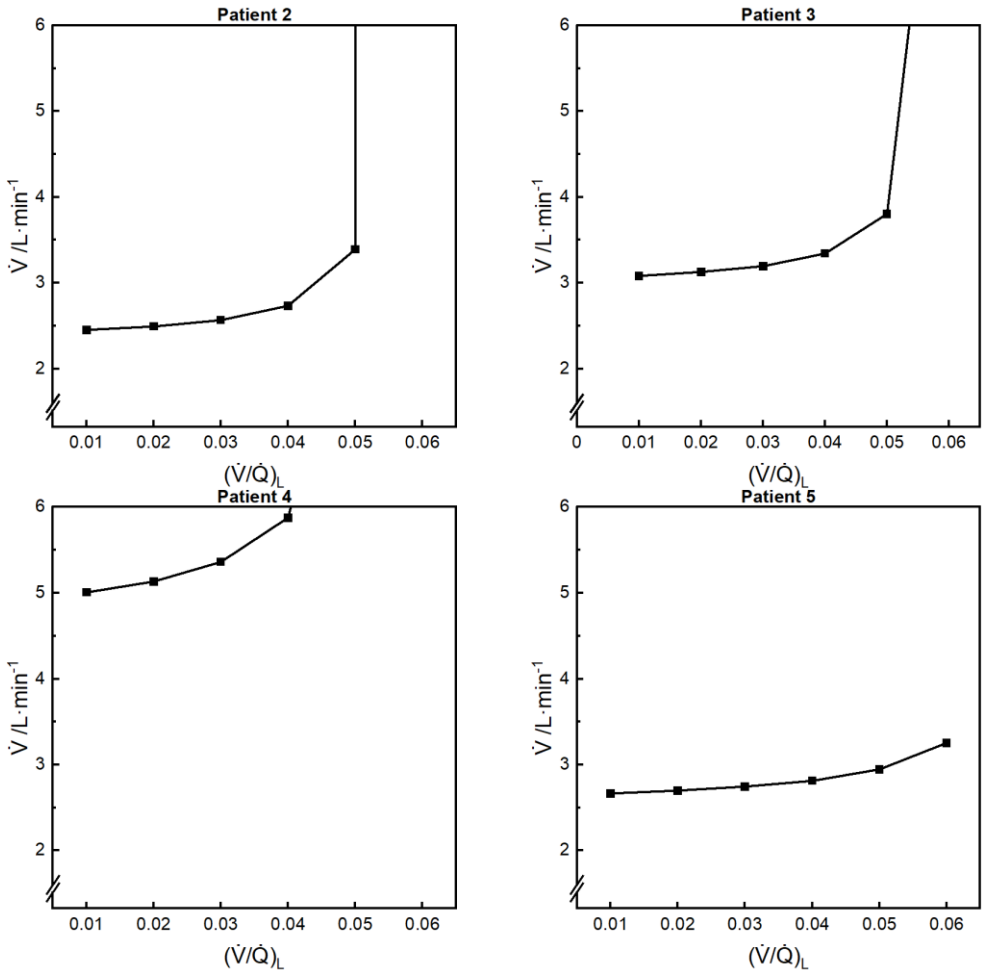


Figure 3. Total ventilation as a function of $(\dot{V}/\dot{Q})_L$. Results shown for patients 2-5. Some values off-scale for higher values of $(\dot{V}/\dot{Q})_L$. Differences between measured and calculated arterial partial pressures for CO_2 and O_2 < $1x10^{-2}$ mmHg for all distributions illustrated. $\dot{V}$, total ventilation.

Figure 3 illustrates the increase in the total combined ventilation to both compartments as the value for $\dot{V}/\dot{Q}$ associated with the low $\dot{V}/\dot{Q}$ compartment increased. In contrast to perfusion, where there was a fixed value for $\dot{Q}ns_{BM}$ for each patient, Busana *et al* did not provide information to allow the specification of a fixed value for alveolar ventilation for each patient. Were such information to be available, then the monotonic increasing nature of the ventilation in Fig. 3 suggests that there would be only one pair of $\dot{V}/\dot{Q}$ units that could satisfy constraints on the values for both $\dot{Q}ns_{BM}$ and alveolar ventilation.

Ventilation-perfusion distributions assuming multiple perfused compartment pairs

Figure 4 illustrates a $\dot{V}/\dot{Q}$ distribution for each patient based on the beta distribution with an assumed shape parameter μ (= $\alpha + \beta$) of 10. For each patient, the residual numerical error in the estimate for their Pa_{CO2} and Pa_{O2} was 10^{-3} mmHg or less. Figure 5 (upper and bottom left-hand panels) illustrates the effect of varying the shape parameter (μ = 5, 10, 20) on the distribution for patient 4. Higher values of μ were associated with steeper peaks and higher total overall values for ventilation. Finally, the right-hand lower panel of Fig. 5 illustrates the shape of the distribution for a hypothetical healthy person breathing air with $P\bar{v}_{CO2}$ = 46 mmHg, $P\bar{v}_{O2}$ = 40 mmHg, Pa_{CO2} = 40 mmHg, Pa_{O2} = 96 mmHg, and a presumed efficiency of use for the blood of 0.987. Here the separate $\dot{V}/\dot{Q}$ peaks in the high and low $\dot{V}/\dot{Q}$ regions have been lost and the calculation has resulted in a single central peak for the $\dot{V}/\dot{Q}$ distribution.

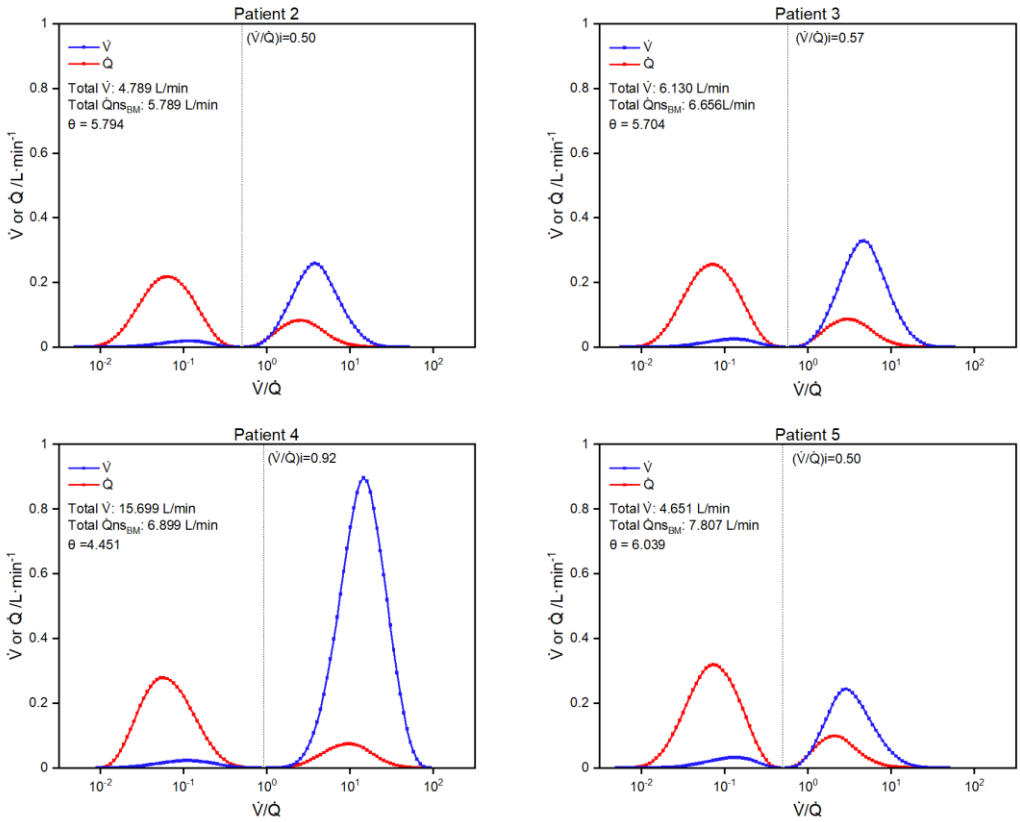


Figure 4. Multi-compartment distributions for V̇/Q̇. Results shown for patients 2-5. Distribution based on beta distribution with parameter μ = 10, as defined in Eq. 33. Differences between measured and calculated arterial partial pressures for CO_2 and O_2 < 1x10^{-3} mmHg for all distributions. Q̇, perfusion; Q̇ns$_{BM}$, total non-shunt perfusion where shunt fraction has been based on the non-aerated lung fraction; θ, parameter (estimated) for beta distribution as defined in Eq. 32; (V̇/Q̇)i, V̇/Q̇ value for ideal compartment for three-compartment model of lung.

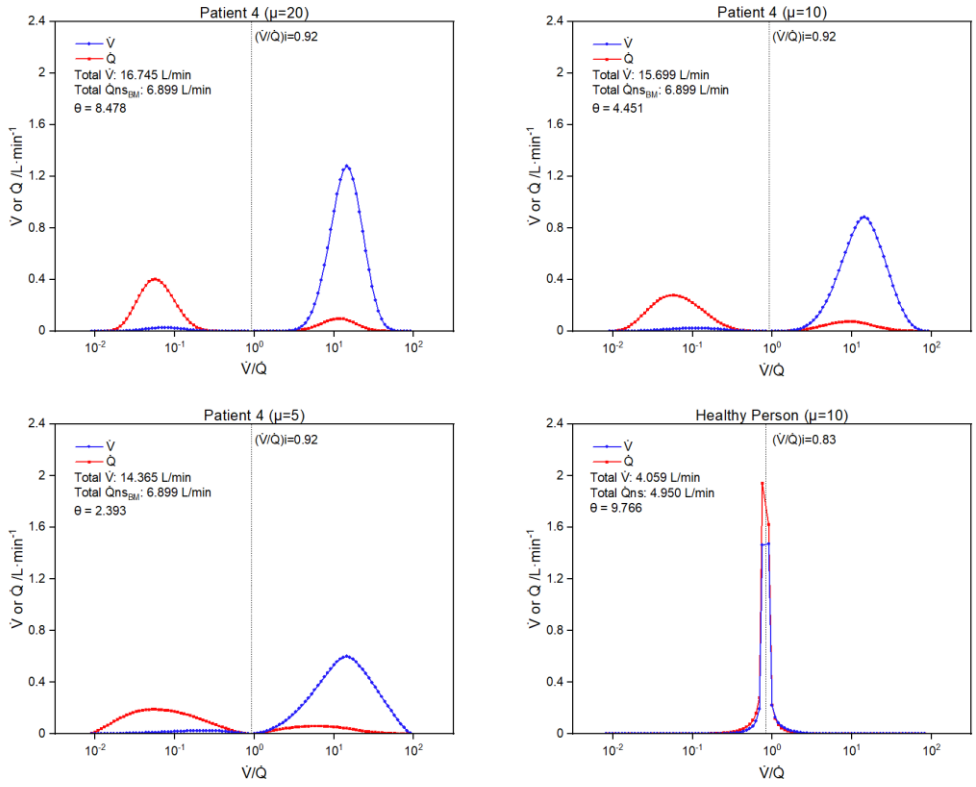


Figure 5. Variations in multi-compartment V̇/Q̇ distribution generated by changing parameters of the beta distribution and by changing physiological status. Results for top-left, top-right, and bottom-left panels are for patient 4 with μ = 20, 10 and 5, respectively. Results for bottom right panel are for standard blood gas values for a healthy individual with μ = 10. Differences between measured and calculated arterial partial pressures for CO_2 and O_2 < $1x10^{-3}$ mmHg for all distributions. Q̇ns, total non-shunt blood flow.

DISCUSSION

Busana *et al.* [2] reported on five patients with severe COVID-19 pneumonia; they hypothesised that the shunt blood flow within the lungs was proportional to the fraction of non-aerated lung tissue quantified by CT, and they subsequently employed a random simulation approach that identified candidate V̇/Q̇ distributions in four out of five patients that replicated the patients' Pa_{CO2} and Pa_{O2} values with limited precision. The purpose of the present study was to seek higher precision solutions that would then be within the accuracy of the blood-gas data, by developing a method that enabled direct calculation of candidate V̇/Q̇

distributions without using their random simulation approach. For the patient for whom Busana et al could find no $\dot{V}/\dot{Q}$ distributions, we were able to show that the shunt flow assumption resulted in a remaining non-shunt blood flow that was simply too low to support the gas exchange required, and therefore no solutions exist. For the other four patients, we have demonstrated that multiple, indeed infinite sets, of potential $\dot{V}/\dot{Q}$ distributions exist that were capable of reproducing the patients' Pa_{CO2} and Pa_{O2} values precisely. We have identified a few of these solutions, both in the form of single pairs of $\dot{V}/\dot{Q}$ compartments and in the form of distributions of multiple simultaneous pairs of $\dot{V}/\dot{Q}$ compartments.

Why the approach of Busana *et al.* did not lead to solutions very close to the patients' Pa_{CO2} and Pa_{O2} values is not entirely clear. One possibility is that 10^6 randomly chosen simulations is simply an insufficient number. This may appear strange, but Busana *et al.* report that their distribution has 5 parameters, and if each random choice of one parameter were to be permuted with every random choice of the other, then that would only allow 16 random choices for each parameter ($16^5 \approx 10^6$). While this is possible, we suspect a more likely reason is that it is difficult to design a strategy for ensuring that any random process of generating distributions provides an even remotely even coverage of possible values for Pa_{CO2} and Pa_{O2}. Evidence of this is very clear in their Fig. 6, which is an arterial P_{CO2}/P_{O2} diagram, and shows regions where the density of possible $\dot{V}/\dot{Q}$ distributions is very high, and other regions that are covered by no possible $\dot{V}/\dot{Q}$ distributions at all. The present study obviates this difficulty by showing that it is possible directly to construct putative $\dot{V}/\dot{Q}$ distributions that are guaranteed to reproduce the Pa_{CO2} and Pa_{O2} of individual patients based on the classical mass balance relations that have been established for gas exchange in the lung.

Busana *et al.* did not provide data concerning the patient's ventilation. The simulations constructed here vary substantially in relation to total alveolar ventilation (see Fig. 3). If this

ventilation were known for a patient, then it should be possible to use that information to select the particular pair of high and low $\dot{V}/\dot{Q}$ compartments consistent with the patient's gas exchange, or alternatively select the particular shape parameter for the beta distribution (μ) based on the ventilation (see Fig. 5).

Experimentally, the physiological approach that comes closest to providing a $\dot{V}/\dot{Q}$ distribution for a patient is the multiple inert gas elimination technique (MIGET) developed by Wagner and West [8]. This involves infusing into a vein a range of dissolved gases and measuring their retention and excretion ratios. In relation to the present study, it is of note that a retention for a very insoluble gas in the arterial blood would effectively provide the fraction of total blood flow that is pure shunt, and an excretion for a very soluble gas would effectively provide the fraction of total ventilation that is alveolar. Therefore, using the methodology developed in the present study, such information in combination with the P_{CO2} and P_{O2} values would be sufficient to calculate directly a single pair of low and high $\dot{V}/\dot{Q}$ compartments, or alternatively calculate a single beta distribution for $\dot{V}/\dot{Q}$, that is most representative of the $\dot{V}/\dot{Q}$ distribution within a patient.

Turning from the methodology to the results, what is evident from our solutions for the $\dot{V}/\dot{Q}$ distributions from both the methods we employed (Fig. 2 and Fig. 4) is that the assumption that the shunt fraction is proportional to the fraction of non-ventilated lung (proposed by Busana *et al*) led to compartments with extremely low estimates for $\dot{V}/\dot{Q}$. For example, the maximum possible values for $\dot{V}/\dot{Q}$ for the $(\dot{V}/\dot{Q})_L$ compartment were below 0.09 for all four patients. Similarly for the beta distribution, a considerable fraction of the total non-shunt perfusion was assigned to units of very low $\dot{V}/\dot{Q}$. In relation to this, we have considerable reservations as to whether the classical theory developed in relation to $\dot{V}/\dot{Q}$ distribution is actually applicable when very low $\dot{V}/\dot{Q}$ ratios are calculated for patients who are breathing gas containing a high inspired fraction of O_2, such as in these COVID-19

patients. This is because the classical theory makes no allowance for the movement of gases by diffusion other than that across the alveolar membrane. An extreme example would be apnoeic oxygenation, where the lung is motionless and the airway connected to 100% O_2. Classical $\dot{V}/\dot{Q}$ theory would predict that the alveolar gases would equilibrate with venous blood and no gas exchange would occur, whereas the reality is that the N_2 in the alveolar spaces diffuses away and the lung oxygenates the blood (the diffusional uptake of O_2 across the alveolar membrane generates a convective flow of O_2 in the airway). By way of specific example, the inspired gas for patient 2 had a P_{O2} of 606 mmHg. For a $\dot{V}/\dot{Q}$ of 0.05, the P_{N2} calculated for the low $\dot{V}/\dot{Q}$ compartment was 527 mmHg, which compares with a P_{N2} of 103 mmHg calculated for the high $\dot{V}/\dot{Q}$ compartment and a P_{N2} of 107.0 mmHg in the inspired gas. Inevitably, this will generate significant diffusion out of the low $\dot{V}/\dot{Q}$ alveolar space, both back into the airways and also into the blood stream once the P_{N2} of the blood has been lowered sufficiently by its exposure to lower values for P_{N2} associated with other, higher $\dot{V}/\dot{Q}$ compartments. Theoretically, the problem arises because *Eq. 1-3* deal only with convection, and assume that the movement of gas by diffusion within the gas phase can be neglected. Under conditions where the N_2 concentration gradients in the lung are going to be very large and convection slow, such as predicted in these patients, the use of *Eqns 1-3* is not valid.

Several limitations exist with this study. First, the analysis is limited to the five patients for whom Busana *et al*. were able to collect the necessary data. This number is insufficient to generalise any results to the overall patient population with any degree of certainty. Second, some starting parameters had to be estimated, for example the mixed venous concentrations and partial pressures, from measurements of mixed venous saturation. Third, the absence of any data pertaining to ventilation meant that a useful constraint on possible solutions was also missing.

In conclusion, the $\dot{V}/\dot{Q}$ distributions that arise when the shunt blood flow fraction is assumed proportional to the non-aerated lung fraction are unlikely to represent the true state of gas exchange in these severely ill COVID-19 patients. We feel a more likely interpretation of the derangements of gas exchange in these patients is that the $\dot{V}/\dot{Q}$ distributions are not as extreme as calculated by either Busana *et al*. or ourselves, but rather that the shunt fraction is higher than the fraction of non-aerated lung. One possible explanation may be that infection with Sars-CoV-2 impairs hypoxic pulmonary vasoconstriction (HPV), which normally would cause vasoconstriction within the non-aerated lung, limiting the blood supply to these regions. This impairment of HPV, which may well arise from direct infection and damage of the pulmonary vascular endothelium by Sars-Cov-2 [9, 10], could contribute to a shunt fraction that is greater than that expected from the amount of non-aerated (consolidated) lung. It seems to us that a simple statistic of interest would be the ratio between the shunt flow fraction calculated for the three-compartment model relative to the fraction of non-aerated lung ($\dot{Q}s_{3CM}/\dot{Q}s_{BM}$). This statistic could be compared with the same statistic calculated for patients suffering from non-COVID-19 ARDS. Busana *et al.* describe such control patients in the appendix to their paper, but there is not sufficient detail to undertake the calculation and compare the results with those for the COVID-19 patients.

Reference: see published website.

Bibliography

1. Vos T, Lim SS, Abbafati C, Abbas KM, Abbasi M, Abbasifard M, et al. Global burden of 369 diseases and injuries in 204 countries and territories, 1990–2019: A systematic analysis for the global burden of disease study 2019. Lancet. 2020;396(10258):1204-22.

2. Asthma + Lung UK. Asthma [Internet]. 2025 [cited 2025]. Available from: https://www.asthmaandlung.org.uk/conditions/asthma.

3. Asthma + Lung UK. 'Asthma care is in crisis' - charity sounds the siren as asthma death toll rises [Internet]. 2024. Available from: https://www.asthmaandlung.org.uk/media/press-releases/asthma-care-crisis-charity-sounds-siren-asthma-death-toll-rises.

4. Orlovic M, Tzelis D, Guerra I, Bar-Katz V, Woolley N, Bray H, et al. Environmental, healthcare and societal impacts of asthma: A UK model-based assessment. ERJ Open Research. 2024;10(4):00577-2023.

5. GINA Committee. Global strategy for asthma management and prevention (2024 update). Guideline. GINA; 2024. Available from: https://ginasthma.org/2024-report/.

6. Asthma: Diagnosis, monitoring and chronic asthma management Guideline. BTS/NICE/SIGN; 2024. Available from: https://www.nice.org.uk/guidance/ng245/chapter/Recommendations.

7. Byrnes CA, Dinarevic S, Busst C, Bush A, Shinebourne EA. Is nitric oxide in exhaled air produced at airway or alveolar level? Eur Respir J. 1997;10(5):1021-5.

8. Rackemann FM. A working classification of asthma. Am J Med. 1947;3(5):601-6.

9. Robinson DS, Hamid Q, Ying S, Tsicopoulos A, Barkans J, Bentley AM, et al. Predominant TH2-like bronchoalveolar T-lymphocyte population in atopic asthma. N Engl J Med. 1992;326(5):298-304.

10. Ying S, Durham SR, Corrigan CJ, Hamid Q, Kay AB. Phenotype of cells expressing mRNA for TH2-type (interleukin 4 and interleukin 5) and TH1-type (interleukin 2 and interferon gamma) cytokines in bronchoalveolar lavage and bronchial biopsies from atopic asthmatic and normal control subjects. American Journal of Respiratory Cell and Molecular Biology. 1995;12(5):477-87.

11. Wenzel SE, Schwartz LB, Langmack EL, Halliday JL, Trudeau JB, Gibbs RL, et al. Evidence that severe asthma can be divided pathologically into two inflammatory subtypes with distinct physiologic and clinical characteristics. Am J Respir Crit Care Med. 1999;160(3):1001-8.

12. Zhu J. T helper 2 (Th2) cell differentiation, type 2 innate lymphoid cell (ILC2) development and regulation of interleukin-4 (IL-4) and IL-13 production. Cytokine. 2015;75(1):14-24.

13. Fahy JV. Type 2 inflammation in asthma--present in most, absent in many. Nat Rev Immunol. 2015;15(1):57-65.

14. Lambrecht BN, Hammad H, Fahy JV. The cytokines of asthma. Immunity. 2019;50(4):975-91.

15. Busse WW, Kraft M, Rabe KF, Deniz Y, Rowe PJ, Ruddy M, et al. Understanding the key issues in the treatment of uncontrolled persistent asthma with type 2 inflammation. Eur Respir J. 2021;58(2):2003393.

16. Habib N, Pasha MA, Tang DD. Current understanding of asthma pathogenesis and biomarkers. Cells. 2022;11(17):2764.

17. Niessen NM, Fricker M, McDonald VM, Gibson PG. T2-low: What do we know?: Past, present, and future of biologic therapies in noneosinophilic asthma. Annals of Allergy, Asthma & Immunology. 2022;129(2):150-9.

18. Liu T, Woodruff PG, Zhou X. Advances in non-type 2 severe asthma: From molecular insights to novel treatment strategies. Eur Respir J. 2024;64(2):2300826.

19. Hinks TSC, Levine SJ, Brusselle GG. Treatment options in type-2 low asthma. Eur Respir J. 2021;57(1):2000528.

20. Haldar P, Pavord ID, Shaw DE, Berry MA, Thomas M, Brightling CE, et al. Cluster analysis and clinical asthma phenotypes. Am J Respir Crit Care Med. 2008;178(3):218-24.

21. Moore WC, Meyers DA, Wenzel SE, Teague WG, Li H, Li X, et al. Identification of asthma phenotypes using cluster analysis in the severe asthma research program. Am J Respir Crit Care Med. 2010;181(4):315-23.

22. Shaw DE, Sousa AR, Fowler SJ, Fleming LJ, Roberts G, Corfield J, et al. Clinical and inflammatory characteristics of the european u-biopred adult severe asthma cohort. Eur Respir J. 2015;46(5):1308-21.

23. Loza MJ, Djukanovic R, Chung KF, Horowitz D, Ma K, Branigan P, et al. Validated and longitudinally stable asthma phenotypes based on cluster analysis of the adept study. Respir Res. 2016;17(1):165.

24. Kaur R, Chupp G. Phenotypes and endotypes of adult asthma: Moving toward precision medicine. J Allergy Clin Immunol. 2019;144(1):1-12.

25. Anderson GP. Endotyping asthma: New insights into key pathogenic mechanisms in a complex, heterogeneous disease. Lancet. 2008;372(9643):1107-19.

26. Ray A, Das J, Wenzel SE. Determining asthma endotypes and outcomes: Complementing existing clinical practice with modern machine learning. Cell Rep Med. 2022;3(12):100857.

27. Ramonell RP, Gauthier MC, Ray A, Wenzel SE. Biologic medications for severe asthma: Implications for understanding pathogenic heterogeneity and endotypes. Annu Rev Med. 2025;76(1):339-55.

28. Bradding P, Porsbjerg C, Côté A, Dahlén S-E, Hallstrand TS, Brightling CE. Airway hyperresponsiveness in asthma: The role of the epithelium. J Allergy Clin Immunol. 2024;153(5):1181-93.

29. Hammad H, Lambrecht BN. The basic immunology of asthma. Cell. 2021;184(6):1469-85.

30. Lajiness JD, Cook-Mills JM. Catching our breath: Updates on the role of dendritic cell subsets in asthma. Adv Biol (Weinh). 2023;7(6):e2200296.

31. Elieh Ali Komi D, Bjermer L. Mast cell-mediated orchestration of the immune responses in human allergic asthma: Current insights. Clin Rev Allergy Immunol. 2019;56(2):Lancet234-47.

32. Camoretti-Mercado B, Lockey RF. Airway smooth muscle pathophysiology in asthma. J Allergy Clin Immunol. 2021;147(6):1983-95.

33. Harker JA, Lloyd CM. T helper 2 cells in asthma. J Exp Med. 2023;220(6).

34. Kim CK, Callaway Z, Pawankar R. Eosinophil granule proteins as a biomarker in managing asthma and allergies. Asia Pac Allergy. 2023;13(2):66-71.

35. Fulkerson PC, Rothenberg ME. Eosinophil development, disease involvement, and therapeutic suppression. Adv Immunol. 2018;138:1-34.

36. Barnes PJ. Targeting cytokines to treat asthma and chronic obstructive pulmonary disease. Nat Rev Immunol. 2018;18(7):454-66.

37. Pelaia C, Heffler E, Crimi C, Maglio A, Vatrella A, Pelaia G, et al. Interleukins 4 and 13 in asthma: Key pathophysiologic cytokines and druggable molecular targets. Front Pharmacol. 2022;13:851940.

38. AbuJabal R, Ramakrishnan RK, Bajbouj K, Hamid Q. Role of IL-5 in asthma and airway remodelling. Clin Exp Allergy. 2024;54(8):538-49.

39. Marone G, Granata F, Pucino V, Pecoraro A, Heffler E, Loffredo S, et al. The intriguing role of interleukin 13 in the pathophysiology of asthma. Front Pharmacol. 2019;10:1387.

40. Guo FH, Uetani K, Haque SJ, Williams BR, Dweik RA, Thunnissen FB, et al. Interferon gamma and interleukin 4 stimulate prolonged expression of inducible nitric oxide synthase in human airway epithelium through synthesis of soluble mediators. J Clin Invest. 1997;100(4):829-38.

41. Guo FH, Erzurum SC. Characterization of inducible nitric oxide synthase expression in human airway epithelium. Environ Health Perspect. 1998;106 Suppl 5(Suppl 5):1119-24.

42. Chibana K, Trudeau JB, Mustovitch AT, Hu H, Zhao J, Balzar S, et al. IL-13 induced increases in nitrite levels are primarily driven by increases in inducible nitric oxide synthase as compared with effects on arginases in human primary bronchial epithelial cells. Clin Exp Allergy. 2008;38(6):936-46.

43. Porsbjerg C, Melén E, Lehtimäki L, Shaw D. Asthma. Lancet. 2023;401(10379):858-73.

44. Macklem PT, Mead J. Resistance of central and peripheral airways measured by a retrograde catheter. J Appl Physiol. 1967;22(3):395-401.

45. Lipworth B, Manoharan A, Anderson W. Unlocking the quiet zone: The small airway asthma phenotype. Lancet Respir Med. 2014;2(6):497-506.

46. Mead J. The lung's quiet zone. N Engl J Med. 1970;282(23):1318-9.

47. Erjefält JS. Anatomical and histopathological approaches to asthma phenotyping. Respir Med. 2023;210:107168.

48. Hamid Q. Pathogenesis of small airways in asthma. Respiration. 2012;84(1):4-11.

49. Hamid QA. Peripheral inflammation is more important than central inflammation. Respir Med. 1997;91 Suppl A:11-2.

50. Minshall EM, Hogg JC, Hamid QA. Cytokine mRNA expression in asthma is not restricted to the large airways. J Allergy Clin Immunol. 1998;101(3):386-90.

51. Balzar S, Chu HW, Strand M, Wenzel S. Relationship of small airway chymase-positive mast cells and lung function in severe asthma. Am J Respir Crit Care Med. 2005;171(5):431-9.

52. Dweik RA, Boggs PB, Erzurum SC, Irvin CG, Leigh MW, Lundberg JO, et al. An official ATS clinical practice guideline: Interpretation of exhaled nitric oxide levels (FENO) for clinical applications. Am J Respir Crit Care Med. 2011;184(5):602-15.

53. BTS/NICE/SIGN. Evidence reviews for diagnostic accuracy of fractional exhaled nitric oxide (FeNO) measures. Evidence reviews. BTS/NICE/SIGN; 2024. Available from: https://www.nice.org.uk/guidance/ng245/evidence/evidence-review-f-accuracy-and-clinical-and-cost-effectiveness-of-feno-in-the-diagnosis-of-asthma-pdf-13558146739.

54. Petsky HL, Kew KM, Turner C, Chang AB. Exhaled nitric oxide levels to guide treatment for adults with asthma. Cochrane Database Syst Rev. 2016;9(9):Cd011440.

55. Committee G. Difficult-to-treat & severe asthma (2024). 2024.

56. NICE. Dupilumab for treating severe asthma with type 2 inflammation Guidance. NICE; 2021. Available from: https://www.nice.org.uk/guidance/ta751/chapter/1-Recommendations.

57. McNicholl DM, Stevenson M, McGarvey LP, Heaney LG. The utility of fractional exhaled nitric oxide suppression in the identification of nonadherence in difficult asthma. Am J Respir Crit Care Med. 2012;186(11):1102-8.

58. Butler CA, Heaney LG. Fractional exhaled nitric oxide and asthma treatment adherence. Curr Opin Allergy Clin Immunol. 2021;21(1):59-64.

59. Lopez AF, Sanderson CJ, Gamble JR, Campbell HD, Young IG, Vadas MA. Recombinant human interleukin 5 is a selective activator of human eosinophil function. J Exp Med. 1988;167(1):219-24.

60. Van Hulst G, Batugedara HM, Jorssen J, Louis R, Bureau F, Desmet CJ. Eosinophil diversity in asthma. Biochem Pharmacol. 2020;179:113963.

61. Hussain M, Liu G. Eosinophilic asthma: Pathophysiology and therapeutic horizons. Cells. 2024;13(5).

62. Shen K, Zhang M, Zhao R, Li Y, Li C, Hou X, et al. Eosinophil extracellular traps in asthma: Implications for pathogenesis and therapy. Respir Res. 2023;24(1):231.

63. Bousquet J, Chanez P, Lacoste JY, Barnéon G, Ghavanian N, Enander I, et al. Eosinophilic inflammation in asthma. N Engl J Med. 1990;323(15):1033-9.

64. Horn BR, Robin ED, Theodore J, Van Kessel A. Total eosinophil counts in the management of bronchial asthma. N Engl J Med. 1975;292(22):1152-5.

65. Mallah N, Rodriguez-Segade S, Gonzalez-Barcala F-J, Takkouche B. Blood eosinophil count as predictor of asthma exacerbation. A meta-analysis. Pediatr Allergy Immunol. 2021;32(3):465-78.

66. Price DB, Rigazio A, Campbell JD, Bleecker ER, Corrigan CJ, Thomas M, et al. Blood eosinophil count and prospective annual asthma disease burden: A UK cohort study. Lancet Respir Med. 2015;3(11):849-58.

67. Couillard S, Laugerud A, Jabeen M, Ramakrishnan S, Melhorn J, Hinks T, et al. Derivation of a prototype asthma attack risk scale centred on blood eosinophils and exhaled nitric oxide. Thorax. 2022;77(2):199-202.

68. Pelaia C, Paoletti G, Puggioni F, Racca F, Pelaia G, Canonica GW, et al. Interleukin-5 in the pathophysiology of severe asthma. Front Physiol. 2019;10:1514.

69. Ortega HG, Liu MC, Pavord ID, Brusselle GG, FitzGerald JM, Chetta A, et al. Mepolizumab treatment in patients with severe eosinophilic asthma. N Engl J Med. 2014;371(13):1198-207.

70. Ortega HG, Yancey SW, Mayer B, Gunsoy NB, Keene ON, Bleecker ER, et al. Severe eosinophilic asthma treated with mepolizumab stratified by baseline eosinophil thresholds: A secondary analysis of the dream and mensa studies. Lancet Respir Med. 2016;4(7):549-56.

71. Abdo M, Trinkmann F, Kirsten A-M, Pedersen F, Herzmann C, von Mutius E, et al. Small airway dysfunction links asthma severity with physical activity and symptom control. J Allergy Clin Immunol Pract. 2021;9(9):3359-68.e1.

72. Kjellberg S, Houltz BK, Zetterström O, Robinson PD, Gustafsson PM. Clinical characteristics of adult asthma associated with small airway dysfunction. Respir Med. 2016;117:92-102.

73. Asma A, Lorenzo P, Nicholas MJS, Haopeng X, Dominic S, Graham R, et al. Effects of biologic therapy on novel indices of lung inhomogeneity in patients with severe type-2 high asthma. BMJ Open Respir Res. 2025;12(1).

74. Mepolizumab. Drugs and lactation database (lactmed®). Bethesda (MD): National Institute of Child Health and Human Development; 2006.

75. Reslizumab. Drugs and lactation database (lactmed®). Bethesda (MD): National Institute of Child Health and Human Development; 2006.

76. Benralizumab. Drugs and lactation database (lactmed®). Bethesda (MD): National Institute of Child Health and Human Development; 2006.

77. NICE. Mepolizumab for treating severe eosinophilic asthma. Guidance. NICE; 2024. Available from: https://www.nice.org.uk/guidance/ta671/chapter/1-Recommendations.

78. NICE. Benralizumab for treating severe eosinophilic asthma. Guidance. NICE; 2024. Available from: https://www.nice.org.uk/guidance/ta565/chapter/1-Recommendations.

79. Farne HA, Wilson A, Milan S, Banchoff E, Yang F, Powell CVE. Anti-il-5 therapies for asthma. Cochrane Database Syst Rev. 2022(7).

80. Pavord ID, Korn S, Howarth P, Bleecker ER, Buhl R, Keene ON, et al. Mepolizumab for severe eosinophilic asthma (dream): A multicentre, double-blind, placebo-controlled trial. Lancet. 2012;380(9842):651-9.

81. Weibel ER, Sapoval B, Filoche M. Design of peripheral airways for efficient gas exchange. Respir Physiol Neurobiol. 2005;148(1):3-21.

82. Weibel ER. Geometry and dimensions of airways of the respiratory zone. In: Weibel ER, editor. Morphometry of the human lung. Berlin, Heidelberg: Springer Berlin Heidelberg; 1963. p. 56-73.

83. Kapwatt. Lung volumes [Internet]. 2024 [cited 2025]. Available from: https://commons.wikimedia.org/w/index.php?curid=74891988.

84. Fowler WS. Lung function studies. II. The respiratory dead space. American Journal of Physiology-Legacy Content. 1948;154(3):405-16.

85. Cross ME, Plunkett EVE. Fowler’s method. In: Cross ME, Plunkett EVE, editors. Physics, pharmacology and physiology for anaesthetists: Key concepts for the FRCA. 2 ed. Cambridge: Cambridge University Press; 2014. p. 220-.

86. Anderson JT, Owings JT, Goodnight JE. Bedside noninvasive detection of acute pulmonary embolism in critically ill surgical patients. Arch Surg. 1999;134(8):869-74; discussion 74-5.

87. Bartels J, Severinghaus JW, Forster RE, Briscoe WA, Bates DV. The respiratory dead space measured by single breath analysis of oxygen, carbon dioxide, nitrogen or helium. J Clin Invest. 1954;33(1):41-8.

88. Fletcher R, Jonson B, Cumming G, Brew J. The concept of deadspace with special reference to the single breath test for carbon dioxide. Br J Anaesth. 1981;53(1):77-88.

89. Nassar BS, Schmidt GA. Capnography during critical illness. Chest. 2016;149(2):576-85.

90. Nassar BS, Schmidt GA. Capnography for monitoring of the critically ill patient. Clin Chest Med. 2022;43(3):393-400.

91. Rackley CR. Monitoring during mechanical ventilation. Respir Care. 2020;65(6):832-46.

92. Preston RR. Gas exchange. In: Wilson TE, editor. Lippincott® illustrated reviews: Physiology, 3e: Lippincott Williams & Wilkins, a Wolters Kluwer business; 2025. p. 0.

93. Cloutier MMMD. Oxygen and carbon dioxide transport. In: Cloutier MMMD, editor. Respiratory physiology2019. p. 101-18.

94. Lumb AB. Chapter 7 - distribution of pulmonary ventilation and perfusion. In: Lumb AB, editor. Nunn's applied respiratory physiology (eighth edition): Elsevier; 2017. p. 109-35.e2.

95. Graham BL, Steenbruggen I, Miller MR, Barjaktarevic IZ, Cooper BG, Hall GL, et al. Standardization of spirometry 2019 update. An official American Thoracic Society and european respiratory society technical statement. Am J Respir Crit Care Med. 2019;200(8):e70-e88.

96. Stanojevic S, Kaminsky DA, Miller MR, Thompson B, Aliverti A, Barjaktarevic I, et al. ERS/ATS technical standard on interpretive strategies for routine lung function tests. Eur Respir J. 2022;60(1):2101499.

97. Initiative GLF. Global Lung Function Initiative calculators [Internet]. Global Lung Functin Initiative; [cited 2025]. Available from: https://gli-calculator.ersnet.org/.

98. Siora A, Vontetsianos A, Chynkiamis N, Anagnostopoulou C, Bartziokas K, Anagnostopoulos N, et al. Small airways in asthma: From inflammation and pathophysiology to treatment response. Respir Med. 2024;222:107532.

99. Coates A, Peslin R, Rodenstein D, Stocks J. Measurement of lung volumes by plethysmography. Eur Respir J.10(6):1415-27.

100. DuBois AB, Brody AW, Lewis DH, Burgess BF. Oscillation mechanics of lungs and chest in man. J Appl Physiol. 1956;8(6):587-94.

101. Bickel S, Popler J, Lesnick B, Eid N. Impulse oscillometry: Interpretation and practical applications. Chest. 2014;146(3):841-7.

102. Oostveen E, Boda K, van der Grinten CPM, James AL, Young S, Nieland H, et al. Respiratory impedance in healthy subjects: Baseline values and bronchodilator response. Eur Respir J. 2013;42(6):1513-23.

103. Kraft M, Richardson M, Hallmark B, Billheimer D, Van den Berge M, Fabbri LM, et al. The role of small airway dysfunction in asthma control and exacerbations: A longitudinal, observational analysis using data from the atlantis study. Lancet Respir Med. 2022;10(7):661-8.

104. Postma DS, Brightling C, Baldi S, Van den Berge M, Fabbri LM, Gagnatelli A, et al. Exploring the relevance and extent of small airways dysfunction in asthma (atlantis): Baseline data from a prospective cohort study. Lancet Respir Med. 2019;7(5):402-16.

105. Fowler WS, Cornish ER, Jr., Kety SS. Lung function studies. Viii. Analysis of alveolar ventilation by pulmonary N2 clearance curves. J Clin Invest. 1952;31(1):40-50.

106. Engel LA, Macklem PT. Gas mixing and distribution in the lung. Int Rev Physiol. 1977;14:37-82.

107. Robinson PD, Latzin P, Verbanck S, Hall GL, Horsley A, Gappa M, et al. Consensus statement for inert gas washout measurement using multiple- and single- breath tests. Eur Respir J.41(3):507-22.

108. Crawford AB, Makowska M, Paiva M, Engel LA. Convection- and diffusion-dependent ventilation maldistribution in normal subjects. J Appl Physiol (1985). 1985;59(3):838-46.

109. Jetmalani K, Chapman DG, Thamrin C, Farah CS, Berend N, Salome CM, et al. Bronchodilator responsiveness of peripheral airways in smokers with normal spirometry. Respirology. 2016;21(7):1270-6.

110. Farah CS, King GG, Brown NJ, Peters MJ, Berend N, Salome CM. Ventilation heterogeneity predicts asthma control in adults following inhaled corticosteroid dose titration. J Allergy Clin Immunol. 2012;130(1):61-8.

111. Nuttall AG, Beardsmore CS, Gaillard EA. Ventilation heterogeneity in children with severe asthma. Eur J Pediatr. 2021;180(11):3399-404.

112. Mountain JE, Santer P, O'Neill DP, Smith NMJ, Ciaffoni L, Couper JH, et al. Potential for noninvasive assessment of lung inhomogeneity using highly precise, highly time-resolved measurements of gas exchange. J Appl Physiol (1985). 2018;124(3):615-31.

113. O'Neill DP, Robbins PA. A mechanistic physicochemical model of carbon dioxide transport in blood. J Appl Physiol (1985). 2017;122(2):283-95.

114. Nitric oxide [Internet]. Wikipedia; 2025. Available from: https://en.wikipedia.org/wiki/Nitric_oxide#Biological_functions.

115. Wu G, Morris SM, Jr. Arginine metabolism: Nitric oxide and beyond. Biochem J. 1998;336 (1):1-17.

116. Ricciardolo FLM, Sterk PJ, Gaston B, Folkerts G. Nitric oxide in health and disease of the respiratory system. Physiol Rev. 2004;84(3):731-65.

117. Cinelli MA, Do HT, Miley GP, Silverman RB. Inducible nitric oxide synthase: Regulation, structure, and inhibition. Med Res Rev. 2020;40(1):158-89.

118. Jackson CL, Lucas JS, Walker WT, Owen H, Premadeva I, Lackie PM. Neuronal NOS localises to human airway cilia. Nitric Oxide. 2015;44:3-7.

119. Şelaru M, Rusu MC, Jianu AM. Expression of nNOS in the human larynx. Anat Sci Int. 2015;90(4):327-30.

120. Mattila JT, Thomas AC. Nitric oxide synthase: Non-canonical expression patterns. Front Immunol. 2014;5:478.

121. Siragusa M, Fleming I. The eNOS signalosome and its link to endothelial dysfunction. Pflugers Arch. 2016;468(7):1125-37.

122. Marozkina N, Smith L, Zhao Y, Zein J, Chmiel JF, Kim J, et al. Somatic cell hemoglobin modulates nitrogen oxide metabolism in the human airway epithelium. Sci Rep. 2021;11(1):15498.

123. Pechkovsky DV, Zissel G, Goldmann T, Einhaus M, Taube C, Magnussen H, et al. Pattern of NOS2 and NOS3 mRNA expression in human A549 cells and primary cultured AEC II. Am J Physiol Lung Cell Mol Physiol. 2002;282(4):L684-92.

124. Morris SM, Billiar TR. New insights into the regulation of inducible nitric oxide synthesis. Am J Physiol Endocrinol Metab. 1994;266(6):E829-E39.

125. Guo FH, De Raeve HR, Rice TW, Stuehr DJ, Thunnissen FB, Erzurum SC. Continuous nitric oxide synthesis by inducible nitric oxide synthase in normal human airway epithelium in vivo. Proc Natl Acad Sci U S A. 1995;92(17):7809-13.

126. Kumagai J, Kiuchi M, Kokubo K, Yagyu H, Nemoto M, Tsuji K, et al. The USP7-STAT3-granzyme-Par-1 axis regulates allergic inflammation by promoting differentiation of IL-5-producing Th2 cells. Proc Natl Acad Sci U S A. 2023;120(49):e2302903120.

127. Maniscalco M, Vitale C, Vatrella A, Molino A, Bianco A, Mazzarella G. Fractional exhaled nitric oxide-measuring devices: Technology update. Med Devices (Auckl). 2016;9(null):151-60.

128. Cristescu SM, Mandon J, Harren FJ, Meriläinen P, Högman M. Methods of NO detection in exhaled breath. J Breath Res. 2013;7(1):017104.

129. Korn S, Wilk M, Voigt S, Weber S, Keller T, Buhl R. Measurement of fractional exhaled nitric oxide: Comparison of three different analysers. Respiration. 2020;99(1):1-8.

130. Menzies D, Nair A, Lipworth BJ. Portable exhaled nitric oxide measurement: Comparison with the "gold standard" technique. Chest. 2007;131(2):410-4.

131. Taylor DR, Palmay R, Cowan JO, Herbison GP. Long term performance characteristics of an electrochemical nitric oxide analyser. Respir Med. 2011;105(2):211-7.

132. Moskalenko KL, Nadezhdinskii AI, Adamovskaya IA. Human breath trace gas content study by tunable diode laser spectroscopy technique. Infrared Phys Technol. 1996;37(1):181-92.

133. McKellar ARW. Mid-infrared laser magnetic resonance spectroscopy. Faraday Discuss Chem Soc. 1981;71(0):63-76.

134. Menzel L, Kosterev AA, Curl RF, Tittel FK, Gmachl C, Capasso F, et al. Spectroscopic detection of biological NO with a quantum cascade laser. Appl Phys B. 2001;72(7):859-63.

135. Petralia LS, Bahl A, Peverall R, Richmond G, Couper JH, Hancock G, et al. Accurate real-time f(e)no expirograms using complementary optical sensors. J Breath Res. 2020;14(4):047102.

136. Tsoukias NM, George SC. A two-compartment model of pulmonary nitric oxide exchange dynamics. J Appl Physiol. 1998;85(2):653-66.

137. George SC, Hogman M, Permutt S, Silkoff PE. Modeling pulmonary nitric oxide exchange. J Appl Physiol. 2004;96(3):831-9.

138. Jorres R. Modelling the production of nitric oxide within the human airways. Eur Respir J. 2000;16(3):555-60.

139. Shin H-W, George SC. Impact of axial diffusion on nitric oxide exchange in the lungs. J Appl Physiol. 2002;93(6):2070-80.

140. Kerckx Y, Michils A, Van Muylem A. Airway contribution to alveolar nitric oxide in healthy subjects and stable asthma patients. J Appl Physiol (1985). 2008;104(4):918-24.

141. Shin H-W, Condorelli P, Rose-Gottron CM, Cooper DM, George SC. Probing the impact of axial diffusion on nitric oxide exchange dynamics with heliox. J Appl Physiol. 2004;97(3):874-82.

142. Condorelli P, Shin H-W, Aledia AS, Silkoff PE, George SC. A simple technique to characterize proximal and peripheral nitric oxide exchange using constant flow exhalations and an axial diffusion model. J Appl Physiol. 2007;102(1):417-25.

143. Suresh V, Shelley DA, Shin H-W, George SC. Effect of heterogeneous ventilation and nitric oxide production on exhaled nitric oxide profiles. J Appl Physiol. 2008;104(6):1743-52.

144. Karamaoun C, Van Muylem A, Haut B. Modeling of the nitric oxide transport in the human lungs. Front Physiol. 2016;7:255.

145. Buess A, Van Muylem A, Nonclercq A, Haut B. Modeling of the transport and exchange of a gas species in lungs with an asymmetric branching pattern. Application to nitric oxide. Front Physiol. 2020;11:570015.

146. Högman M, Drca N, Ehrstedt C, Meriläinen P. Exhaled nitric oxide partitioned into alveolar, lower airways and nasal contributions. Respir Med. 2000;94(10):985-91.

147. Pietropaoli AP, Perillo IB, Torres A, Perkins PT, Frasier LM, Utell MJ, et al. Simultaneous measurement of nitric oxide production by conducting and alveolar airways of humans. J Appl Physiol. 1999;87(4):1532-42.

148. Silkoff PE, Sylvester JT, Zamel N, Permutt S. Airway nitric oxide diffusion in asthma: Role in pulmonary function and bronchial responsiveness. Am J Respir Crit Care Med. 2000;161(4 Pt 1):1218-28.

149. Eckel SP, Linn WS, Berhane K, Rappaport EB, Salam MT, Zhang Y, et al. Estimation of parameters in the two-compartment model for exhaled nitric oxide. PLoS One. 2014;9(1):e85471.

150. Tsoukias NM, Tannous Z, Wilson AF, George SC. Single-exhalation profiles of NO and CO2 in humans: Effect of dynamically changing flow rate. J Appl Physiol. 1998;85(2):642-52.

151. Weng J, Molshatzki N, Marjoram P, Gauderman WJ, Gilliland FD, Eckel SP. Hierarchical bayesian estimation of covariate effects on airway and alveolar nitric oxide. Sci Rep. 2021;11(1):17180.

152. Weng J, Molshatzki N, Marjoram P, Gauderman WJ, Gilliland FD, Eckel SP. Longitudinal hierarchical bayesian models of covariate effects on airway and alveolar nitric oxide. Sci Rep. 2023;13(1):5346.

153. Paredi P, Kharitonov SA, Meah S, Barnes PJ, Usmani OS. A novel approach to partition central and peripheral airway nitric oxide. Chest. 2014;145(1):113-9.

154. Karvonen T, Lehtimäki L. Flow-independent nitric oxide parameters in asthma: A systematic review and meta-analysis. J Breath Res. 2019;13(4):044001.

155. Mahut B, Trinquart L, Le Bourgeois M, Becquemin MH, Beydon N, Aubourg F, et al. Multicentre trial evaluating alveolar no fraction as a marker of asthma control and severity. Allergy. 2010;65(5):636-44.

156. Asano T, Kanemitsu Y, Takemura M, Fukumitsu K, Kurokawa R, Inoue Y, et al. Small airway inflammation is associated with residual airway hyperresponsiveness in Th2-high asthma. J Asthma. 2020;57(9):933-41.

157. Fukumitsu K, Nishiyama H, Kanemitsu Y, Takeda N, Kurokawa R, Tajiri T, et al. Pretreatment alveolar nitric oxide levels predict improvement of pulmonary function 1 year following anti-asthma treatments in patients with inhaled corticosteroid-naïve asthma. Int Arch Allergy Immunol. 2022;183(5):479-89.

158. Berry M, Hargadon B, Morgan A, Shelley M, Richter J, Shaw D, et al. Alveolar nitric oxide in adults with asthma: Evidence of distal lung inflammation in refractory asthma. Eur Respir J.25(6):986-91.

159. Hodgson D, Anderson J, Reynolds C, Meakin G, Bailey H, Pavord I, et al. A randomised controlled trial of small particle inhaled steroids in refractory eosinophilic asthma (SPIRA). Thorax. 2015;70(6):559-65.

160. Gelb AF, George SC, Silkoff PE, Krishnan A, Fraser C, Taylor CF, et al. Central and peripheral airway/alveolar sites of exhaled nitric oxide in acute asthma. Thorax. 2010;65(7):619-25.

161. Magor-Elliott SRM, Fullerton CJ, Richmond G, Ritchie GAD, Robbins PA. A dynamic model of the body gas stores for carbon dioxide, oxygen, and inert gases that incorporates circulatory transport delays to and from the lung. J Appl Physiol (1985). 2021;130(5):1383-97.

162. Ciaffoni L, O'Neill DP, Couper JH, Ritchie GA, Hancock G, Robbins PA. In-airway molecular flow sensing: A new technology for continuous, noninvasive monitoring of oxygen consumption in critical care. Sci Adv. 2016;2(8):e1600560.

163. Cummings B, Hamilton ML, Ciaffoni L, Pragnell TR, Peverall R, Ritchie GA, et al. Laser-based absorption spectroscopy as a technique for rapid in-line analysis of respired gas concentrations of O2 and CO2. J Appl Physiol (1985). 2011;111(1):303-7.

164. Valentin J. Basic anatomical and physiological data for use in radiological protection: Reference values:Icrp publication 89: Approved by the commission in september 2001. Annals of the ICRP. 2002;32(3):1-277.

165. Avolio AP. Multi-branched model of the human arterial system. Med Biol Eng Comput. 1980;18(6):709-18.

166. Smith NMJ, Couper J, Fullerton CJ, Richmond G, Talbot NP, Hancock G, et al. Novel measure of lung function for assessing disease activity in asthma. BMJ Open Respir Res. 2020;7(1).

167. Smith NMJ, Magor-Elliott SRM, Fullerton CJ, Couper JH, Richmond G, Hancock G, et al. The lognormal lung: A new approach to quantifying lung inhomogeneity in COPD. Front Physiol. 2022;13:1032126.

168. Xu H, Smith N, Alamoudi A, Petralia L, Sandhu D, Richmond G, et al. P253 association between a computed cardiopulmonography (CCP) ventilation-inhomogeneity index and conventional markers of small-airway function. Thorax. 2024;79(Suppl 2):A260-A1.

169. Redmond JL, Kendall F, Smith NMJ, Magor-Elliott SRM, Hallifax RJ, Fullerton CJ, et al. Computed cardiopulmonography for the detection of early smoking-related changes in the lungs of young individuals who smoke. Chest. 2024;165(5):1107-10.

170. Magor-Elliott SRM, Alamoudi A, Chamley RR, Xu H, Wellalagodage T, McDonald RP, et al. Altered lung physiology in two cohorts after COVID-19 infection as assessed by computed cardiopulmonography. J Appl Physiol (1985). 2022;133(5):1175-91.

171. Alamoudi A. Assessment of inhomogeneity in gas exchange using a novel methodology. Oxford: University of Oxford; 2024.

172. Högman M, Bowerman C, Chavez L, Dressel H, Malinovschi A, Radtke T, et al. ERS technical standard: Global Lung Function Initiative reference values for exhaled nitric oxide fraction (FENO50). Eur Respir J. 2024;63(1):2300370.

173. Hartl S, Breyer M-K, Burghuber OC, Ofenheimer A, Schrott A, Urban MH, et al. Blood eosinophil count in the general population: Typical values and potential confounders. Eur Respir J. 2020;55(5):1901874.

174. Hartl S, Breyer MK, Burghuber O, Schiffers C, Puchhammer P, Ofenheimer A, et al. How consistent are blood eosinophil counts in a general population? Eur Respir J.60(suppl 66):2698.

175. Dhumal P, Singh V, Sarkar M, Padmanabhan A, Swarnakar R, Christopher D, et al. Absolute blood eosinophil counts among 3,763 healthy, asthmatic, and COPD subjects across india. Eur Respir J.62(suppl 67):PA3602.

176. Lee S-H, Ahn K-M, Lee S-Y, Kim S-S, Park H-W. Blood eosinophil count as a predictor of lung function decline in healthy individuals. J Allergy Clin Immunol Pract. 2021;9(1):394-9.e1.

177. Hancox RJ, Pavord ID, Sears MR. Associations between blood eosinophils and decline in lung function among adults with and without asthma. Eur Respir J. 2018;51(4):1702536.

178. Park HY, Chang Y, Kang D, Hong YS, Zhao D, Ahn J, et al. Blood eosinophil counts and the development of obstructive lung disease: The Kangbuk Samsung health study. Eur Respir J. 2021;58(4):2003823.

179. Çolak Y, Afzal S, Marott JL, Vestbo J, Nordestgaard BG, Lange P. Type-2 inflammation and lung function decline in chronic airway disease in the general population. Thorax. 2024;79(4):349-58.

180. Pizzichini E, Pizzichini MM, Leigh R, Djukanović R, Sterk PJ. Safety of sputum induction. Eur Respir J 2002;37 suppl:9s-18s.

181. Jaffe MB. Mainstream or sidestream capnography. White paper. Wallingford CT: Respironics Novametrix, Inc; 2002. Contract No.: 5. Available from: https://www.med-sys.ru/pdf/Main%20vs%20Side.pdf.

182. Kodali BS. Physics of capnography - types of capnographs [Internet]. 1998 [cited 2024]. Available from: https://www.capnography.com/types-of-capnographs/.

183. ATS/ERS recommendations for standardized procedures for the online and offline measurement of exhaled lower respiratory nitric oxide and nasal nitric oxide, 2005. Am J Respir Crit Care Med. 2005;171(8):912-30.

184. Verscheure S, Massion PB, Verschuren F, Damas P, Magder S. Volumetric capnography: Lessons from the past and current clinical applications. Critical Care. 2016;20(1):184.

185. Corbelli R, Hammer J. Measurement of nasal nitric oxide. Paediatr Respir Rev. 2007;8(3):269-72.

186. Encyclopædia Britannica Inc. Sagittal view of the human nasal cavity. 2024. Available from: https://www.britannica.com/facts/soft-palate#/media/1/552432/70985

187. Mountain J. The lognormal lung : Quantifying inhomogeneity of ventilation. Oxford: University of Oxford; 2016.

188. Cicchetti DV. Guidelines, criteria, and rules of thumb for evaluating normed and standardized assessment instruments in psychology. US: American Psychological Association; 1994. p. 284-90.

189. Saito J, Gibeon D, Macedo P, Menzies-Gow A, Bhavsar PK, Chung KF. Domiciliary diurnal variation of exhaled nitric oxide fraction for asthma control. Eur Respir J. 2014;43(2):474-84.

190. Georges G, Bartelson BB, Martin RJ, Silkoff PE. Circadian variation in exhaled nitric oxide in nocturnal asthma. J Asthma. 1999;36(5):467-73.

191. Stark H, Purokivi M, Kiviranta J, Randell J, Tukiainen H. Short-term and seasonal variations of exhaled and nasal no in healthy subjects. Respir Med. 2007;101(2):265-71.

192. Verleden SE, Kirby M, Everaerts S, Vanstapel A, McDonough JE, Verbeken EK, et al. Small airway loss in the physiologically ageing lung: A cross-sectional study in unused donor lungs. Lancet Respir Med. 2021;9(2):167-74.

193. Fedosenko S, Venegas Garrido C, Nair P. Recent advances in asthma mucus biology and emerging treatment strategies. Curr Opin Pulm Med. 2025;31(3):251-61.

194. Farkas Á, Horváth A, Tomisa G, Kovács T, Böcskei RM, Kis E, et al. Do we really target the receptors? Deposition and co-deposition of ICS-LABA fixed combination drugs. Eur J Pharm Sci. 2022;174:106186.

195. Rhodes GR, Rohatagi S, Gillen MS, Deluccia F, Banerji DD, Chaikin P. In vitro and in vivo techniques used in drug development for evaluation of dose delivery of inhaled corticosteroids. J Clin Pharmacol. 2001;41(1):7-18.

196. Aung HWW, Boddy CE, Hampson E, Bell M, Parnell LA, Balasundaram K, et al. Assessing inhaled corticosteroid adherence and responsiveness in severe asthma using beclometasone dipropionate/formoterol nexthaler dose-counting and nitric oxide monitoring. J Allergy Clin Immunol Pract. 2024;12(6):1539-46.e5.

197. Couillard S, Shrimanker R, Lemaire-Paquette S, Hynes GM, Borg C, Connolly C, et al. Longitudinal changes in sputum and blood inflammatory mediators during FeNO suppression testing. Thorax. 2022;77(9):933-8.

198. Heaney LG, Busby J, Bradding P, Chaudhuri R, Mansur AH, Niven R, et al. Remotely monitored therapy and nitric oxide suppression identifies nonadherence in severe asthma. Am J Respir Crit Care Med. 2018;199(4):454-64.

199. Papi A, Brightling C, Pedersen SE, Reddel HK. Asthma. Lancet. 2018;391(10122):783-800.

200. Oppenheimer J, Hoyte FCL, Phipatanakul W, Silver J, Howarth P, Lugogo NL. Allergic and eosinophilic asthma in the era of biomarkers and biologics: Similarities, differences and misconceptions. Ann Allergy Asthma Immunol. 2022;129(2):169-80.

201. Habener A, Grychtol R, Gaedcke S, DeLuca D, Dittrich AM, Happle C, et al. IgA(+) memory B-cells are significantly increased in patients with asthma and small airway dysfunction. Eur Respir J. 2022;60(5).

202. Ciprandi G, Capasso M. Association of childhood perennial allergic rhinitis with subclinical airflow limitation. Clin Exp Allergy. 2010;40(3):398-402.

203. Riley CM, Wenzel SE, Castro M, Erzurum SC, Chung KF, Fitzpatrick AM, et al. Clinical implications of having reduced mid forced expiratory flow rates (FEF25-75), independently of FEV1, in adult patients with asthma. PLoS One. 2015;10(12):e0145476.

204. Svenningsen S, Haider E, Boylan C, Mukherjee M, Eddy RL, Capaldi DPI, et al. CT and functional MRI to evaluate airway mucus in severe asthma. Chest. 2019;155(6):1178-89.

205. Ragunayakam N, Thakar A, Sadafi H, Venegas Garrido C, Friedlander Y, Kjarsgaard M, et al. Computational fluid dynamics model predictions of inhaled corticosteroid deposition in patients with severe asthma. Thorax. 2025:thorax-2024-222444.

206. Zhang X, Rajaraman PK, Li F, Choi S, Comellas AP, Hoffman EA, et al. Assessment of ventilation heterogeneity and particle deposition in asthmatics using combined SPECT/CT imaging and computational modeling approaches. Eur J Pharm Sci. 2025;209:107093.

207. Castro M, Wenzel SE, Bleecker ER, Pizzichini E, Kuna P, Busse WW, et al. Benralizumab, an anti-interleukin 5 receptor α monoclonal antibody, versus placebo for uncontrolled eosinophilic asthma: A phase 2b randomised dose-ranging study. Lancet Respir Med. 2014;2(11):879-90.

208. Sorkness RL, Bleecker ER, Busse WW, Calhoun WJ, Castro M, Chung KF, et al. Lung function in adults with stable but severe asthma: Air trapping and incomplete reversal of obstruction with bronchodilation. J Appl Physiol. 2008;104(2):394-403.

209. Scichilone N, Battaglia S, Olivieri D, Bellia V. The role of small airways in monitoring the response to asthma treatment: What is beyond FEV1? Allergy. 2009;64(11):1563-9.

210. Chupp GL, Bradford ES, Albers FC, Bratton DJ, Wang-Jairaj J, Nelsen LM, et al. Efficacy of mepolizumab add-on therapy on health-related quality of life and markers of asthma control in severe eosinophilic asthma (musca): A randomised, double-blind, placebo-controlled, parallel-group, multicentre, phase 3b trial. Lancet Respir Med. 2017;5(5):390-400.

211. Sposato B, Camiciottoli G, Bacci E, Scalese M, Carpagnano GE, Pelaia C, et al. Mepolizumab effectiveness on small airway obstruction, corticosteroid sparing and maintenance therapy step-down in real life. Pulm Pharmacol Ther. 2020;61:101899.

212. Chan R, Lipworth BJ. Real-life effects of benralizumab on airway oscillometry in severe eosinophilic asthma. BMJ Open Respir Res. 2023;10(1).

213. Shirai T, Akamatsu T, Hirai K, Watanabe H, Tamura K, Kishimoto Y, et al. Oscillometry improves earlier than spirometry after benralizumab initiation in severe asthma. Allergy. 2020;75(10):2678-80.

214. Tracking development assistance for health and for COVID-19: A review of development assistance, government, out-of-pocket, and other private spending on health for 204 countries and territories, 1990-2050. Lancet. 2021;398(10308):1317-43.

215. Busana M, Giosa L, Cressoni M, Gasperetti A, Di Girolamo L, Martinelli A, et al. The impact of ventilation–perfusion inequality in COVID-19: A computational model. J Appl Physiol. 2021;130(3):865-76.

216. Xu H, Petousi N, Robbins PA. Identifying putative ventilation-perfusion distributions in COVID-19 pneumonia. PLoS One. 2022;17(8):e0273214.

217. Xu H, Petousi N, Robbins PA. Ventilation-perfusion inequality in COVID-19 pneumonia. J Appl Physiol (1985). 2021;131(2):868-9.